# Renewable Natural Polymer Thin Films and Their Interactions with Biomacromolecules

Chao Wang

Dissertation submitted to the faculty of the
Virginia Polytechnic Institute and State University
in partial fulfillment of the requirements for the degree of

**Doctor of Philosophy**
**in**
**Chemistry**

Alan R. Esker, Chair
Kevin J. Edgar
Harry W. Gibson
S. Richard Turner

July 30, 2014
Blacksburg, VA

Keywords: Chitin, Lignin, Cellulose, Hemicelluloses, Proteins, Thin Films, Enzymatic Degradation, Adsorption, Quartz Crystal Microbalance with Dissipation Monitoring, Surface Plasmon Resonance, Atomic Force Microscopy

**Natural Polymer Thin Films and Their Interactions with Biomacromolecules**

Chao Wang

## Abstract

Natural polymers from renewable resources have attracted increasing interest as candidates for renewable energy and functional materials. In this work, the interactions between natural polymer thin films and biomacromolecules were studied via surface analysis techniques, such as a quartz crystal microbalance with dissipation monitoring (QCM-D), surface plasmon resonance (SPR) and atomic force microscopy (AFM).

Chitinase activity on regenerated chitin (RChitin) films was studied by QCM-D and AFM. The optimal temperature and pH for chitinase activity on surfaces determined by QCM-D and AFM were consistent with bulk solution studies in the literature. Results from QCM-D also indicated that chitinase showed higher activity on fully acetylated chitin than highly deacetylated chitosan.

Nanocrystalline chitin (Chitin NC) thin films were prepared by spincoating a nanocrystalline chitin colloidal suspension onto solid surfaces. Solvent exchange experiments via QCM-D with $H_2O/D_2O$ revealed that Chitin NC films had more water than RChitin films of similar thickness. Results from QCM-D demonstrated that Chitin NC films had high bovine serum albumin loading capacity, and chitinase not only degraded, but also caused swelling of the chitin nanocrystals.

Adsorption of human serum albumin (HSA) and fibrinogen (HFN) onto bare gold, regenerated cellulose (RC) and RChitin thin films was studied by SPR and QCM-D. Studies by SPR indicated that HSA and HFN formed close-packed monolayers on gold surfaces and sub-

monolayers on polysaccharide surfaces, and the adsorption affinity of HSA for polysaccharide surfaces was greater than that of HFN. Results from QCM-D and SPR showed that the protein layers on polysaccharide surfaces had more associated water than proteins on gold surfaces.

The dehydrogenative polymerization of monolignols catalyzed by physically immobilized horseradish peroxidase was investigated using QCM-D and AFM. Results from QCM-D and AFM showed that coniferyl and *p*-coumaryl alcohol underwent polymerization directly, whereas sinapyl alcohol required the addition of a nucleophile for polymerization. Studies by QCM-D and AFM also indicated that the surface-initiated polymerization was greatly affected by the support surface, monolignol concentration, hydrogen peroxide concentration and temperature.

Thin films of dehydrogenative polymer (DHP), kraft (KL), organosolv (OL) and milled wood (MWL) lignins were used to study the enzymatic degradation of lignin mediated by lignin peroxidase (LiP) and manganese peroxidase (MnP). Results from QCM-D showed that the initial rates for degradation catalyzed by LiP increased in the order: KL < OL < MWL < guaiacyl DHP (G-DHP) < *p*-hydroxyphenyl DHP (H-DHP). In contrast, manganese peroxidase only degraded DHP films with a faster initial rate for G-DHP than H-DHP.

Adsorption of hemicelluloses onto KL, OL and MWL thin films was studied by QCM-D and SPR. Results from QCM-D showed that hemicelluloses with different structures displayed very different adsorption behavior. Adsorption isotherms from QCM-D and SPR indicated that xyloglucan possessed stronger affinity for KL and OL films than MWL films. Data from QCM-D and SPR revealed that xyloglucan formed less hydrated layers on lignin surfaces compared to RC surfaces, and the adsorbed xyloglucan layers on different lignin films had similar percentages of coupled water.

## Acknowledgments

First and foremost, I would like to thank for my advisor, Dr. Alan R. Esker, for his support, guidance, motivation and patience during the past five years. I appreciate all his contributions of time, ideas and funding to make my Ph.D. life easier and productive. I would also like to thank my committee members, Dr. Kevin J. Edgar, Dr. S. Richard Turner and Dr. Harry W. Gibson, for their insightful suggestions and constructive feedback on my work.

I am grateful to all my colleagues in the Esker research group, Dr. Qiongdan Xie, Dr. Zelin Liu, Dr. Yang Liu, Chuanzi Ouyang, Dr. Xiaosong Du, Dr. Joshua D. Kittle, Chen Qian, Xiao Zhang, Ying Ni, Sumin Shen, Jianzhao Liu, Michael R. Whitacre and Candace E. Wall, for their friendship and collaboration. In particular, I would like to thank Dr. Joshua D. Kittle, Chen Qian and Michael R. Whitacre for their help in my research, and thank Candace E. Wall for her help in editing my thesis.

I am grateful to Dr. Maren Roman, Dr. Wolfgang G. Glasser, Dr. Robert B. Moore, Dr. John R. Morris, Dr. Nicole R. Brown (Penn State University) and Dr. Paul Gatenholm (Chalmers University of Technology) for providing research samples and sharing equipment. I would like to thank my research collaborators, Dr. Michael S. Kent (Sandia National Lab) and Dr. Bingbing Li (Central Michigan University).

I would like to thank my friends, Zhengmian Chang, Mingqiang Zhang, Yaoying Wu, Dr. Jue Liang, Xi Geng, Ming Li, Dr. Xu Zhou, Jin Huang, whose support and help made my life in Blacksburg better. I am also grateful to all my basketball buddies in Blacksburg and my

teammates for the North East Chinese Basketball League (NECBL) tournament, who filled my Ph.D. life with enthusiasm and energy.

I would like to thank the Department of Chemistry for offering me teaching assistantships, a fellowship and research award. I am also grateful to the Center for Lignocellulose Structure & Formation (CLSF), an Energy Frontier Research Center funded by the U.S. Department of Energy, Office of Science, Office of Basic Energy Sciences under Award Number DESC0001090 for financial support for my research and USDA NIFA grant # 2010-65504-20429 for a travel grant.

Finally, I would like to thank my father, Jiashun Wang and my mother, Juan Xu for their love, support and encouragement over the years. I spent less than two months with them in the past five years, however, they are always there for me throughout my life. I am also grateful to my wife, Wenjun Zhao, for her love, understanding and patience. In the past five years, I could not be with her while she needed to work hard and lonely for her Ph.D. degree.

## Table of Contents

## List of Figures

**Chapter 2**

**Chapter 7**

## List of Tables

**Chapter 8**



**Chapter 9**

# Chapter 1: Overview

As the most abundant materials in nature, natural polymers (e.g., cellulose, chitin and lignin) have attracted increasing interest as candidates for renewable energy[1-3] and functional materials.[4-6] In this dissertation, thin films of natural polymers were employed as platforms to study their biosynthesis, enzymatic degradation and interactions with proteins and polysaccharides. A variety of surface analysis techniques, including a quartz crystal microbalance with dissipation monitoring (QCM-D), surface plasmon resonance (SPR) and atomic force microscopy (AFM), provided real-time and label-free approaches for monitoring the interactions between natural polymer thin films and biomacromolecules.

This dissertation consists of ten chapters.

Chapter 2 provides a general introduction to natural polymers (including both lignocellulosic biomass and chitin) and natural polymer-degrading enzymes (including cellulases, chitinases and ligninolytic enzymes). Additionally, literature methods for preparing cellulose, lignin and chitin thin films are reviewed. Finally, a brief introduction to the major surface analysis techniques used in this dissertation, including QCM-D, SPR and AFM, is presented.

Chapter 3 details the materials, synthesis, thin film preparation, experimental procedures and data analysis methods used in this dissertation.

Chapter 4 introduces a real-time and label-free method to assay chitinase activity using QCM-D and AFM. Chitinase (from *Streptomyces griseus*) activity on amorphous regenerated chitin (RChitin) thin films at various enzyme concentrations, temperatures, pH and degrees of acetylation (DA) was investigated by QCM-D and AFM. The optimal experimental conditions

for studies of chitinase activity on surfaces are compared with bulk solution studies in the literature.

Chapter 5 presents a simple method to prepare nanocrystalline chitin (Chitin NC) thin films by spincoating a colloidal suspension of chitin nanocrystals onto a gold substrate modified by an amine-terminated self-assembled monolayer. The Chitin NC film was characterized by X-ray diffraction (XRD) and AFM. The water content of the Chitin NC film was determined using QCM-D and $H_2O/D_2O$ solvent exchange. The chitinase-catalyzed hydrolysis of these Chitin NC films was investigated via QCM-D. The utility of these Chitin NC films as potential enzyme immobilization supports was demonstrated through the adsorption of bovine serum albumin (BSA) onto the films in QCM-D studies.

Chapter 6 involves adsorption studies of two human plasma proteins, serum albumin (HSA) and fibrinogen (HFN), onto amorphous regenerated cellulose (RC) and RChitin surfaces using SPR and QCM-D. Adsorption isotherms for HSA and HFN adsorption onto RC and RChitin thin films under biomimetic conditions (37°C and pH = 7.4) were obtained from SPR measurements. Water contents of the adsorbed proteins on bare gold, RC and RChitin surfaces were determined by SPR and QCM-D.

In Chapter 7, the polymerization of three lignin monomers (monolignols) initiated by horseradish peroxidase (HRP) immobilized on various solid surfaces was monitored by QCM-D, and the morphologies of the resulting dehydrogenative polymer (DHP) lignin thin films were studied by AFM. The effects of the type of solid surface, presence of nucleophiles, monolignol concentration, hydrogen peroxide ($H_2O_2$) concentration and temperature on the dehydrogenative polymerization were investigated and are discussed in this chapter.

Chapter 8 presents studies of the enzymatic degradation of lignin (including DHP, kraft, organosolv and milled wood lignins) thin films in the presence of lignin peroxidase/$H_2O_2$ and manganese peroxidase/$H_2O_2$/Mn (II). The degradation kinetics were monitored by QCM-D, and morphological changes of the lignin films were studied by AFM.

Chapter 9 presents adsorption studies for a variety of hemicelluloses onto thin films of lignins (including kraft, organosolv and milled wood lignins) using QCM-D and SPR, specifically focusing on the adsorption of xyloglucan (from tamarind seeds). Adsorption isotherms for xyloglucan adsorption onto the lignin films and the water contents of the adsorbed xyloglucan layers were obtained from QCM-D and SPR measurements.

Chapter 10 summarizes the overall conclusions and provides suggestions for future work related to the studies in this dissertation.

**References**

(1) Hamelinck, C. N.; Hooijdonk, G. v.; Faaij, A. P. C. *Biomass Bioenergy* **2005,** 28, 384-410.

(2) Farrell, A. E.; Plevin, R. J.; Turner, B. T.; Jones, A. D.; O'Hare, M.; Kammen, D. M. *Science* **2006,** 311, 506-508.

(3) Carroll, A.; Somerville, C. *Annu. Rev. Plant Biol.* **2009,** 60, 165-182.

(4) Czaja, W.; Krystynowicz, A.; Bielecki, S.; Brown Jr, R. M. *Biomaterials* **2006,** 27, 145-151.

(5) Ravi Kumar, M. N. V. *React. Funct. Polym.* **2000,** 46, 1-27.

(6) Jayakumar, R.; Prabaharan, M.; Sudheesh Kumar, P. T.; Nair, S. V.; Tamura, H. *Biotechnol. Adv.* **2011,** 29, 322-337.

# Chapter 2: Introduction and Review

## 2.1 Introduction to Natural Polymers

Modern industries rely on petroleum, coal and natural gas as energy resources and organic chemical feedstocks.[1] However, the possible crisis of fossil resource availability and global environmental problems require energy and raw material replacements from non-fossil or renewable resources. Natural polymers, including polysaccharides, proteins, polynucleotides, lignin and naturally occurring miscellaneous polymers, are polymers produced by living organisms.[2] As the most abundant natural polymer-based raw material on the earth, lignocellulosic biomass is recognized as one of the most important resources for biofuel production.[3-5] Additionally, polysaccharides (e.g., cellulose and chitin) and their derivatives are widely used as biomaterials, food additives and textile fibers.[6-8]

## 2.2 Lignocellulosic Biomass

Lignocellulosic biomass is plant biomass that is mainly composed of carbohydrate polymers (cellulose, hemicelluloses and pectins) and phenylpropanoid polymers (lignins). Common examples of lignocellulosic biomass include woody biomass, non-woody biomass (e.g., straws, bagasse and stover) and organic wastes (e.g., industrial processing residues and municipal solid waste).[9] Lignocellulosic biomass can be converted to cellulosic ethanol via three steps: 1) delignification, 2) degradation of carbohydrate polymers to generate fermentable sugars (e.g., glucose and xylose) and 3) fermentation to produce ethanol or other liquid fuels.[10] Compared to starch ethanol (mainly from corn) and sugarcane ethanol, cellulosic ethanol is environmentally favorable since it reduces greenhouse gas emission by over 85%, protects biodiversity, and does not compete with food production.[11] However, the complexity of lignocellulosic biomass

requires more pretreatment and thus increases the cost and limits the yield of fermentable sugars compared to corn or sugarcane.[12-14] The improvement of lignocellulosic biomass via bioengineering strategies and the investigation of more efficient and robust hydrolytic enzymes may reduce the cost and increase the yield of fermentable sugars.[15, 16]

### 2.2.1 Introduction to Plant Cell Walls

Plant cell walls are semi-rigid layers composed of polysaccharides, lignins and structural proteins which are located outside the cell membranes.[17] Plant cell walls play important roles in protection, structural support, transport, filtration of large molecules, absorption and secretion of substances in plants.[17, 18] Instead of tough and constant layers, plant cell walls are dynamic structures in which the compositions and properties vary in response to the growth of a plant cell. The cell wall expands via enzymatic hydrolysis of the polysaccharide matrix or the rearrangement (or slippage) of the matrix.[17, 19, 20] The cell wall makes plant cells different from animal cells. Because of rigid plant cell walls, trees can grow to heights of tens of meters with good mechanical strength. On the other hand, plants lose opportunities to develop nervous systems, immune systems, and mobility because of the rigid structure encased by cell walls.

### 2.2.2 Structures of Plant Cell Walls

A plant cell wall consists of three different layers: the middle lamella, the primary cell wall and the secondary cell wall.[21] These regions are schematically depicted in **Figure 2.1**.

The middle lamella is the outermost layer of a plant cell wall and it glues adjacent cells together.[22] The middle lamella is the first layer formed at the time of cytokinesis. The major components in the middle lamella are calcium and magnesium pectates. If the middle lamella is destroyed, the cells become isolated as occurs in autumn when leaves fall.

The primary cell wall is formed in the growth period of a plant cell, and it is a flexible and extendable layer. A primary cell wall is composed of cellulose (15 ~ 30%), hemicelluloses (25%), pectins (10 ~ 30%) and proteins (20%).[23] Cellulose exists in the form of microfibrils in primary cell walls, and the microfibrils are physically cross-linked by hemicelluloses to form a cellulose-hemicellulose network. Xyloglucan and glucuronarabinoxylan are the most common hemicelluloses in the primary cell walls of woody plants and grasses, respectively.[24]

The secondary cell wall is a thick layer found between a primary cell wall and the cell membrane and is deposited when the cells stop growing or begin to differentiate. The secondary cell wall, with a thickness of 5 ~ 10 μm, is the major component of woody tissues. The secondary cell wall can be divided into three different layers: $S_1$, $S_2$ and $S_3$, in which the orientations of the cellulose microfibrils are different. The main components in secondary cell walls include cellulose (35 ~ 50%), hemicelluloses (20 ~ 35%) and lignin (10 ~ 25%).[25] Lignin fills the spaces between the cellulose-hemicellulose network, making the vascular tissue waterproof and providing mechanical strength. Unlike primary cell walls, there are almost no proteins, enzymes or pectins in secondary cell walls.

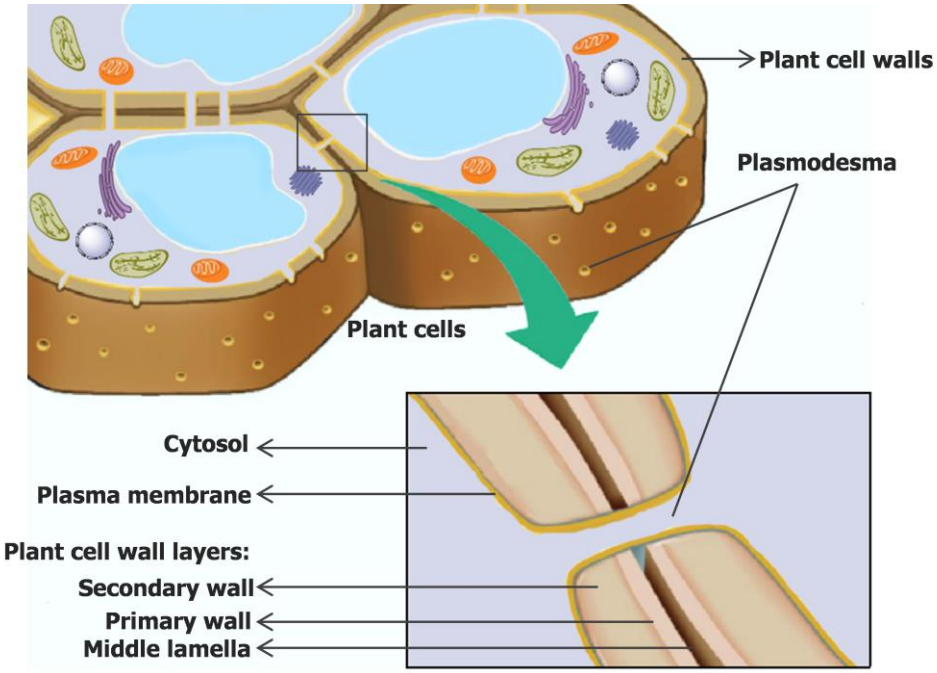


**Figure 2.1.** Depiction of the structure of a plant cell wall. Adapted from Campbell et al.[21]

### 2.2.3 Principal Components of Plant Cell Walls

#### 2.2.3.1 Cellulose

Cellulose is the most abundant organic substance on earth and accounts for about 33% of all plant matter and 40 ~ 50% of dry wood by mass.[26] Cellulose is a linear polysaccharide composed of D-glucose units linked by β-(1→4) glycosidic bonds. Cellulose from different resources and processing methods has different chain lengths or degrees of polymerization (DP). For example, the DP ranges between 300 and 1700 for cellulose from wood pulp, and 800 and 10000 for cellulose from cotton fibers and bacteria.[27] The actual repeating unit of cellulose is a dimer known as cellobiose (**Figure 2.2**). Cellulose is tasteless, odorless, biodegradable and biocompatible, and natural cellulose is highly crystalline and insoluble in water and most organic solvents. However, crystalline cellulose can be dissolved in several solvent systems, including

aqueous alkali containing solvents (e.g., sodium hydroxide (NaOH)/urea), ionic liquids (e.g., imidazole based ionic liquids) and organic solvent/salt systems (e.g., *N*,*N*-dimethylacetamide (DMAc)/lithium chloride (LiCl)).[28] In industry, cellulose is mainly used as pulp, textile raw materials and food additives. Cellulose can be converted into ether or ester derivatives via heterogeneous or homogeneous reactions, and such derivatives show widespread applications in the biomedical, plastic, food, paint and coating industries.[29] Recently, converting cellulose into biofuels, such as cellulosic ethanol, has been proposed as a cost-effective alternative for fossil fuels.[4, 11]

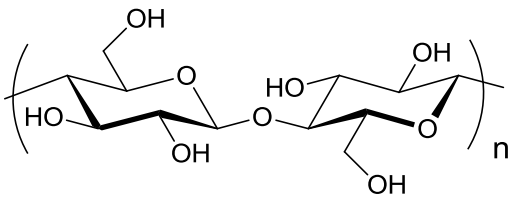


**Figure 2.2.** Repeating unit of cellulose, cellobiose.

Seven different crystalline structures of cellulose (I, II, $III_1$, $III_{11}$, $IV_1$, $IV_{11}$) are known to exist and differ with respect to the locations of hydrogen bonds between and within strands.[30] The interrelationships between different polymorphs of cellulose are summarized in **Figure 2.3**. Natural cellulose is cellulose I and the dominant intermolecular and intramolecular bonds in cellulose I are O6-H···O3 and O3-H···O5, respectively.[31] Cellulose I is a mixture of cellulose $I_\alpha$ and cellulose $I_\beta$. Natural cellulose produced by bacteria consists mainly of cellulose $I_\alpha$, while natural cellulose from plants is cellulose $I_\beta$.[30] Cellulose II is obtained from cellulose I by either regeneration (in which cellulose I is dissolved in solvents followed by reprecipitation) or mercerization (in which cellulose I is swollen in NaOH solution followed by removal of the swelling agent). The dominant intermolecular and intramolecular bonds in cellulose II are O6-H···O2 and O3-H···O5, respectively.[32] The conversion from cellulose I to cellulose II is

irreversible, which indicates that cellulose I is not a thermodynamically stable polymorph. Cellulose $III_1$ and $III_{11}$ are obtained by treating cellulose I and II with liquid ammonia, respectively. Cellulose $IV_1$ and $IV_{11}$ are formed by heating Cellulose $III_1$ and $III_{11}$ to 200 °C in glycerol, respectively.[30] The crystalline structures of cellulose can be determined by solid state NMR, X-Ray or neutron diffraction.[33, 34]

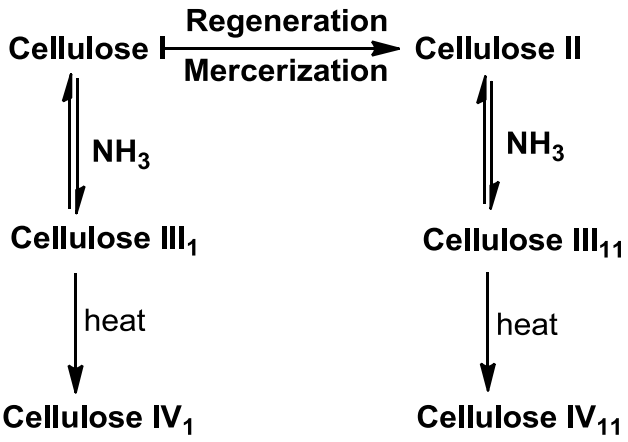


**Figure 2.3.** Interconversion of the polymorphs of cellulose. Adapted from O'Sullivan et al.[30]

In plant cell walls, the cellulose microfibrils are highly crystalline structures but also contain some disordered regions. The cellulose microfibrils in plant cell walls have diameters of 2 to 10 nm and lengths of 5 to 10 μm. These dimensions vary with the biological source and measurement methods.[35] The cellulose microfibrils are reported to be either right-handed or left-handed helically twisted due to the hydrogen bonding within glucan chains.[36] The cellulose microfibrils are biosynthesized by cellulose synthase (CESA) enzyme complexes which are embedded in the plasma membrane. The complexes have hexameric rosette structures with a diameter of 25 to 30 nm.[37-39] The CESAs are encoded by CESA genes which were discovered in the late 1990s. The CESA family contains about ten different genes which are expressed in different cells and tissues.[37-39]

### 2.2.3.2 Hemicelluloses

Hemicelluloses are among the most abundant organic substances in a plant, comprising 25 to 33% of plant matter by mass. Hemicelluloses are also the most complex components in plant cell walls. Generally, hemicelluloses are amorphous and branched polysaccharides composed of a variety of monosaccharides, such as D-xylose, D-galactose, D-mannose, D-arabinose, L-rhamnose, D-glucuronic acid, 4-O-methyl-D-glucuronic acid and D-galacturonic acid (**Figure 2.4**). Hemicelluloses have shorter chain lengths or DP compared to cellulose and are easily hydrolyzed by dilute base or acid. Commercially available hemicelluloses are usually extracted from plant tissues by aqueous alkaline solutions or steam explosion.[40] Hemicelluloses have widespread uses in food, biomedical, pulp and paper, packaging and energy industries.[40]

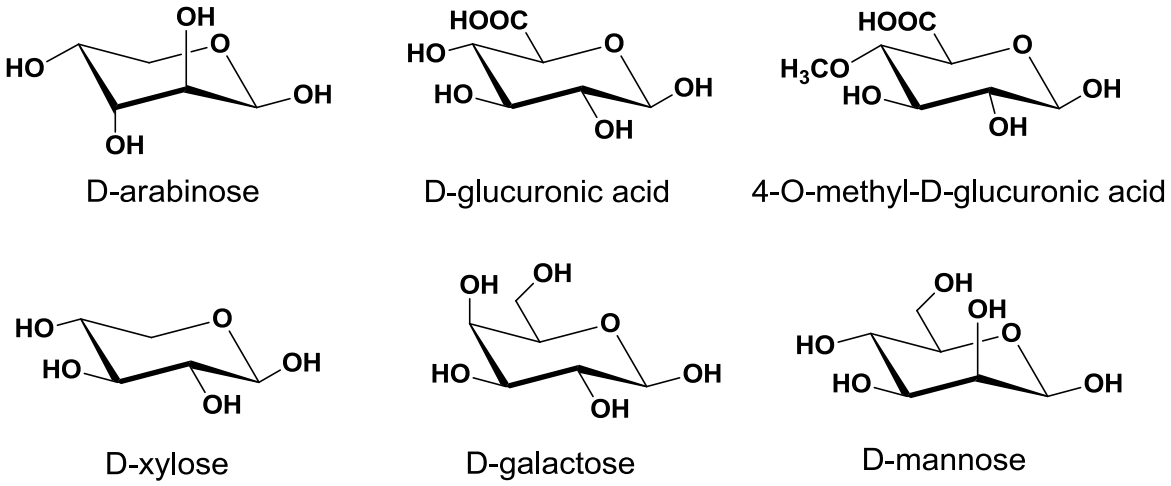


**Figure 2.4.** Sugar monomers of hemicelluloses.

The types and contents of hemicelluloses vary in different plants (**Table 2.1**). In general, hemicelluloses could be categorized as xyloglucans, xylans, mannans (glucomannans), and mixed-linkage $\beta$-glucans ($\beta$-(1→3,1→4)-glucans).[24] Xyloglucans are the most abundant hemicelluloses in the primary cell walls of non-graminaceous plants.[24, 41] Xyloglucans have a backbone of $\beta$-(1→4) linked D-glucose with ~ 75 % of the O-6 positions substituted with $\alpha$-D-

xylosyl residues. The xylosyl residues could also be decorated with $\beta$-D-galactosyl and $\alpha$-L-fucosyl residues.[24, 41] Xylans are polysaccharides which feature a backbone of $\beta$-(1→4) linked D-xylose and substituents on the O-2 and O-3 positions with $\alpha$-D-glucuronosyl, $\alpha$-4-O-methyl D-glucuronosyl, $\alpha$-L-arabinosyl and acetyl residues. Glucuronoxylans are the most abundant hemicelluloses in the secondary cell walls of dicots, and glucuronoarabinoxylans and arabinoxylans are the major hemicelluloses in both the primary and secondary cell walls of grasses.[24] Mannans are polysaccharides with backbones composed of $\beta$-(1→4) linked D-mannose or a combination of D-mannose and D-glucose (glucomannan). Mannans are usually acetylated and the O-6 positions are commonly modified with $\alpha$-D-galactosyl residues. Galactoglucomannans are the dominant hemicelluloses in the secondary cell walls of gymnosperms (e.g., conifers).[24, 42] The representative chemical structures for xyloglucans, galactomannans, glucomannans, arabinoxylan and glucuronoarabinoxylans are depicted in **Figure 2.5**.

**Table 2.1.** Percentages (% w/w) of hemicelluloses in primary and secondary cell walls of plants. Adapted from Scheller et al.[24]

| Hemicelluloses | Dicot walls | | Grass walls | | Conifer walls | |
|---|---|---|---|---|---|---|
| | **Primary** | **Secondary** | **Primary** | **Secondary** | **Primary** | **Secondary** |
| Xyloglucans | 20 ~ 25 | minor | 2 ~ 5 | minor | 10 | --[a] |
| Glucuronoxylans | -- | 20 ~ 30 | -- | -- | -- | -- |
| Glucurono-arabinoxylans | ~ 5 | -- | 20 ~ 40 | 40 ~ 50 | ~ 2 | 5 ~ 15 |
| Glucomannan | 3 ~ 5 | 2 ~ 5 | ~ 2 | 0 ~ 5 | -- | -- |
| Galacto-glucomannans | -- | 0 ~ 3 | -- | -- | data N/A | 10 ~ 30 |
| Mixed-linkage $\beta$-glucans | Absent | Absent | 2 ~ 15 | Minor | Absent | Absent |

[a]--: absent or minor.

In plant cell walls, hemicelluloses physically link to cellulose by hydrogen bonds and bind to lignin through both covalent and physical interactions. Hemicelluloses with higher degrees of side-chains bind less tightly to cellulose but are more water-soluble, while hemicelluloses with fewer side-chain substitution bind tightly to cellulose but are less water-soluble.[43] Hemicelluloses are biosynthesized from nucleotide sugars (e.g., guanosine diphosphate mannose and uridine diphosphate galactose)[44] in the Golgi apparatus by glycan synthases and are transported to the plasma membrane via Golgi vesicles.[37, 44]

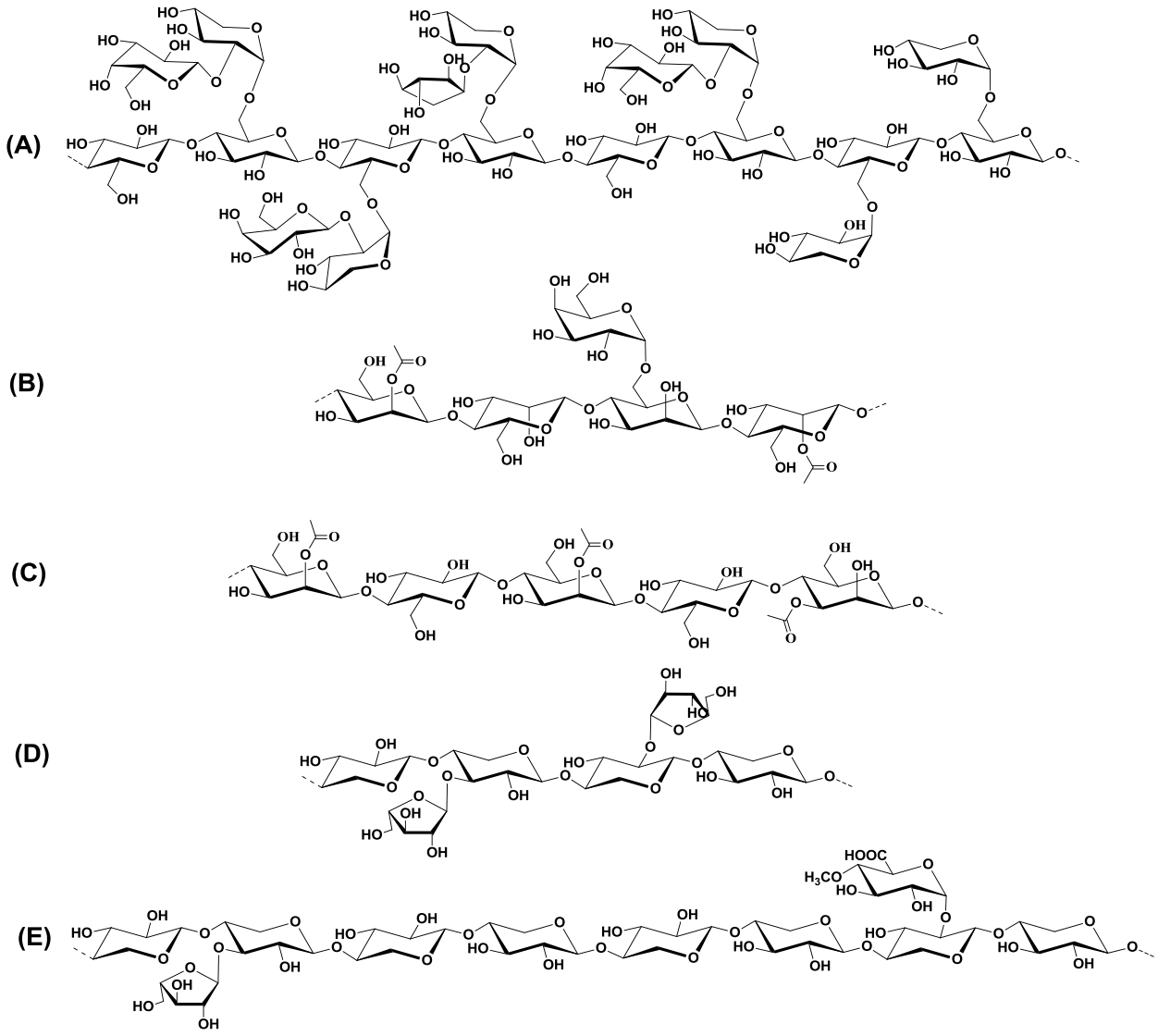


**Figure 2.5.** Representative structures of (A) a xyloglucan, (B) a galactomannan, (C) a glucomannan, (D) an arabinoxylan and (E) a glucuronoarabinoxylan. Adapted from Ebringerová et al.[40]

### 2.2.3.3 Lignins

Lignins are complex phenolic heteropolymers derived from the xylem tissues of vascular plants. Lignins are among the most abundant biopolymers, and account for about 30% of the non-fossil organic carbon in the biosphere.[45] As one of the most hydrophobic components in

plant cell walls, lignins play important roles in waterproofing the vascular tissues, thereby enabling the transport of water and nutrients, and protecting plants against pathogens.[16, 45, 46] In plant cells, lignins are primarily synthesized through the dehydrogenative polymerization of three hydroxycinnamyl alcohol monomers (monolignols), namely 4-hydroxycinnamyl (*p*-coumaryl, H) alcohol, 4-hydroxy-3-methoxycinnamyl (coniferyl, G) alcohol and 4-hydroxy-3,5-dimethoxycinnamyl (sinapyl, S) alcohol, differing in the degree of methoxylation (**Figure 2.6**). The content and composition of lignins vary among tissues and species. Softwood (gymnosperm) lignins contain mostly G units and a small quantity of H units, and hardwood (dicotyledonous angiosperm) lignins are composed of G and S units, with traces of H units, whereas lignins from grasses are usually a mixture of H, G and S units.[16, 45, 47] Although many efforts have been made to determine the structures of native lignins, the exact structure is still unknown due to their complexity. The major chemical linkages in soft wood lignins were summarized by Chakar et al. and are depicted in **Figure 2.7**. The major linkages include *β*-O-4 (45 ~ 50 %), 5-5 (18 ~ 25 %), *β*-5 (9 ~ 12 %), *α*-O-4 (6 ~ 8 %), 4-O-5 (4 ~ 8 %), *β*-1 (7 ~ 10 %), *β*-*β* (~ 3 %) and dibenzodioxocin (5 ~ 7 %).[47, 48]

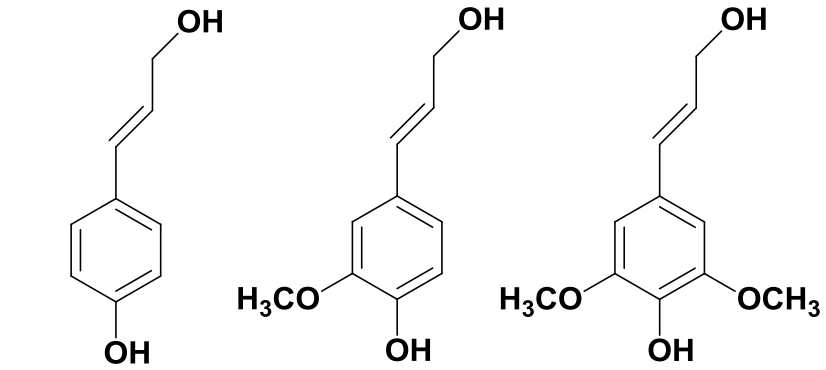


**Figure 2.6.** Chemical structures of monolignols.

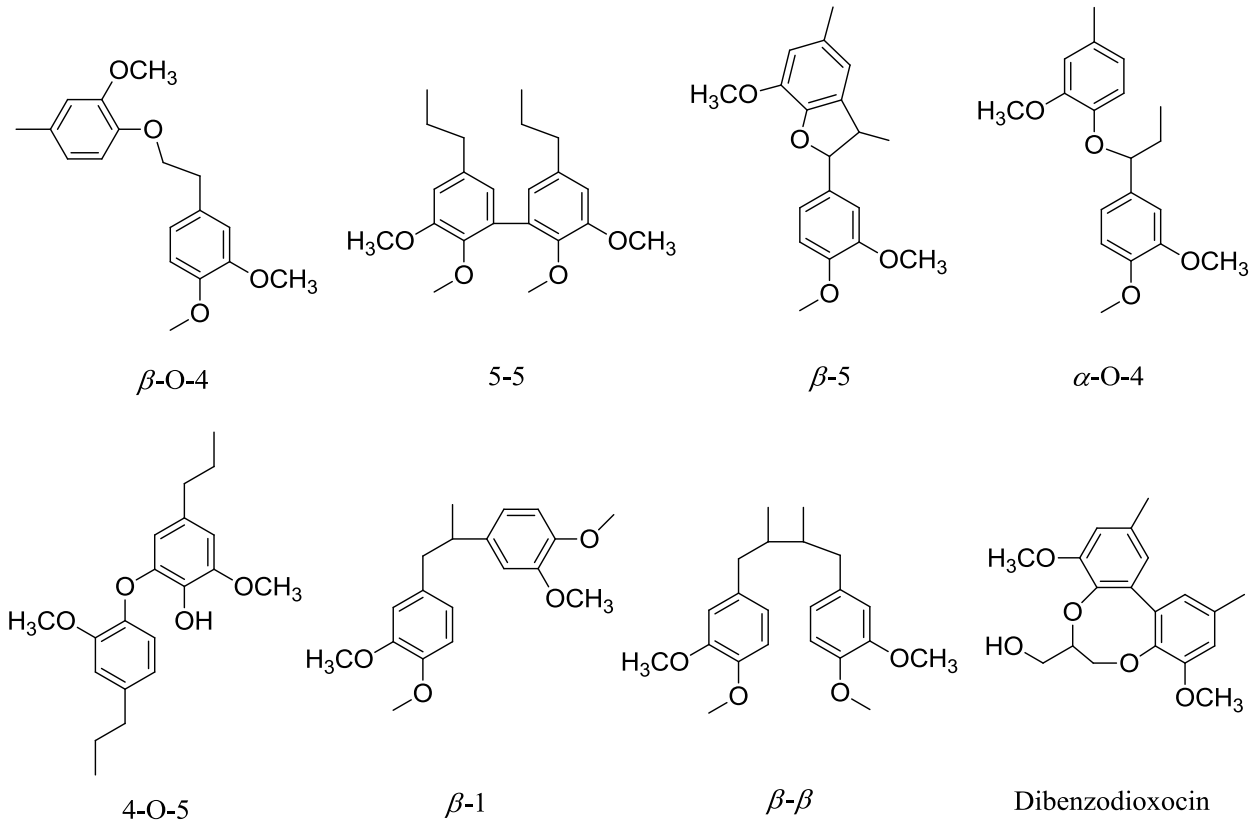


**Figure 2.7.** Possible chemical linkages in a softwood lignin. Adapted from Chakar et al.[48]

The exact structure and DP of native lignins are unknown because the structures of native lignins are destroyed during isolation. Lignins are usually isolated from woody tissues by either dissolving lignin via solvent extraction or removing carbohydrate components via enzymatic hydrolysis.[49, 50] The reaction conditions of the isolation processes are usually harsh with high temperature, high pressure and high (or low) pH, so the chemical structures and linkages of the native lignins are altered during isolation. Most of the commercially available lignin is a by-product from the kraft pulping process in which wood chips are treated with cooking liquor (a solution of sodium hydroxide and sodium sulfide) at ~ 170 °C. In a kraft process, lignin is fragmented mainly via the cleavage of $\alpha$-aryl ether and $\beta$-aryl ether bonds by the hydroxide and hydrosulfide anions in the cooking liquor.[48] Kraft lignin (KL) has relatively low molar mass and

contains thiol groups. Organosolv lignin (OL) and milled wood lignin (MWL) are also commonly used isolated lignins in industry and research. The OLs are by-products from organosolv pulping in which lignin is extracted from wood chips with organic solvents (e.g., alcohols, ketones and glycols) with a little water, acid or base as a catalyst under relatively mild conditions.[51] The MWLs are isolated via neutral solvents (e.g., aqueous dioxane or acetone) by extraction of finely milled wood meal at room temperature. As MWLs are isolated under the most mild conditions, MWLs are considered to have structures that best represent native lignin (especially lignin in the secondary cell wall).[52, 53] Lignins have been viewed as waste by-products from pulp and papermaking. Recently, lignins have revealed enormous potential as fillers or precursors for various polymeric materials (e.g., polyurethanes and epoxy resins),[54, 55] precursors for carbon materials (e.g., carbon fibers and active carbon)[56] and feedstocks for various useful chemicals (e.g., toluene and vanillin)[47] via depolymerization, hydrogenolysis, pyrolysis, hydrolysis and oxidation.[57]

The biosynthetic pathway to lignin has been studied for more than a century, and has been reviewed in detail elsewhere.[16, 45, 46, 58] In general, the biosynthesis of lignin can be classified into three stages: biosynthesis of monolignols, transport of monolignols to the cell wall, and the dehydrogenative polymerization of monolignols in the cell wall. In the cytosol, monolignols are derived from phenylalanine through a multistep process under strict regulation, including the deamination, hydroxylation and methoxylation of the aromatic ring.[45, 46] Monolignol glucosides which are generated by glycosylating the phenolic groups are believed to serve as both transport and storage intermediates for monolignols.[46] The glucosides are transported across the cell membrane to the cell wall via Golgi-derived vesicles or ATP-binding cassette-like transporters,[58-60] where the glycosidic bonds are cleaved by $\beta$-glucosidases to liberate

monolignols. In the cell wall, monolignols are dehydrogenated by cell wall-bound enzymes to form phenolic radicals in a complex matrix containing polysaccharides and proteins that can influence the structure of the lignin that forms. The coupling of these radicals gives rise to polymeric species with variable substitution patterns, linear segments, and lignin carbohydrate complexes (LCCs) that effectively form a three-dimensional network.[61] This process is also called lignification, and is hypothesized to proceed after the division and expansion of the cells.[62] The enzymes involved in the dehydrogenative polymerization include peroxidases, laccases and other oxidases. Peroxidases are a family of heme-containing enzymes that oxidize various organic substrates in the presence of hydrogen peroxide ($H_2O_2$).[63] Laccases are multinuclear copper-containing enzymes that utilize molecular oxygen ($O_2$) to convert monolignols into radicals in plant cell walls.[64]

### 2.3 Chitin

Chitin is a natural polysaccharide composed of $\beta$-(1→4) linked *N*-acetyl-D-glucosamine units (**Figure 2.8**). As one of the most abundant biopolymers in nature, chitin is widely distributed in the exoskeletons of crustaceans (e.g., shrimps, crabs and lobsters) and insects, the cell walls of fungi, and the beaks of cephalopods (e.g., octopi and squid).[65] In nature, chitin occurs as ordered crystalline microfibrils which associate with proteins, lipids, polysaccharides, calcium carbonate, and pigments to form natural composites.[66] In the exoskeletons of crustaceans, $\alpha$-chitin crystals are wrapped by proteins to form nanofibrils with diameters of 2 to 5 nm and lengths of ~ 300 nm, and these nanofibrils cluster into long chitin-protein fibers with diameters of 50 to 300 nm.[66] The spaces between the chitin-protein fibers are filled with proteins and calcium carbonate (**Figure 2.9**). In fungal cell walls, chitin microfibrils cross-link with a variety of amorphous glucans (including $\beta$-1,3-, and $\alpha$-1,3- and mixed $\beta$-1,3-/$\beta$-1,4-, $\beta$-1,6- glucans) and glycoproteins and

mannans to form a complex network.[67, 68] As crystalline polymers, chitin microfibrils significantly contribute to the stiffness and integrity of fungal cell walls.

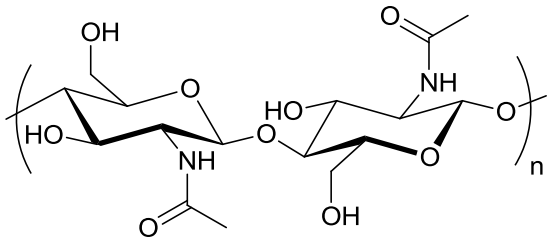


**Figure 2.8.** Repeating unit of chitin.

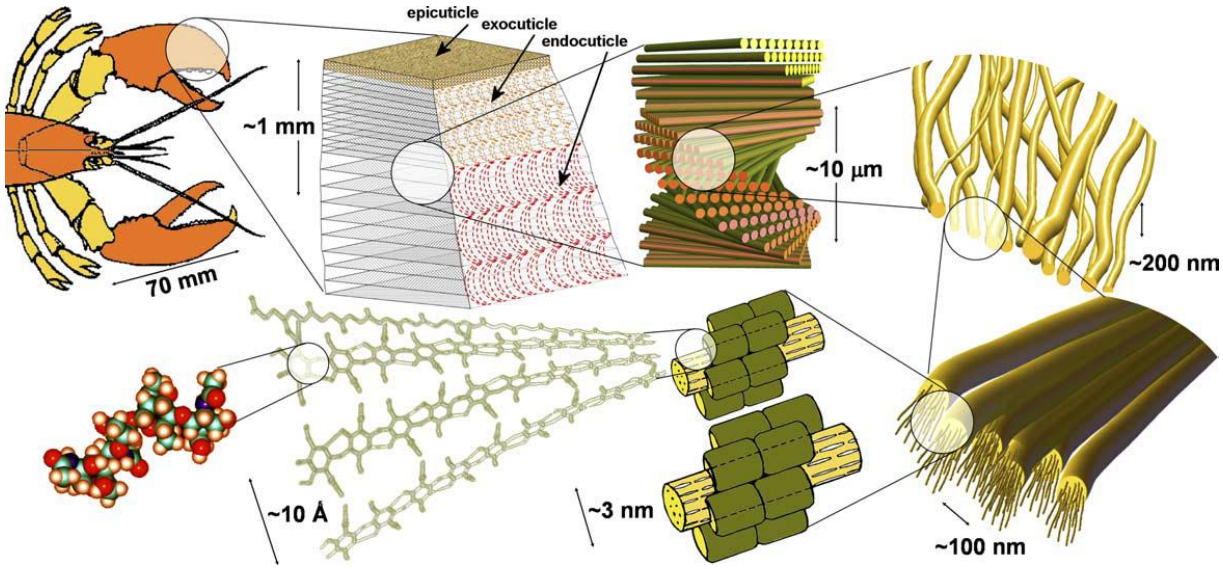


**Figure 2.9.** The structure of the exoskeleton of *H. americanus* (American lobster).[66] "Reprinted from Raabe, D.; Sachs, C.; Romano, P. *Acta Mater.* **2005,** 53, 4281-4292. Copyright (2005), with permission from Elsevier."

Two polymorphs of chitin ($\alpha$ and $\beta$) have been reported, differing with respect to the locations and quantity of hydrogen bonds.[69, 70] $\alpha$-Chitin is the most abundant and stable form, and it is derived from crustacean tendons and shells, yeast and fungal cell walls, as well as insect cuticles.[71, 72] $\beta$-Chitin is less abundant and stable than $\alpha$-chitin, and it is found in squid pens and

tubeworms.[73, 74] Compared to $\alpha$-chitin, $\beta$-chitin is more susceptible to swelling. $\beta$-Chitin can be reversibly swelled by water, alcohols or amines, and irreversibly swelled by strongly acidic or basic solutions.[75, 76] $\beta$-Chitin can also be converted into thermodynamically stable $\alpha$-chitin via dissolution or extensive swelling under strongly acidic or basic conditions.[76, 77]

Similar to cellulose, chitin is also insoluble in water and common organic solvents due to the strong intermolecular and intramolecular hydrogen bonds. Several solvent systems have been developed for the dissolution of chitin, in which chitin could be processed or modified homogeneously. Such solvent systems include strong acid (e.g., trichloroacetic acid),[78] polar fluorinated solvents (e.g., hexafluoroisopropanol),[78] DMAc/LiCl,[79, 80] aqueous alkali containing solvents (e.g., NaOH/urea)[81] and ionic liquids.[82] Upon partial deacetylation by exposure to alkaline conditions, chitin becomes chitosan, which is biocompatible, biodegradable, and water-soluble at low pH. Chitin, chitosan and their derivatives have been widely used in heavy metal ion and dye containing wastewater treatment, biomedical materials, pharmaceutical formulations and papermaking.[7, 65] In biomedical areas, wound-dressing materials,[8, 83] drug carriers,[84, 85] tissue engineering scaffolds,[86, 87] enzyme and cell immobilization supports,[88, 89] and biosensors [90, 91] have been fabricated based upon chitin and chitosan for their biocompatibility, biodegradability, affinity for proteins, antimicrobial, physiological inertness and gel-forming properties.

### 2.4 Natural Polymer Degrading Enzymes

The biodegradation of natural polymers is not only essential for maintaining the carbon cycle in the biosphere, but is also crucial for many industrial applications, such as the biorefinery, waste treatment, biopulping and biobleaching. In nature, the biodegradation of natural polymers

is usually performed by microorganisms (e.g., bacteria, protozoa and fungi) with the participation of a variety of hydrolytic or oxidative enzymes under precise regulation.

### 2.4.1 Cellulases

Cellulases are a family of enzymes that catalyze the hydrolysis of cellulose, and cellulases are produced by fungi, bacteria, protozoans and ruminants. Commercially available cellulases are usually derived from fungi, because fungal cellulases are available in larger quantities than cellulases from other sources and do not form physical complexes (cellulosomes) with each other.[92, 93] Cellulases have attracted increasing interest for food, wine and beer, textile and laundry, pulp and paper, animal feed and agricultural applications.[94]

Cellulases can be divided into three categories:[95] endo-1,4-$\beta$-glucanases (EGs) that attack cellulose chains in random locations along the cellulose microfibrils to disrupt the crystalline structure; exo-glucanases or exo-cellobiohydrolases (CBHs) that cleave 2 to 4 glucose units from either the reducing or non-reducing ends of the cellulose chains to form cellobiose or tetrasaccharides; and $\beta$-glucosidases (BGLs) that hydrolyze the exo-glucanase products to glucose. Although they play different roles in the hydrolysis of cellulose, the overall hydrolysis is attributed to the synergistic interactions of the different cellulases.

Many cellulases, especially exo-glucanases, have modular structures composed of two independent modules,[95, 96] with a catalytic module (CM) responsible for the hydrolysis of cellulose, and a cellulose-binding module (CBM) which lacks catalytic activity but is responsible for the adsorption of the enzyme onto cellulose. The two domains are connected by a flexible linker peptide. However, some exceptions exist. For example, some EGs do not have CBMs.

The hydrolysis of cellulose is catalyzed by carboxyl groups in the catalytic module of cellulases as depicted in **Figure 2.10**. The configurations of the anomeric carbon in the cellulose chain are either inverted or retained during enzymatic hydrolysis. A one-step mechanism has been proposed for cellulases that invert the configuration, where one carboxyl group acts as an acid and the other acts as a base. In contrast, a two-step mechanism has been proposed for cellulases that retain the configuration, where one carboxyl group acts as both an acid and a base and the other acts as both a nucleophile and a leaving group.[95, 97, 98]

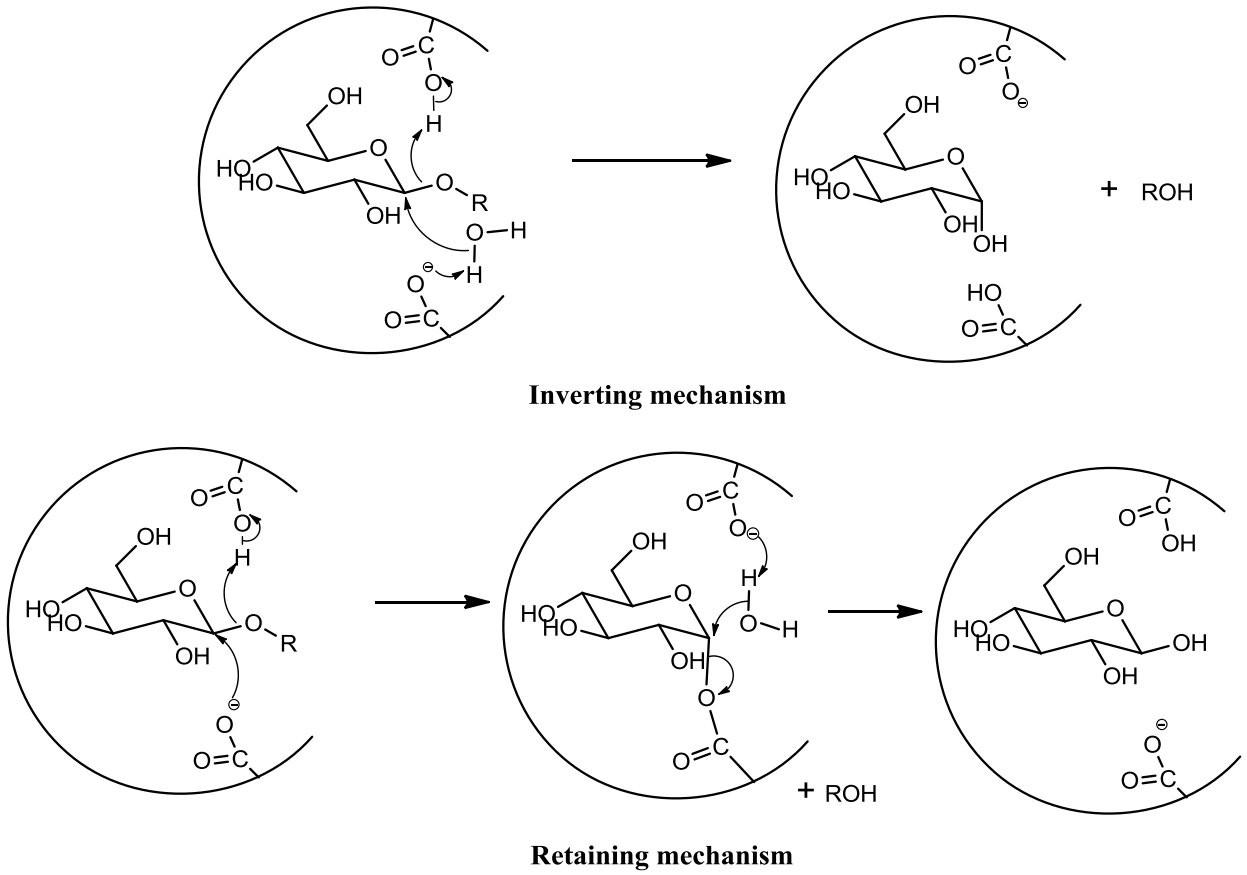


**Figure 2.10.** Schematic representations of cellulose hydrolysis mechanisms catalyzed by cellulases. Adapted from McCarter et al.[97]

### 2.4.2 Chitinases

Chitinases are hydrolytic enzymes that cleave $\beta$-(1→4) glycosidic bonds between two consecutive *N*-acetyl-D-glucosamines of chitin. Chitinases can be classified into: endochitinases, exochitinases, chitobiases and $\beta$-*N*-acetylglucosaminidases.[99-101] Endochitinases cleave randomly within a chitin chain, exochitinases cleave chitobioses (dimers of $\beta$-(1→4) linked *N*-acetyl-D-glucosamine units) mainly from the non-reducing end of the polymer, chitobiases hydrolyze chitobioses to *N*-acetyl-D-glucosamine, and $\beta$-*N*-acetylglucosaminidases are defined as enzymes that release *N*-acetyl-D-glucosamine from chitin. Similar to cellulases, many chitinases also have modular structures with CMs and chitin-binding modules (ChBMs) connected by linker peptides.[102, 103] Similar to the hydrolysis of cellulose, chitin is hydrolyzed by chitinolytic enzymes (e.g., chitinases and lysozymes) via similar inverting or retaining mechanisms,[104] as depicted in **Figure 2.10**.

In nature, chitinases are widely distributed in plants, fungi, bacteria and insects.[99] In plants, chitinases play important roles in defense against pathogens.[105] In fungi, chitinases are involved in growth regulation, including spore germination, mycelial development and exponential growth.[106] In bacteria, chitinases play roles in nutrition and parasitism.[104] Chitinases also have wide-ranging applications in the pharmaceutical, biotechnological and agricultural industries, such as the preparation of pharmaceutically important chito-oligosaccharides, control of malaria transmission, isolation of protoplasts, control of pathogenic fungi and decomposition of crustacean chitin waste.[104]

### 2.4.3 Ligninolytic Enzymes

Microbial biodegradation of lignin has been studied for more than half a century, and a variety of bacteria (mainly *Actinomycetes*) and fungi have been reported to be involved in lignin biodegradation.[107] Among these microorganisms, certain fungi cause white-rot (e.g., *Phanerochaete chrysosporium*), brown-rot (e.g., *Gloeophyllum trabeum*) and soft-rot (e.g., *Chaetomium globosum*) decay of wood.[108-110] The most efficient degradation is caused by white-rot fungi.

Unlike the hydrolysis of polysaccharides, the enzymatic degradation of lignin is nonspecific and oxidative, and this mechanism is sometimes called enzymatic "combustion".[109] Lignin degradation is usually catalyzed by extracellular enzymes due to its large size and heterogeneity. Since lignin peroxidase (ligninase, LiP) was identified from *P. chrysosporium* in 1983,[111, 112] several ligninolytic enzymes have been isolated and characterized. The major ligninolytic enzymes include LiP, manganese peroxidase (MnP) and laccases. Several other enzymes, such as veratryl alcohol oxidase,[113] glyoxal oxidase,[114] aryl alcohol dehydrogenase[115] and vanillate hydroxylase,[116] have also been reported to participate in lignin degradation mainly as hydrogen peroxide ($H_2O_2$) generators.

As heme-containing glycoproteins, LiP and MnP catalyze the degradation of lignin in the presence of $H_2O_2$. Various isozymes of LiP have been found in various fungi and filamentous bacteria.[117] Most LiP isozymes have molar masses of 38 to 45 kD, and isoelectric points (p*I*) of 3.2 to 4.1.[108] The redox potential of LiP (1.2 ~ 1.4 V) is higher than those of classical peroxidases (e.g., ~ 0.95 V for horseradish peroxidases (HRP)),[118-120] and thus can oxidize compounds with high redox potential, including both phenolic and non-phenolic lignin. For LiP,

lignin degradation occurs via a classical peroxidase catalytic mechanism in which the Fe (III) ground state of the peroxidase donates two electrons to $H_2O_2$ to form an intermediate termed compound I and water. Compound I consists of an oxo-Fe (IV) center and a porphyrin-based cation radical. The cation radical in compound I is reduced by electron-donating substrates to generate an oxo-Fe (IV) porphyrin intermediate compound II. Compound II is further reduced through a one-electron reduction step to regenerate the Fe (III) ground state.[63] The typical catalytic cycle of a Fe-based peroxidase is depicted in **Figure 2.11**. Lignin model compound studies indicated possible reactions that occur during the LiP-catalyzed lignin degradation include $C_\alpha$-$C_\beta$ cleavage, benzyl alcohol and phenol oxidation, benzylic methylene hydroxylation and aromatic ring opening.[120, 121]

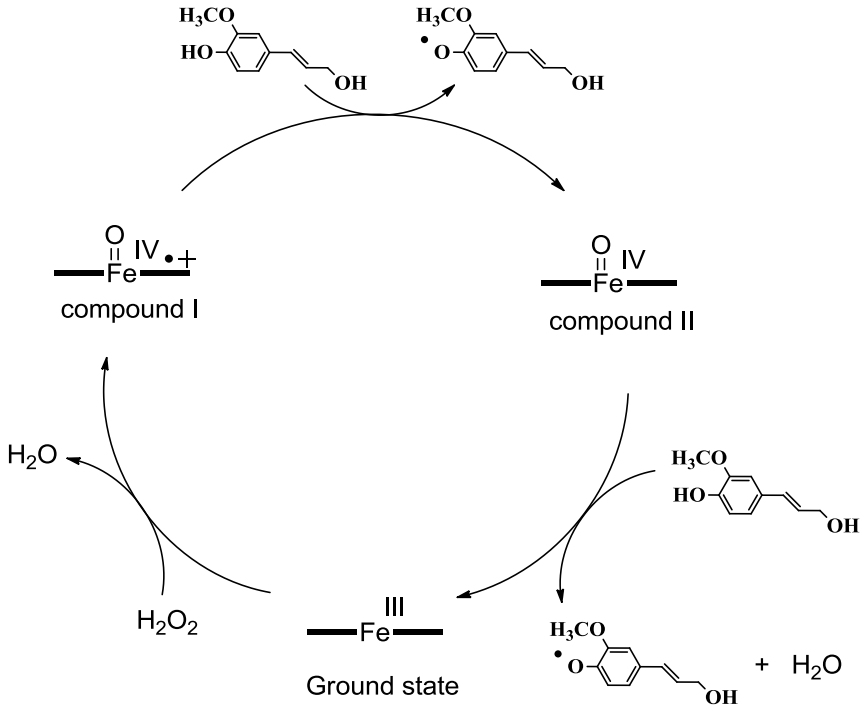


**Figure 2.11.** The general catalytic cycle of a Fe-based peroxidase in the presence of $H_2O_2$. Adapted from Veitch et al.[63]

The discovery of MnP in *P. chrysosporium* was slightly after LiP,[122] and a series of isozymes have been found in various basidiomycetous fungi where it coexists and works synergistically with LiP or laccases.[123, 124] The molar mass of MnP ranges from 38 to 62 kDa, but the molar mass for most purified isozymes is ~ 45 kDa.[123] As MnP has a strong preference for Mn (II) as a substrate, MnP oxidizes Mn (II) to Mn (III) in the presence of $H_2O_2$. The resulting Mn (III) is chelated by some organic acids (e.g., oxalate) as a redox-mediator to attack phenolic compounds.[125, 126] The redox potential for the Mn (III)-oxalate complex in a MnP-catalyzed reaction (~ 0.80 V)[127] is lower than that of LiP, and thus MnP is usually believed to focus on the degradation of phenolic lignin.[128] Possible reactions in MnP-catalyzed lignin degradation identified by studies with lignin model compounds include $C_\alpha$-$C_\beta$ cleavage, $C_\alpha$ oxidation and alkyl-phenyl cleavage.[129, 130]

Laccases are a family of multicopper-containing oxidases that catalyze the oxidation of a broad range of organic compounds at the expense of molecular oxygen.[64] With a relatively low redox potential (0.4 ~ 0.8 V),[131, 132] laccases prefer to catalyze the oxidation of phenolic compounds. However, laccase-catalyzed oxidations of non-phenolic lignin model compounds have been reported when redox mediators (e.g., 1-hydroxybenzotriazole) are present.[133]

**2.5 Natural Polymer Thin Films**

Natural polymers usually form composites with a variety of inorganic and organic compounds. The complex chemical compositions and morphology of the natural composites lead to difficulties in both research and interpretation of experimental studies.[134] In surface chemistry, model thin films are composed of a small amount of defined compounds or particles deposited onto flat surfaces. Smooth model thin films of natural polymers provide a simplified and convenient approach to study their biosynthesis, surface modification, enzymatic degradation,

and interactions with other biomacromolecules and inorganic minerals under carefully controlled experimental conditions.

The techniques used for the preparation of model thin films include dip coating, solvent casting, spincoating and Langmuir-Blodgett (LB) deposition.[135] Spincoating and LB-deposition are the two main techniques used to prepare smooth model thin films for natural polymers. In spincoating, an excess amount of a solution is deposited on a small solid surface, which is rotated at high speed to spread the solution and to evaporate the solvent. In LB-deposition, the coating material is deposited as a monomolecular film on the surface of a liquid (normally water), and then the film is transferred onto a solid surface as it is passed through the air/liquid interface.

### 2.5.1 Cellulose Thin Films

The preparation and application of cellulose thin films have been reported since the 1980s for the unique role of cellulose in nature and industries.[135] Both native cellulose and regenerated cellulose thin films have been prepared via spincoating or LB-deposition. The major methods in the literature for preparing cellulose thin films are summarized in **Table 2.2**.

**Table 2.2.** Methods for preparing cellulose thin films.

| Cellulose Source | Preparation Method | Solid Substrate | Roughesses | References |
|---|---|---|---|---|
| Regenerated cellulose (mainly amorphous) | Regenerated from Langmuir-Blodgett TMSC films | Hydrophobic silicon wafer | < 1 nm | 136-139 |
| Regenerated cellulose (mainly amorphous) | Regenerated from Spincoated TMSC films | Silicon wafer, gold and PS-*b*-P4VP[a] modified silicon wafer | 1 ~ 2 nm (from toluene) | 139-142 |
| Microcrystalline cellulose (Avicel) (Cellulose II) | Spincoating from DMAc/LiCl solution | Silicon wafer, PEI[b] modified silicon wafer | ~ 5 nm | 143-145 |
| Wood pulp (Cellulose II) | Spincoating from NMMO/DMSO solution | Silicon wafer modified with chitosan, PVAm and G-PAM[c] | 5 ~ 12 nm | 146-148 |
| Sulfated nanocrystalline cellulose (Cellulose I) | Spincoating from aqueous colloidal suspension | Mica, PS petri dishes, silicon wafer and SAM-$NH_2$[d] modified gold | 1 ~ 5 nm | 142, 149, 150 |
| Sulfated nanocrystalline cellulose (Cellulose I) | Langmuir-Blodgett deposition | Silicon wafer | 2 ~ 3 nm | 151 |
| Desulfated nanocrystalline cellulose (Cellulose I) | Spincoating from aqueous colloidal suspension | Silica QCM-D crystals and SAM-$NH_2$ modified gold | 2.5 ~ 3 nm | 142, 152, 153 |
| Cellulose nanofibrils (Cellulose I containing amorphous regions) | Spincoating from aqueous dispersion | Silica QCM-D crystals modified with PVAm, APTS and $TiO_2$[e] | 1 ~ 10 nm | 154, 155 |
| Cellulose-TSC[f] (Possible Cellulose I) | Self-assembled monolayer of cellulose-TSC | Gold | N/A[g] | 156 |

[a]PS-*b*-P4VP: poly(4-vinyl pyridine)-*b*-polystyrene block copolymers, [b]PEI: polyethyleneimine, [c]PVAm: polyvinylamine and G-PAM: glyoxalated polyacrylamide, [d]SAM-$NH_2$: amine-terminated self-assembled monolayer, [e]PVAm: poly(vinylamine) APTS: 3-aminopropyltrimethoxysilane and $TiO_2$: titanium dioxide, [f]cellulose-TSC: cellulose thiosemicarbazone and [g]not available.

### 2.5.1.1 Regenerated Cellulose Thin Films

Regenerated cellulose is cellulose recovered after dissolution or from a derivative.[157] Several solvent systems have been reported to dissolve cellulose, which can be categorized into two families: aqueous (protic) solvents and non-aqueous solvents.[28, 158] Aqueous solvents include: 1) basic complexing agents composed of transition metals and amine/ammonium (e.g., Schweizer's reagent ($[Cu(NH_3)_4(H_2O)_2](OH)_2$)), 2) aqueous alkali containing solvents (e.g., NaOH/urea and NaOH/poly(ethylene glycol)) and 3) aqueous salt containing solvents, which are mainly inorganic molten salt hydrates (e.g., $LiClO_4 \cdot 3H_2O$ and $FeCl_3 \cdot 6H_2O$). Non-aqueous solvents include: 1) ionic liquids composed of organic ions (e.g., imidazole based ionic liquids), 2) amine oxides (e.g., *N*-methylmorpholine-*N*-oxide (NMMO)) and 3) organic solvent/salt mixtures (e.g., dimethyl sulfoxide (DMSO)/tetrabutylammonium fluoride trihydrate ($TBAF \cdot 3H_2O$) and DMAc/LiCl). The chemical structures of 1-allyl-3-methylimidazolium chloride (AMIMCl, a commonly used imidazolium ionic liquid), NMMO and TBAF are shown in **Figure 2.12**.

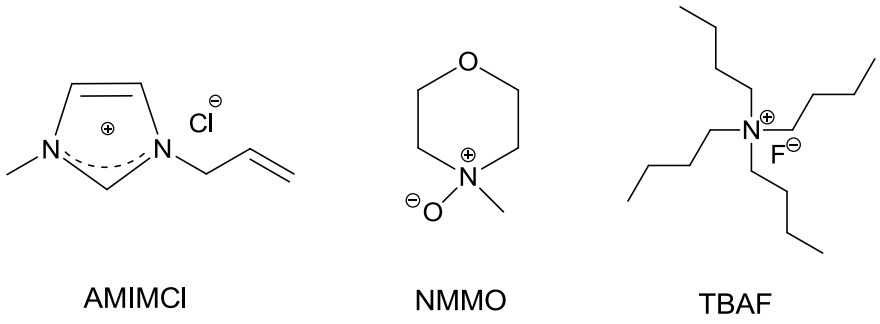


**Figure 2.12.** The chemical structures of three common cellulose solvents.

Among the cellulose solvents, NMMO/DMSO[147, 148] and DMAc/LiCl[143, 144] have been reported as solvents for the preparation of regenerated cellulose thin films. Wågberg et al.[147, 148] prepared regenerated cellulose thin films by spincoating wood pulp from NMMO/DMSO

solutions onto silicon wafers (with surface $SiO_2$ layers) modified with anchoring polymers (e.g., poly(vinylamine)) followed by rinsing with water for the removal of the high boiling point solvents. Cellulose films with different thicknesses were prepared in their studies. The morphology, thicknesses and crystal structures of the cellulose films were determined by AFM, ellipsometry and $^{13}C$ NMR. Eriksson et al.[143, 144] prepared regenerated cellulose thin films by spincoating microcrystalline cellulose from its DMAc/LiCl solution onto polyacrylamide coated silicon wafers (with surface $SiO_2$ layers). The films were dried at 100$^oC$ for 30 minutes followed by rinsing with water to remove DMAc and LiCl. The thicknesses and root-mean-square (RMS) roughnesses of the cellulose films were ~ 28 nm and ~ 5 nm determined by ellipsometry and AFM, respectively. The enzymatic degradation of the regenerated cellulose thin films catalyzed by different cellulases was also investigated by ellipsometry.

Regenerated cellulose thin films can also be prepared via the regeneration of cellulose from films of derivatives. Among the numerous organo-soluble cellulose derivatives, only a few of them (e.g., trimethylsilyl cellulose (TMSC)[136, 139-141] and cellulose acetate[159]) can be used as precursors for regenerated cellulose thin films due to the difficult and incomplete regeneration from most cellulose derivatives to cellulose. As a consequence of its excellent solubility in many organic solvents and easy and complete removal of trimethylsilyl groups by simple exposure to the vapor of aqueous hydrochloric acid (HCl) (**Figure 2.13**), TMSC is a perfect precursor for regenerated cellulose thin films. Synthesis of TMSC in a variety of solvents, like DMAc/LiCl,[140] liquid ammonia[160] and ionic liquids[161, 162] via the reaction between cellulose and hexamethyldisilazane (HMDS) or trimethylsilyl chloride (TMSCl) gives rise to TMSC with variable degrees of substitution (DS). For TMSC with low DS, polar solvents (e.g., DMSO and

DMAc) lead to complete dissolution, while TMSC with high DS is soluble in non-polar solvents (e.g., chloroform and toluene).[161]

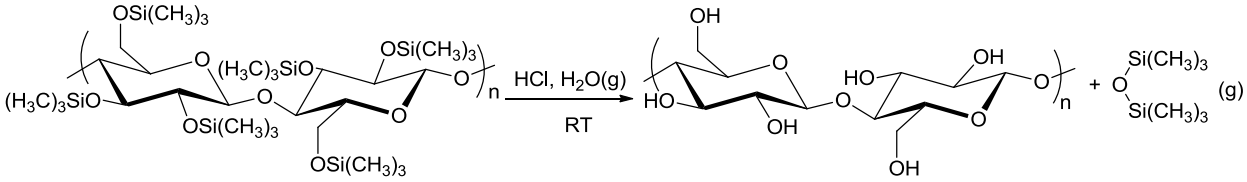


**Figure 2.13.** Desilylation of TMSC for the regeneration of cellulose.

Regenerated cellulose thin films from TMSC were first reported by Schaub *et al*. in 1993.[136] In their work, ultrathin cellulose films with RMS roughnesses less than 1 nm were regenerated from TMSC thin films prepared by the LB-technique. The thicknesses of the regenerated cellulose thin films were proportional to the number of monolayers of TMSC transferred to solid surfaces. Cellulose thin films can also be regenerated from spincoated TMSC films. Geffroy et al.[141] spincoated a TMSC chloroform solution onto a silicon wafer (with a surface $SiO_2$ layer) followed by removal of TMS groups in the presence of HCl vapor. The cellulose films had thicknesses of ~ 100 nm with RMS roughnesses of ~ 2 nm. This procedure was further improved by Kontturi et al.,[140] in which the dependences of film thicknesses, roughnesses and morphologies on spinning speeds, solvents, concentration of the solutions and exposure time to HCl vapor were investigated via ellipsometry, AFM and X-ray photoelectron spectroscopy (XPS). X-ray diffraction (XRD) and reflection absorption infrared spectroscopy (RAIRS) studies indicated that the regenerated cellulose thin films from TMSC were essentially amorphous.[163, 164]

#### 2.5.1.2 Native Cellulose Thin Films

Cellulose I is converted to cellulose II or an amorphous structure during regeneration due to a change of intermolecular and intramolecular hydrogen bonds. For cellulose, the enzymatic degradation and interactions with water and biopolymers are strongly influenced by the crystal structure. Cellulose I thin films with crystal structures similar to native cellulose have been prepared via the deposition of cellulose nanocrytals and cellulose microfibrils.

Cellulose nanocrystals (nanowhiskers) are rod-like nanocrystals prepared by the controlled acidic hydrolysis (e.g., sulfuric acid or hydrochloric acid) or oxidation (e.g., 2,2,6,6-tetramethylpiperidine-1-oxyl radical (TEMPO) mediated oxidation) of the disordered regions of native cellulose nanofibrils.[165] Recently, cellulose nanocrystals have attracted significant interest for their self-assembly into chiral nematic liquid crystalline phases with helical arrangements under appropriate conditions.[165, 166] Edgar et al.[149] reported the preparation of smooth cellulose I thin films by solvent casting nanocrystalline cellulose colloidal suspensions onto mica and polystyrene (PS) petri dishes in 2003. Results from AFM showed that the films were smooth with relatively small RMS roughnesses (1 ~ 2.5 nm) and X-ray diffraction (XRD) data indicated that the films were cellulose I. Lefebvre et al.[150] prepared nanocrystalline cellulose thin films by spincoating and found that the spincoated films exhibited different colors from transparent to purple as thicknesses increased. Interactions between the spincoated nanocrystalline cellulose thin films and polyelectrolytes were also investigated using AFM in their study.

Cellulose thin films containing both amorphous and cellulose I regions were prepared by Ahola et al.[154] via spincoating of aqueous nanofibrillar cellulose dispersions onto silicon or 3-aminopropyltrimethoxysilane (APTS) modified silicon surfaces. The low charge density (LC)

and high charge density (HC) cellulose nanofibrils were prepared by disintegrating bleached sulfite pulp using a high-pressure fluidizer with enzymatic hydrolysis and enzymatic hydrolysis followed by carboxymethylation, respectively. The resulting cellulose films had thicknesses of ~ 6 nm for LC and ~ 4 nm for HC films with average RMS roughnesses of ~ 4 nm and ~ 2 nm, respectively. Swelling of the films in water and electrolyte solutions with different ionic strengths and pH was also studied using QCM-D and AFM. Enzymatic hydrolysis of the nanofibrillar cellulose thin films was also investigated and compared with other regenerated and native cellulose thin films in their subsequent study.[155]

A novel method to prepare cellulose I thin films was reported by Yokota et al.[156] in 2007. In their work, a cellulose derivative, cellulose-thiosemicarbazone (cellulose-TSC) was prepared in 80% aqueous NMMO solution. Cellulose-TSC formed a self-assembled monolayer (SAM) on gold surfaces from aqueous NMMO solutions. Electron diffraction suggested that a cellulose I structure was obtained during the formation of the cellulosic SAM. However, the authors did not have sufficient evidence to prove that the cellulose films were identical to native cellulose I.

### 2.5.2 Lignin Thin Films

Lignin and lignin model compounds from sources including KL from softwood,[52, 167-169] MWL from softwood[52, 170-172] and hardwood,[52] OL from softwood[173] and sugar cane bagasse[173-176] and dehydrogenative polymer (DHP) lignin[177, 178] have been used for the preparation of lignin thin films on various substrates via spincoating,[52, 167-169, 178] Langmuir-Blodgett deposition[173-176] and solvent casting.[177] The major methods in the literature for preparing lignin thin films are summarized in **Table 2.3**.

**Table 2.3.** Methods for preparing lignin thin films.

| Lignin Source | Preparation Method | Solid Substrate | Roughesses | References |
|---|---|---|---|---|
| Organosolv lignin extracted from sugar cane bagasse and pine sawdust | Langmuir-Blodgett deposition | Aluminized glass and calcium fluoride plates | N/A[a] | 173, 174 |
| Organosolv lignin extracted from sugar cane bagasse | Langmuir-Blodgett deposition | Mica | 0.25 ~ 5 nm | 175, 176 |
| Kraft lignin | Spincoating from aqueous ammonia solutions | Silicon wafers and silica QCM-D crystals | 1 ~ 2 nm | 167-169 |
| Milled wood lignin from hardwood and softwood | Spincoating from aqueous ammonia solutions | Silicon wafers | 1 ~ 2 nm | 52 |
| Dehydrogenative polymer | Solvent casting | Gold, mica, graphite and cellulose ester | N/A[a] | 177, 179 |
| Dehydrogenative polymer | Spincoating from aqueous suspension | Glass | N/A[a] | 178 |
| Sulfonated lignin | Self-assembly | POEA modified glass, quartz and PET[b] | 1 ~ 3 nm | 180 |
| Kraft lignin | Self-assembly | Cationic starch modified mica and cellulose fiber | < 1 nm | 181 |

[a]Not available and [b]POEA: poly(*o*-ethoxyaniline) and PET: polyethylene terephthalate.

Lignin thin films prepared by LB-deposition were first reported by Constantino et al. in 1996.[173] Lignins extracted from sugar cane bagasse and *Pinus caribaea hondurensis* sawdust were dissolved in tetrahydrofuran (THF). The lignin/THF solution was spread onto ultrapure water followed by transfer onto aluminized glass slides. Ellipsometry data showed that the

thicknesses of the lignin films were proportional to the number of layers transferred, with a thickness of ~ 6 nm per monolayer. However, the morphology, roughness and coverage of the lignin films were not determined in this work. In order to promote the stability and transferability of lignin, subsequent work used sugar cane bagasse lignin and amphiphilic cadmium stearate for the preparation of composite LB-films in 1998.[174]

Pasquini et al.[175, 176] also prepared lignin thin films by LB-deposition. Lignins were extracted from sugar cane bagasse via different methods, including ethanol-water, acetone/water/sulfuric acid (SAC), acetone–oxygen (AO) and soda (SO). These lignins were dissolved in THF or chloroform and were spread onto ultrapure water followed by deposition onto mica. Images from AFM showed that EW and AO lignins (containing more –COOH groups) formed smooth films with RMS roughnesses for five-layer LB films of 0.24 and 0.30 nm, respectively. However, aggregates were observed on the SO and SAC lignin surfaces, and the RMS roughnesses for five-layer LB films were 1.25 and 3.80 nm, respectively.

Smooth lignin thin films were prepared by Norgren and Notley et al.[52, 167-169] via spincoating KL and MWL (from both hardwood and softwood) from aqueous ammonia solutions onto silicon wafers (with surface $SiO_2$ layers). The thicknesses of the resulting lignin thin films ranged from 20 to 140 nm, and RMS roughnesses were ~ 1 nm.[52, 167] The surface energy of these spincoated lignin thin films[52] and the adsorption of polyelectrolytes onto these well-defined and stable lignin thin films[169] were also investigated in their studies.

### 2.5.3 Chitin Thin Films

The preparation and application of chitin thin films have not been as extensively studied as cellulose and most of the reported chitin films are not smooth nor uniform enough for the study

of surface interactions between chitin and biomacromolecules. The major methods in the literature for preparing chitin thin films are summarized in **Table 2.4**.

**Table 2.4.** Methods for preparing chitin thin films.*

| Chitin Source | Preparation Method | Solid Substrate | References |
|---|---|---|---|
| $\beta$-Chitin | Spincoating from hexafluoroiso-propanol solution | Silicon wafers | [182] |
| $\alpha$-Chitin | Dip-coating from hexafluoroiso-propanol solution | Silicon wafers | [183] |
| Chitin | Solvent casting followed by regeneration by ethanol | Free standing films | [184] |
| $\alpha$-Chitin and $\beta$-Chitin | Solvent casting followed by regeneration by water or methanol | Free standing films | [185] |
| $\beta$-Chitin | Airbrushing | Silicon wafers and glass slides | [186, 187] |
| Chitosan | Acetylation of chitosan films | Free standing films | [188] |

*Unlike **Tables 2.2** and 2.3, roughnesses were not available in the literature for any of the films in this table.

Kikkawa et al.[182] prepared $\beta$-chitin thin films to study the binding interactions of chitinases onto chitin surfaces. The chitin films were prepared by spincoating $\beta$-chitin from hexafluoroisopropanol solutions onto silicon wafers (with a surface $SiO_2$ layer). However, AFM image indicated that the films were neither smooth nor homogeneous. Montiel-González et al.[183]

dissolved $\alpha$-chitin in hexafluoroisopropanol and prepared chitin films with thicknesses of 120 to 200 nm by dip-coating.

Yusof et al.[184] dissolved chitin in DMAc/LiCl and obtained a 0.5% chitin solution. Transparent and flexible chitin films were prepared via solvent casting followed by the removal of DMAc using ethanol. However, those chitin films were not thin enough, with thicknesses that ranged from 25 to 80 μm.

Wu et al.[185] prepared chitin solutions with concentrations of 1.0 ~ 4.0 % by the dissolution of $\alpha$-chitin and $\beta$-chitin in an ionic liquid, 1-butyl-3-methylimidazolium acetate (BMINAc). Chitin films and sponges were prepared via regeneration of chitin using water or methanol.

Zhong et al.[186, 187] prepared nanofibrillar chitin films and nano-patterned nanofibrillar chitin films by airbrushing "chitin nanofiber inks" (chitin/hexafluoroisopropanol and chitin/DMAc/LiCl solutions with critical concentrations > 0.002 wt% and > 0.02 wt%, respectively) onto silicon wafers (with surface $SiO_2$ layers) and glass slides. Images from AFM showed that the diameters of the chitin nanofibers regenerated from hexafluoroisopropanol and DMAc/LiCl were 3 and 10 nm, respectively. Data from FTIR and XRD showed that the regenerated chitin nanofibers were $\alpha$-chitin with high crystallinity.

## 2.6 Surface Analysis Techniques

### 2.6.1 Quartz Crystal Microbalance with Dissipation Monitoring (QCM-D)

A quartz crystal microbalance with dissipation monitoring (QCM-D) is an acoustic instrument that provides real-time and label-free monitoring of molecular interactions (e.g., adsorption and degradation) on various surfaces.

The quartz crystal microbalance (QCM) technique is based upon the piezoelectric properties of a quartz crystal. A typical QCM crystal is a circular AT-cut (cut at a 35°10′ from the z-axis of a quartz crystal)[189] quartz crystal coated with two gold (or platinum) electrodes. A gold or silica coated QCM crystal is shown in **Figure 2.14A**. A mechanical shear strain parallel to the crystal surface will be induced in the crystal when an electrical field is applied. Consequently, mechanical shear waves will be created in the crystal, or in other words, the crystal will oscillate in a shear thickness mode, by applying an alternating electric filed (**Figure 2.14B**). Resonance is excited when the thickness of the quartz crystal is an odd integer of the half wavelengths of the induced mechanical shear waves. The resonant frequency ($f$) can be calculated from:[190]

$$f = n\left(\frac{v_q}{2t_q}\right) = nf_0 \tag{2.1}$$

where, $v_q$ is the acoustic speed in the quartz crystal, $t_q$ is the thickness of the quartz crystal, $n$ is the overtone number, which is the number of nodal planes parallel to the crystal surfaces and only odd overtones can induce charges of opposite sign at the crystal surfaces, and $f_0$ is the fundamental resonant frequency when $n$ = 1. The change in frequency with respect to mass is given as:

$$df = -\left(\frac{f}{m_q}\right)dm_q = -\left(\frac{f}{\rho_q t_q}\right)dm_q \tag{2.2}$$

where, $m_q$ is the mass per area ($kg \cdot m^{-2}$) of the quartz crystal, and $\rho_q$ is the density of the quartz crystal.

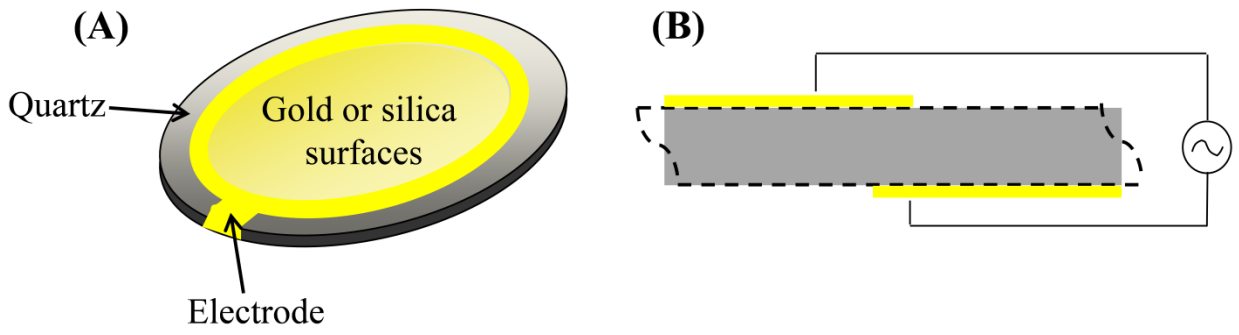


**Figure 2.14.** Schematic depiction (A) a QCM crystal and (B) a QCM crystal oscillating in a shear thickness mode in an alternating electric field.

A thin film bound to the crystal surface could be treated as part of the QCM crystal. When the thin film is rigid and evenly distributed on the crystal surface, and the mass of the film is small compared to the QCM crystal, Equation 2.2 can be written as:[190]

$$\Delta f = df = -\left(\frac{f}{\rho_q t_q}\right)\Delta m = -n\left(\frac{2f_0^2}{\rho_q v_q}\right)\Delta m = -n\frac{1}{C}\Delta m \qquad (2.3)$$

where the density of quartz crystal is $\rho_q$ = 2650 kg·m$^{-3}$, and $v_q$ = 3340 m·s$^{-1}$. Therefore, the constant $C$ = 0.177 mg·m$^{-2}$·Hz$^{-1}$ or 17.7 ng·cm$^{-2}$·Hz$^{-1}$ for a 5 MHz crystal.

As seen in Equation 2.3, the mass of the attached thin film is linearly proportional to the frequency shift of the quartz crystal, and this relationship was reported by Sauerbrey in 1959.[191] The Sauerbrey relationship was mainly used to study gas phase deposition, metal surface oxidation, gas adsorption and desorption in the early days.[192] Since the 1980s, the application of the Sauerbrey relationship has been extended to liquid systems, thereby widening the application scope for the technique.[193, 194]

Frequently, the attached film is not rigid, and the assumptions of the Sauerbrey relationship are no longer valid. A viscoelastic (or soft) film cannot fully couple to the oscillatory motion of

the QCM crystal or dissipate the oscillation, and therefore the Sauerbrey relationship underestimates the mass of a viscoelastic film. A QCM with dissipation monitoring (QCM-D) can be used to study viscoelastic films by measuring the oscillation decay of the crystal after the electric field is switched off. Information about the rigidity/softness of the adsorbed film can be obtained in a QCM-D study. The dissipation factor ($D$) is defined as the ratio between the energy dissipated ($E_{dissipated}$) and the energy stored ($E_{stored}$) during a single oscillation period.

$$D = \frac{E_{dissipated}}{2\pi E_{stored}} \tag{2.4}$$

Energy dissipates slowly for a rigid film and $D$ is small, whereas energy dissipates rapidly for a soft film and $D$ is large (**Figure 2.15**).

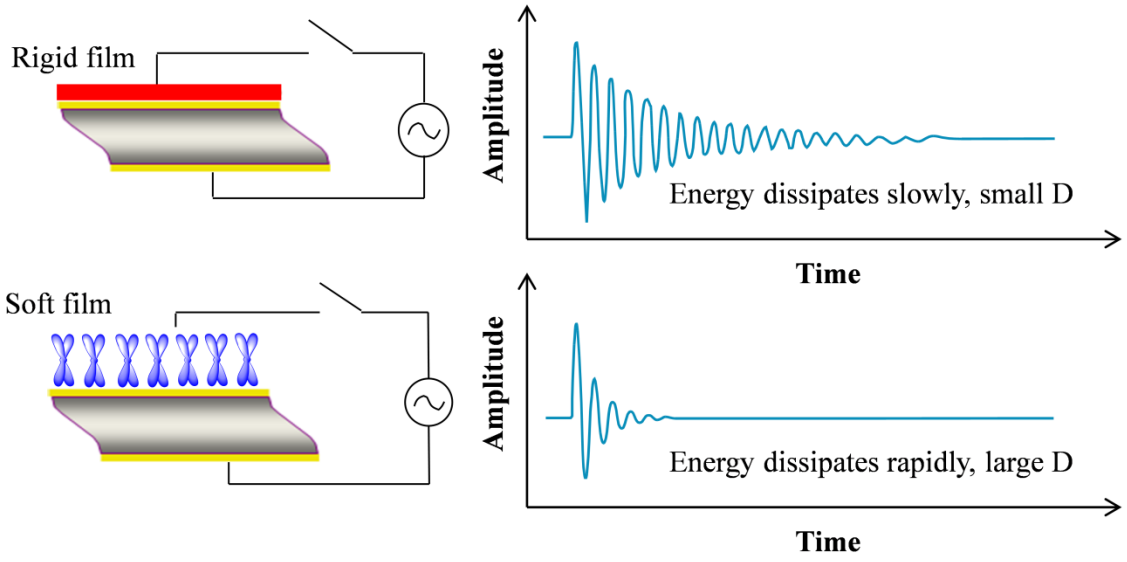


**Figure 2.15.** Schematic illustration of the energy dissipation after the driving power is switched off in a QCM-D study.

For a viscoelastic film at a liquid/solid interface, QCM-D data can be quantitatively analyzed using modeling methods. The viscoelastic properties of materials are usually modeled using a

combination of elastic springs and viscous dashpots. The Maxwell model[195] is composed of an elastic spring and a viscous dashpot connected in series, and is usually used to simulate a viscoelastic material which is more viscous than elastic. On the other hand, the Voigt (Kelvin-Voigt) model[196] is composed of an elastic spring and a viscous dashpot connected in parallel, and is usually used to describe a viscoelastic material which is more elastic than viscous. The Voigt model is given as:[196]

$$G = G' + iG'' = \mu_f + i2\pi f \eta_f = \mu_f + i\omega\eta_f \tag{2.5}$$

where $G$ is the complex shear modulus, $G'$ is the storage modulus, $G''$ is the loss modulus, $\mu_f$ is the elastic shear modulus, $\eta_f$ is the shear viscosity, $f$ is the oscillation frequency and $\omega$ is the angular frequency of oscillation. In the Voigt model, the adsorbed viscoelastic film is treated as a no-slip layer between the purely elastic QCM-D crystal and a semi-infinite viscous (Newtonian) liquid. Four parameters are used to describe the adsorbed viscoelastic film, including density ($\rho_f$), thickness ($h_f$), elastic shear modulus ($\mu_f$) and viscosity ($\eta_f$) (**Figure 2.16**). In the Voigt model, the relationship between the QCM-D responses and these four parameters of the adsorbed films can be expressed as:[196]

$$\Delta f \approx -\frac{1}{2\pi\rho_q h_q}\left(\frac{\eta_l}{\delta_l} + h_f\rho_f\omega - 2h_f\left(\frac{\eta_l}{\delta_l}\right)^2\frac{\eta_f\omega^2}{\mu_f^2 + \omega^2\eta_f^2}\right) \tag{2.6}$$

$$\Delta D \approx \frac{1}{\pi f\rho_q h_q}\left(\frac{\eta_l}{\delta_l} + 2h_f\left(\frac{\eta_l}{\delta_l}\right)^2\frac{\eta_f\omega}{\mu_f^2 + \omega^2\eta_f^2}\right) \tag{2.7}$$

$$\delta_l = \sqrt{\frac{2\eta_l}{\rho_l\omega}} = \sqrt{\frac{\eta_l}{\pi f\rho_l}} = \sqrt{\frac{\eta_l}{n\pi f_0\rho_l}} \tag{2.8}$$

where $\rho_q$ and $h_q$ are the density and thickness of the QCM-D crystal, respectively, $\rho_l$ and $\eta_l$ are the density and viscosity of the bulk liquid, respectively, and $\delta_l$ is the penetration depth of the

shear wave into the bulk liquid. The penetration depth decreases as the overtone number increases. In water, the penetration depth is 250 nm for $n$ = 1.[197] The thickness, elastic shear modulus and viscosity values of the viscoelastic film can be obtained by fitting the data with a Voigt model.

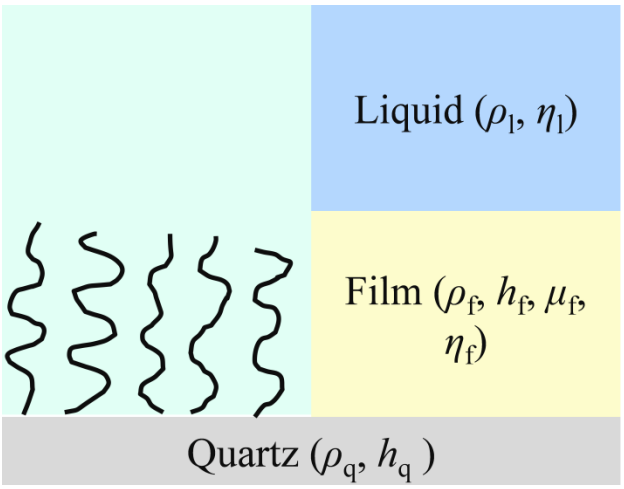


**Figure 2.16.** Schematic depiction of the parameters simulated by the Voigt viscoelastic model in a QCM-D study. Adapted from Höök et al.[198]

In recent times, QCM-D has been used to monitor molecular interactions at solid/liquid interfaces in both chemical and biological research. Specific examples can be found for polymer[199-201] and surfactant[202, 203] adsorption, protein anti-fouling surface design,[204, 205] thin film crosslinking[198, 206, 207] and enzymatic degradation,[155, 208] surface-initiated polymerization,[209-211] DNA–protein interactions[212, 213] and cell attachment and spreading.[214, 215]

### 2.6.2 Surface Plasmon Resonance (SPR)

Surface plasmon resonance (SPR) is an optical technique that monitors molecular interactions at the surfaces of planar metal films (typically gold and silver) or metal nanoparticles. Binding interactions between an analyte in solution and a molecule immobilized on the metal surface can

be monitored in a real-time and label-free manner by measuring the change in resonant angle caused by refractive index changes associated with analyte composition changes in the vicinity of the interface.

A surface plasmon is an electromagnetic wave that propagates along the metal/dielectric (e.g., metal/air or metal/water) interface in response to oscillations of surface electrons. The term surface plasmon was introduced by Ritchie[216] in 1957 as an explanation for the energy loss when fast electrons traveled through metal thin films. Surface plasmon resonance can be excited by an electron or light beam. In order to excite the surface plasmon resonance by *p*-polarized light, the frequency of the light should be equal to the frequency of the surface plasmon and the surface-parallel wave vector of the light should also match the wave vector of the propagating surface plasmon.[217] The frequency match is easily satisfied, but the wave vector match can only be achieved via specific experimental arrangements. Two experimental setups based on the phenomenon of total internal reflection (TIR) were designed by Otto[218] and Kretschmann[219] in the 1960s to satisfy the wave vector match. However, most of the modern SPR instruments are fabricated based upon the Kretschmann configuration.

A typical SPR system based upon the Kretschmann configuration is composed of a *p*-polarized light source, a glass prism, a photodetector and a SPR sensor (**Figure 2.17**). A SPR sensor is a glass chip coated with a semitransparent gold thin layer. The SPR sensor is coupled to the prism through a refractive index matching oil or gel. The sample solution is pumped into the sensor chamber and flowed through the sensor surface to enable monitoring.

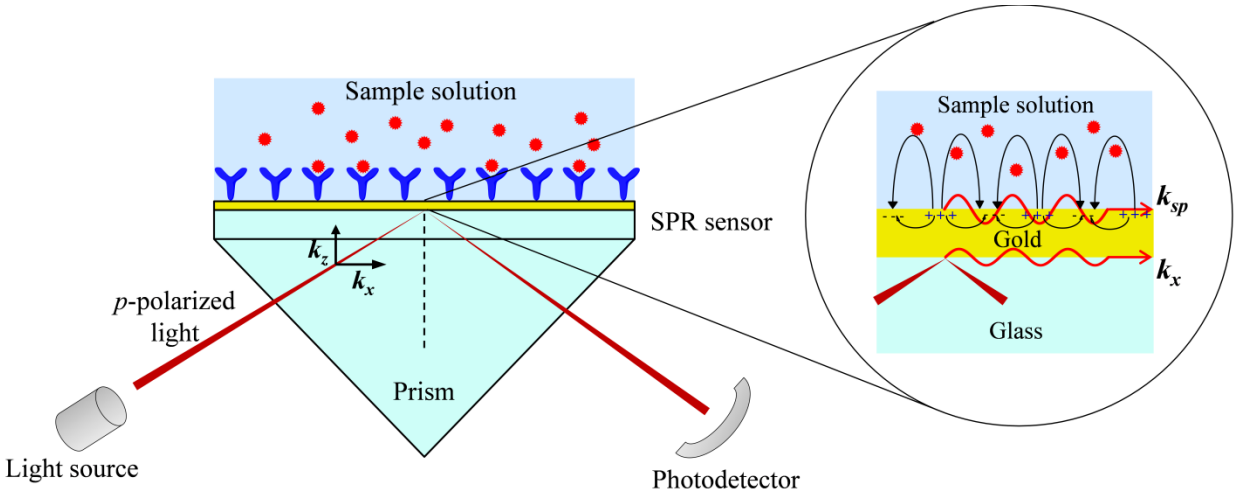


**Figure 2.17.** Schematic depiction of the Kretschmann configuration. The inset shows the evanescent field when surface plasmon resonance is excited by *p*-polarized light.

As shown in **Figure 2.18**, when light passes through the interface of two media, the relationship between the angles of incidence and refraction is described by Snell's Law:

$$n_1 sin\theta_1 = n_2 sin\theta_2 \tag{2.9}$$

where $n_1$ and $n_2$ are the refractive indices of medium 1 and medium 2, respectively, and $\theta_1$ and $\theta_2$ are the incident angle of light in medium 1 and refractive angle of light in medium 2, respectively. For TIR, light is entirely reflected and no light passes into the medium with lower refractive index. Assuming $n_1 > n_2$ and $\theta_2 = 90°$ the critical incident angle ($\theta_c$) for TIR can be determined from the following equation:

$$sin\,\theta_c = \frac{n_2}{n_1} \tag{2.10}$$

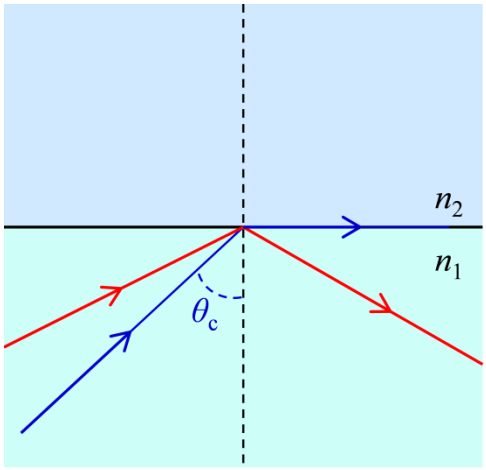


**Figure 2.18.** Schematic depiction of total internal reflection.

During TIR, the light beam is entirely reflected and thus does not lose energy via refraction. However, the light beam creates an evanescent electric field at the TIR interface that extends into the medium with a lower refractive index. The intensity of the evanescent wave exhibits exponential decay as a function of the distance away from the TIR interface. If a TIR interface is coated with a thin conductive layer as is the case of the SPR sensor, the evanescent wave can penetrate the metal layer and excite the surface plasmon in the metal layer.[217] In other words, the energy and momentum are transferred from the photons to the surface plasmon. Consequently, an enhanced evanescent wave is created (**Figure 2.17**). The evanescent wave only penetrates a short distance into the medium with lower refractive index, and the approximate penetration depth is about one-quarter of the wavelength of the incident light.[220]

As mentioned above, the surface-parallel wave vector of the photons should be equal to the surface plasmon for the excitation the surface plasmon resonance. For light traveling through the prism at a specific angle $\theta$ ($\theta > \theta_c$), the wave vector ($k$) of the light is:[221]

$$k = \frac{2\pi}{\lambda}\sqrt{\varepsilon_g} = \frac{2\pi n_g}{\lambda} \qquad (2.11)$$

where $\lambda$ is the wavelength of the incident light in a vacuum, $\varepsilon_g$ is the relative permittivity (dielectric constant) of the glass prism and $n_g$ is the refractive index of the glass prism. Permittivity is a term that describes how an electric field affects a material, and relative permittivity is the ratio of the permittivity of a material relative to vacuum permittivity. The relative permittivity of a perfect conductor is $\infty$ and the relative permittivity of a perfect dielectric material is 0. For most of the naturally occurring materials, $n = \sqrt{\varepsilon}$.[221] The surface-parallel wave vector ($k_x$) of the incident *p*-polarized light is:[221]

$$k_x = ksin\theta = \frac{2\pi n_g}{\lambda} sin\theta \tag{2.12}$$

On the other hand, the wave vector of a surface plasmon wave ($k_{sp}$) is expressed as:[221]

$$k_{sp} = \frac{2\pi}{\lambda}\sqrt{\frac{\varepsilon_m \varepsilon_a}{\varepsilon_m + \varepsilon_a}} = \frac{2\pi}{\lambda}\sqrt{\frac{n_m^2 n_a^2}{n_m^2 + n_a^2}} \tag{2.13}$$

where $\lambda$ is the wavelength of the incident light in a vacuum, $\varepsilon_m$ and $\varepsilon_a$ are the relative permittivity of the metal and the ambient medium, respectively and $n_m$ and $n_a$ are the refractive indices of the metal and the ambient medium, respectively. In order to excite surface plasmon resonance, $k_x$ should be equal to $k_{sp}$. Thus,

$$n_g sin\theta_{sp} = \sqrt{\frac{n_m^2 n_a^2}{n_m^2 + n_a^2}} \tag{2.14}$$

where $\theta_{sp}$ is called the SPR angle and the minimum reflection is detected by the photodetector at $\theta_{sp}$. With a *p*-polarized light source, the response of the prism and the metal layer on the SPR sensor are constant throughout the measurement. Thus, $\theta_{sp}$ is only sensitive to the refractive index changes within the ambient medium. For instance, solvent molecules are replaced by

analyte molecules at the solid/liquid (or metal/ambient medium) interface in a typical adsorption or binding process. The change of the average refractive index of the ambient medium after adsorption or binding leads to a change of $\theta_{sp}$. A schematic illustration of a typical SPR profile for antibody-antigen interactions is shown in **Figure 2.19**.

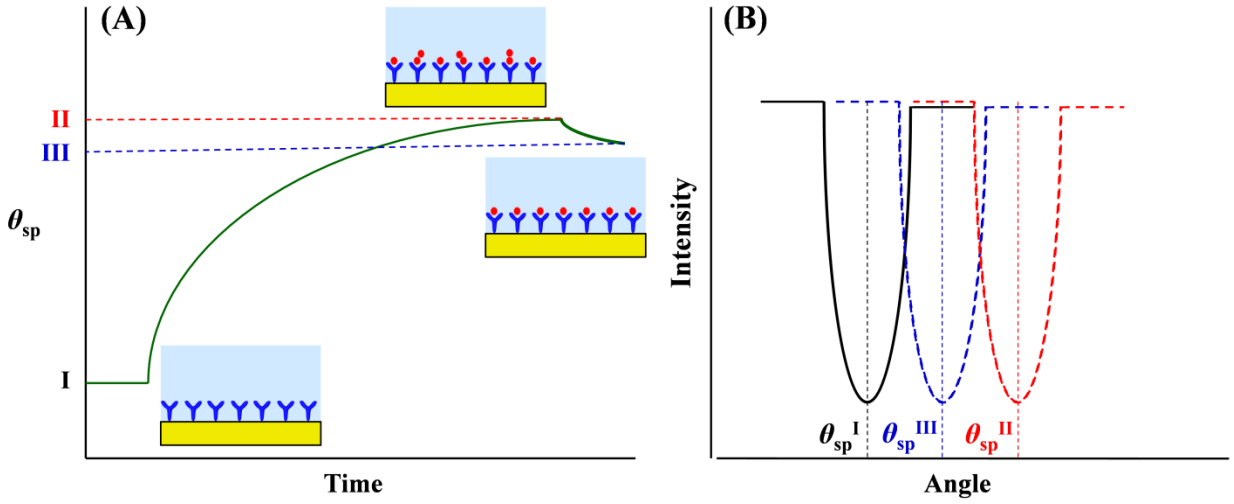


**Figure 2.19.** Schematic illustration of (A) a typical SPR profile for antibody-antigen interactions and (B) the change of $\theta_{sp}$ during the binding between the antibody and the antigen from a SPR measurement.

Changes in $\theta_{sp}$ ($\Delta\theta_{sp}$) can be converted to surface concentration ($\Gamma$) using the formula given by de Feijter et al.,[222]

$$\Gamma = \frac{L(n_a - n_s)}{dn/dc} = \frac{\Delta\theta_a}{d\theta/dL}\frac{(n_f - n_s)}{dn/dc} \quad (2.15)$$

where $L$ is the thickness of the adsorbed film, $n_a$ is the average refractive index of the ambient medium after adsorption, $n_f$ is the refractive index of the adsorbed film, $n_s$ is the refractive index of the solvent, $dn/dc$ is the refractive index increment of the analyte solution which can be determined using a differential refractometer, $d\theta/dL$ is the change in resonant angle as a function

of the adsorbed film thickness and is deduced from the Fresnel equations,[223] and $\Delta\theta_a$ is the change in resonant angle due to analyte adsorption or binding by subtracting the contribution of refractive index changes of the bulk solution from $\Delta\theta_{sp}$:[224, 225]

$$\Delta\theta_a = \Delta\theta_{sp} - \mathrm{c}\left(\frac{d\theta_{sp}}{dc}\right) = \Delta\theta_{sp} - \mathrm{c}\left(\frac{d\theta_{sp}}{dn}\frac{dn}{dc}\right) \quad (2.16)$$

where c is the bulk concentration of the analyte solution and $d\theta_{sp}/dn$ is an instrument specific constant (e.g., 61.5 ° obtained by calibration with ethylene glycol standards for the SPR instrument used in this work).[223]

As a real-time, label-free method with high sensitivity, SPR has been widely used to monitor adsorption and binding events. SPR based sensors have shown a wide range of applications in chemical and biological analyte detection, food quality and safety analysis, medical diagnostics and environmental pollutant monitoring.[221, 226-228]

### 2.6.3 Atomic Force Microscopy (AFM)

Atomic force microscopy (AFM) is a high-resolution scanning probe method that creates three-dimensional topographical images by measuring the forces between a sharp probe (or tip) and the sample surface. Binnig et al. invented AFM in 1986[229] with an instrument design based upon scanning tunneling microscopes.[230]

A typical AFM system (**Figure 2.20**) contains a tiny cantilever, a laser beam, a photodiode, a piezoelectric scanner and a feedback control system.[231] The cantilever is usually made of silicon or silicon nitride attached at one end with a sharp tip at the free end. When the tip approaches a sample surface, the forces (attractive or repulsive) between the tip and the surface lead to a deflection of the cantilever. According to Hooke's law, the deflection of the cantilever is

proportional to the strength of the interaction. The back surface of the cantilever is usually coated with a metallic thin film to promote the reflectance of light. A laser beam is reflected from the top surface of the cantilever into a photodiode for the measurement of cantilever deflection. A photodiode is a photodetector that converts light signals into electric signals. The electric signals are then analyzed and amplified by the feedback system to control the movement of the cantilever or the sample surface via a piezoelectric scanner. The piezoelectric scanner is a tube-shaped scanner that expands and contracts in the x, y and z dimensions under an applied voltage. The piezoelectric scanner manipulates the movements of the cantilever or the sample surface in response to the feedback signals.[232]

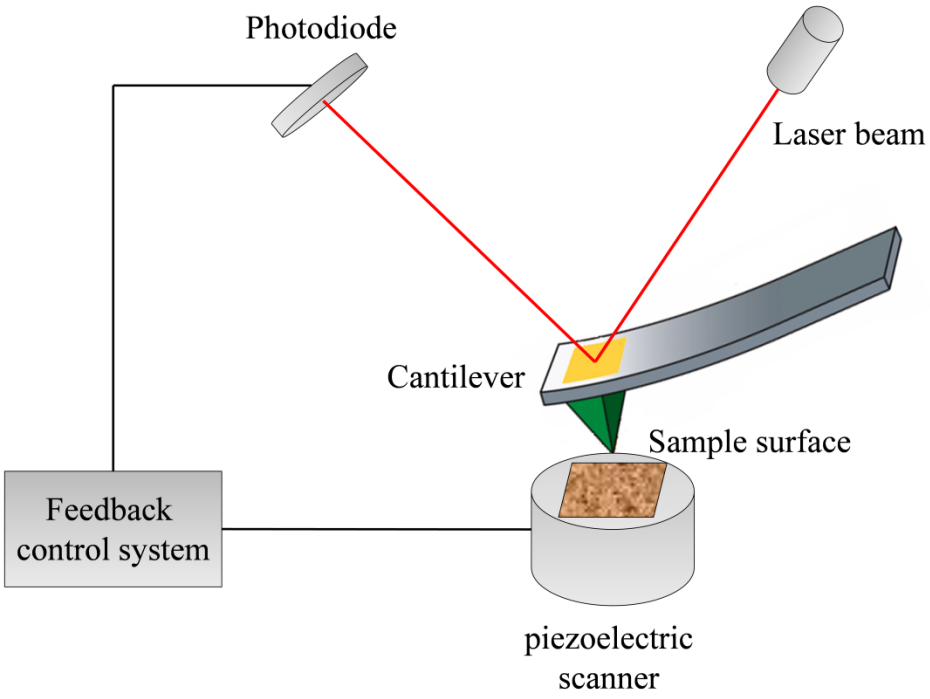


**Figure 2.20.** Schematic illustration of a typical AFM system.

AFM has two main operational modes, including static (contact) mode and dynamic (non-contact) mode. In static mode, the tip is in direct contact with the sample surface and thus a soft

cantilever is preferred to avoid damage to the sample surface. The static mode can be carried out at constant height or constant force. In the constant height mode, the distance between the end of the cantilever and the surface is fixed, and the changes in the deflection data are used to generate topographic data for the sample surface. In the constant force mode, the cantilever deflection is kept constant and the piezoelectric scanner moves up and down in a z-direction. The variations of the feedback voltage signals are used to create the topography.

In the dynamic mode, the tip is not in direct contact with the sample surface but oscillates either at its resonant frequency (amplitude modulation (AM) mode) or with a constant vibrating amplitude (frequency modulation (FM) mode).[233] The AM mode was first introduced by Binnig et al.[229] in 1986, and the FM mode was reported by Albrecht et al.[234] in 1991. The variations of vibrating amplitude provide the topographic data in AM mode, while the changes of oscillation frequency provide information about the topography of the sample surface in FM mode. Atomic resolution is possible with FM-AFM especially in ultra-high vacuum conditions, since frequency can be measured with high sensitivity. Recently, Gross et al.[235-237] used FM-AFM to directly image chemical bonds in pentacene and fullerenes using an extremely stiff cantilever whose tip apex was functionalized with carbon monoxide.

In the static mode, the predominant forces are short-range repulsive forces since the tip and the surface are close to each other. Therefore, the tip and the surface are considered to be in "contact", i.e., where the repulsive forces are dominant. On the other hand, the predominant forces are long-range attractive forces (e.g., van der Waals forces) in the dynamic mode (**Figure 2.21**).[232] Tapping (intermittent contact or semi-contact) mode is a modified AM mode and this term came from the trademark name "TappingMode™" of Veeco (one of the major producers of commercial atomic force microscopes).[238] Different from the traditional AM mode where the tip

oscillates freely in the attractive force dominated region, the oscillating tip enters the repulsive forces dominated region in the tapping mode. In other words, the tip oscillates up and down near the sample surface while intermittently tapping or touching the sample surface. The tapping mode has the advantages of both contact and AM modes. It minimizes possible damage of the sample surface relative to contact mode and reduces the interference by surface contaminants (e.g., moisture) in the traditional AM mode.[239]

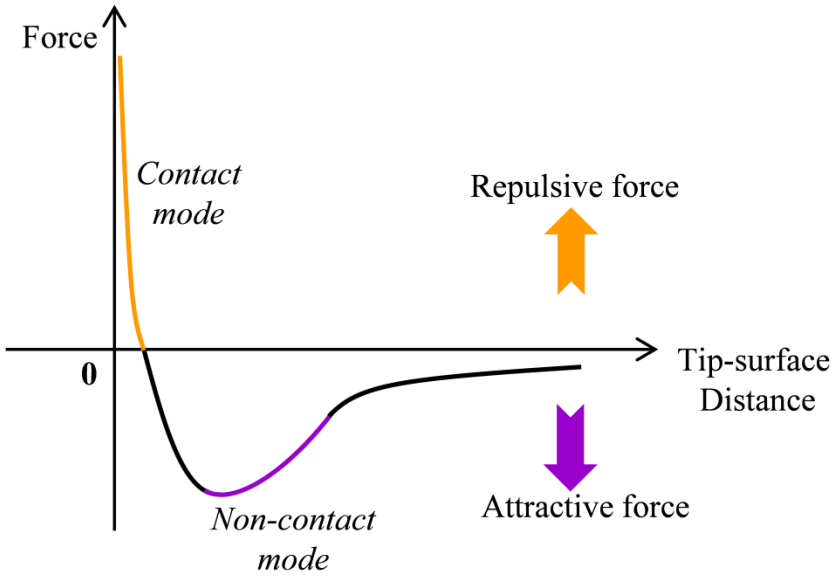


**Figure 2.21.** Schematic illustration of an atomic force-distance curve.

In a typical study using tapping mode AFM, amplitude, height and phase images are obtained. The amplitude image is raw data collected by the photodiode. The height image is created based upon the amplitude data and is the most common type of image in the literature. From the height image, the three-dimensional topography and the surface roughness of the sample surface can be obtained. A phase image is created by mapping the "delay" of the oscillation while tapping the sample surface compared to the free oscillation (**Figure 2.22**).[240] This "delay" is caused by energy dissipation during contact between the sample surface and the tip, and thus the phase

signal is sensitive to the viscoelastic properties of the sample surface. Therefore, tapping mode AFM provides a convenient and powerful approach to study phase separated polymer blends or block (graft) copolymer thin films.[241, 242]

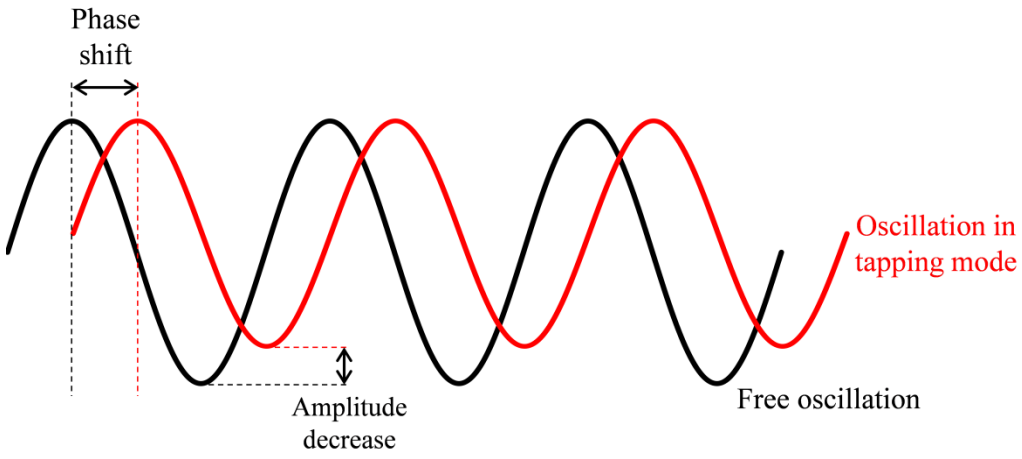


**Figure 2.22.** Schematic illustration of the cantilever's oscillation in the tapping mode. Adapted from Eaton et al.[240]

## 2.7 References

(1) Binder, J. B.; Raines, R. T. *J. Am. Chem. Soc.* **2009,** 131, 1979-1985.

(2) Ravve, A. Naturally Occurring Polymers. In *Principles of Polymer Chemistry*, Springer US: 2000; pp 449-475.

(3) Hamelinck, C. N.; Hooijdonk, G. v.; Faaij, A. P. C. *Biomass Bioenergy* **2005,** 28, 384-410.

(4) Farrell, A. E.; Plevin, R. J.; Turner, B. T.; Jones, A. D.; O'Hare, M.; Kammen, D. M. *Science* **2006,** 311, 506-508.

(5) Carroll, A.; Somerville, C. *Annu. Rev. Plant Biol.* **2009,** 60, 165-182.

(6) Czaja, W.; Krystynowicz, A.; Bielecki, S.; Brown Jr, R. M. *Biomaterials* **2006,** 27, 145-151.

(7) Ravi Kumar, M. N. V. *React. Funct. Polym.* **2000,** 46, 1-27.

(8) Jayakumar, R.; Prabaharan, M.; Sudheesh Kumar, P. T.; Nair, S. V.; Tamura, H. *Biotechnol. Adv.* **2011,** 29, 322-337.

(9) Wyman, C. E. *Bioresour. Technol.* **1994,** 50, 3-15.

(10) Lee, J. *J. Biotechnol.* **1997,** 56, 1-24.

(11) Solomon, B. D.; Barnes, J. R.; Halvorsen, K. E. *Biomass Bioenergy* **2007,** 31, 416-425.

(12) Mosier, N.; Wyman, C.; Dale, B.; Elander, R.; Lee, Y. Y.; Holtzapple, M.; Ladisch, M. *Bioresour. Technol.* **2005,** 96, 673-686.

(13) Hendriks, A. T. W. M.; Zeeman, G. *Bioresour. Technol.* **2009,** 100, 10-18.

(14) Kumar, P.; Barrett, D. M.; Delwiche, M. J.; Stroeve, P. *Ind. Eng. Chem. Res.* **2009,** 48, 3713-3729.

(15) Himmel, M. E.; Ding, S.-Y.; Johnson, D. K.; Adney, W. S.; Nimlos, M. R.; Brady, J. W.; Foust, T. D. *Science* **2007,** 315, 804-807.

(16) Bonawitz, N. D.; Chapple, C. *Annu. Rev. Genet.* **2010,** 44, 337-363.

(17) Cosgrove, D. J. *Nat. Rev. Mol. Cell Biol.* **2005,** 6, 850-861.

(18) Somerville, C.; Bauer, S.; Brininstool, G.; Facette, M.; Hamann, T.; Milne, J.; Osborne, E.; Paredez, A.; Persson, S.; Raab, T.; Vorwerk, S.; Youngs, H. *Science* **2004,** 306, 2206-2211.

(19) Cosgrove, D. J. *Nature* **2000,** 407, 321-326.

(20) Cosgrove, D. J. *Plant Physiol.* **2001,** 125, 131-134.

(21) Campbell, N. A.; Reece, J. B. *Biology*; 8th ed.; benjamin cummings: San Francisco, CA, 2007.

(22) Jarvis, M. C.; Briggs, S. P. H.; Knox, J. P. *Plant, Cell Environ.* **2003,** 26, 977-989.

(23) Salisbury, F. B.; Ross, C. W. Plant Physiology and Plant Cells. In *Plant Physiol.*, Wadsworth, Inc.: Belmont, CA, 1992; pp 3-26.

(24) Scheller, H. V.; Ulvskov, P. *Annu. Rev. Plant Biol.* **2010,** 61, 263-289.

(25) Zhong, R.; Ye, Z.-H. Secondary Cell Walls. In *ELS*, John Wiley & Sons, Ltd: 2001.

(26) Sjostrom, E. *Wood Chemistry: Fundamentals and Applications*; 2nd ed.; Academic Press: San Diego, CA, 1993.

(27) Klemm, D.; Heublein, B.; Fink, H.-P.; Bohn, A. *Angew. Chem. Int. Ed.* **2005,** 44, 3358-3393.

(28) Liebert, T. Cellulose Solvents - Remarkable History, Bright Future. In *Cellulose Solvents: For Analysis, Shaping and Chemical Modification*, American Chemical Society: 2010; Vol. 1033, pp 3-54.

(29) Edgar, K. J.; Buchanan, C. M.; Debenham, J. S.; Rundquist, P. A.; Seiler, B. D.; Shelton, M. C.; Tindall, D. *Prog. Polym. Sci.* **2001,** 26, 1605-1688.

(30) O'Sullivan, A. *Cellulose* **1997,** 4, 173-207.

(31) Gardner, K. H.; Blackwell, J. *Biopolymers* **1974,** 13, 1975-2001.

(32) Langan, P.; Nishiyama, Y.; Chanzy, H. *J. Am. Chem. Soc.* **1999,** 121, 9940-9946.

(33) Wada, M.; Okano, T.; Sugiyama, J. *Cellulose* **1997,** 4, 221-232.

(34) Wada, M.; Chanzy, H.; Nishiyama, Y.; Langan, P. *Macromolecules* **2004,** 37, 8548-8555.

(35) Nishiyama, Y. *J. Wood Sci.* **2009,** 55, 241-249.

(36) Watts, H. D.; Mohamed, M. N. A.; Kubicki, J. D. *Phys. Chem. Chem. Phys.* **2011,** 13, 20974-20985.

(37) Lerouxel, O.; Cavalier, D. M.; Liepman, A. H.; Keegstra, K. *Curr. Opin. Plant Biol.* **2006,** 9, 621-630.

(38) Paredez, A. R.; Somerville, C. R.; Ehrhardt, D. W. *Science* **2006,** 312, 1491-1495.

(39) Somerville, C. *Annu. Rev. Cell Dev. Biol.* **2006,** 22, 53-78.

(40) Ebringerová, A.; Hromádková, Z.; Heinze, T. Hemicellulose. In *Polysaccharides I*, Heinze, T., Ed. Springer Berlin Heidelberg: 2005; Vol. 186, pp 1-67.

(41) Hayashi, T. *Annu. Rev. Plant Physiol. Plant Mol. Biol.* **1989,** 40, 139-168.

(42) Moreira, L. R. S.; Filho, E. X. F. *Appl. Microbiol. Biotechnol.* **2008,** 79, 165-178.

(43) Sun, R.; Sun, X. F.; Tomkinson, J. Hemicelluloses and Their Derivatives. In *Hemicelluloses: Science and Technology*, American Chemical Society: 2003; Vol. 864, pp 2-22.

(44) Pauly, M.; Gille, S.; Liu, L.; Mansoori, N.; Souza, A.; Schultink, A.; Xiong, G. *Planta* **2013,** 238, 627-642.

(45) Boerjan, W.; Ralph, J.; Baucher, M. *Annu. Rev. Plant Biol.* **2003,** 54, 519-546.

(46) Whetten, R.; Sederoff, R. *Plant Cell* **1995,** 7, 1001-1013.

(47) Zakzeski, J.; Bruijnincx, P. C. A.; Jongerius, A. L.; Weckhuysen, B. M. *Chem. Rev.* **2010,** 110, 3552-3599.

(48) Chakar, F. S.; Ragauskas, A. J. *Ind. Crop. Prod.* **2004,** 20, 131-141.

(49) Guerra, A.; Filpponen, I.; Lucia, L. A.; Saquing, C.; Baumberger, S.; Argyropoulos, D. S. *J. Agric. Food. Chem.* **2006,** 54, 5939-5947.

(50) da Costa Sousa, L.; Chundawat, S. P. S.; Balan, V.; Dale, B. E. *Curr. Opin. Biotechnol.* **2009,** 20, 339-347.

(51) McDonough, T. J. *Tappi J.* **1993,** 76, 186-193.

(52) Notley, S. M.; Norgren, M. *Langmuir* **2010,** 26, 5484-5490.

(53) Ikeda, T.; Holtman, K.; Kadla, J. F.; Chang, H.-m.; Jameel, H. *J. Agric. Food. Chem.* **2001,** 50, 129-135.

(54) Hatakeyama, H.; Hatakeyama, T. Lignin Structure, Properties, and Applications. In *Biopolymers*, Abe, A.; Dusek, K.; Kobayashi, S., Eds.; Springer Berlin Heidelberg: 2010; Vol. 232, pp 1-63.

(55) Stewart, D. *Ind. Crop. Prod.* **2008,** 27, 202-207.

(56) Baker, D. A.; Rials, T. G. *J. Appl. Polym. Sci.* **2013,** 130, 713-728.

(57) Pandey, M. P.; Kim, C. S. *Chem. Eng. Technol.* **2011,** 34, 29-41.

(58) Li, X.; Chapple, C. *Plant Physiol.* **2010,** 154, 449-452.

(59) Miao, Y.-C.; Liu, C.-J. *Proc. Natl. Acad. Sci. U.S.A.* **2010,** 107, 22728-22733.

(60) Sibout, R.; Höfte, H. *Curr. Biol.* **2012,** 22, 533-535.

(61) Chen, Y.-r.; Sarkanen, S. *Phytochemistry* **2010,** 71, 453-462.

(62) Hertzberg, M.; Aspeborg, H.; Schrader, J.; Andersson, A.; Erlandsson, R.; Blomqvist, K.; Bhalerao, R.; Uhlén, M.; Teeri, T. T.; Lundeberg, J.; Sundberg, B.; Nilsson, P.; Sandberg, G. *Proc. Natl. Acad. Sci. U.S.A.* **2001,** 98, 14732-14737.

(63) Veitch, N. C. *Phytochemistry* **2004,** 65, 249-259.

(64) Riva, S. *Trends Biotechnol.* **2006,** 24, 219-226.

(65) Rinaudo, M. *Prog. Polym. Sci.* **2006,** 31, 603-632.

(66) Raabe, D.; Sachs, C.; Romano, P. *Acta Mater.* **2005,** 53, 4281-4292.

(67) Bowman, S. M.; Free, S. J. *Bioessays* **2006,** 28, 799-808.

(68) Ruiz-Herrera, J. *Fungal Cell Wall: Structure, Synthesis, and Assembly, Second Edition* CRC Press, LLC Boca Raton, Florida, 2012.

(69) Muzzarelli, R. A. A. Nanochitins and Nanochitosans, Paving the Way to Eco-Friendly and Energy-Saving Exploitation of Marine Resources. In *Polymer Science: A Comprehensive Reference*, Krzysztof, M.; Martin, M., Eds.; Elsevier BV: Amsterdam, 2012; pp 153-164.

(70) Zeng, J.-B.; He, Y.-S.; Li, S.-L.; Wang, Y.-Z. *Biomacromolecules* **2012,** 13, 1-11.

(71) Muzzarelli, R. A. Chitin Nanostructures in Living Organisms. In *Chitin*, Gupta, N. S., Ed. Springer Netherlands: 2011; Vol. 34, pp 1-34.

(72) Muzzarelli, R. A. A.; Boudrant, J.; Meyer, D.; Manno, N.; DeMarchis, M.; Paoletti, M. G. *Carbohydr. Polym.* **2012,** 87, 995-1012.

(73) Blackwell, J.; Parker, K. D.; Rudall, K. M. *J. Mar. Biol. Assoc. U.K.* **1965,** 45, 659-661.

(74) Rudall, K. M.; Kenchington, W. *Biol. Rev.* **1973,** 48, 597-633.

(75) Saito, Y.; Okano, T.; Gaill, F.; Chanzy, H.; Putaux, J.-L. *Int. J. Biol. Macromol.* **2000,** 28, 81-88.

(76) Saito, Y.; Putaux, J. L.; Okano, T.; Gaill, F.; Chanzy, H. *Macromolecules* **1997,** 30, 3867-3873.

(77) Noishiki, Y.; Takami, H.; Nishiyama, Y.; Wada, M.; Okada, S.; Kuga, S. *Biomacromolecules* **2003,** 4, 896-899.

(78) Pillai, C. K. S.; Paul, W.; Sharma, C. P. *Prog. Polym. Sci.* **2009,** 34, 641-678.

(79) Terbojevich, M.; Carraro, C.; Cosani, A.; Marsano, E. *Carbohydr. Res.* **1988,** 180, 73-86.

(80) de Vasconcelos, C. L.; Bezerril, P. M.; Pereira, M. R.; Ginani, M. F.; Fonseca, J. L. C. *Carbohydr. Res.* **2011,** 346, 614-618.

(81) Hu, X.; Du, Y.; Tang, Y.; Wang, Q.; Feng, T.; Yang, J.; Kennedy, J. F. *Carbohydr. Polym.* **2007,** 70, 451-458.

(82) Xie, H.; Zhang, S.; Li, S. *Green Chem.* **2006,** 8, 630-633.

(83) Kumar, P. T. S.; Abhilash, S.; Manzoor, K.; Nair, S. V.; Tamura, H.; Jayakumar, R. *Carbohydr. Polym.* **2010,** 80, 761-767.

(84) Rejinold N, S.; Chennazhi, K. P.; Tamura, H.; Nair, S. V.; Rangasamy, J. *ACS Appl. Mater. Interfaces* **2011,** 3, 3654-3665.

(85) Mi, F.-L.; Shyu, S.-S.; Lin, Y.-M.; Wu, Y.-B.; Peng, C.-K.; Tsai, Y.-H. *Biomaterials* **2003,** 24, 5023-5036.

(86) Freier, T.; Montenegro, R.; Shan Koh, H.; Shoichet, M. S. *Biomaterials* **2005,** 26, 4624-4632.

(87) Noh, H. K.; Lee, S. W.; Kim, J.-M.; Oh, J.-E.; Kim, K.-H.; Chung, C.-P.; Choi, S.-C.; Park, W. H.; Min, B.-M. *Biomaterials* **2006,** 27, 3934-3944.

(88) Krajewska, B. *Enzyme Microb. Technol.* **2004,** 35, 126-139.

(89) Muzzarelli, R. A. A. *Enzyme Microb. Technol.* **1980,** 2, 177-184.

(90) Ohashi, E.; Karube, I. *J. Biotechnol.* **1995,** 40, 13-19.

(91) Ohashi, E.; Koriyama, T. *Anal. Chim. Acta* **1992,** 262, 19-25.

(92) Resch, M. G.; Donohoe, B. S.; Baker, J. O.; Decker, S. R.; Bayer, E. A.; Beckham, G. T.; Himmel, M. E. *Energy Environ. Sci.* **2013,** 6, 1858-1867.

(93) Bayer, E. A.; Belaich, J.-P.; Shoham, Y.; Lamed, R. *Annu. Rev. Microbiol.* **2004,** 58, 521-554.

(94) Bhat, M. K. *Biotechnol. Adv.* **2000,** 18, 355-383.

(95) Bayer, E. A.; Chanzy, H.; Lamed, R.; Shoham, Y. *Curr. Opin. Struct. Biol.* **1998,** 8, 548-557.

(96) Henrissat, B. *Cellulose* **1994,** 1, 169-196.

(97) McCarter, J. D.; Withers, S. G. *Curr. Opin. Struct. Biol.* **1994,** 4, 885-892.

(98) Knowles, J.; Lehtovaara, P.; Teeri, T. *Trends Biotechnol.* **1987,** 5, 255-261.

(99) Flach, J.; Pilet, P. E.; Jollès, P. *Experientia* **1992,** 48, 701-716.

(100) Souza, R. F.; Gomes, R. C.; Coelho, R. R. R.; Alviano, C. S.; Soares, R. M. A. *FEMS Microbiol. Lett.* **2003,** 222, 45-50.

(101) Patil, R. S.; Ghormade, V.; Deshpande, M. V. *Enzyme Microb. Technol.* **2000,** 26, 473-483.

(102) Hardt, M.; Laine, R. A. *Arch. Biochem. Biophys.* **2004,** 426, 286-297.

(103) Kezuka, Y.; Ohishi, M.; Itoh, Y.; Watanabe, J.; Mitsutomi, M.; Watanabe, T.; Nonaka, T. *J. Mol. Biol.* **2006,** 358, 472-484.

(104) Dahiya, N.; Tewari, R.; Hoondal, G. *Appl. Microbiol. Biotechnol.* **2006,** 71, 773-782.

(105) Collinge, D. B.; Kragh, K. M.; Mikkelsen, J. D.; Nielsen, K. K.; Rasmussen, U.; Vad, K. *Plant J.* **1993,** 3, 31-40.

(106) Gooday, G. W.; Zhu, W.-Y.; O'Donnell, R. W. *FEMS Microbiol. Lett.* **1992,** 100, 387-391.

(107) Crawford, D. L.; Crawford, R. L. *Enzyme Microb. Technol.* **1980,** 2, 11-22.

(108) Hatakka, A. Biodegradation of Lignin. In *Biopolymers Online*, Wiley-VCH Verlag GmbH & Co. KGaA: 2005.

(109) Kirk, T. K.; Farrell, R. L. *Annu. Rev. Microbiol.* **1987,** 41, 465-501.

(110) Buswell, J. A.; Odier, E.; Kirk, T. K. *Crit. Rev. Biotechnol.* **1987,** 6, 1-60.

(111) Tien, M.; Kirk, T. K. *Science* **1983,** 221, 661-663.

(112) Glenn, J. K.; Morgan, M. A.; Mayfield, M. B.; Kuwahara, M.; Gold, M. H. *Biochem. Biophys. Res. Commun.* **1983,** 114, 1077-1083.

(113) Bourbonnais, R.; Paice, M. G. *Biochem. J.* **1988,** 255, 445-450.

(114) Kersten, P. J.; Kirk, T. K. *J. Bacteriol.* **1987,** 169, 2195-2201.

(115) Gutiérrez, A.; Caramelo, L.; Prieto, A.; Martínez, M. J.; Martínez, A. T. *Appl. Environ. Microbiol.* **1994,** 60, 1783-1788.

(116) Buswell, J. A.; Eriksson, K.-E. Vanillate hydroxylase from Sporotrichum pulverulentum. In *Methods Enzymol.*, Willis A. Wood, S. T. K., Ed. Academic Press: 1988; Vol. Volume 161, pp 274-281.

(117) Niladevi, K. N. Ligninolytic Enzymes. In *Biotechnology for Agro-Industrial Residues Utilisation*, Nigam, P.; Pandey, A., Eds.; Springer Netherlands: 2009; pp 397-414.

(118) Kersten, P. J.; Kalyanaraman, B.; Hammel, K. E.; Reinhammar, B.; Kirk, T. K. *Biochem. J.* **1990,** 268, 475-480.

(119) Smith, A. T.; Doyle, W. A.; Dorlet, P.; Ivancich, A. *Proc. Natl. Acad. Sci. U.S.A.* **2009**.

(120) Wong, D. S. *Appl. Biochem. Biotechnol.* **2009,** 157, 174-209.

(121) Higuchi, T. Mechanisms of Lignin Degradation by Lignin Peroxidase and Laccase of White-Rot Fungi. In *Plant Cell Wall Polymers*, American Chemical Society: 1989; Vol. 399, pp 482-502.

(122) Kuwahara, M.; Glenn, J. K.; Morgan, M. A.; Gold, M. H. *FEBS Lett.* **1984,** 169, 247-250.

(123) Hofrichter, M. *Enzyme Microb. Technol.* **2002,** 30, 454-466.

(124) Hatakka, A. *FEMS Microbiol. Rev.* **1994,** 13, 125-135.

(125) Wariishi, H.; Valli, K.; Gold, M. H. *J. Biol. Chem.* **1992,** 267, 23688-23695.

(126) Wariishi, H.; Akileswaran, L.; Gold, M. H. *Biochemistry* **1988,** 27, 5365-5370.

(127) Cui, F.; Dolphin, D. *Holzforschung* **1990,** 44, 279-283.

(128) Hammel, K. E.; Jensen, K. A.; Mozuch, M. D.; Landucci, L. L.; Tien, M.; Pease, E. A. *J. Biol. Chem.* **1993,** 268, 12274-12281.

(129) Wariishi, H.; Valli, K.; Gold, M. H. *Biochemistry* **1989,** 28, 6017-6023.

(130) Tuor, U.; Wariishi, H.; Schoemaker, H. E.; Gold, M. H. *Biochemistry* **1992,** 31, 4986-4995.

(131) Reinhammar, B. R. M. *Biochim. Biophys. Acta Bioenerg.* **1972,** 275, 245-259.

(132) Xu, F.; Berka, R. M.; Wahleithner, J. A.; Nelson, B. A.; Shuster, J. R.; Brown, S. H.; Palmer, A. E.; Solomon, E. I. *Biochem. J* **1998,** 334, 63-70.

(133) Bourbonnais, R.; Paice, M. G.; Freiermuth, B.; Bodie, E.; Borneman, S. *Appl. Environ. Microbiol.* **1997,** 63, 4627-4632.

(134) Kontturi, E.; Tammelin, T.; Osterberg, M. *Chem. Soc. Rev.* **2006,** 35, 1287-1304.

(135) Roman, M. Model Cellulosic Surfaces: History and Recent Advances. In *Model Cellulosic Surfaces*, American Chemical Society: 2009; Vol. 1019, pp 3-53.

(136) Schaub, M.; Wenz, G.; Wegner, G.; Stein, A.; Klemm, D. *Adv. Mater.* **1993,** 5, 919-922.

(137) Wegner, G.; Buchholz, V.; Ödberg, L.; Stemme, S. *Adv. Mater.* **1996,** 8, 399-402.

(138) Tammelin, T.; Saarinen, T.; Österberg, M.; Laine, J. *Cellulose* **2006,** 13, 519-535.

(139) Rehfeldt, F.; Tanaka, M. *Langmuir* **2002,** 19, 1467-1473.

(140) Kontturi, E.; Thüne, P. C.; Niemantsverdriet, J. W. *Langmuir* **2003,** 19, 5735-5741.

(141) Geffroy, C.; Labeau, M. P.; Wong, K.; Cabane, B.; Cohen Stuart, M. A. *Colloids Surf., A: Physicochem. Eng. Aspects* **2000,** 172, 47-56.

(142) Kittle, J. D.; Du, X.; Jiang, F.; Qian, C.; Heinze, T.; Roman, M.; Esker, A. R. *Biomacromolecules* **2011,** 12, 2881-2887.

(143) Eriksson, J.; Malmsten, M.; Tiberg, F.; Callisen, T. H.; Damhus, T.; Johansen, K. S. *J. Colloid Interface Sci.* **2005,** 284, 99-106.

(144) Eriksson, J.; Malmsten, M.; Tiberg, F.; Callisen, T. H.; Damhus, T.; Johansen, K. S. *J. Colloid Interface Sci.* **2005,** 285, 94-99.

(145) Aulin, C.; Ahola, S.; Josefsson, P.; Nishino, T.; Hirose, Y.; Österberg, M.; Wågberg, L. *Langmuir* **2009,** 25, 7675-7685.

(146) Gunnars, S.; Wågberg, L.; Cohen Stuart, M. A. *Cellulose* **2003,** 10, 185-185.

(147) Fält, S.; Wågberg, L.; Vesterlind, E. L.; Larsson, P. T. *Cellulose* **2004,** 11, 151-162.

(148) Notley, S. M.; Wågberg, L. *Biomacromolecules* **2005,** 6, 1586-1591.

(149) Edgar, C.; Gray, D. *Cellulose* **2003,** 10, 299-306.

(150) Lefebvre, J.; Gray, D. *Cellulose* **2005,** 12, 127-134.

(151) Habibi, Y.; Foulon, L.; Aguié-Béghin, V.; Molinari, M.; Douillard, R. *J. Colloid Interface Sci.* **2007,** 316, 388-397.

(152) Kittle, J. D.; Wondraczek, H.; Wang, C.; Jiang, F.; Roman, M.; Heinze, T.; Esker, A. R. *Langmuir* **2012,** 28, 11086-11094.

(153) Jiang, F.; Kittle, J. D.; Tan, X.; Esker, A. R.; Roman, M. *Langmuir* **2013,** 29, 3280-3291.

(154) Ahola, S.; Salmi, J.; Johansson, L. S.; Laine, J.; Österberg, M. *Biomacromolecules* **2008,** 9, 1273-1282.

(155) Ahola, S.; Turon, X.; Österberg, M.; Laine, J.; Rojas, O. J. *Langmuir* **2008,** 24, 11592-11599.

(156) Yokota, S.; Kitaoka, T.; Sugiyama, J.; Wariishi, H. *Adv. Mater.* **2007,** 19, 3368-3370.

(157) Fink, H. P.; Weigel, P.; Purz, H. J.; Ganster, J. *Prog. Polym. Sci.* **2001,** 26, 1473-1524.

(158) Heinze, T.; Koschella, A. *Polimeros* **2005,** 15, 84-90.

(159) Luner, P.; Sandell, M. *J. Polym. Sci., Part C: Polym. Symp.* **1969,** 28, 115-142.

(160) Mormann, W.; Wagner, T. *Carbohydr. Polym.* **2000,** 43, 257-262.

(161) Mormann, W.; Wezstein, M. *Macromol. Biosci.* **2009,** 9, 369-375.

(162) Köhler, S.; Liebert, T.; Heinze, T. *J. Polym. Sci., Part A: Polym. Chem.* **2008,** 46, 4070-4080.

(163) Kontturi, E.; Suchy, M.; Penttilä, P.; Jean, B.; Pirkkalainen, K.; Torkkeli, M.; Serimaa, R. *Biomacromolecules* **2011,** 12, 770-777.

(164) Kaya, A.; Du, X.; Liu, Z.; Lu, J. W.; Morris, J. R.; Glasser, W. G.; Heinze, T.; Esker, A. R. *Biomacromolecules* **2009,** 10, 2451-2459.

(165) Habibi, Y.; Lucia, L. A.; Rojas, O. J. *Chem. Rev.* **2010,** 110, 3479-3500.

(166) Lagerwall, J. P. F.; Schutz, C.; Salajkova, M.; Noh, J.; Hyun Park, J.; Scalia, G.; Bergstrom, L. *NPG Asia Mater.* **2014,** 6, e80.

(167) Norgren, M.; Notley, S. M.; Majtnerova, A.; Gellerstedt, G. *Langmuir* **2006,** 22, 1209-1214.

(168) Norgren, M.; Gärdlund, L.; Notley, S. M.; Htun, M.; Wågberg, L. *Langmuir* **2007,** 23, 3737-3743.

(169) Notley, S. M.; Norgren, M. *Biomacromolecules* **2008,** 9, 2081-2086.

(170) Saarinen, T.; Orelma, H.; Grönqvist, S.; Andberg, M.; Holappa, S.; Laine, J. *BioResources* **2009,** 4, 94-110.

(171) Tammelin, T.; Österberg, M.; Johansson, L.-S.; Laine, J. *Nord. Pulp Paper Res. J.* **2006,** 21, 444-450.

(172) Tammelin, T.; Johnsen, I. A.; Österberg, M.; Stenius, P.; Laine, J. *Nord. Pulp Paper Res. J.* **2007,** 22, 93-101.

(173) Constantino, C. J. L.; Juliani, L. P.; Botaro, V. R.; Balogh, D. T.; Pereira, M. R.; Ticianelli, E. A.; Curvelo, A. A. S.; Oliveira Jr, O. N. *Thin Solid Films* **1996,** 284–285, 191-194.

(174) Constantino, C. J. L.; Dhanabalan, A.; Curvelo, A. A. S.; Oliveira Jr, O. N. *Thin Solid Films* **1998,** 327–329, 47-51.

(175) Pasquini, D.; Balogh, D. T.; Antunes, P. A.; Constantino, C. J. L.; Curvelo, A. A. S.; Aroca, R. F.; Oliveira, O. N. *Langmuir* **2002,** 18, 6593-6596.

(176) Pasquini, D.; Balogh, D. T.; Oliveira Jr, O. N.; Curvelo, A. A. S. *Colloids Surf., A: Physicochem. Eng. Aspects* **2005,** 252, 193-200.

(177) Micic, M.; Radotic, K.; Jeremic, M.; Leblanc, R. M. *Macromol. Biosci.* **2003,** 3, 100-106.

(178) Micic, M.; Radotic, K.; Jeremic, M.; Djikanovic, D.; Kämmer, S. B. *Colloids Surf., B: Biointerfaces* **2004,** 34, 33-40.

(179) Micic, M.; Radotic, K.; Benitez, I.; Ruano, M.; Jeremic, M.; Moy, V.; Mabrouki, M.; Leblanc, R. M. *Biophys. Chem.* **2001,** 94, 257-263.

(180) Paterno, L. G.; Mattoso, L. H. C. *Polymer* **2001,** 42, 5239-5245.

(181) Maximova, N.; Österberg, M.; Laine, J.; Stenius, P. *Colloids Surf., A: Physicochem. Eng. Aspects* **2004,** 239, 65-75.

(182) Kikkawa, Y.; Tokuhisa, H.; Shingai, H.; Hiraishi, T.; Houjou, H.; Kanesato, M.; Imanaka, T.; Tanaka, T. *Biomacromolecules* **2008,** 9, 2126-2131.

(183) Montiel-González, Z.; Luna-Bárcenas, G.; Mendoza-Galván, A. *Phys. Stat. Sol. C.* **2008,** 5, 1434-1437.

(184) Yusof, N. L. B. M.; Lim, L. Y.; Khor, E. *Carbohydr. Res.* **2004,** 339, 2701-2711.

(185) Wu, Y.; Sasaki, T.; Irie, S.; Sakurai, K. *Polymer* **2008,** 49, 2321-2327.

(186) Zhong, C.; Cooper, A.; Kapetanovic, A.; Fang, Z.; Zhang, M.; Rolandi, M. *Soft Matter* **2010,** 6, 5298-5301.

(187) Zhong, C.; Kapetanovic, A.; Deng, Y.; Rolandi, M. *Adv. Mater.* **2011,** 23, 4776-4781.

(188) East, G. C.; Qin, Y. *J. Appl. Polym. Sci.* **1993,** 50, 1773-1779.

(189) Janshoff, A.; Galla, H.-J.; Steinem, C. *Angew. Chem. Int. Ed.* **2000,** 39, 4004-4032.

(190) Höök, F. PhD Thesis, Chalmers University of Technology, Göteborg, Sweden, 1997.

(191) Sauerbrey, G. *Z. Phys.* **1959,** 155, 206-222.

(192) Marx, K. A. *Biomacromolecules* **2003,** 4, 1099-1120.

(193) Konash, P. L.; Bastiaans, G. J. *Anal. Chem.* **1980,** 52, 1929-1931.

(194) Nomura, T.; Okuhara, M. *Anal. Chim. Acta* **1982,** 142, 281-284.

(195) Schiessel, H.; Metzler, R.; Blumen, A.; Nonnenmacher, T. F. *J. Phys. A: Math. Gen.* **1995,** 28, 6567.

(196) Voinova, M. V.; Rodahl, M.; Jonson, M.; Kasemo, B. *Phys. Scr.* **1999,** 59, 391.

(197) Dixon, M. C. *J Biomol. Tech.* **2008,** 19, 151-158.

(198) Höök, F.; Kasemo, B.; Nylander, T.; Fant, C.; Sott, K.; Elwing, H. *Anal. Chem.* **2001,** 73, 5796-5804.

(199) Notley, S. M.; Eriksson, M.; Wågberg, L. *J. Colloid Interface Sci.* **2005,** 292, 29-37.

(200) Vogt, B. D.; Soles, C. L.; Lee, H.-J.; Lin, E. K.; Wu, W.-l. *Langmuir* **2004,** 20, 1453-1458.

(201) Michel, M.; Vautier, D.; Voegel, J.-C.; Schaaf, P.; Ball, V. *Langmuir* **2004,** 20, 4835-4839.

(202) Caruso, F.; Serizawa, T.; Furlong, D. N.; Okahata, Y. *Langmuir* **1995,** 11, 1546-1552.

(203) Naderi, A.; Claesson, P. M. *Langmuir* **2006,** 22, 7639-7645.

(204) George, P. A.; Donose, B. C.; Cooper-White, J. J. *Biomaterials* **2009,** 30, 2449-2456.

(205) Marie, R.; Beech, J. P.; Vörös, J.; Tegenfeldt, J. O.; Höök, F. *Langmuir* **2006,** 22, 10103-10108.

(206) Berglin, M.; Delage, L.; Potin, P.; Vilter, H.; Elwing, H. *Biomacromolecules* **2004,** 5, 2376-2383.

(207) Knowles, T. P. J.; Shu, W.; Devlin, G. L.; Meehan, S.; Auer, S.; Dobson, C. M.; Welland, M. E. *Proc. Natl. Acad. Sci. U.S.A.* **2007,** 104, 10016-10021.

(208) Snabe, T.; Petersen, S. B. *Chem. Phys. Lipids* **2003,** 125, 69-82.

(209) Fu, L.; Chen, X.; He, J.; Xiong, C.; Ma, H. *Langmuir* **2008,** 24, 6100-6106.

(210) Heeb, R.; Bielecki, R. M.; Lee, S.; Spencer, N. D. *Macromolecules* **2009,** 42, 9124-9132.

(211) Stengel, G.; Höök, F.; Knoll, W. *Anal. Chem.* **2005,** 77, 3709-3714.

(212) Su, X.; Robelek, R.; Wu, Y.; Wang, G.; Knoll, W. *Anal. Chem.* **2003,** 76, 489-494.

(213) Su, X.; Wu, Y.-J.; Robelek, R.; Knoll, W. *Langmuir* **2004,** 21, 348-353.

(214) Modin, C.; Stranne, A.-L.; Foss, M.; Duch, M.; Justesen, J.; Chevallier, J.; Andersen, L. K.; Hemmersam, A. G.; Pedersen, F. S.; Besenbacher, F. *Biomaterials* **2006,** 27, 1346-1354.

(215) Lord, M. S.; Modin, C.; Foss, M.; Duch, M.; Simmons, A.; Pedersen, F. S.; Milthorpe, B. K.; Besenbacher, F. *Biomaterials* **2006,** 27, 4529-4537.

(216) Ritchie, R. H. *Phys. Rev.* **1957,** 106, 874-881.

(217) Barnes, W. L.; Dereux, A.; Ebbesen, T. W. *Nature* **2003,** 424, 824-830.

(218) Otto, A. *Z. Phys.* **1968,** 216, 398-410.

(219) Kretschmann, E.; Raether, H. *Z. Naturforsch. A* **1968,** 23, 2135–2136.

(220) Nedelkov, D.; Nelson, R. W. *Trends Biotechnol.* **2003,** 21, 301-305.

(221) Homola, J. *Surface Plasmon Resonance Based Sensors*; Springer: Berlin, Germany, 2006; Vol. 4.

(222) De Feijter, J. A.; Benjamins, J.; Veer, F. A. *Biopolymers* **1978,** 17, 1759-1772.

(223) Liu, Z.; Choi, H.; Gatenholm, P.; Esker, A. R. *Langmuir* **2011,** 27, 8718-8728.

(224) Sigal, G. B.; Mrksich, M.; Whitesides, G. M. *Langmuir* **1997,** 13, 2749-2755.

(225) Tulpar, A.; Ducker, W. A. *J. Phys. Chem. B* **2004,** 108, 1667-1676.

(226) Homola, J. *Chem. Rev.* **2008,** 108, 462-493.

(227) Green, R. J.; Frazier, R. A.; Shakesheff, K. M.; Davies, M. C.; Roberts, C. J.; Tendler, S. J. B. *Biomaterials* **2000,** 21, 1823-1835.

(228) Homola, J.; Yee, S. S.; Gauglitz, G. *Sensors Actuators B: Chem.* **1999,** 54, 3-15.

(229) Binnig, G.; Quate, C. F.; Gerber, C. *Phys. Rev. Lett.* **1986,** 56, 930-933.

(230) Binnig, G.; Rohrer, H. *Surf. Sci.* **1983,** 126, 236-244.

(231) Moreno-Herrero, F.; Gomez-Herrero, J. AFM: Basic Concepts. In *Atomic Force Microscopy in Liquid*, Wiley-VCH Verlag GmbH & Co. KGaA: 2012; pp 1-34.

(232) Yongho, S.; Wonho, J. *Rep. Prog. Phys.* **2008,** 71, 016101.

(233) García, R.; Pérez, R. *Surf. Sci. Rep.* **2002,** 47, 197-301.

(234) Albrecht, T. R.; Grütter, P.; Horne, D.; Rugar, D. *J. Appl. Phys.* **1991,** 69, 668-673.

(235) Gross, L.; Mohn, F.; Liljeroth, P.; Repp, J.; Giessibl, F. J.; Meyer, G. *Science* **2009,** 324, 1428-1431.

(236) Gross, L.; Mohn, F.; Moll, N.; Liljeroth, P.; Meyer, G. *Science* **2009,** 325, 1110-1114.

(237) Gross, L.; Mohn, F.; Moll, N.; Schuler, B.; Criado, A.; Guitián, E.; Peña, D.; Gourdon, A.; Meyer, G. *Science* **2012,** 337, 1326-1329.

(238) Zhong, Q.; Inniss, D.; Kjoller, K.; Elings, V. B. *Surf. Sci.* **1993,** 290, L688-L692.

(239) Haugstad, G. Overview of AFM. In *Atomic Force Microscopy*, John Wiley & Sons, Inc.: 2012; pp 1-32.

(240) Eaton, P.; West, P. *Atomic Force Microscopy*; Oxford University Press: New York, United States, 2010.

(241) Boltau, M.; Walheim, S.; Mlynek, J.; Krausch, G.; Steiner, U. *Nature* **1998,** 391, 877-879.

(242) Rockford, L.; Liu, Y.; Mansky, P.; Russell, T. P.; Yoon, M.; Mochrie, S. G. J. *Phys. Rev. Lett.* **1999,** 82, 2602-2605.

# Chapter 3: Materials and Experimental Methods

## 3.1 Synthesis of Trimethylsilyl Cellulose (TMSC) and Trimethylsilyl Chitin (TMSChitin)

### 3.1.1 Materials

Microcrystalline cellulose (Avicel PH-101) was purchased from Fluka. $\alpha$-Chitin from shrimp shells (practical grade, >95% acetylated), chlorotrimethylsilane (TMSCl), hexamethyldisilazane (HMDS), dimethylacetamide (DMAc, anhydrous), pyridine (anhydrous) and lithium chloride (LiCl) were purchased from Sigma-Aldrich. All other chemicals and solvents were obtained from Fisher Scientific and used as received.

### 3.1.2 Synthesis of Trimethylsilyl Cellulose (TMSC)

Microcrystalline cellulose was dissolved in DMAc/LiCl following a procedure reported by Edgar et al.[1] 2.00 g microcrystalline cellulose was suspended in 75 mL DMAc, and this mixture was heated to 150 °C in a round-bottom flask equipped with a short-path distillation apparatus. 3.75 g LiCl was added to the mixture and the mixture was heated to 170 °C. The mixture was cooled to room temperature after about 20 mL of solvent was distilled at 170 °C. The mixture was stirred overnight and a clear yellowish solution was obtained. Cellulose was then converted to trimethylsilyl cellulose (TMSC) according to a procedure reported by Kontturi et al.[2] (**Figure 3.1A**). The cellulose solution was heated to 80 °C and 20 mL of HMDS was added to the solution under a nitrogen atmosphere. The reaction mixture was stirred at 80 °C overnight and raw TMSC was obtained via precipitation in methanol. The raw TMSC was purified by dissolving in tetrahydrofuran (THF) followed by re-precipitation in methanol. The purified white solid (4.2 g, 90 % yield) was collected via filtration and dried in vacuo at 50 °C.

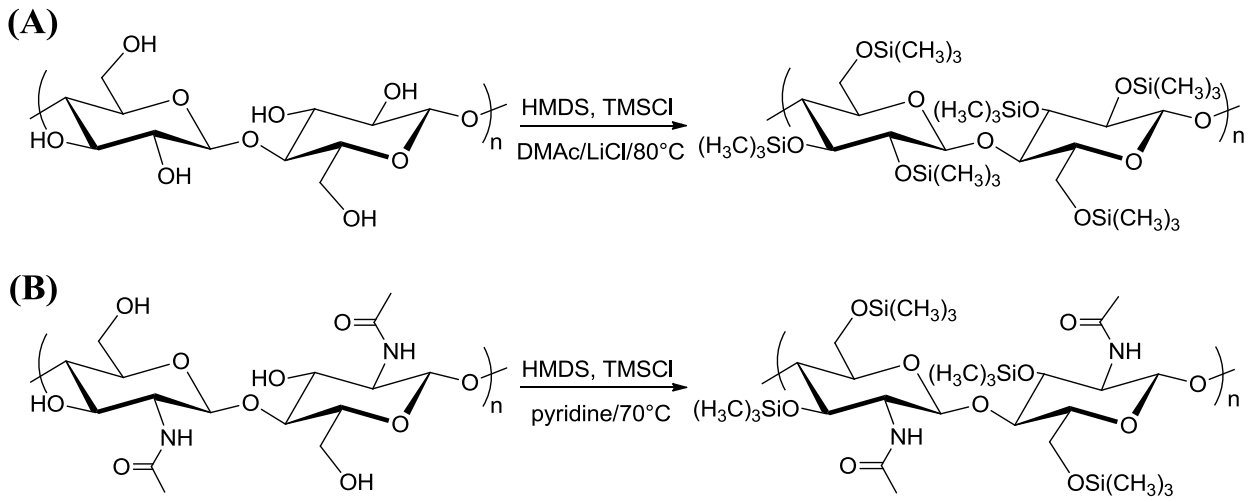


**Figure 3.1.** Reaction schemes for the synthesis of (A) TMSC and (B) TMSChitin.

$^1$H NMR spectra were recorded on a Varian INOVA-400 spectrometer at 400 MHz. TMSC was dissolved in $CDCl_3$ at a concentration of ~ 10 mg·mL$^{-1}$. The $^1$H NMR spectrum for TMSC in $CDCl_3$ is shown in **Figure 3.2**. The integrated area between chemical shifts (δ) of 2.5 and 5.2 ppm corresponds to 7 protons in an anhydro-glucose unit (AGU). The degree of substitution (DS) was defined as the number of TMS groups per AGU and was obtained from Equation 3.1. The calculated DS was 3.0, indicating that all three hydroxyl groups were substituted by TMS groups. The TMSC with high DS values showed good solubility in chloroform and toluene.

$$DS = \frac{Area_{TMS}/9}{Area_{Pyranose}/7} \tag{3.1}$$

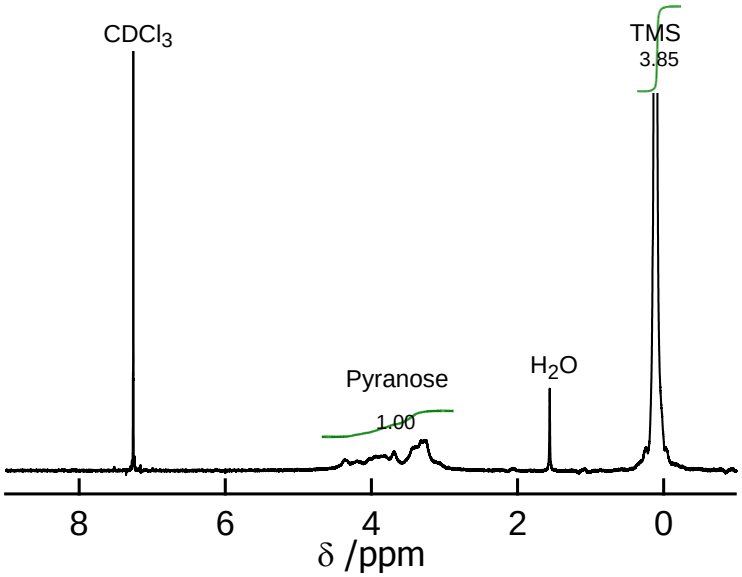


**Figure 3.2.** $^{1}$H NMR spectrum of TMSC in $CDCl_3$.

### 3.1.3 Synthesis of Trimethylsilyl Chitin (TMSChitin)

α-Chitin from shrimp shells was converted to trimethylsilyl chitin (TMSChitin) under heterogeneous conditions as previously reported by Kurita et al.[3] 0.5 g chitin was dispersed in 50 mL pyridine and the mixture was heated at 100 °C for 24 h. After cooling to room temperature, 5.15 mL of HMDS and 3.15 mL TMSCl were added to the mixture. The reaction mixture was stirred at 70 °C for 72 h. The brown supernatant was added dropwise to 500 mL acetone and led to a white cloudy dispersion. After filtering using a glass microfiber filter (VWR), the clear solution was collected and concentrated under reduced pressure. The resulting brown solution was added dropwise to 1 L of cold water to give a white precipitate. The white precipitate (0.29 g, 34 % yield) was collected via filtration, rinsed with water several times and dried in vacuo at 50 °C.

$^{1}$H NMR spectra were recorded on a Varian INOVA-400 spectrometer at 400 MHz. For $^{1}$H NMR measurements, TMSChitin was dissolved in $(CD_3)_2CO$ at a concentration of ~ 10 mg·mL$^{-1}$.

The $^{1}$H NMR spectrum for TMSChitin in $(CD_3)_2CO$ is shown in **Figure 3.3**. $^{1}$H NMR (400 MHz, acetone-$d_6$): δ = 0.15 (s, Si-$CH_3$, 18H), 1.98 (s, CO-$CH_3$, 3H), 3.35 (br s, pyranose, 1H), 3.80 (br m, pyranose, 5H), 4.43 (br s, pyranose, 1H), and 7.20 ppm (br s, N-H, 1H). The integrated area between chemical shifts (δ) of 3.0 and 4.6 ppm corresponds to 7 protons in an anhydro-*N*-acetylglucosamine unit (ANU). The degree of substitution (DS) was defined as the number of TMS groups per ANU and was obtained from equation 3.1. The calculated DS was 2.0, indicating that both of the hydroxyl groups were substituted by TMS groups. The TMSChitin with high DS values showed good solubility in acetone, isopropanol, pyridine and chloroform.

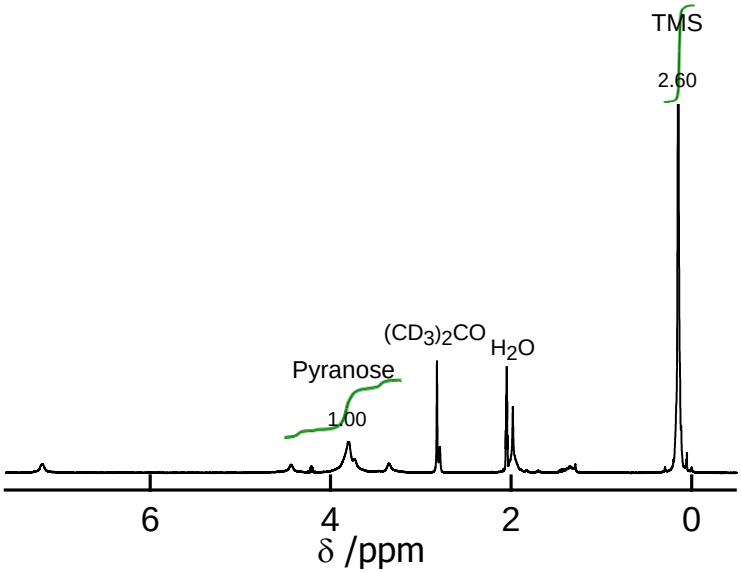


**Figure 3.3.** $^{1}$H NMR spectrum of TMSChitin in $(CD_3)_2CO$.

### 3.2 Synthesis of Nanocrystalline Cellulose (CNC) and Nanocrystalline Chitin (Chitin NC)

#### 3.2.1 Materials

Softwood sulfite pulp (Temalfa 93A-A) was kindly provided by Tembec, Inc. *α*-Chitin from shrimp shells (practical grade, >95% acetylated) was purchased from Sigma-Aldrich. Sulfuric acid (95.9 %), pyridine (99.5 %) and hydrochloric acid (37.3 %) were purchased from Fisher

Scientific. All other chemicals and solvents were obtained from Fisher Scientific and used as received.

### 3.2.2 Synthesis of Nanocrystalline Cellulose (CNC)

Colloidal suspensions of sulfated and desulfated nanocrystalline celluloses were prepared by the Roman group (Virginia Tech) according to a previous reported procedure.[4] Sulfated nanocrystalline cellulose (SNC) was prepared by sulfuric acid hydrolysis of softwood pulp and desulfated nanocrystalline cellulose (DNC) was prepared from SNC via a pyridine-based desulfation procedure. Representative heights and lengths of the DNC from AFM were 4.8 ± 1.4 and 154 ± 84 nm, respectively.[4] Conductometric titration study showed that the charge densities for SNC and DNC obtained via this procedure were 0.293 and 0.007 mequiv·$g^{-1}$, respectively.[4]

### 3.2.3 Synthesis of Nanocrystalline Chitin (Chitin NC)

Colloidal suspensions of nanocrystalline chitin (Chitin NC) were prepared through a hydrochloric acid hydrolysis procedure reported by Goodrich et al.[5] $\alpha$-Chitin was milled in a Thomas Wiley Mini-Mill (Thomas Scientific) and passed through a 60-mesh screen for the removal of large particles. The $\alpha$-chitin fine powder was hydrolyzed in 3 M hydrochloric acid for 1.5 h at 90 °C. The chitin was collected by centrifugation at 25 °C and 4500 rpm for 15 min with a Thermo IEC Centra-GP8R refrigerated centrifuge (Thermo Fisher Scientific, Inc.). This hydrolysis-recovery process was repeated three times. The final nanocrystalline chitin was re-suspended in water and dialyzed against water using a Spectra/Por regenerated cellulose dialysis tubing (molecular weight cut-off (MWCO): 12 ~ 14 kDa, Spectrum Lab, Inc.) for 3 days until pH = 6 was reached. The neutralized Chitin NC suspension was further dispersed in water using an APV Gaulin 1000 homogenizer.

### 3.3 Synthesis of Monolignols

#### 3.3.1 Materials

Trans-4-hydroxycinnamic (*p*-coumaric) acid, 4-hydroxy-3-methoxycinnamic (ferulic) acid and 3,5-dimethoxy-4-hydroxycinnamic (sinapic) acid were purchased from Alfa Aesar. Diisobutylaluminum hydride (DiBAl-H, 25 wt % in toluene) was purchased from Sigma-Aldrich. All other chemicals and solvents were obtained from Fisher Scientific.

#### 3.3.2 Synthesis of Monolignols

As shown in **Figure 3.4**, monolignols were prepared through a two-step reaction from their corresponding hydroxycinnamic acids.

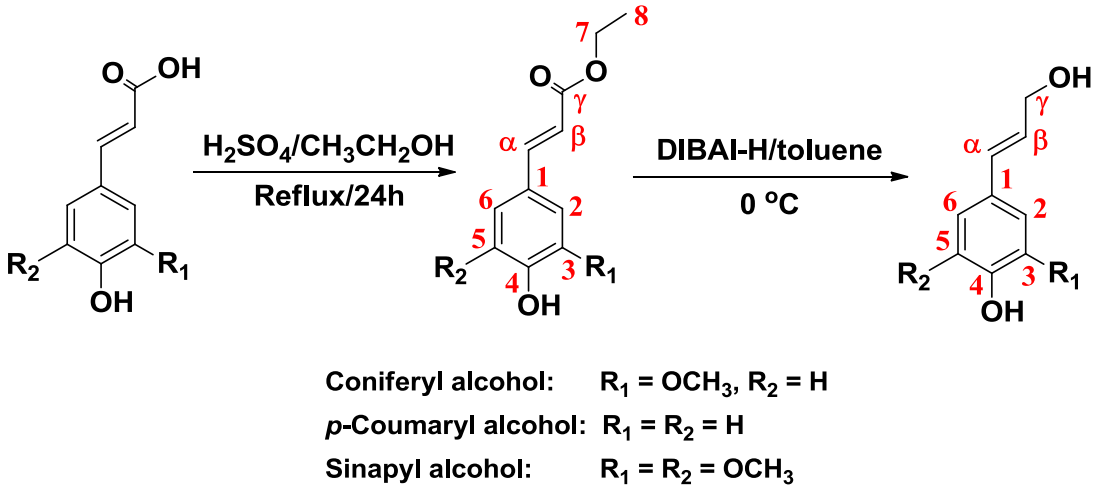


**Figure 3.4.** Reaction scheme for the synthesis of monolignols. Red numbers and greek letters correspond to $^{1}H$ and $^{13}C$ NMR spectral assignments.

*General Esterification Procedure*. Hydroxycinnamic acid (15.0 mmol, *p*-coumaric acid (2.45 g), ferulic acid (2.91 g) and sinapic acid (3.36 g)) was dissolved in 50 mL ethanol containing ~ 1 mL of concentrated $H_2SO_4$. The solution was refluxed at 80 °C for about 24 h. After

concentration under reduced pressure, the solution was diluted with ethyl acetate (EtOAc) and washed with a 5 % by mass $NaHCO_3$ aqueous solution (3×50 mL) and water (3×50 mL). After drying over anhydrous $Na_2SO_4$, the volatiles were removed in vacuo. The raw products were purified by column chromatography on silica gel using EtOAc/hexane mixtures as eluents.

*Ferulic acid ethyl ester*. Yield: 3.0 g (90 %); white crystals; $R_f$ = 0.25 (EtOAc/hexane=3/1); m.p.: 58-59.5 °C (lit. 57-58 °C);[6] $^1$H NMR (400 MHz, DMSO-$d_6$): δ = 7.58 (d, *J* = 16 Hz, 1H, $H_\alpha$), 7.36 (d, *J* = 2 Hz, 1H, $H_6$), 7.15 (dd, *J* = 8 Hz, 2 Hz, 1H, $H_2$), 6.82 (d, *J* = 8 Hz, 1H, $H_5$), 6.51 (d, *J* = 16 Hz, 1H, $H_\beta$), 4.20 (q, *J* = 7 Hz, 2H, $H_7$), 3.85 (s, 3H, $OCH_3$), 1.28 ppm (t, *J* = 7 Hz, 3H, $H_8$); $^{13}$C NMR (100 MHz, DMSO-$d_6$): δ = 167.57 ($C_\gamma$), 150.23 ($C_3$), 148.85 ($C_4$), 145.86 ($C_\alpha$), 126.52 ($C_1$), 124.05 ($C_6$), 116.41 ($C_\beta$), 115.49 ($C_5$), 112.10 ($C_2$), 60.63 ($C_7$), 56.62 ($OCH_3$), 15.21 ppm ($C_8$).

*p-Coumaric acid ethyl ester*. Yield: 2.5 g (87 %); white crystals; $R_f$ = 0.29 (EtOAc/hexane=7/2); m.p.: 75-77 °C (lit. 80-83 °C);[7] $^1$H NMR (400 MHz, DMSO-$d_6$): δ = 7.59 (dd, *J* = 9 Hz, 4 Hz, 3H, $H_{\alpha,2,6}$), 6.83 (d, *J* = 9 Hz, 2H, $H_{3,5}$), 6.42 (d, *J* = 16 Hz, 1H, $H_\beta$), 4.19 (q, *J* = 7 Hz, 2H, $H_7$), 1.28 ppm (t, *J* = 7 Hz, 3H, $H_8$); $^{13}$C NMR (100 MHz, DMSO-$d_6$): δ = 167.53 ($C_\gamma$), 160.74 ($C_4$), 145.52 ($C_\alpha$), 131.23 ($C_{2,6}$), 126.02 ($C_1$), 116.68 ($C_{3,5}$), 115.19 ($C_\beta$), 60.64 ($C_7$), 15.21 ppm ($C_8$).

*Sinapic acid ethyl ester*. Yield: 3.1 g (83 %); yellowish crystals; $R_f$ = 0.36 (EtOAc/hexane=2/3); m.p.: 63-64.5 °C (lit. 59-61 °C);[8] $^1$H NMR (400 MHz, DMSO-$d_6$): δ = 7.59 (d, *J* = 16 Hz, 1H, $H_\alpha$), 7.07 (s, 2H, $H_{2,6}$), 6.57 (d, *J* = 16 Hz, 1H, $H_\beta$), 4.20 (q, *J* = 7 Hz, 2H, $H_7$), 3.85 (s, 6H, $OCH_3$), 1.29 ppm (t, *J* = 7 Hz, 3H, $H_8$); $^{13}$C NMR (100 MHz, DMSO-$d_6$): δ =

167.55 ($C_\gamma$), 148.94 ($C_{3,5}$), 146.19 ($C_\alpha$), 139.17 ($C_4$), 125.33 ($C_1$), 115.92 ($C_\beta$), 107.13 ($C_{2,6}$), 60.65 ($C_7$), 57.01 ($OCH_3$), 15.21 ppm ($C_8$).

*General Reduction Procedure*. The hydroxycinnamic acid ethyl esters were reduced to monolignols following a procedure reported elsewhere.[6, 9] Hydroxycinnamic acid ethyl ester (10 mmol, *p*-coumaric acid ethyl ester (1.92 g), ferulic acid ethyl ester (2.22 g) and sinapic acid ethyl ester (2.52 g)) was dissolved in 100 mL toluene, and 24 mL of DiBAl-H (25 % by mass in toluene) were added dropwise into the solution at 0 °C under argon. The solution was stirred at 0 °C for 1 h and quenched by the addition of 15 mL ethanol. The volatiles were removed in vacuo, and the residue was treated with 100 mL of water and extracted with EtOAc (3×100 mL). The organic layers were collected and dried over anhydrous $Na_2SO_4$. The volatiles were then removed in vacuo, and the raw products were purified by column chromatography on silica gel using dichloromethane (DCM) with a small amount of methanol as eluents.

*Coniferyl alcohol*. Yield: 1.3 g (73 %); white crystals; $R_f$ = 0.22 (DCM with 1.7 % methanol by volume); m.p.: 74.5-76.5 °C (lit. 74-76 °C);[9] $^1$H NMR (400 MHz, DMSO-$d_6$): δ = 7.03 (d, *J* = 2 Hz, 1H, $H_2$), 6.83 (dd, *J* = 8 Hz, 1.8 Hz, 1H, $H_6$), 6.74 (d, *J* = 8 Hz, 1H, $H_5$), 6.45 (d, *J* = 16 Hz, 1H, $H_\alpha$), 6.22 (dt, *J* = 16 Hz, 6 Hz, 1H, $H_\beta$), 4.80 (t, *J* = 5 Hz, 1H, γ-OH), 4.11 (td, *J* = 6 Hz, 1.6 Hz, 2H, $H_\gamma$), 3.82 ppm (s, 3H, $OCH_3$); $^{13}$C NMR (100 MHz, DMSO-$d_6$): δ = 148.62 ($C_3$), 147.07 ($C_4$), 129.90 ($C_\alpha$), 129.40 ($C_1$), 128.41 ($C_\beta$), 120.35 ($C_6$), 116.37 ($C_5$), 110.57 ($C_2$), 62.66 ($C_\gamma$), 56.47 ppm ($OCH_3$).

*p-Coumaryl alcohol*. Yield: 1.1g (71 %); white crystals; $R_f$ = 0.34 (DCM with 3.3 % methanol by volume); m.p.: 117-123 °C (lit. 118-124 °C);[10] $^1$H NMR (400 MHz, DMSO-$d_6$): δ = 7.26 (m, 2H, $H_{2,6}$), 6.74 (m, 2H, $H_{3,5}$), 6.45 (d, *J* = 16 Hz, 1H, $H_\alpha$), 6.17 (dt, *J* = 16 Hz, 6 Hz, 1H, $H_\beta$),

4.79 (t, $J$ = 5 Hz, 1H, γ-OH), 4.10 ppm (td, $J$ = 6 Hz, 1.6 Hz, 2H, $H_\gamma$); $^{13}$C NMR (100 MHz, DMSO-$d_6$): δ = 157.73 ($C_4$), 129.59 ($C_\alpha$), 128.82 ($C_1$), 128.31 ($C_{2,6}$), 128.08 ($C_\beta$), 116.29 ($C_{3,5}$), 62.66 ppm ($C_\gamma$).

*Sinapyl alcohol*. Yield: 1.4 g (69 %); yellowish solid; $R_f$ = 0.28 (DCM with 1.7 % methanol by volume); m.p.: 59.5-61.5 °C (lit. 63-65 °C);[9] $^1$H NMR (400 MHz, DMSO-$d_6$): δ = 6.72 (s, 2H, $H_{2,6}$), 6.46 (d, $J$ = 16 Hz, 1H, $H_\alpha$), 6.26 (dt, $J$ = 16 Hz, 6 Hz, 1H, $H_\beta$), 4.82 (t, $J$ = 5 Hz, 1H, γ-OH), 4.12 (td, $J$ = 6 Hz, 1.6 Hz, 2H, $H_\gamma$), 3.81 ppm (s, 6H, $OCH_3$); $^{13}$C NMR (100 MHz, DMSO-$d_6$): δ = 148.95 ($C_{3,5}$), 136.09 ($C_4$), 130.12 ($C_\alpha$), 128.85 ($C_1$), 128.33 ($C_\beta$), 104.69 ($C_{2,6}$), 62.60 ($C_\gamma$), 56.86 ppm ($OCH_3$).

The $^1$H NMR and $^{13}$C NMR spectra for ferulic acid ethyl ester, *p*-coumaric acid ethyl ester, sinapic acid ethyl ester, coniferyl alcohol, *p*-coumaryl alcohol and sinapyl alcohol in DMSO-$d_6$ are shown in **Figures 3.5** and **3.6**, respectively.

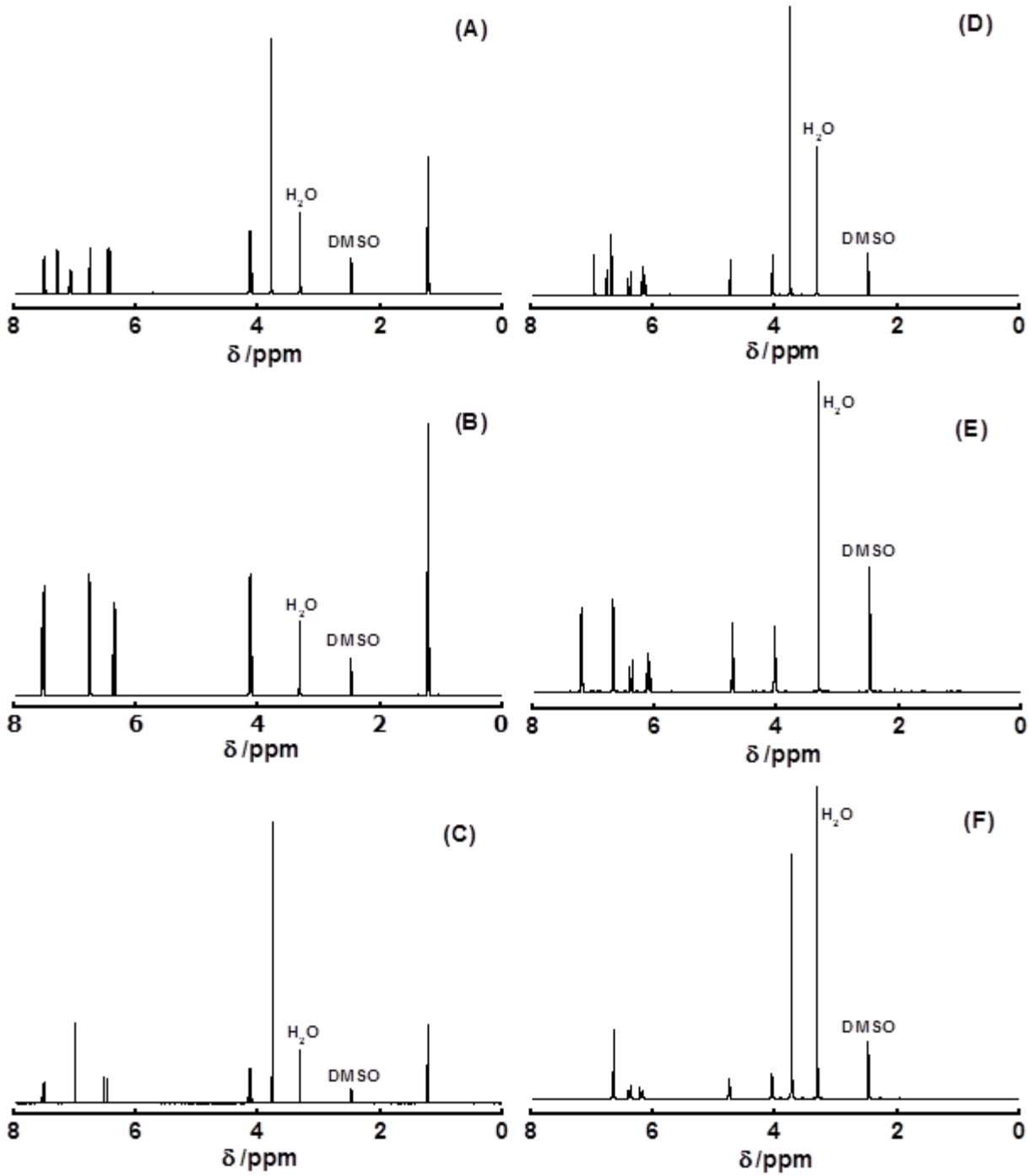


**Figure 3.5.** $^{1}$H NMR spectra (400 MHz, DMSO-$d_6$) for (A) ferulic acid ethyl ester, (B) *p*-coumaric acid ethyl ester, (C) sinapic acid ethyl ester, (D) coniferyl alcohol, (E) p-coumaryl alcohol and (F) sinapyl alcohol.

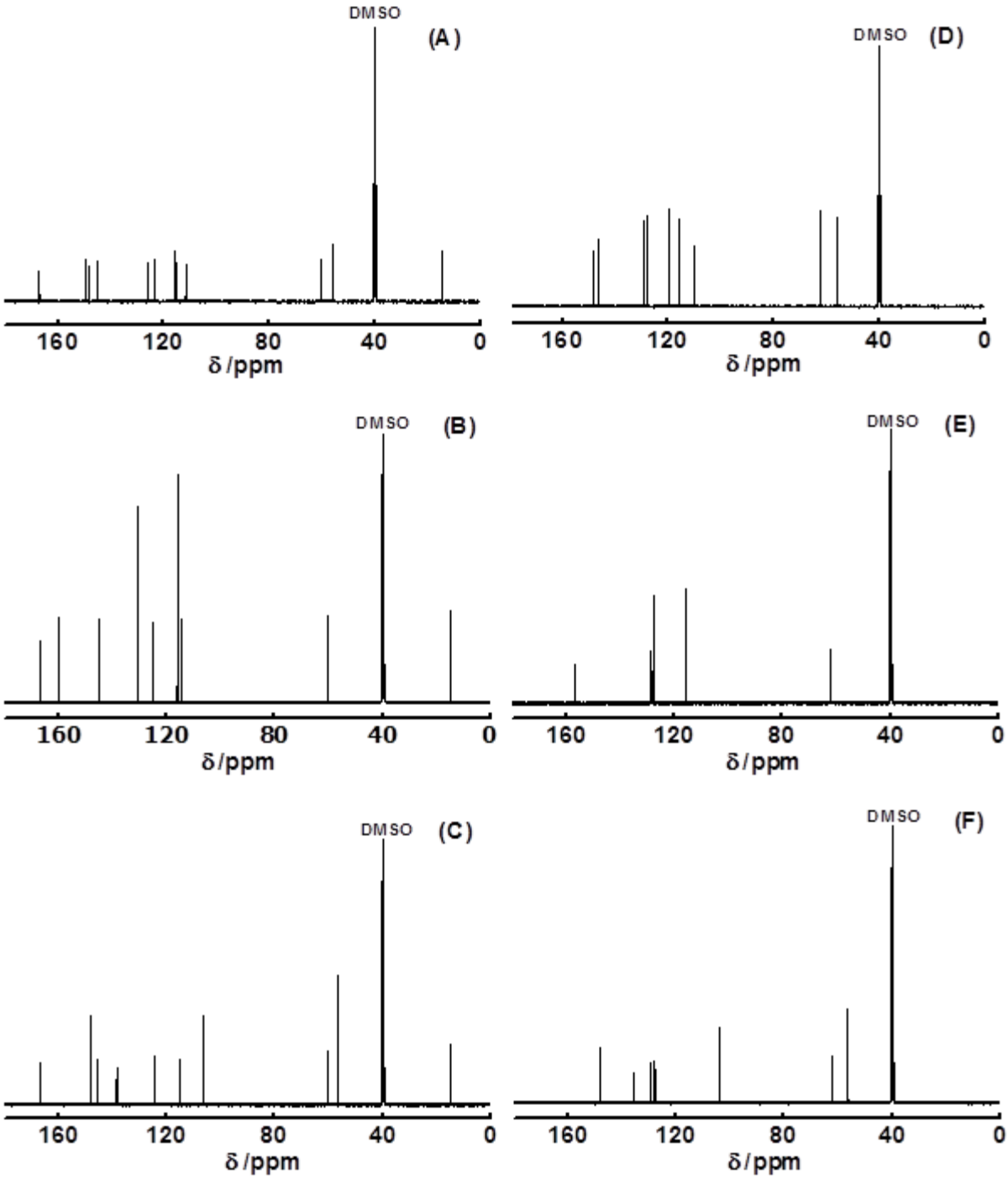


**Figure 3.6.** $^{13}C$ NMR spectra (100 MHz, DMSO-$d_6$) for (A) ferulic acid ethyl ester, (B) *p*-coumaric acid ethyl ester, (C) sinapic acid ethyl ester, (D) coniferyl alcohol, (E) p-coumaryl alcohol and (F) sinapyl alcohol.

### 3.4 Thin Film Preparation

#### 3.4.1 Materials

Silica (QSX-303, 5 MHz) and gold (QSX-301, 5 MHz) coated QCM-D sensors were purchased from Q-Sense and gold SPR sensor chips were purchased from Reichert (#13206060). Kraft lignin (KL) with a number-average molar mass ($M_n$) of ~ 5 kDa and a weight-average molar mass ($M_w$) of ~ 28 kDa was purchased from Sigma-Aldrich. Milled wood lignin (MWL, extracted from hemlock (T*suga sp*.) with aqueous dioxane, $M_n$ ~ 2.6 kDa and $M_w$ ~ 15.2 kDa)[11] and Organosolv lignin (OL, extracted from P*opulus trichocharpa* with aqueous ethanol, $M_n$ ~ 1 kDa and $M_w$ ~ 3 kDa)[11] were kindly provided by Prof. Wolfgang G. Glasser (Virginia Tech). Chitosan (medium molar mass, Fluka) was purchased from Sigma-Aldrich. Hydrogen peroxide (30 % w/w), $H_2SO_4$ (conc) and ammonium hydroxide (28 % w/w) were used to clean the substrates and were purchased from EM Science, VWR International, and Fisher Scientific, respectively. Ultrapure water with a resistivity of 18 MΩ·cm and < 5 ppb inorganic impurities was used in all experiments (Milli-QGradient A-10, Millipore).

#### 3.4.2 Solid Substrate Cleaning

Silica coated QCM-D sensors were cleaned prior to use by immersion in a 7:3 v/v solution of sulfuric acid: hydrogen peroxide, followed by a rinse with ultrapure water and drying with nitrogen. Gold coated QCM-D sensors and gold SPR sensor chips were cleaned prior to use by exposure to UV/ozone for 20 min, immersion in a 1:1:5 v/v/v solution of ammonium hydroxide: hydrogen peroxide: water at 80 °C for 1 h, followed by a rinse with ultrapure water and drying with nitrogen.

### 3.4.3 Regenerated Cellulose (RC) Thin Films

Smooth and uniform RC thin films were prepared following the procedure of Liu et al.[12] TMSC was dissolved in toluene to form a 1.0 % TMSC solution by mass. The solution was filtered through a 0.45 μm syringe filter (VWR PTFE) to remove dust particles and aggregates and then spincoated onto QCM-D or SPR sensors at a spinning speed of 2000 rpm for 1 min. The resulting TMSC films were exposed to the vapor of 10 % by mass aqueous hydrochloric acid solution to obtain regenerate RC films with thicknesses of ~ 20 nm.

### 3.4.4 Regenerated Chitin (RChitin) Thin Films

The details of the preparation and characterization of the smooth and amorphous RChitin thin films were previously reported by our group.[13] The TMSChitin was dissolved in a chloroform/tetrachloroethane (4/1 v/v) mixture to form 0.6 % TMSChitin solutions by mass. These solutions were filtered through a 0.45 μm syringe filter (VWR PTFE) to remove dust particles and aggregates and then spincoated onto QCM-D or SPR sensors at a spinning speed of 3000 rpm for 1 min. The resulting TMSChitin films were exposed to the vapor of 10 % by mass aqueous hydrochloric acid solution to obtain RChitin films with thicknesses of ~ 20 nm.

### 3.4.5 Desulfated Nanocrystalline Cellulose (DNC) Thin Films

Prior to DNC film formation, the cleaned QCM-D or SPR sensors were immersed in a 1 mM solution of 11-amino-1-undecanol in ethanol for 24 h to form an amine-terminated self-assembled monolayer (SAM-$NH_2$). DNC films with thicknesses of ~ 16 nm were prepared by spincoating from 1.0 % by mass DNC suspension onto the SAM-$NH_2$ coated gold sensors at 4000 rpm for 60 s. Films were subsequently dried overnight at 70 °C before thicknesses were determined by ellipsometry.

### 3.4.6 Nanocrystalline Chitin (Chitin NC) Thin Films

A SAM-$NH_2$ was formed on a cleaned gold QCM-D sensor crystal after immersion in a 1 mM solution of 11-amino-1-undecanol in ethanol for 24 h. Films of Chitin NC with different thicknesses were obtained by spincoating at 4000 rpm for 1 min from colloidal suspensions of Chitin NCs with concentrations that ranged from 0.50 to 2.20 % by mass. Films were then dried overnight at 70 °C before thicknesses were determined.

### 3.4.7 Chitosan Thin Films

Chitosan was purified by the procedure of Wang et al.[14] The chitosan sample was determined to have a degree of acetylation of ~ 12% and a viscosity-average molar mass of 240 kDa.[14] Chitosan films were prepared by a method similar to a previous report.[15] The chitosan was dissolved in 2 % aqueous acetic acid solutions to form 0.5 % chitosan solutions by mass. These solutions were filtered through a 1.0 μm syringe filter (Whatman GF/b w/GMF) to remove dust particles and aggregates and then spincoated onto silica QCM-D sensors at a spinning speed of 4000 rpm for 1 min. The obtained chitosan films with thicknesses of ~ 20 nm were neutralized with an aqueous 0.1 M NaOH solution for several minutes and then rinsed with ultrapure water for several minutes.

### 3.4.8 Lignin Thin Films

Samples of KL, OL and MWL were dialyzed against ultrapure water using Spectra/Por regenerated cellulose dialysis tubing (MWCO: 12 ~ 14 kDa, Spectrum Lab, Inc.) for ~ 1 week to remove any water-soluble impurities and the low molecular weight fractions. After dialysis, the lignin suspensions were lyophilized using Freezone 4.5 L freeze-dry system (Labconco Corp.). Lignin solutions with concentration of 1 % by mass were prepared by dissolving KL and MWL

in 0.75 M and OL in 1.5 M aqueous ammonia. These solutions were filtered through a 1.0 μm syringe filter (Whatman GF/b w/GMF) to remove dust particles and aggregates and then spincoated onto gold-coated QCM-D or SPR sensors at a spinning speed of 4000 rpm for 1 min. Lignin films were subsequently dried at 70 °C for several hours before adsorption measurements.

### 3.5 Experimental Methods and Data Analysis

#### 3.5.1 X-ray Diffraction (XRD) Measurements

X-ray diffraction patterns of lyophilized Chitin NCs, raw $\alpha$-chitin and regenerated chitin powders were obtained on a Rigaku MiniFlex II Desktop X-Ray Diffractometer. The radiation source was Cu(Kα) radiation, with a wavelength of 1.54 Å. The angular scanning range was $2\theta$ = 5° to 50° with 0.01° steps.

#### 3.5.2 Ellipsometry Measurements

Ellipsometry measurements of thin films were conducted at multiple-angles-of-incidence (60 to 80º, 1º steps) using a He: Ne laser at a constant wavelength of 632.8 nm (Picometer Ellipsometer, Beaglehole Instruments). The thicknesses of the films were deduced from modelling with TFCompanion software (Semiconsoft) and an assumption of a refractive index of 1.51 for RC,[12, 16] RChitin,[13, 17] DNC[16] and Chitin NC films.

#### 3.5.3 Atomic Force Microscopy (AFM) Measurements

All the surfaces were imaged in tapping mode with an Asylum Research AFM (MFP-3D-BIO, Asylum Research). Height images were collected under ambient conditions (22 °C, 50 % relative humidity) using a silicon tip (OMCL-AC160TS, Olympus Corp.). The reported roughnesses were determined from the root-mean-square (RMS) values of 2 μm x 2 μm, 5 μm x 5 μm or 10

μm × 10 μm scan areas. Specific scan areas are provided where appropriate in subsequent chapters.

In order to observe the morphology of Chitin NCs, Chitin NCs were deposited onto SAM-$NH_2$ coated gold substrates through spincoating of a 0.005 % by mass Chitin NC suspension at 4000 rpm for 1 min. The samples were then dried overnight at 70 °C before imaging.

### 3.5.4 Quartz Crystal Microbalance with Dissipation Monitoring (QCM-D) Measurements

An E4 quartz crystal microbalance with dissipation monitoring (QCM-D, Q-Sense AB) was used to investigate the adsorption of proteins or hemicelluloses onto natural polymer thin films, the enzymatic degradation of the natural polymer thin films and the surface-initiated dehydrogenative polymerization of monolignols.

In a typical QCM-D measurement, the QCM-D sensor was placed in a flow cell and allowed to equilibrate in water or buffer to obtain a stable baseline. Sample (adsorbates, enzymes or monolignols) solution was then injected into the flow cell at a specific rate at the indicated temperature. Frequency ($\Delta f$) and dissipation ($\Delta D$) changes for the fundamental frequency (4.95 MHz for both silica and gold coated quartz crystals) and six odd overtones ($n$ = 3 ~ 13) were monitored simultaneously. At the end of the measurement, water or buffer was typically flowed through the system for the removal of residual and reversibly adsorbed sample and degradation products. The adsorption curves from the fifth overtone ($n$ = 5) are provided for all graphs as representative curves.

For QCM-D measurements, if the attached mass is evenly distributed, rigidly attached, and small compared to the mass of the crystal, the surface concentration ($\Gamma_{QCM}$) can be calculated from the Sauerbrey equation:[18]

$$\Delta m = -C\left(\frac{\Delta f}{n}\right) \tag{3.1}$$

where $n$ is the overtone number and $C$ is a constant (0.177 mg·m$^{-2}$·Hz$^{-1}$). However, the linear relationship between the adsorbed mass and the scaled frequency change ($\Delta f/n$) is not valid for viscoelastic layers adsorbed onto solid surfaces. By measuring the dissipation of energy in the adsorbed layers simultaneously with the frequency change, information is obtained about the rigidity/softness of the adsorbed layer. The dissipation factor ($D$) is defined as a ratio between the energy dissipated and the energy stored during a single oscillation.

$$D = \frac{E_{dissipated}}{2\pi E_{stored}} \tag{3.2}$$

### 3.5.5 Surface Plasmon Resonance (SPR) Measurements

Protein adsorption onto RC and RChitin surfaces and the adsorption of hemicelluloses onto lignin thin films were probed using surface plasmon resonance (SPR) spectroscopy (SR7000, Reichert Inc.). The SPR system used a laser diode with an emission wavelength of 780 nm. The SPR flow cell was equipped with a Viton gasket (Dupont Dow Elastomers LLC) and was mounted on top of the sensor slide. Buffer (or water) or adsorbate (proteins or hemicelluloses) solutions were pumped into the flow cell via Teflon tubing connected to a cartridge pump (Masterflex). The pump was connected to a switch valve in order to switch between the adsorbate solutions and buffer (or water) without the introduction of air bubbles into the flow cell.

After the SPR sensor chip was placed in the SPR flow cell, buffer (or water) was introduced into the flow cell at a specific flow rate at the indicated temperature until a stable baseline was obtained. Degassed adsorbate solutions with different concentrations were then pumped into the

flow cell at the same flow rate and temperature. Adsorbate solution flowed over the sensor until equilibrium adsorption was obtained. At the end of the measurement, buffer (or water) was typically flowed through the system for the removal of the reversibly adsorbed adsorbates. Experiments were run in triplicate and reported values indicate the averages ± one standard deviation.

Changes in resonant angle were converted to surface concentration ($\Gamma_{SPR}$) using the equation of de Feijter et al.[19]

$$\Delta\theta_a = \Delta\theta_{sp} - c\left(\frac{d\theta_{sp}}{dc}\right) = \Delta\theta_{sp} - c\left(\frac{d\theta_{sp}}{dn}\frac{dn}{dc}\right) \tag{3.3}$$

$$\Gamma_{SPR} = \frac{L(n_a - n_s)}{dn/dc} = \frac{\Delta\theta_a}{d\theta/dL}\frac{(n_f - n_s)}{dn/dc} \tag{3.4}$$

where $\Delta\theta_a$ is the change in resonant angle due to adsorbate adsorption obtained by subtraction of the contribution of bulk refractive index changes in the dielectric medium from the observed changes in the resonant angle ($\Delta\theta_{sp}$), $c$ is the bulk concentration of adsorbate solution, $d\theta_{sp}/dn$ was an instrument specific constant obtained during instrument calibration with ethylene glycol standards (61.5 °), $dn/dc$ is the refractive index increment of the adsorbate solution (0.137 mL·g$^{-1}$ for xyloglucan[20] and 0.189 mL·g$^{-1}$ for both human serum albumin (HSA) and human fibrinogen (HFN)[21]), $n_f$ is the refractive index of the substrate (assuming 1.45[12, 13, 22, 23] for general organic materials), $n_s$ is the refractive index of the buffer or water (1.345 for 50 mM phosphate buffer[24] and 1.328 for water[12, 22, 25]) and $d\theta/dL$ is the change in resonant angle with respect to adsorbed layer thickness changes as modeled by the Fresnel equations (0.042 deg·nm$^{-1}$ for RC and RChitin films[12, 13, 22] and 0.051 deg·nm$^{-1}$ for lignin films simulated based on a multilayer model composed of six layers). The parameters for the different layers in the Fresnel simulations were summarized in **Table 3.1**.

**Table 3.1.** Parameters for different layers used in the Fresnel simulations of d$\theta$/d$L$.

| | Layer | Thickness /nm | Refractive index, $n$ | Absorption coefficient, $K$ |
|---|---|---|---|---|
| L1 | sapphire prism | $5 \times 10^5$ | 1.76074[26] | 0 |
| L2 | chromium | 2 | 4.1106[27] | 4.3492[27] |
| L3 | gold | 48 | 0.174[27] | 4.86[27] |
| L4 | lignin | 20 | 1.60[28-31] | 0 |
| L5 | xyloglucan | variable | 1.45[12, 22] | 0 |
| L6 | water | 50 | 1.32813[25] | 0 |

## 3.6 References


(1) Edgar, K. J.; Arnold, K. M.; Blount, W. W.; Lawniczak, J. E.; Lowman, D. W. *Macromolecules* **1995,** 28, 4122-4128.

(2) Kontturi, E.; Thüne, P. C.; Niemantsverdriet, J. W. *Langmuir* **2003,** 19, 5735-5741.

(3) Kurita, K.; Sugita, K.; Kodaira, N.; Hirakawa, M.; Yang, J. *Biomacromolecules* **2005,** 6, 1414-1418.

(4) Jiang, F.; Esker, A. R.; Roman, M. *Langmuir* **2010,** 26, 17919-17925.

(5) Goodrich, J. D.; Winter, W. T. *Biomacromolecules* **2007,** 8, 252-257.

(6) Pickel, B.; Constantin, M.-A.; Pfannstiel, J.; Conrad, J.; Beifuss, U.; Schaller, A. *Angew. Chem. Int. Ed.* **2010,** 49, 202-204.

(7) Carta, F.; Vullo, D.; Maresca, A.; Scozzafava, A.; Supuran, C. T. *Biorg. Med. Chem.* **2013,** 21, 1564-1569.

(8) Ren, X.; Chen, X.; Peng, K.; Xie, X.; Xia, Y.; Pan, X. *Tetrahedron: Asymmetry* **2002,** 13, 1799-1804.

(9) Quideau, S.; Ralph, J. *J. Agric. Food Chem.* **1992,** 40, 1108-1110.

(10) Aulin-Erdtman, G.; Sanden, R. *Acta Chem. Scand.* **1968,** 22, 1187-1209.

(11) Glasser, W. G.; Barnett, C. A.; Sano, Y. *J. Appl. Polym. Sci.: Appl. Polym. Symp.* **1983,** 37, 441-460.

(12) Liu, Z.; Choi, H.; Gatenholm, P.; Esker, A. R. *Langmuir* **2011,** 27, 8718-8728.

(13) Kittle, J. D.; Wang, C.; Qian, C.; Zhang, Y.; Zhang, M.; Roman, M.; Morris, J. R.; Moore, R. B.; Esker, A. R. *Biomacromolecules* **2012,** 13, 714-718.

(14) Wang, H.; Roman, M. *Biomacromolecules* **2011,** 12, 1585-1593.

(15) Murray, C. A.; Dutcher, J. R. *Biomacromolecules* **2006,** 7, 3460-3465.

(16) Kittle, J. D.; Du, X.; Jiang, F.; Qian, C.; Heinze, T.; Roman, M.; Esker, A. R. *Biomacromolecules* **2011,** 12, 2881-2887.

(17) Montiel-González, Z.; Luna-Bárcenas, G.; Mendoza-Galván, A. *Phys. Stat. Sol. C.* **2008,** 5, 1434-1437.

(18) Sauerbrey, G. *Z. Phys.* **1959,** 155, 206-222.

(19) De Feijter, J. A.; Benjamins, J.; Veer, F. A. *Biopolymers* **1978,** 17, 1759-1772.

(20) Kittle, J. D. PhD Thesis, Virginia Tech, Blacksburg, VA, 2012.

(21) Zhao, H.; Brown, Patrick H.; Schuck, P. *Biophys. J.* **2011,** 100, 2309-2317.

(22) Kaya, A.; Du, X.; Liu, Z.; Lu, J. W.; Morris, J. R.; Glasser, W. G.; Heinze, T.; Esker, A. R. *Biomacromolecules* **2009,** 10, 2451-2459.

(23) Kittle, J. D.; Wondraczek, H.; Wang, C.; Jiang, F.; Roman, M.; Heinze, T.; Esker, A. R. *Langmuir* **2012,** 28, 11086-11094.

(24) Diéguez, L.; Darwish, N.; Mir, M.; Martínez, E.; Moreno, M.; Samitier, J. *Sensor Lett.* **2009,** 7, 851-855.

(25) Harvey, A. H.; Gallagher, J. S.; Sengers, J. M. H. L. *J. Phys. Chem. Ref. Data* **1998,** 27, 761-774.

(26) Malitson, I. H. *J. Opt. Soc. Am.* **1962,** 52, 1377-1379.

(27) Palik, E. D. *Handbook of Optical Constants of Solids*; Academic Press: Orlando, FL, 1985.

(28) Norgren, M.; Notley, S. M.; Majtnerova, A.; Gellerstedt, G. *Langmuir* **2006,** 22, 1209-1214.

(29) Notley, S. M.; Norgren, M. *Langmuir* **2010,** 26, 5484-5490.

(30) Donaldson, L. A. *New Zeal. J. For. Sci.* **1985,** 5, 349-360.

(31) Donaldson, L.; Hague, J.; Snell, R. *Holzforschung* **2001,** 55, 379-385.

# Chapter 4: Chitinase Activity on Amorphous Chitin Thin Films

Published Chapter: Wang, C.; Kittle, J. D.; Qian, C.; Roman, M.; Esker, A. R. *Biomacromolecules* **2013**, 14 (8), 2622-2628.

## 4.1 Abstract

Chitinases are widely distributed in nature and have wide-ranging pharmaceutical and biotechnological applications. This work highlights a real-time and label-free method to assay chitinase activity via a quartz crystal microbalance with dissipation monitoring (QCM-D) and atomic force microscopy (AFM). The chitin substrate was prepared by spincoating a trimethylsilyl chitin solution onto a silica substrate, followed by regeneration to amorphous chitin (RChitin). The QCM-D and AFM results clearly showed that the hydrolysis rate of RChitin films increased as chitinase (from *Streptomyces griseus*) concentrations increased, and the optimal temperature and pH for chitinase activity was around 37 °C and 6 ~ 8, respectively. The chitinase showed greater activity on chitin substrates, having a high degree of acetylation, than on chitosan substrates, having a low degree of acetylation.

## 4.2 Introduction

Chitinase activity has been assayed by various methods, although the most common are viscosimetric,[1] colorimetric[2] and radiochemical methods.[3] In the viscosimetric method, chitinase activity is assayed by monitoring the viscosity change of solutions of water-soluble chitin derivatives, such as carboxymethylchitin and glycol chitin. The viscosimetric method is more sensetive to endochitinases than other methods and is strongly affected by the degree of polymerization of the substrates as well as the ionic strength and pH of the solutions. The

colorimetric method is based upon the determination of *N*-acetyl-D-glucosamine monomers released from colloidal chitin upon exposure to *p*-dimethylaminobenzaldehyde (DMAB).[2] Since DMAB is only sensitive to monosaccharides, it is necessary to include a source of *β*-*N*-acetylglucosaminidases to convert oligosaccharides to monosaccharides. The radiochemical method is one of the most sensitive assay methods, in which tritium-labeled chitin is incubated with the chitinase solution, and chitinase activity is assayed by determining the radioactivity of the water-soluble chito-oligosaccharides formed.[3] However, this method requires a radioactive substrate and specialized equipment. Although these methods have proven successful in assaying chitinase activity, a simple and sensitive assay method without intricate synthesis, a time-consuming procedure or radioactive labeling is desirable for both research and industry.

The QCM-D technique has been used to study enzyme kinetics of various natural and synthetic polymers, including cellulose,[4-11] xyloglucan,[12] amylopectin,[13] pullulan,[13] dextran,[14] lipids,[15] poly-L-lysine-polygalacturonic acid multilayers,[16] and poly(*ε*-caprolactone).[17] However, the utilization of QCM-D to study the enzyme kinetics on chitin has not been reported because of the difficulty in preparing ultrathin chitin films. Recently, our group reported a simple method to prepare homogeneous, smooth and ultrathin chitin films by spincoating from a solution of trimethylsilyl chitin (TMSChitin) in the mixture of chloroform and tetrachloroethane onto a silica or gold substrate and regenerating to amorphous chitin by exposure of the film to the vapor of a hydrochloric acid solution.[18] The successful preparation of amorphous chitin thin films makes it possible to study real-time chitinase activity via QCM-D and therefore provides a simple and sensitive method to assay chitinase acitivity.

This study used QCM-D and atomic force microscopy (AFM) to investigate the activity of chitinases from *Streptomyces griseus* on chitin thin films at various enzyme concentrations,

temperatures, pH and degrees of acetylation (DA). This information is expected to provide a convenient and sensitive method to assay the enzyme kinetics of various chitinolytic enzymes under carefully controlled conditions of enzyme concentration, temperature and pH. Therefore it is anticipated that this technique will be suitable for quantitative comparisons of chitinase activity, studies of chitin-based biomaterial stability and the design of novel pathogenic fungal inhibitors.

### 4.3 Experimental

Chitinase (from S*treptomyces griseus*, lyophilized powder, ≥ 200 units·$g^{-1}$ solid) is an extracellular enzyme complex[19] with a molar mass of ~ 30 kDa and was purchased from Sigma-Aldrich. Sodium phosphate monobasic monohydrate, sodium phosphate dibasic heptahydrate, sodium hydroxide and citric acid were purchased from Sigma-Aldrich and used as received to prepare buffer solutions (pH = 4.0, 6.0, 8.0 and 10.0). All other chemicals and solvents were obtained from Fisher Scientific and used as received. Ultrapure water with a resistivity of 18 MΩ·cm and < 5 ppb inorganic impurities was used in all experiments (Milli-QGradient A-10, Millipore). The synthesis and film preparation procedure for RChitin and chitosan films were given in Chapter 3.4.

AFM and ellipsometry measurements were performed as outlined in Chapter 3.5. All QCM-D measurements were conducted as outlined in Chapter 3.5.4, with the following details specific to this work. The QCM-D sensor was placed in a flow cell and allowed to equilibrate for 1 to 1.5 h in buffer to obtain a stable baseline. 1.0 mL of chitinase solution was then injected into the flow cell at a rate of 0.100 mL·$min^{-1}$ at the indicated temperature. The flow was stopped and the measurements were made in the absence of flow. At the end of the measurement, buffer was

flowed through the system for the removal of residual and reversibly adsorbed enzyme and degradation products.

## 4.4 Results and Discussion

### 4.4.1 Chitinase Activity on RChitin Films

**Figure 4.1** shows typical QCM-D data for chitinase activity on RChitin films. After the RChitin film was equilibrated for 1 h in pH = 6.0 phosphate buffer, chitinase solution was injected into the flow cell. The instantaneous frequency decrease, corresponding to $\Delta f/n$ ~ 20 Hz after the injection of chitinase solution, was attributed to both chitinase adsorption and changes of liquid properties (viscosity and density). Similar $\Delta f/n$ decreases have been observed in the enzymatic hydrolysis of cellulose monitored by QCM-D.[5, 6, 20] The effects of changes in liquid properties (density and viscosity) at different temperature, pH and chitinase concentration on the $\Delta f/n$ shifts were investigated through the Stockbridge equation.[6, 21]

$$\Delta f = \sqrt{\frac{n}{\pi}} \frac{f_0^{3/2}}{\nu\rho} \sqrt{\rho_L \eta_L} \tag{4.1}$$

where $n$ is the overtone number, $v$ = 3340 m·s$^{-1}$ is the wave propagation velocity of in quartz, $\rho$ = 2649 kg·m$^{-3}$ is the density of quartz crystal, $f_0$ is the fundamental frequency of the quartz crystal, which is equal to 2.5 MHz, 1/2 of the first overtone of the QCM-D sensor,[21] $\rho_L$ and $\eta_L$ are the density and dynamic viscosity of the buffer and chitinase solution. The results are shown in **Tables 4.1**, **4.2** and **4.3**. The results agree with the previous QCM-D studies on cellulase activity on cellulose films that the $\Delta f/n$ changes were caused primarily by enzyme adsorption or binding, while $\Delta f/n$ changes caused by density and viscosity changes of the liquid were negligible.[5, 6, 21] Similar to cellulases, many chitinases have carbohydrate-binding domains, which assist the

adsorption of chitinases onto chitin surfaces.[22] Recently, a chitinase separated from *Streptomyces griseus*, chitinase C, was determined to be composed of a C-terminal catalytic module connected to an *N*-terminal chitin-binding module (ChBM) by a ten residue linker peptide.[23] The ChBM is composed of a *β*-protein with two tryptophan residues (Trp59 and Trp60) aligned parallel to the substrate. They also studied the binding mechanism via molecular dynamics simulations and found that the ChBM binds to chitin surfaces through stacking interactions and hydrogen bonding of the Trp59 and Trp60 residues.[23]

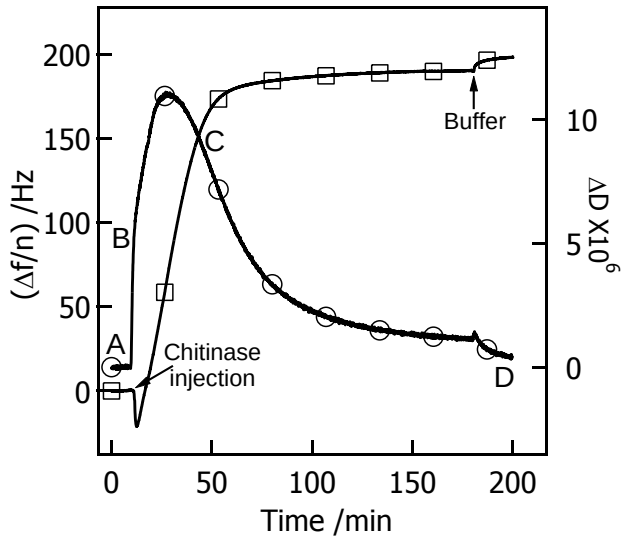


**Figure 4.1.** Representative (□) Δ*f*/*n* and (○) Δ*D* versus time for chitinase activity on a RChitin film at 37 °C for a 0.5 mg·mL$^{-1}$ chitinase solution in a 50 mM pH = 6.0 phosphate buffer. Curves correspond to the fifth overtone. Letters on the graph roughly correspond to the times where AFM images in **Figure 4.2** were taken for similar RChitin films.

**Table 4.1.** Density, viscosity, and calculated $\Delta f$ from the Stockbridge equation at different temperatures.

| Temp /°C | pH = 6.0 Buffer | | | 0.5 mg·mL$^{-1}$ Chitinase solution | | | $\Delta f$ /Hz [c] |
|---|---|---|---|---|---|---|---|
| | $\rho$ /g·mL$^{-1}$ [a] | $\eta$ /10$^{-3}$ kg·s$^{-1}$·m$^{-1}$ [a] | $\Delta f_1$ /Hz [b] | $\rho$ /g·mL$^{-1}$ [a] | $\eta$ /10$^{-3}$ kg·s$^{-1}$·m$^{-1}$ [a] | $\Delta f_2$ /Hz [b] | |
| 17 | 1.004 | 1.104 | -593.6 | 1.003 | 1.094 | -591.5 | 2.1 |
| 27 | 0.998 | 0.869 | -525.1 | 0.999 | 0.859 | -522.3 | 2.8 |
| 37 | 0.997 | 0.702 | -471.5 | 0.997 | 0.694 | -468.9 | 2.6 |
| 47 | 0.995 | 0.600 | -435.3 | 0.995 | 0.588 | -431.2 | 4.1 |

[a] $\rho$: density, $\eta$: dynamic viscosity. Both density and dynamic viscosity values are the average of three measurements. [b] Both $\Delta f_1$ and $\Delta f_2$ are calculated from Stockbridge equation. [c] $\Delta f = \Delta f_2 - \Delta f_1$.

**Table 4.2.** Density, viscosity, and calculated $\Delta f$ from the Stockbridge equation at different pH.

| pH | Buffer | | | 0.5 mg·mL$^{-1}$ Chitinase solution | | | $\Delta f$ /Hz |
|---|---|---|---|---|---|---|---|
| | $\rho$ /g·mL$^{-1}$ [a] | $\eta$ /10$^{-3}$ kg·s$^{-1}$·m$^{-1}$ [a] | $\Delta f_1$ /Hz [b] | $\rho$ /g·mL$^{-1}$ [a] | $\eta$ /10$^{-3}$ kg·s$^{-1}$·m$^{-1}$ [a] | $\Delta f_2$ /Hz [b] | |
| 4.0 | 0.999 | 0.698 | -470.8 | 0.997 | 0.704 | -472.4 | -1.6 |
| 6.0 | 0.997 | 0.702 | -471.5 | 0.997 | 0.694 | -468.9 | 2.6 |
| 8.0 | 0.997 | 0.705 | -472.7 | 0.997 | 0.696 | -469.7 | 3.0 |
| 10.0 | 0.998 | 0.697 | -470.2 | 0.998 | 0.694 | -469.1 | 1.1 |

[a] $\rho$: density, $\eta$: dynamic viscosity. Both density and dynamic viscosity values are the average of three measurements. [b] Both $\Delta f_1$ and $\Delta f_2$ are calculated from Stockbridge equation. [c] $\Delta f = \Delta f_2 - \Delta f_1$.

**Table 4.3.** Density, viscosity, and calculated $\Delta f$ from the Stockbridge equation for pH = 6.0 buffer and chitinase solutions with different enzyme concentrations at 37 °C.

| Enzyme concentration /mg·mL$^{-1}$ | pH = 6.0 Buffer | | | Chitinase solution | | | $\Delta f$ /Hz |
|---|---|---|---|---|---|---|---|
| | $\rho$ /g·mL$^{-1}$ [a] | $\eta$ /10$^{-3}$ kg·s$^{-1}$·m$^{-1}$ [a] | $\Delta f_1$ /Hz [b] | $\rho$ /g·mL$^{-1}$ [a] | $\eta$ /10$^{-3}$ kg·s$^{-1}$·m$^{-1}$ [a] | $\Delta f_2$ /Hz [b] | |
| 0.05 | 0.997 | 0.702 | -471.5 | 0.998 | 0.700 | -471.1 | 0.4 |
| 0.2 | | | | 0.998 | 0.702 | -471.7 | -0.2 |
| 0.5 | | | | 0.997 | 0.694 | -468.9 | 2.6 |
| 1.0 | | | | 0.999 | 0.710 | -474.9 | -3.4 |

[a] $\rho$: density, $\eta$: dynamic viscosity. Both density and dynamic viscosity values are the average of three measurements. [b] Both $\Delta f_1$ and $\Delta f_2$ are calculated from Stockbridge equation. [c] $\Delta f = \Delta f_2 - \Delta f_1$.

After the initial $\Delta f/n$ decrease, the $\Delta f/n$ increased rapidly for ~ 80 min before a plateau was achieved. Similar to previous studies of cellulose hydrolysis of cellulose thin films,[5] this $\Delta f/n$ increase was attributed to the hydrolysis of the amorphous RChitin film and the release of chito-oligosaccharides, chitobiose or monosaccharides to the bulk solution. The $\Delta f/n$ plateaued after the chitin in the film was exhausted or the chitinase lost its activity (e.g., under extreme pH). After the enzymatic hydrolysis proceeded for 180 min, phosphate buffer was again introduced into the flow cell for 20 min to rinse the film. Reversibly adsorbed chitinase and degradation products were removed by the buffer, causing an additional $\Delta f/n$ increase of about 8 Hz.

Changes in the viscoelastic properties of the RChitin film are consistent with the energy dissipation profile. Similar to the enzymatic hydrolysis of cellulose,[5, 6, 11, 20] an instantaneous $\Delta D$ increase was observed after the injection of chitinase solution (**Figure 4.1**). This feature was attributed to the adsorption of chitinase and its coupled water. The enhancement of $\Delta D$ was attributed to the penetration of chitinase into the RChitin film as the hydrolysis proceeded. A

maximum in $\Delta D$ (~ $1\times10^{-5}$) at a time of ~ 30 min nearly coincided with the maximum hydrolysis rate (the maximum slope of $\Delta f/n$ versus time). This point may correspond to the maximum accessibility of the substrate to enzymatic attack. Following this peak value, $\Delta D$ decreased rapidly. After ~ 90 min, the dissipation decrease slowed, possibly due to the exhaustion of chitin substrate for hydrolysis. After the removal of the reversibly adsorbed chitinase and degradation products by buffer at ~ 180 min, $\Delta D$ approached zero.

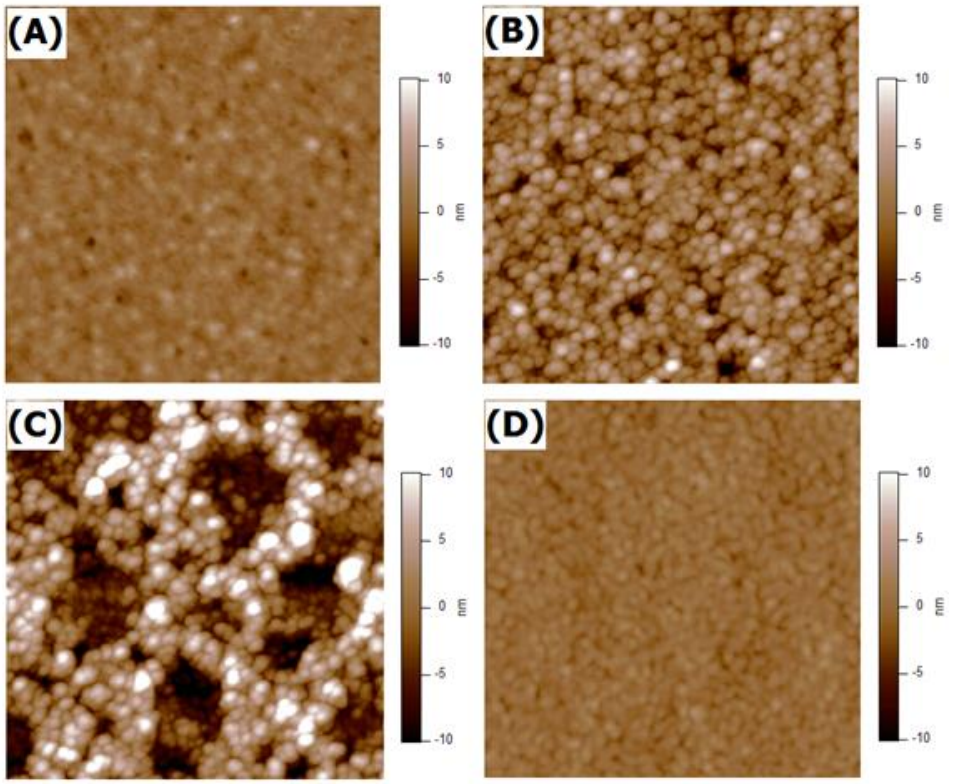


**Figure 4.2.** Representative 2 μm × 2 μm AFM height images of RChitin films on silica coated QCM-D sensors during enzymatic hydrolysis. Letters for different images roughly correspond to the letters indicated on **Figure 4.1**. RMS roughnesses for the images are: (A) ~ 1.2 nm, (B) ~ 2.7 nm, (C) ~ 5.6 nm, and (D) ~ 0.9 nm.

Images from AFM tracked the morphological changes of RChitin films during enzymatic hydrolysis. **Figure 4.2** contains AFM images taken at points roughly represented by the letters on **Figure 4.1**. As shown in **Figure 4.2A**, before chitinase treatment, the RChitin film was smooth and homogeneous, with a RMS roughness of ~ 1.2 nm. As reported elsewhere, the RMS roughness for spincoated regenerated cellulose films from TMSC with a similar thickness (~ 20 nm) was ~ 1.5 nm,[24] and is comparable to this work. **Figure 4.2B** shows the morphology after chitinase adsorption. The surface was filled with chitinase aggregates and the RMS roughness increased from ~ 1.2 nm to ~ 2.7 nm. **Figure 4.2B** further supported the QCM-D data that the dissipation increase after the injection of chitinase solution, attributable to the adsorption of chitinase and its coupled water onto chitin. After an ~ 40 min incubation, some of the chitin substrate was degraded and the RMS roughness increased to ~ 5.6 nm (**Figure 4.2C**). As shown in **Figure 4.2D**, after hydrolysis, the RMS roughness returned to that of typical bare silica coated QCM-D sensors (~ 0.9 nm). An AFM height image of a bare silica coated QCM-D sensor is provided in **Figure 4.3A** for comparison. The smooth, aggregate-free surface morphology in **Figure 4.2D** suggested that the interactions between chitinase and silica were weak.

In order to further test the hypothesis that interactions between the chitinase and silica were weak, the adsorption of chitinase onto silica coated QCM-D sensors was also studied by QCM-D (**Figure 4.3B**). As expected, a frequency decrease and dissipation increase were detected for chitinase adsorption onto the silica substrate. The initial adsorption was fast and reached a gradual, reversible second adsorption stage in ~ 10 min. The small irreversible $\Delta f/n$ ~ 4 Hz after the surface was rinsed with buffer was consistent with the conclusion drawn from **Figure 4.2D** that very little chitinase remained on the silica substrate after complete hydrolysis of the RChitin.

It also suggested that a significant portion of the increase in Δ*f*/*n* observed during rinsing in **Figure 4.1** arose from enzyme desorption.

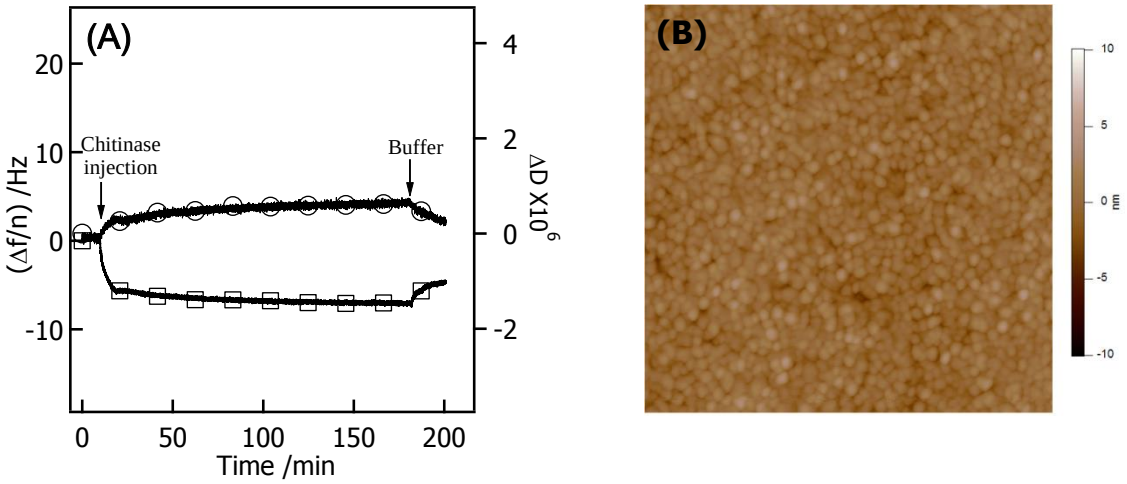


**Figure 4.3.** (A) Representative (□) Δ*f*/*n* and (○) Δ*D* versus time for 0.5 mg·mL$^{-1}$ chitinase adsorption onto silica coated quartz crystal sensor at 37 °C from a 50 mM pH = 6.0 phosphate buffer. Curves correspond to the fifth overtone. (B) Representative 2 μm × 2 μm AFM height image of silica coated QCM-D sensor. RMS roughness for the image is: ~ 1.0 nm.

### 4.4.2 Effect of Temperature on Chitinase Activity

The effects of temperature, pH and enzyme concentration, as well as the degree of acetylation of the substrates on the enzymatic hydrolysis of chitin films were also probed. **Figure 4.4** shows Δ*f*/*n* versus time for the chitinase activity on RChitin films at 17, 27, 37 and 47 °C. The inset of **Figure 4.4** shows the relative hydrolysis rate at the time of maximum Δ*D* (the ratio of the slopes of Δ*f*/*n* versus time at the time of maximum Δ*D* at a given temperature to the value at 17 °C, $[d(\Delta f/n)/dt]_{\max\ \Delta D}/[d(\Delta f/n)/dt]_{\max\ \Delta D,17}$) as a function of temperature. As seen in **Figure 4.4**, chitinase showed the greatest activity at 37 °C for the temperatures probed and agrees with the optimal temperature for chitinase (from S*treptomyces griseus*) activity provided by the supplier.

This optimal temperature is also consistent with turbidity studies of Berger et al.[19] who observed decreases in the turbidity of standardized colloidal chitin suspensions treated with the chitinase.

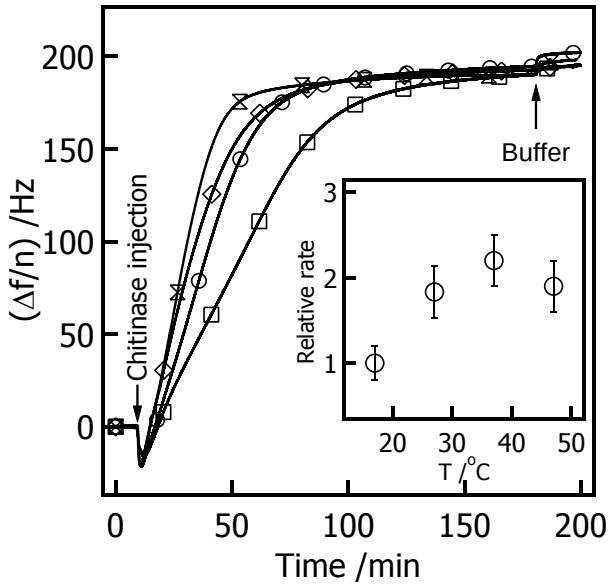


**Figure 4.4.** Representative $\Delta f/n$ versus time for chitinase activity on RChitin films at (□) 17 °C, (○) 27 °C, (⧖) 37 °C and (◊) 47 °C for a 0.5 mg·mL$^{-1}$ chitinase solution in a 50 mM pH = 6.0 phosphate buffer. Curves correspond to the fifth overtone. The inset contains reaction rates relative to 17 °C ($[d(\Delta f/n)/dt]_{\max \Delta D}/[d(\Delta f/n)/dt]_{\max \Delta D,17}$ with one standard deviation error bars as a function of temperature, where average $[d(\Delta f/n)/dt]_{\max \Delta D,17}$ = 2.6 Hz·min$^{-1}$ or ~ 0.46 mg·m$^{-2}$·min$^{-1}$).

As seen in **Figure 4.5A**, $(\Delta f/n)_{\min}$ are not significantly affected by temperature and are relatively broad. This observation means that the $(\Delta f/n)_{\min}$ does not arise purely from adsorption, but is rather a convolution of mass changes arising from enzyme adsorption and hydrolysis of the film. Likewise, the initial slope is not purely due to hydrolysis, but also contains some component of enzyme adsorption. For this reason, the inset of **Figure 4.4** was made using $[d(\Delta f/n)/dt]_{\max \Delta D}$ as an unbiased and purely empirical experimental parameter. As seen in **Table**

**4.4**, analysis of initial rates, rates at maximum Δ*D*, or the overall maximum hydrolysis rate yield the same qualitative trend within experimental error.

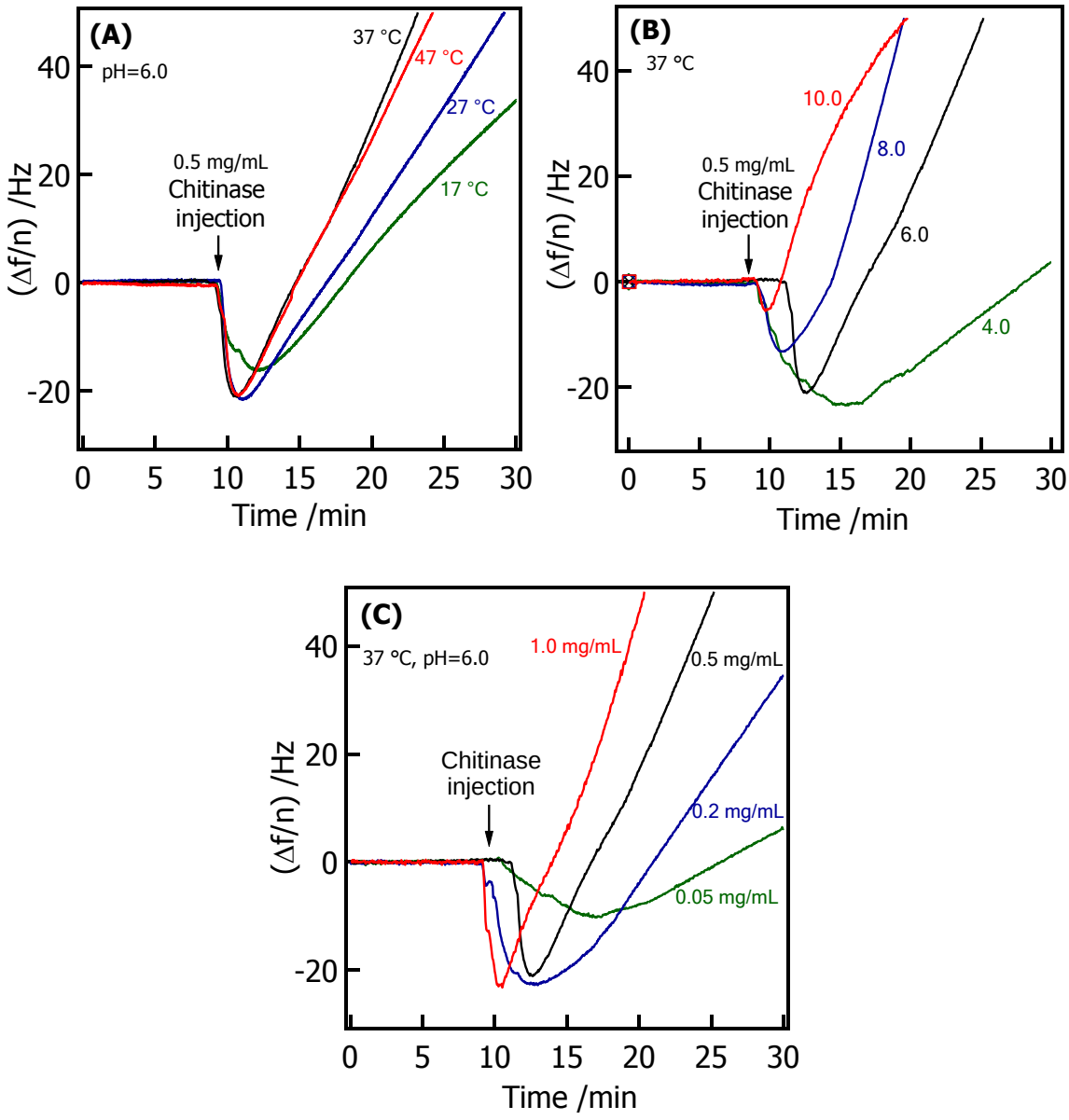


**Figure 4.5.** Representative Δ*f*/*n* versus time for chitinase activity on RChitin films at different (A) temperatures, (B) pH and (C) enzyme concentrations. Curves correspond to the fifth overtone.

**Table 4.4.** Relative hydrolysis rates for RChitin films at different temperatures (pH = 6.0).[a]

| Temperature /°C | Concentration /mg·mL$^{-1}$ | Relative initial rate[b] | Relative rate at maximum $\Delta D$[c] | Relative maximum rate[d] |
|---|---|---|---|---|
| 17 | 0.5 | 1.0 ± 0.1 | 1.0 ± 0.2 | 1.0 ± 0.2 |
| 27 | 0.5 | 1.4 ± 0.1 | 1.8 ± 0.3 | 1.3 ± 0.2 |
| 37 | 0.5 | 1.8 ± 0.2 | 2.2 ± 0.3 | 1.7 ± 0.2 |
| 47 | 0.5 | 1.4 ± 0.2 | 1.9 ± 0.3 | 1.4 ± 0.3 |

[a]The relative hydrolysis rate is the ratio of the hydrolysis rate at a given enzyme concentration to the value at 17 °C. [b]Initial rate is obtained from the initial slopes of $\Delta f/n$ versus time after the minimum in $\Delta f/n$, $[\mathrm{d}(\Delta f/n)/\mathrm{d}t]_{\text{initial, 17 C}}$ = 3.1 Hz·min$^{-1}$. [c]Rate at maximum $\Delta D$ is obtained from the slopes of $\Delta f/n$ versus time at the time of maximum $\Delta D$, $[\mathrm{d}(\Delta f/n)/\mathrm{d}t]_{\text{max }\Delta D\text{, 17 C}}$ = 2.6 Hz·min$^{-1}$. [d]Maximum rate is obtained from the maximum slopes of $\Delta f/n$ versus time, $[\mathrm{d}(\Delta f/n)/\mathrm{d}t]_{\text{max, 17 C}}$ = 4.0 Hz·min$^{-1}$.

### 4.4.3 Effect of pH on Chitinase Activity

Solution pH also had a strong influence on chitinase activity. As shown in **Figure 4.6**, the QCM-D results indicated that chitinase showed activity over a broad pH range (pH = 4.0 ~ 10.0), but $[d(\Delta f/n)/dt]_{\text{max }\Delta D}$ of the RChitin films varied with pH. These differences are expressed as the hydrolysis rate at the time of maximum $\Delta D$ at a given pH to the value at pH = 4.0 ($[d(\Delta f/n)/dt]_{\text{max }\Delta D}/[d(\Delta f/n)/dt]_{\text{max }\Delta D,4.0}$) and plotted in the inset of **Figure 4.6**. Near neutral pH, the hydrolysis rates were fast and reached a plateau in ~ 60 and ~ 80 min for pH = 8.0 and pH = 6.0, respectively. This observation is consistent with a previous review which summarized that the optimal pH values for most microbial chitinases in solution are between 5.0 and 8.0.[25] At basic pH (10.0), the hydrolysis rate was initially fast (with an initial hydrolysis rate comparable to pH = 8.0, **Table 4.5**), but was considerably slower after ~ 30 min until the plateau was reached at ~

500 min. This result suggests that chitinase was not stable at basic pH and started losing activity after a relatively short incubation period. At acidic pH (4.0), the $[d(\Delta f/n)/dt]_{\max \Delta D}$ was slower than at higher pH and reached a plateau in ~ 200 min. However, the plateau value of $\Delta f/n$ was smaller at pH = 4.0 ($\Delta f/n$ ~ 145 Hz) than at other pH values ($\Delta f/n$ = 185 ~ 195 Hz). As the RChitin films were prepared under the same experimental conditions and ellipsometry data indicated that all the RChitin films had similar thicknesses (~ 20 nm), similar magnitudes of the frequency shifts were expected for complete hydrolysis. The smaller $\Delta f/n$ decrease for the case of acidic pH was attributed to inactivation of chitinase after incubation in an acidic environment. To further test this hypothesis, AFM was employed to study the morphology of the RChitin films after enzymatic hydrolysis at different pH values and the results are shown in **Figure 4.7**. After hydrolysis at pH = 4.0, large chitin aggregates (RMS roughness ~ 17 nm, on the order of the thickness of the film) were still present on the AFM height image. In contrast, the RMS roughnesses for the RChitin films hydrolyzed at pH = 8.0 and 10.0 were very small (similar to pH = 6.0 in **Figure 2D**), and the morphology was similar to bare silica coated QCM-D sensors (**Figure 4.3B**).

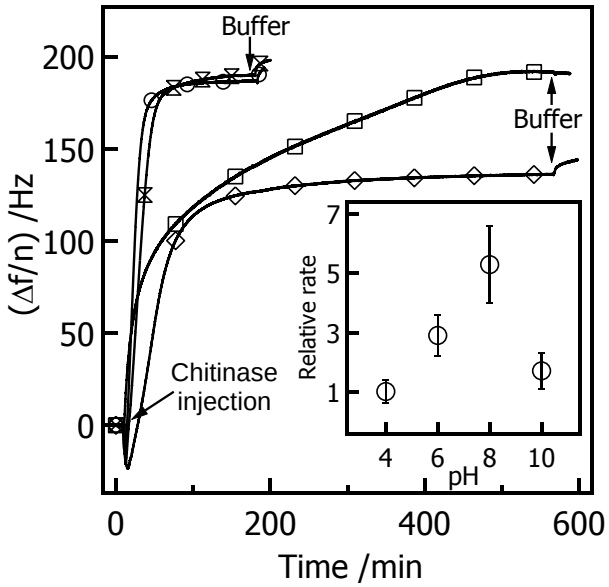


**Figure 4.6.** Representative $\Delta f/n$ versus time for chitinase (0.5 mg·mL$^{-1}$) activity on RChitin films at 37 °C in (◊) 50 mM pH = 4.0 citrate-phosphate buffer, (⧖) 50 mM pH = 6.0 phosphate buffer, (○) 50 mM pH = 8.0 phosphate buffer and (□) 50 mM pH = 10.0 phosphate buffer. Curves correspond to the fifth overtone. The inset contains reaction rates relative to pH=4.0 ($[d(\Delta f/n)/dt]_{\max \Delta D}/[d(\Delta f/n)/dt]_{\max \Delta D,4.0}$ with one standard deviation error bars as a function of pH, where average $[d(\Delta f/n)/dt]_{\max \Delta D,4.0}$ = 2.4 Hz·min$^{-1}$ or ~ 0.43 mg·m$^{-2}$·min$^{-1}$).

In contrast to the temperature study, there was a systematic change in the minimum value of $\Delta f$/n as seen in **Figure 4.5B**. Smaller $\Delta f$/n decreases with increasing pH are consistent with less adsorbed enzyme even though the initial hydrolysis rates for higher pH were greater than the initial hydrolysis rate at pH = 4.0. These results clearly show that the adsorbed enzyme concentration was not the most important variable for determining chitinase activity.

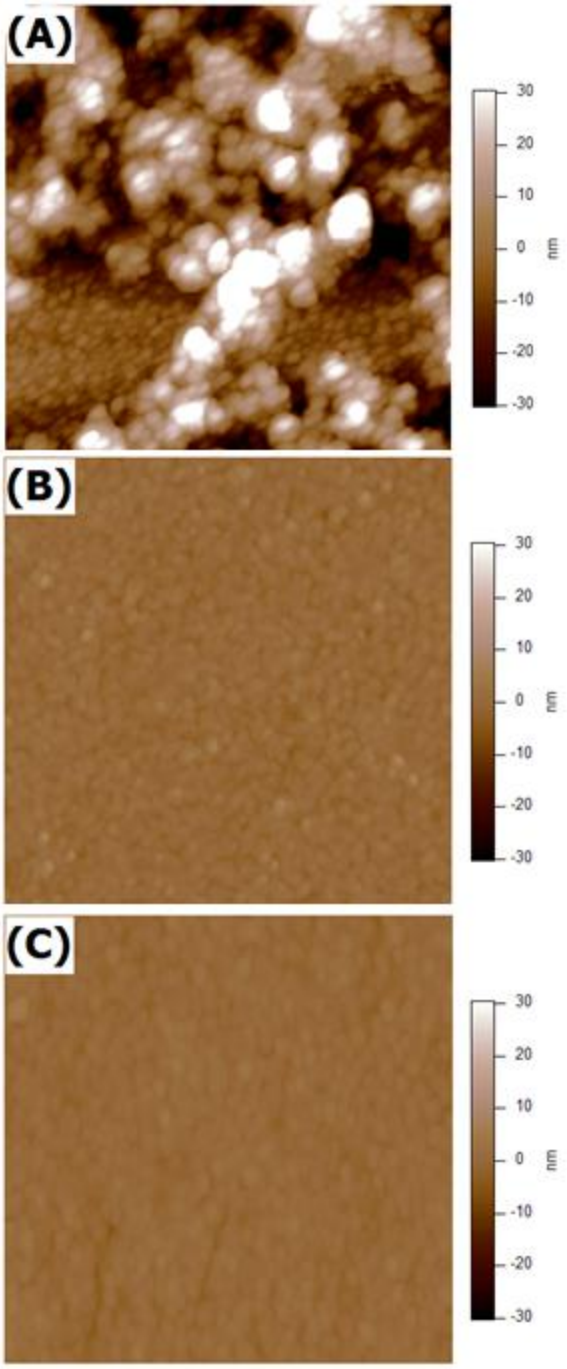


**Figure 4.7.** Representative 2 μm × 2 μm AFM height images of RChitin films on silica coated QCM-D sensors after enzymatic hydrolysis at (A) pH = 4.0, (B) pH = 8.0 and (C) pH = 10.0 (for pH = 6.0 see **Figure 4.2D**). The incubation times and conditions were the same as those in **Figure 4.6**. RMS roughnesses for the images are: (A) ~16.6 nm, (B) ~1.2 nm, and (C) ~1.1 nm.

**Table 4.5.** Relative hydrolysis rates for RChitin films at different pH (37 °C).[a]

| pH | Concentration /mg·mL$^{-1}$ | Relative initial rate[b] | Relative rate at maximum $\Delta D$[c] | Relative maximum rate[d] |
|---|---|---|---|---|
| 4.0 | 0.5 | 1.0 ± 0.4 | 1.0 ± 0.4 | 1.0 ± 0.5 |
| 6.0 | 0.5 | 2.0 ± 0.6 | 2.9 ± 0.7 | 1.9 ± 0.7 |
| 8.0 | 0.5 | 1.9 ± 0.8 | 5.3 ± 1.3 | 4.4 ± 1.8 |
| 10.0 | 0.5 | 2.7 ± 1.0 | 1.7 ± 0.6 | 2.7 ± 1.0 |

[a]The relative hydrolysis rate is the ratio of the hydrolysis rate at a given enzyme concentration to the value at pH = 4.0. [b]Initial rate is obtained from the initial slopes of $\Delta f/n$ versus time after the minimum in $\Delta f/n$, $[d(\Delta f/n)/dt]_{initial,\ 4.0}$ = 2.8 Hz·min$^{-1}$. [c]Rate at maximum $\Delta D$ is obtained from the slopes of $\Delta f/n$ versus time at the time of maximum $\Delta D$, $[d(\Delta f/n)/dt]_{max\ \Delta D,\ 4.0}$ = 2.4 Hz·min$^{-1}$. [d]Maximum rate is obtained from the maximum slopes of $\Delta f/n$ versus time, $[d(\Delta f/n)/dt]_{max,\ 4.0}$ = 3.6 Hz·min$^{-1}$.

### 4.4.4 Effect of Chitinase Concentration on Chitinase Activity

**Figure 4.8** shows $\Delta f/n$ versus time for the enzymatic hydrolysis of RChitin films at different enzyme concentrations ($C$). As shown in the inset of **Figure 4.8**, the relative hydrolysis rates at the time of maximum $\Delta D$ are 1:2.3:4.7:6.5 for 0.05:0.2:0.5:1.0 mg·mL$^{-1}$ chitinase, which shows that the hydrolysis rate increased with enzyme concentration. Similar trends were observed for the initial and maximum hydrolysis rate (**Table 4.6**). This observation was consistent with previous results by Berger et al,[19] where the optical density of colloidal chitin suspensions decreased as enzyme concentration increased as the change in optical density was quantitatively proportional to chitinase (from *Streptomyces griseus*) concentration. This trend is attributed to the formation of more chain ends by endochitinases at higher concentrations, thereby allowing greater access throughout the film for exochitinase activity. While the lowest enzyme

concentration revealed less adsorption (**Figure 4.5C**), the amount of adsorbed enzyme was more or less constant for the other concentrations, again revealing that adsorbed enzyme concentration is not the determining factor for the chitinase activity.

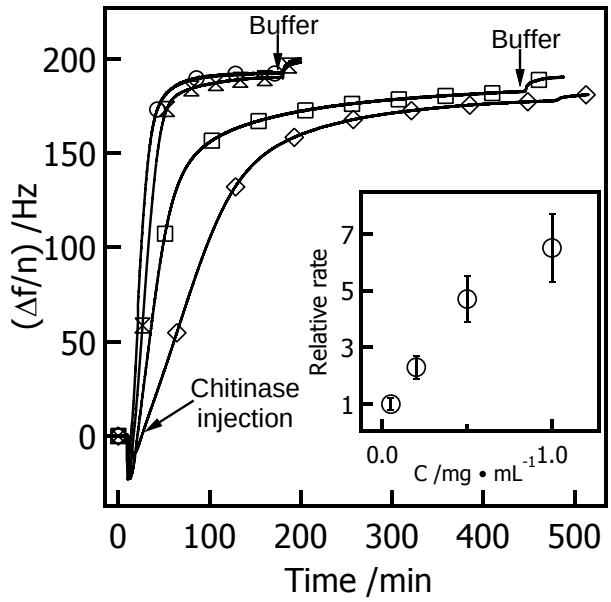


**Figure 4.8.** Representative $\Delta f/n$ versus time for chitinase activity on RChitin films at 37 °C. Chitinase solutions with C = (◊) 0.05 mg·mL$^{-1}$, (□) 0.2 mg·mL$^{-1}$, (⧖) 0.5 mg·mL$^{-1}$, and (○) 1.0 mg·mL$^{-1}$ were prepared in a 50 mM pH = 6.0 phosphate buffer. Curves correspond to the fifth overtone. The inset contains reaction rates relative to C = 0.05 mg·mL$^{-1}$ ($[d(\Delta f/n)/dt]_{\max\ \Delta D}$ /$[d(\Delta f/n)/dt]_{\max\ \Delta D,0.05}$ with one standard deviation error bars as a function of C, where average $[d(\Delta f/n)/dt]_{\max\ \Delta D,0.05}$ = 1.3 Hz·min$^{-1}$ or ~ 0.24 mg·m$^{-2}$·min$^{-1}$.

For enzymes in solution one of the simplest models is the Michaelis-Menten model.[26] This model assumes an enzyme (*E*) binds to a substrate (*S*) to rapidly form an enzyme-substrate complex (*ES*) in an equilibrium fashion, with a second, singular, irreversible and slower pathway to product (*P*) formation:

$$E + S \underset{k_{-1}}{\overset{k_1}{\rightleftarrows}} ES \overset{k_{cat}}{\rightarrow} E + P \tag{4.2}$$

where $k_1$ is the association rate constant and $k_{-1}$ is the dissociation rate constant for the enzyme-substrate complex and $k_{cat}$ is the rate constant for the catalytic step. This pathway leads to an expression for the rate law of:

$$Rate = \frac{k_{cat}[E]_{total}[S]}{[S] + K} \tag{4.3}$$

where $[E]_{total} = [ES] + [E]$ and $K$ is just the equilibrium constant for the formation of the enzyme-substrate complex ($K = k_1/k_{-1}$). Application of the steady state-approximation to this model gives

$$Rate = \frac{k_1 k_{cat}[E]_{total}[S]}{k_1[S] + k_{-1} + k_{cat}} = \frac{k_{cat}[E]_{total}[S]}{[S] + K_M} \tag{4.4}$$

where $K_M = (k_{-1} + k_{cat})/k_1$. Under conditions where $[S] << K_M$, the equation becomes:

$$Rate = \frac{k_{cat}[E]_{total}[S]}{K_M} \tag{4.5}$$

One may assume that converting Equation 4.5 to surface parameters where [*S*] is essentially constant gives the rate being proportional to [*E*], but is [*E*] the surface or bulk concentration?

Applying these same concepts to surfaces, as done by Maurer et al.[27] for a cellulose system is also possible. At surfaces the model becomes one of a hybrid between Langmuir adsorption and Michaelis-Menten kinetics. The Langmuir adsorption isotherm for the surface concentration of adsorbed enzyme is:

$$\Gamma_{enzyme} = \frac{K_L[E]_{total}\Gamma_{max}}{1 + K_L[E]_{total}} \tag{4.6}$$

where $K_L$ represents the ratio of the adsorption and desorption rate constants for enzyme adsorbing from the bulk onto the surface and enzyme desorbing from the surface back into solution, and $\Gamma_{max}$ is the maximum surface concentration for a surface saturated by enzyme with monolayer coverage. Conversion of the Michaelis-Menton model to surface parameters and solving the model under a pseudo-steady-state approximation yields the equation reported by Maurer et al.

$$Rate = \frac{k_1 k_{cat}\Gamma_S\Gamma_{max}K_L[E]_{total}}{k_{-1} + K_L[E]_{total}(k_{-1} + k_1\Gamma_S)} \tag{4.7}$$

where $\Gamma_s$ is the substrate surface concentration. In the limit of low enzyme concentration:

$$Rate = \frac{k_1 k_{cat}\Gamma_S\Gamma_{max}K_L[E]_{total}}{k_{-1}} \; or \; \frac{Rate}{[E]_{total}} = \frac{k_1 k_{cat}\Gamma_S\Gamma_{max}K_L}{k_{-1}} = constsant \tag{4.8}$$

This particular limit says that the normalization is $[E]_{total}$ rather than $[E]_{surface}$. As seen in **Table 4.6**, none of the three methods considered for measuring the rate is directly proportional to $[E]_{total}$ ($[E]_{total}$ and $[E]_{bulk}$ under our conditions).

**Table 4.6.** Relative hydrolysis rates for RChitin films at different chitinase concentrations (pH = 6.0).[a]

| Temperature /°C | Concentration /mg·mL$^{-1}$ | Relative initial rate[b] | Relative rate at maximum $\Delta D$[c] | Relative maximum rate[d] |
|---|---|---|---|---|
| 37 | 0.05 | 1.0 ± 0.1 | 1.0 ± 0.2 | 1.0 ± 0.1 |
| 37 | 0.2 | 1.8 ± 0.1 | 2.3 ± 0.4 | 2.2 ± 0.3 |
| 37 | 0.5 | 3.8 ± 0.4 | 4.7 ± 0.8 | 4.3 ± 0.2 |
| 37 | 1.0 | 4.6 ± 0.4 | 6.5 ± 1.2 | 5.3 ± 0.4 |

[a]The relative hydrolysis rate is the ratio of the hydrolysis rate at a given enzyme concentration to the value at $C$ = 0.05 mg·mL$^{-1}$. [b]Initial rate is obtained from the initial slopes of $\Delta f/n$ versus time after the minimum in $\Delta f/n$, $[d(\Delta f/n)/dt]_{initial,\ 0.05}$ = 1.5 Hz·min$^{-1}$. [c]Rate at maximum $\Delta D$ is obtained from the slopes of $\Delta f/n$ versus time at the time of maximum $\Delta D$, $[d(\Delta f/n)/dt]_{max\ \Delta D,\ 0.05}$ = 1.2 Hz·min$^{-1}$. [d]Maximum rate is obtained from the maximum slopes of $\Delta f/n$ versus time, $[d(\Delta f/n)/dt]_{max,\ 0.05}$ = 1.5 Hz·min$^{-1}$.

### 4.4.5 Effect of the Degree of Acetylation on Chitinase Activity

Chitinolytic microorganisms play significant roles in maintaining carbon and nitrogen cycles in both the soil and the ocean by degrading chitin into small molecules.[28] Natural chitin is highly acetylated, and chitosan is usually prepared from natural chitin through partial deacetylation. Chitinase derived from microorganisms are expected to show higher activity on highly acetylated natural chitin than on semi-synthetic chitosan, which has a lower degree of acetylation than that found in natural systems. In order to test this premise, QCM-D (**Figure 4.9**) tracked the enzymatic hydrolysis of RChitin and chitosan films prepared from commercially available chitosan in the presence of chitinase (from *Streptomyces griseus*). As previously reported by our group, $^1$H NMR and reflection absorption infrared spectroscopy (RAIRS) measurements

demonstrated TMSChitin and RChitin are essentially 100% acetylated,[18] while the degree of acetylation (DA) for the chitosan is ~ 12 %.[29] As mentioned previously, the hydrolysis rate for RChitin films was fast with a plateau value of $\Delta f/n$ ~ 185 Hz for an ~ 20 nm film. However, the hydrolysis rate for the chitosan film was smaller and only a portion of the chitosan film degraded (plateau $\Delta f/n$ ~ 50 Hz for an ~ 20 nm film) even after incubation times as long as 12 h. *N*-acetylated chitosan and deacetylated chitin derivatives have been used as substrates to study the effects of DA on enzymatic hydrolysis catalyzed by chitinase or lysozyme.[30-35] The results showed that partially *N*-acetylated chitosan or deacetylated chitin derivatives with a DA around 60 % are more susceptible to hydrolysis than natural chitin and highly deacetylated chitosan due to the interplay between appropriate *N*-acetyl-D-glucosamine content and solubility, enabling the formation of an enzyme-substrate complex.[34] However, attempts to study this effect in thin films failed because partially deacetylated chitin derivatives with DAs around 60% were too soluble in aqueous media to form stable films over the entire pH range. This observation was consistent with results previously reported by Vårum et al.[36] that DA = 60 % chitosan showed excellent water solubility over a pH range of 4 to 9, while chitosans with DA of 1 % and 17 % became completely insoluble at pH above 7.

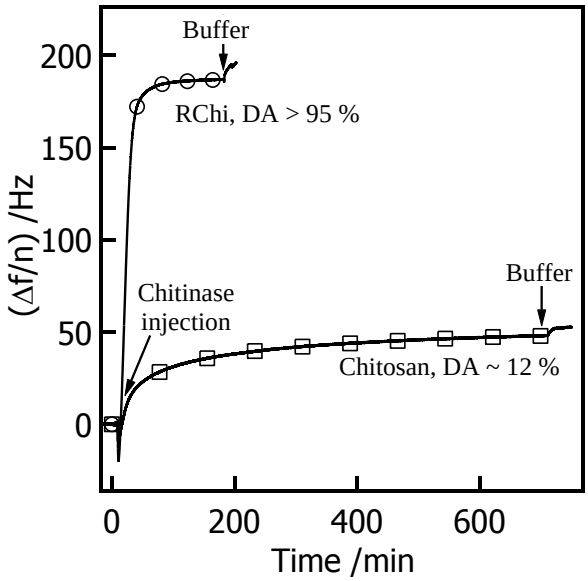


**Figure 4.9.** Representative Δ*f*/*n* versus time for chitinase (0.5 mg·mL$^{-1}$) activity on (○) RChitin and (□) chitosan films at 37 °C in a 50 mM pH = 8.0 phosphate buffer. Curves correspond to the fifth overtone.

As controls, RChitin films were incubated with buffer at different pH values and chitosan films were incubated with buffer (pH = 8.0) at 37 °C. Film stability was monitored by QCM-D over the time frame where hydrolysis occurred. As seen in **Figure 4.10**, the RChitin films were stable over the entire pH range (4.0 ~ 10.0) and chitosan films were stable at pH = 8.0 for at least 2 hours.

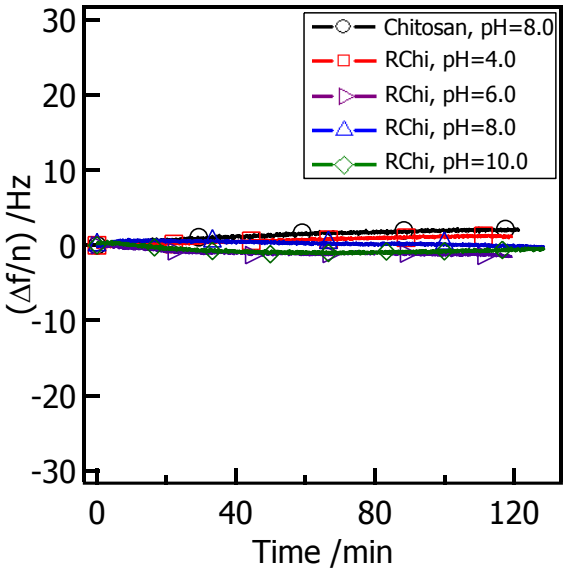


**Figure 4.10.** Representative Δ*f*/*n* versus time for RChitin and chitosan films incubated with buffer at 37 °C. Curves correspond to the fifth overtone.

### 4.5 Conclusions

In summary, this work provides a real-time and label-free method to assay chitinase activity via QCM-D and AFM. Smooth, homogeneous and ultrathin chitin films were prepared by spincoating trimethylsilyl chitin solutions onto silica substrates, followed by regeneration to amorphous chitin in HCl vapor. Chitinase (from *Streptomyces griseus*) activity on the amorphous chitin thin films under various conditions of enzyme concentration, temperature, pH and degree of acetylation was investigated by QCM-D and AFM. The QCM-D and AFM data were consistent with colloidal studies and showed that the hydrolysis rate of RChitin films increased as enzyme concentrations increased, and the optimal temperature and pH for chitinase were around 37 °C and 6 ~ 8, respectively. Chitinase also showed higher activity on fully acetylated chitin than highly deacetylated chitosan. The successful preparation of smooth and homogeneous chitin thin films and the combination of QCM-D and AFM techniques provides a convenient and

promising way to assay the activity of chitinase and other chitinolytic enzymes and is therefore of potential interest to those exploring more robust chitinase or chitinase mixtures, investigating the enzymatic degradation of chitin-based biomaterials, and designing novel pathogenic fungal inhibitors.

### 4.6 References


(1) Ohtakara, A. Viscosimetric assay for chitinase. In *Methods Enzymol.*, Willis A. Wood, S. T. K., Ed. Academic Press: 1988; Vol. Volume 161, pp 426-430.

(2) Boller, T.; Mauch, F. Colorimetric assay for chitinase. In *Methods Enzymol.*, Willis A. Wood, S. T. K., Ed. Academic Press: 1988; Vol. Volume 161, pp 430-435.

(3) Cabib, E. Assay for chitinase using tritiated chitin. In *Methods Enzymol.*, Willis A. Wood, S. T. K., Ed. Academic Press: 1988; Vol. Volume 161, pp 424-426.

(4) Rojas, O. J.; Jeong, C.; Turon, X.; Argyropoulos, D. S. Measurement of Cellulase Activity with Piezoelectric Resonators. In *Materials, Chemicals, and Energy from Forest Biomass*, American Chemical Society: 2007; Vol. 954, pp 478-494.

(5) Turon, X.; Rojas, O. J.; Deinhammer, R. S. *Langmuir* **2008,** 24, 3880-3887.

(6) Hu, G.; Heitmann, J. A.; Rojas, O. J. *J. Phys. Chem. B* **2009,** 113, 14761-14768.

(7) Cheng, G.; Liu, Z.; Murton, J. K.; Jablin, M.; Dubey, M.; Majewski, J.; Halbert, C.; Browning, J.; Ankner, J.; Akgun, B.; Wang, C.; Esker, A. R.; Sale, K. L.; Simmons, B. A.; Kent, M. S. *Biomacromolecules* **2011,** 12, 2216-2224.

(8) Cheng, G.; Datta, S.; Liu, Z.; Wang, C.; Murton, J. K.; Brown, P. A.; Jablin, M. S.; Dubey, M.; Majewski, J.; Halbert, C. E.; Browning, J. F.; Esker, A. R.; Watson, B. J.; Zhang, H.; Hutcheson, S. W.; Huber, D. L.; Sale, K. L.; Simmons, B. A.; Kent, M. S. *Langmuir* **2012,** 28, 8348-8358.

(9) Ahola, S.; Turon, X.; Österberg, M.; Laine, J.; Rojas, O. J. *Langmuir* **2008,** 24, 11592-11599.

(10) Aulin, C.; Ahola, S.; Josefsson, P.; Nishino, T.; Hirose, Y.; Österberg, M.; Wågberg, L. *Langmuir* **2009,** 25, 7675-7685.

(11) Kittle, J. D.; Du, X.; Jiang, F.; Qian, C.; Heinze, T.; Roman, M.; Esker, A. R. *Biomacromolecules* **2011,** 12, 2881-2887.

(12) Nordgren, N.; Eklöf, J.; Zhou, Q.; Brumer, H.; Rutland, M. W. *Biomacromolecules* **2008,** 9, 942-948.

(13) Nishino, H.; Nihira, T.; Mori, T.; Okahata, Y. *J. Am. Chem. Soc.* **2004,** 126, 2264-2265.

(14) Nihira, T.; Mizuno, M.; Tonozuka, T.; Sakano, Y.; Mori, T.; Okahata, Y. *Biochemistry* **2005,** 44, 9456-9461.

(15) Snabe, T.; Petersen, S. B. *Chem. Phys. Lipids* **2003,** 125, 69-82.

(16) Westwood, M.; Roberts, D.; Parker, R. *Carbohydr. Polym.* **2011,** 84, 960-969.

(17) Hou, Y.; Chen, J.; Sun, P.; Gan, Z.; Zhang, G. *Polymer* **2007,** 48, 6348-6353.

(18) Kittle, J. D.; Wang, C.; Qian, C.; Zhang, Y.; Zhang, M.; Roman, M.; Morris, J. R.; Moore, R. B.; Esker, A. R. *Biomacromolecules* **2012,** 13, 714-718.

(19) Berger, L. R.; Reynold, D. M. *Biochim. Biophys. Acta* **1958,** 29, 522-534.

(20) Josefsson, P.; Henriksson, G.; Wågberg, L. *Biomacromolecules* **2008,** 9, 249-254.

(21) Hu, G.; Heitmann, J. A.; Rojas, O. J. *Anal. Chem.* **2009,** 81, 1872-1880.

(22) Hardt, M.; Laine, R. A. *Arch. Biochem. Biophys.* **2004,** 426, 286-297.

(23) Kezuka, Y.; Ohishi, M.; Itoh, Y.; Watanabe, J.; Mitsutomi, M.; Watanabe, T.; Nonaka, T. *J. Mol. Biol.* **2006,** 358, 472-484.

(24) Liu, Z.; Choi, H.; Gatenholm, P.; Esker, A. R. *Langmuir* **2011,** 27, 8718-8728.

(25) Dahiya, N.; Tewari, R.; Hoondal, G. *Appl. Microbiol. Biotechnol.* **2006,** 71, 773-782.

(26) Segel, I. H. *Enzyme Kinetics: Behavior and Analysis of Rapid Equilibrium and Steady-State Enzyme Systems*; Wiley: New York, 1993.

(27) Maurer, S. A.; Bedbrook, C. N.; Radke, C. J. *Ind. Eng. Chem. Res.* **2012,** 51, 11389-11400.

(28) Souza, C.; Almeida, B.; Colwell, R.; Rivera, I. G. *Mar. Biotechnol.* **2011,** 13, 823-830.

(29) Wang, H.; Roman, M. *Biomacromolecules* **2011,** 12, 1585-1593.

(30) Brodel, B.; Touzel, J. P.; Debeire, P.; Paul, F.; Monsan, P.; Gysin, B. *Ann. N.Y. Acad. Sci.* **1995,** 750, 71-74.

(31) Heggset, E. B.; Hoell, I. A.; Kristoffersen, M.; Eijsink, V. G. H.; Vårum, K. M. *Biomacromolecules* **2009,** 10, 892-899.

(32) Shigemasa, Y.; Saito, K.; Sashiwa, H.; Saimoto, H. *Int. J. Biol. Macromol.* **1994,** 16, 43-49.

(33) Kitaura, K.; Kaji, T.; Mori, Y.; Nishiyama, Y. *Carbohydr. Polym.* **2000,** 42, 19-21.

(34) Hirano, S.; Tsuchida, H.; Nagao, N. *Biomaterials* **1989,** 10, 574-576.

(35) Cho, Y.-W.; Jang, J.; Park, C. R.; Ko, S.-W. *Biomacromolecules* **2000,** 1, 609-614.

(36) Vårum, K. M.; Ottøy, M. H.; Smidsrød, O. *Carbohydr. Polym.* **1994,** 25, 65-70.

# Chapter 5: Nanocrystalline Chitin Thin Films and Their Interactions with Biomacromolecules

Published Chapter: Wang, C.; Esker, A. R. *Carbohydrate Polymers* **2014**, 102, 151-158.

## 5.1 Abstract

Natural chitin occurs as ordered crystalline microfibrils in association with other materials as natural composites. Elucidating the interactions between crystalline chitin and various biomacromolecules is of fundamental importance for designing and fabricating chitin-based biomaterials. This work highlights a simple method for the preparation of ultrathin films of chitin nanocrystals by spincoating chitin nanocrystals from a colloidal suspension onto a gold substrate modified by an amine-terminated self-assembled monolayer. Atomic force microscopy confirmed that nanocrystalline chitin (Chitin NC) films are reasonably smooth and homogeneous, and quartz crystal microbalance with dissipation monitoring (QCM-D) solvent exchange experiments demonstrated that Chitin NC films have twice as much water as amorphous regenerated chitin (RChitin) films of similar thickness. The QCM-D data also showed that chitinase-catalyzed hydrolysis of Chitin NC films was much slower than that of RChitin films. Chitinase not only degraded, but also caused swelling of the chitin nanocrystals. Bovine serum albumin (BSA) adsorption studies demonstrated that Chitin NC films have high protein loading capacity, and thus show potential applications for enzyme immobilization.

## 5.2 Introduction

Fundamental knowledge about the interactions between chitin and proteins, polysaccharides, calcium carbonate, enzymes, drugs, cells and synthetic materials is not only important for elucidating biological processes associated with chitin, but also for designing novel chitin-based biomaterials. Well-defined chitin thin films and the development of surface characterization techniques provide a convenient way to study and quantify these interactions. Recently, our group reported a simple method to prepare homogeneous, smooth and ultrathin chitin films by spincoating trimethylsilyl chitin (TMSChitin) from a mixture of chloroform and tetrachloroethane onto silica or gold surfaces. These TMSChitin films were subsequently regenerated to amorphous chitin upon exposure to the vapor of a hydrochloric acid solution. The regenerated chitin thin films were used as a model surface to study the interactions between chitin and bovine serum albumin (BSA) via a quartz crystal microbalance with dissipation monitoring (QCM-D), surface plasmon resonance (SPR) and atomic force microscopy (AFM),[1] as well as chitinases.[2] However, the regenerated chitin films are only representative of amorphous chitin structures, differing in crystallinity from native chitin. Crystalline chitin thin films are expected to provide a better model to study the enzymatic degradation of native chitin, chitin-protein interactions, fungal cell wall component interactions and biomineralization.

Various cellulose thin films (including both amorphous and crystalline) have been prepared via spincoating or the Langmuir-Blodgett techniques.[3-13] Edgar et al.[4] reported the preparation of smooth nanocrystalline cellulose thin films by spincoating colloidal suspensions of cellulose nanocrystals onto mica surfaces. Habibi et al.[8] prepared monolayers of cellulose nanocrystals via the Langmuir–Blodgett technique.

Similar to cellulose, native chitin is highly crystalline with some disordered or paracrystalline regions that arise from defects. The disordered or paracrystalline regions are preferentially hydrolyzed or oxidized under certain conditions, whereas crystalline regions remain intact. Thus, rod-like chitin nanocrystals or whiskers can be produced.[14, 15] Chitin nanocrystals are normally prepared by hydrolysis of chitin in hydrochloric acid solutions.[15-17] The sizes of the chitin nanocrystals are greatly affected by the origin of the chitin, concentration of the hydrochloric acid solution and the hydrolysis time, with the lengths varying over the range of 150 to 2200 nm, and the widths over the range of 10 to 50 nm.[15] Recently, Fan et al. prepared chitin nanocrystals via 2,2,6,6-tetramethylpiperidine-1-oxyl radical (TEMPO) mediated oxidation of $\alpha$-chitin with NaClO as a co-oxidant.[18] The resulting rod-like nanocrystals had high surface charges because some hydroxyl groups on the surface were oxidized to carboxylate groups, and the average nanocrystal length and width were 340 and 8 nm, respectively.

This work presents a simple method to prepare smooth and ultrathin nanocrystalline chitin films. The morphologies, surface roughnesses, thicknesses and water contents of these films were characterized via atomic force microscopy (AFM), ellipsometry and a quartz crystal microbalance with dissipation monitoring (QCM-D). The chitinase-catalyzed hydrolysis of these chitin films was investigated via QCM-D. The utility of these chitin films as potential enzyme immobilization supports was demonstrated through the adsorption of bovine serum albumin (BSA) onto the films in QCM-D studies.

## 5.3 Experimental

Chitinase (from S*treptomyces griseus*, lyophilized powder, ≥200 units·g$^{-1}$ solid) is an extracellular enzyme complex[19] with a molar mass of ~ 30 kDa and was purchased from Sigma-

Aldrich. Bovine serum albumin (lyophilized powder) was purchased from Sigma-Aldrich and used as received. 11-Amino-1-undecanethiol was purchased from Fisher Scientific and used as received. Sodium phosphate monobasic monohydrate and sodium phosphate dibasic heptahydrate were purchased from Sigma-Aldrich and used as received to prepare buffer solutions (pH = 6.0). All other chemicals and solvents were obtained from Fisher Scientific and used as received. Ultrapure water with a resistivity of 18 MΩ·cm and < 5 ppb inorganic impurities was used in all experiments (Milli-Q Gradient A-10, Millipore). Thin films of RChitin and Chitin NC were prepared as outlined in Chapter 3.4.

X-ray diffraction (XRD), AFM and ellipsometry measurements were performed as outlined in Chapter 3.5. All QCM-D measurements were conducted as outlined in Chapter 3.5.4, with the following details specific to this work.

*Water Content*. The water content of Chitin NC films was determined using a $H_2O/D_2O$ solvent exchange procedure as previously reported.[20] A Chitin NC film coated QCM-D sensor was exposed to $H_2O$ until a stable baseline was obtained, and then $H_2O$ was switched to $D_2O$. A change of $\Delta f/n$ was observed that arose from the different physical properties (density, viscosity and molar mass) of the two solvents. The mass of water associated with the film ($\Gamma_{water}$) was calculated from the change in $\Delta f/n$ associated with switching from $H_2O$ to $D_2O$ using the following equations:

$$\left(\frac{\Delta f}{n}\right)_{water} = \frac{\left(\frac{\Delta f}{n}\right)_{film} - \left(\frac{\Delta f}{n}\right)_{gold}}{\left(\frac{\rho_{D_2O}}{\rho_{H_2O}}\right) - 1} \tag{5.1}$$

$$\Gamma_{water} = -C\left(\frac{\Delta f}{n}\right)_{water} \tag{5.2}$$

where $(\Delta f/n)_{gold}$ is the change of $\Delta f/n$ associated with the switch of a bare gold surface from $H_2O$ to $D_2O$, $(\Delta f/n)_{film}$ is the change of $\Delta f/n$ associated with the switch of a Chitin NC film from $H_2O$ to $D_2O$ with $(\Delta f/n)_{water}$ representing the change of $\Delta f/n$ arising from water in the films.

*Enzymatic Degradation*. The QCM-D sensor was placed in a flow cell and allowed to equilibrate for ~ 1 h in pH = 6.0 phosphate buffer to obtain a flat baseline at 37 °C. Chitinase solutions (1.0 mL) were then flowed over the surface at a rate of 0.100 $mL \cdot min^{-1}$. The flow was stopped and the measurements were made in the absence of flow. At the end of the measurement, buffer was typically flowed through the system for the removal of residual and reversibly adsorbed enzyme and degradation products.

*BSA Adsorption*. The QCM-D sensor was placed in a flow cell and allowed to equilibrate for ~ 1 h in water at 25 °C until a flat baseline was obtained. Solutions of BSA in ultrapure water (100 $mg \cdot L^{-1}$) were then introduced for ~ 25 min at a rate of 0.200 $mL \cdot min^{-1}$, followed by a rinse with ultrapure water for ~ 10 min.

## 5.4 Results and Discussion

### 5.4.1 Characterization of Chitin Nanocrystals

The morphology of chitin nanocrystals on gold surfaces modified by SAM-$NH_2$ was observed by AFM, and a height image is provided in **Figure 5.1**. The rod-like nanocrystals are well dispersed on the surface with lengths and widths ranging from 200 to 600 nm and 30 to 70 nm, respectively. Goodrich et al. [16] used the same procedure to prepare chitin nanocrystals, and used transmission electron microscopy to determine that the nanocrystals had lateral and transverse dimensions of 200 to 500 nm and 10 to 15 nm, respectively. They also found that HCl hydrolysis had little effect on the degree of *N*-acetylation via solid-state CP-MAS $^{13}C$ NMR spectra, and

Congo red dye adsorption experiments showed higher surface areas (347 $m^2 \cdot g^{-1}$) for chitin nanocrystals than the original chitin fiber, as well as cellulose nanocrystals prepared by sulfuric acid hydrolysis.[16]

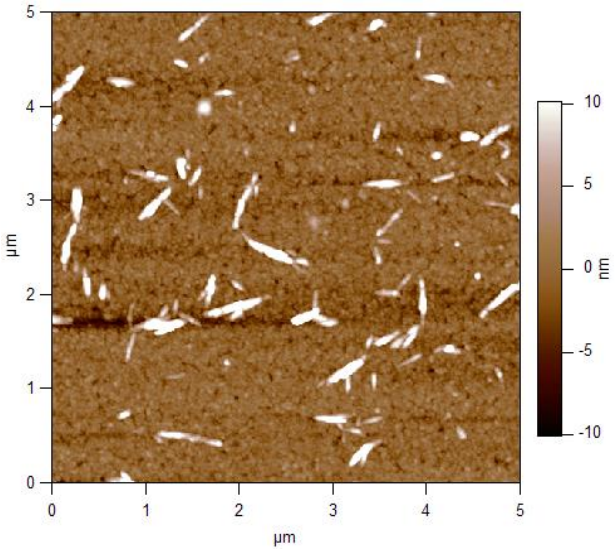


**Figure 5.1.** A representative 5 µm × 5 µm AFM height image of chitin nanocrystals on a SAM-$NH_2$ coated gold surface.

The diffraction patterns of lyophilized chitin nanocrystals, RChitin and raw $\alpha$-chitin prior to hydrolysis are shown in **Figure 5.2**. Both chitin nanocrystals and raw $\alpha$-chitin show the typical reflections of pure $\alpha$-chitin, corresponding to the 020, 021, 110, 120, 130, and 013 crystallographic planes.[16, 21] In contrast, the absence of the characteristic diffraction peaks for RChitin indicated that RChitin is mostly unoriented and amorphous. Crystallinity index (*CI*) has been used for the interpretation of changes in chitosan and chitin crystal structure during physicochemical treatments.[22, 23] Percentage values of *CI* can be calculated from:

$$\text{Crystallinity index } (CI)\ (\%) = [(I_{110}-I_{am})/I_{110}] \times 100 \qquad (5.3)$$

where $I_{110}$ (arbitrary units) is the maximum intensity of the 110 peak at 2θ = 19°, and $I_{am}$ (arbitrary units) is the maximum intensity of the amorphous diffraction at 2θ = 12.6°. The *CI* increased from ~ 91% (raw *α*-chitin) to ~ 97% (chitin nanocrystals), indicating that some of the amorphous regions in raw *α*-chitin were digested during HCl hydrolysis.

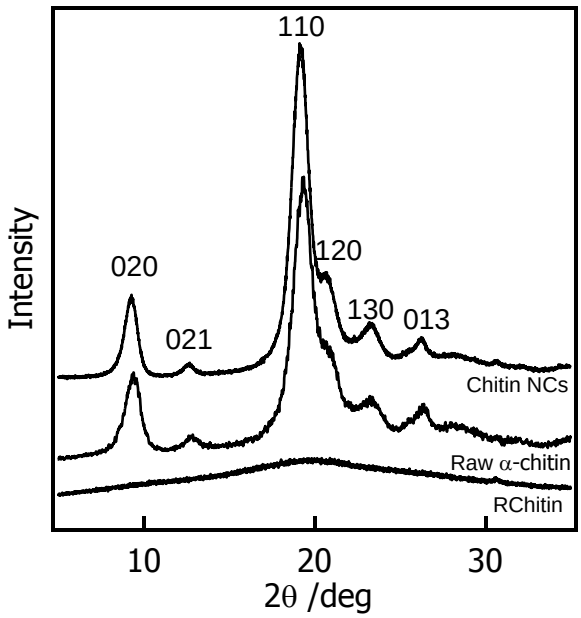


**Figure 5.2.** Powder x-ray diffraction data for chitin nanocrystals, raw *α*-chitin, and RChitin.

### 5.4.2 Preparation of Chitin NC Films

Chitin NC films with different thicknesses were obtained by spincoating from aqueous colloidal nanocrystalline chitin suspensions (0.50 to 2.20 % by mass) onto gold surfaces modified by SAM-$NH_2$. Height images from AFM of Chitin NC films (~ 20 nm thick) spincoated from an aqueous 1.80 % by mass chitin nanocrystal colloidal suspension are shown in **Figure 5.3**. The Chitin NC films are reasonably smooth and homogeneous; however, the rod-like features are clearly present in the AFM images. The Chitin NC films have RMS roughnesses of ~ 6.4 nm for the 10 μm × 10 μm and ~ 6.1 nm for the 2 μm × 2 μm scan area. These roughnesses

are slightly larger than those reported for nanocrystalline cellulose films (e.g., ~ 5.3 nm for sulfated cellulose nanocrystal (SNC) films on silicon wafers (with surface $SiO_2$ layers),[24] ~ 1.5 nm for SNC films on SAM-$NH_2$ coated gold surfaces,[20] and ~ 2.5 nm for solvolytically desulfated nanocrystalline cellulose films on gold surfaces modified by SAM-$NH_2$.[20] The relatively larger roughnesses for Chitin NC films are likely a consequence of the larger size of the chitin nanocrystals relative to the cellulose nanocrystals.[25]

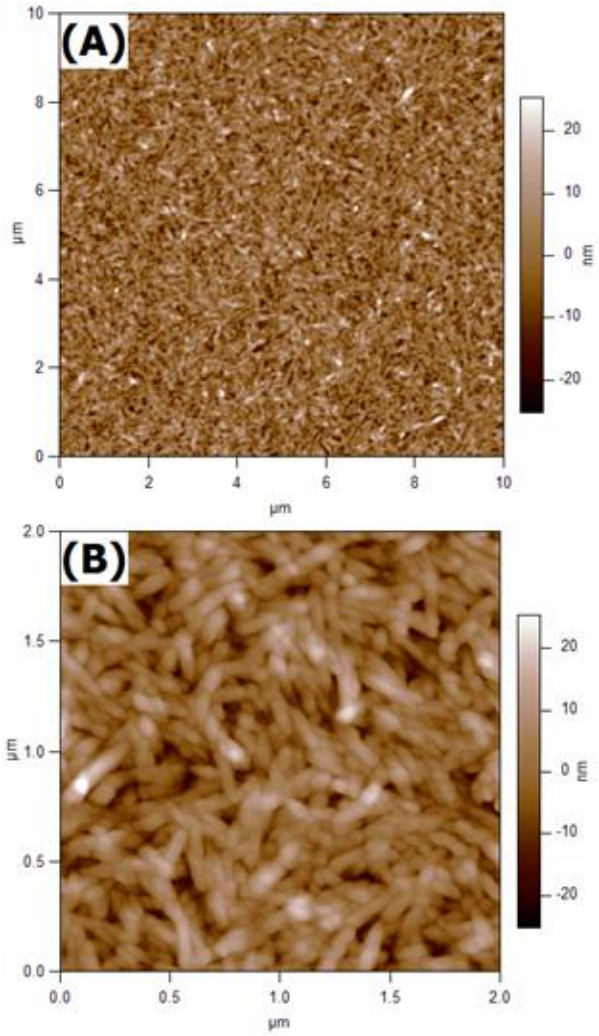


**Figure 5.3.** Representative (A) 10 µm × 10 µm and (B) 2 µm × 2 µm AFM height images of Chitin NC films on gold surfaces modified by SAM-$NH_2$. The RMS roughnesses for the images are: (A) ~ 6.4 nm and (B) ~ 6.1 nm.

### 5.4.3 Water Content of Chitin NC Films

The water content of Chitin NC films was studied using QCM-D and a previously reported $H_2O/D_2O$ solvent exchange procedure.[20] **Figure 5.4** shows representative plots of ($\Delta f/n$) versus time for a bare gold coated QCM-D sensor and two Chitin NC films with different thicknesses switched from $H_2O$ to $D_2O$ and back to $H_2O$. The water contents of Chitin NC and RChitin films as a function of film thickness are shown in **Figure 5.5**. A linear fit of the Chitin NC data gave a slope of 2.50 ± 0.03 $mg \cdot m^{-2} \cdot nm^{-1}$, whereas a linear fit of the RChitin data gave a slope of 1.19 ± 0.05 $mg \cdot m^{-2} \cdot nm^{-1}$. Therefore, Chitin NC films had twice as much water as RChitin films of the same thicknesses. These slopes were converted into mass percentages of water through the same procedure employed by Kittle et al.[20] for cellulose films under the assumption that a chitin monolayer has the same surface concentration ($\Gamma_{monolayer}$ = 0.45 $mg \cdot m^{-2}$)[26] and thickness (0.36 nm)[12] as a cellulose monolayer. This conversion yielded 67 ± 1 % water by mass within the Chitin NC films versus 49 ± 2 % water by mass previously deduced for RChitin films.[1] As was the case for nanocrystalline cellulose versus regenerated cellulose films,[20] this difference is attributed to the voids between individual chitin nanocrystals in Chitin NC films, whereas RChitin films are not porous.[1]

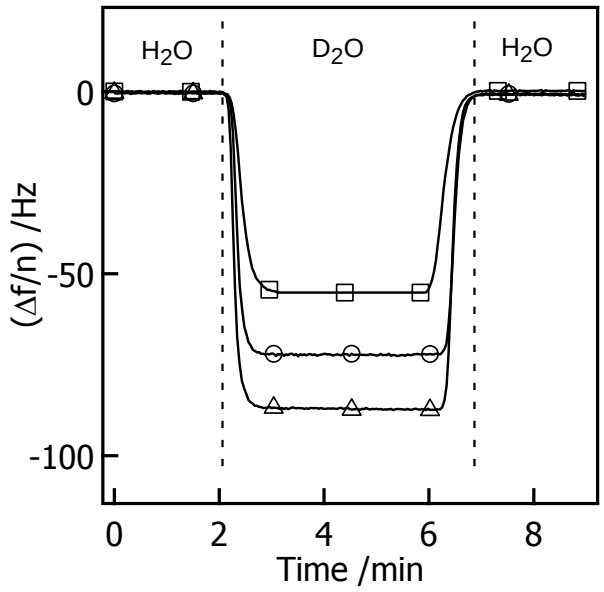


**Figure 5.4.** Representative solvent exchange QCM-D data for (□) a bare gold sensor, (○) a Chitin NC film with a thickness of 8.4 ± 1.1 nm and (Δ) a Chitin NC film with a thickness of 22.6 ± 0.2 nm. Curves correspond to the fifth overtone.

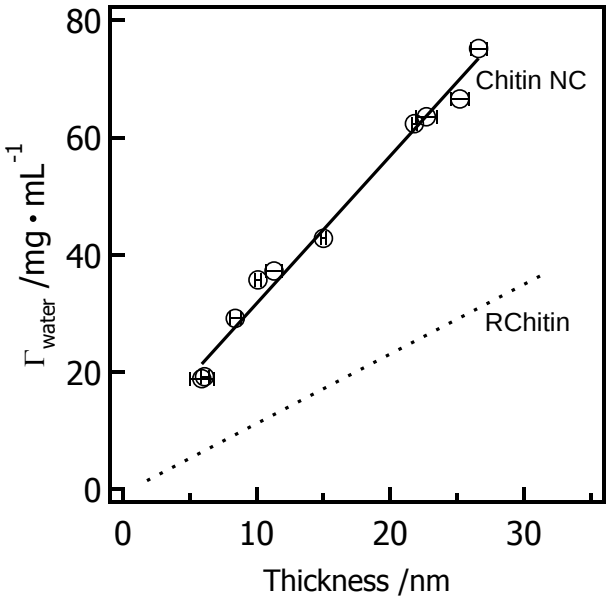


**Figure 5.5.** $\Gamma_{water}$ versus film thickness for (○,—) Chitin NC and (----) RChitin films.[1] One standard deviation error bars are comparable to the size of the symbols for Chitin NC films.

### 5.4.4 Enzymatic Degradation of Nanocrystalline and Amorphous Chitin Films

Crystallinity is one of the most important factors that affects the enzymatic degradation of both natural and synthetic polymers.[27-32] Recently, our group successfully prepared smooth and homogeneous RChitin thin films,[1] and studied the enzymatic degradation of the amorphous RChitin films in the presence of chitinase (from S*treptomyces griseus*) at various conditions via QCM-D and AFM.[2] The combination of RChitin and Chitin NC films provided a good model for the investigation of the effects of crystallinity on the enzymatic degradation of chitin. **Figure 5.6** contains QCM-D data for the enzymatic degradation of RChitin and Chitin NC films. As seen in **Figure 5.6**, the $\Delta f/n$ profile indicated that the RChitin film (with an initial thickness of ~ 20 nm) was hydrolyzed quickly (total hydrolysis in ~ 80 min) as previously reported.[2] Also as previously reported, the dissipation initially increased as chitinase adsorbed onto the film and continued to increase as the chitinase penetrated into the RChitin film.[2] The subsequent drop in $\Delta D$ arose from the exhaustion of the chitin substrate and subsequent chitinase desorption from the film. In contrast, the $\Delta f/n$ profile for Chitin NC film revealed much slower hydrolysis with degradation of only a portion of the Chitin NC film (also with an initial thickness of ~ 20 nm) after 12 h incubation with chitinase. The larger initial $\Delta f/n$ decrease for the Chitin NC film relative to the RChitin film in the inset of **Figure 5.6** indicated that the amount of chitinase adsorbed onto the Chitin NC film was greater than that adsorbed onto the RChitin film. This behavior was attributed to the voids within the Chitin NC film or put another way, an effectively larger accessible surface area. The adsorption of chitinase onto and within the Chitin NC film was accompanied by an instantaneous $\Delta D$ increase. With time, $\Delta D$ grew, however, the rate of growth decreased considerably. One possible explanation for the $\Delta D$ profile is that endochitinase in the chitinase complex disrupted the hydrogen bonds and caused swelling of the chitin nanocrystals.[33]

Similar behavior has been observed for cellulases. Like chitinase, cellulase is also an enzyme cocktail composed of endoglucanases, exoglucanases and cellobiase.[27] Josefsson et al.[34] studied the functions of different pure cellulases on cellulose films via QCM-D, and concluded that endoglucanases not only produced new end groups, but also caused swelling of the cellulose films. Similar behavior was also reported by Cheng et al.[35, 36]

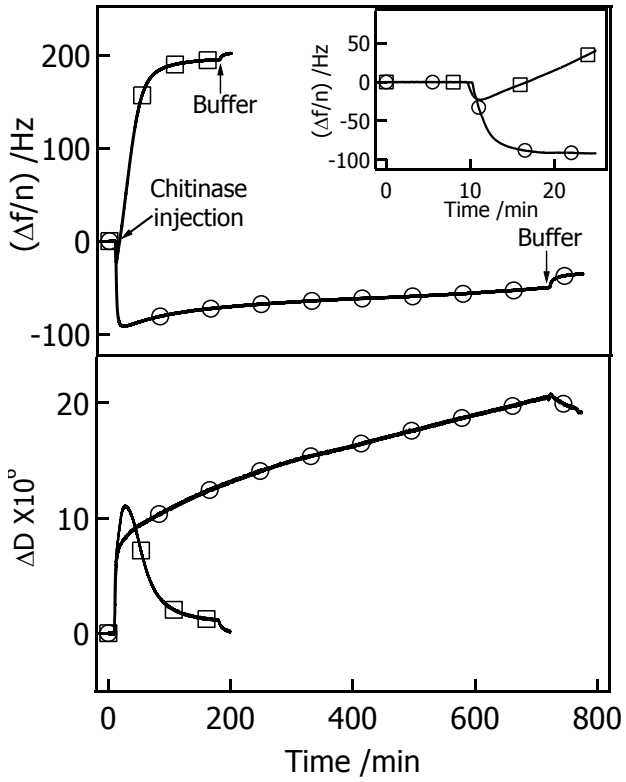


**Figure 5.6.** Representative Δ*f*/*n* and Δ*D* versus time for chitinase (0.5 mg·mL$^{-1}$) activity on (○) Chitin NC and (□) RChitin films at 37 °C in a 50 mM phosphate buffer (pH = 6.0). Curves correspond to the fifth overtone. The inset highlights the region of the Δ*f*/*n* profile dominated by chitinase adsorption onto the chitin films.

Faster hydrolysis of amorphous chitin films than Chitin NC films is also consistent with other studies of enzymatic degradation of semi-crystalline polymers. Various studies have shown that amorphous cellulose was hydrolyzed much faster than crystalline cellulose. In partially crystalline cellulose samples, the amorphous domains were hydrolyzed first, and left the crystalline domains which underwent slower degradation.[27-29, 32] The enzymatic degradation of polyesters has also been widely investigated for their applications as biomaterials.[30, 31, 37] Cai et al.[37] studied the proteinase K-catalyzed degradation of poly(1actic acid), and Kumagai et al.[31] studied the enzymatic degradation of poly(3-hydroxybutyrate) (PHB) in the presence of PHB depolymerase (from *Alcaligenes faecalis*). Both of these studies found that the degradation rate of polyesters decreased with increasing crystallinity of the polymer, and the enzymes hydrolyzed the amorphous domains before the crystalline domains.[31, 37]

### 5.4.5 Adsorption of BSA onto Chitin NC Films

As a biocompatible and biodegradable natural material, chitin is a good support for enzyme immobilization, and thus shows potential applications in biological sensing and biocatalysis.[38-41] Our group used BSA as a model protein for a study of the interactions between RChitin films and proteins, and showed that BSA formed a monolayer ($\Gamma_{QCM\text{-}D}$ = 3.6 ± 0.1 mg·m$^{-2}$) on RChitin surfaces.[1] The value of $\Gamma_{QCM\text{-}D}$ for BSA adsorption onto RChitin films was independent of film thickness. Higher BSA loading because of a large accessible surface area for the porous Chitin NC films was expected. Data from QCM-D studies of BSA adsorption onto Chitin NC films with different thicknesses are provided in **Figure 5.7**. Compared to a RChitin film, BSA showed greater adsorption onto Chitin NC films than RChitin films, and the amount of adsorption was dependent upon the film thickness. The adsorption of BSA onto Chitin NC films with a film thickness of 13.7 ± 0.8 nm yielded $\Delta f/n$ = -75 ± 2 Hz via QCM-D, or $\Gamma_{QCM\text{-}D}$ = 13.3 ± 0.4 mg·m$^{-2}$

according to the Sauerbrey Equation (Equation 3.1). For a thicker Chitin NC film (16.8 ± 0.5 nm), $\Gamma_{QCM\text{-}D}$ increased to 15.0 ± 0.5 mg·m$^{-2}$. After rinsing with water, the amount of BSA on the Chitin NC films was not significantly different from the amount of BSA present prior to rinsing (i.e. BSA adsorption was irreversible). These results were consistent with porous Chitin NC films. Furthermore, Δ*D* profiles in **Figure 5.7** almost instantaneously plateaued after the injection of BSA solution. These Δ*D* changes associated with BSA adsorption are much smaller than those observed for chitinase adsorption (**Figure 5.6**) and did not grow with time. These results show that protein adsorption alone is insufficient to swell a Chitin NC film and that the Δ*D* profile in **Figure 5.6** is a consequence of both adsorption and catalytic activity.

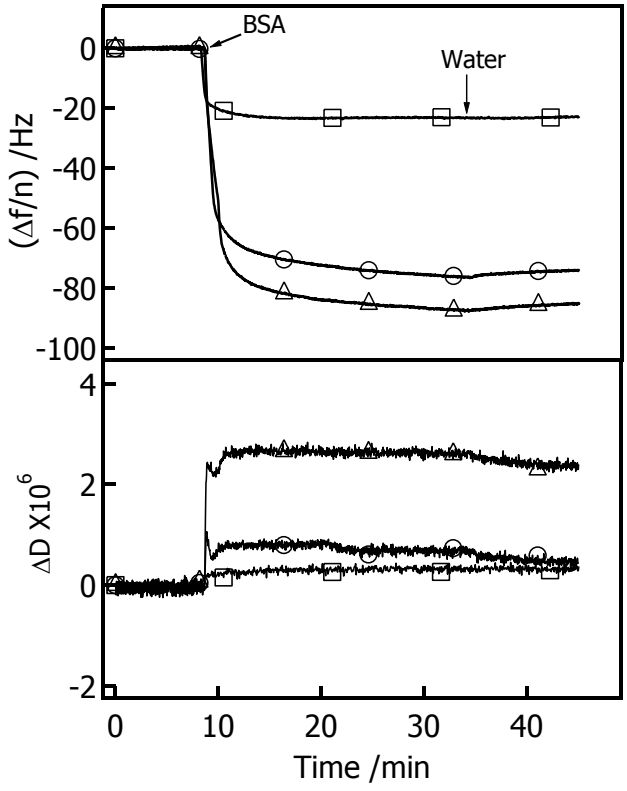


**Figure 5.7.** Representative Δ*f*/*n* and Δ*D* versus time for BSA (100 mg·L$^{-1}$) adsorption onto (□) RChitin, (○) Chitin NC (13.7 ± 0.8 nm) and (Δ) Chitin NC (16.8 ± 0.5 nm) films at 25 °C. Curves correspond to the fifth overtone.

## 5.5 Conclusions

This work provides a simple method for the preparation of nanocrystalline chitin thin films by spincoating from aqueous colloidal nanocrystalline chitin suspensions onto SAM-$NH_2$ coated gold surfaces. The morphology and crystallinity index of the chitin nanocrystals were determined by AFM and XRD. Images obtained from AFM confirmed that Chitin NC films were reasonably smooth and homogeneous, while QCM-D solvent exchange experiments demonstrated that Chitin NC films had twice as much water as RChitin films of similar thickness. Data for the enzymatic degradation of Chitin NC films from QCM-D revealed much slower hydrolysis of Chitin NC films than amorphous RChitin films. The $\Delta D$ profiles from QCM-D were consistent with chitinase induced enhancement of the swelling of Chitin NC films. Studies of BSA adsorption onto Chitin NC films showed Chitin NC films had higher protein loading capacities than RChitin films, an indication that Chitin NC films have potential as biocompatible supports for biological sensors and catalysts.

## 5.6 References

(1) Kittle, J. D.; Wang, C.; Qian, C.; Zhang, Y.; Zhang, M.; Roman, M.; Morris, J. R.; Moore, R. B.; Esker, A. R. *Biomacromolecules* **2012,** 13, 714-718.

(2) Wang, C.; Kittle, J. D.; Qian, C.; Roman, M.; Esker, A. R. *Biomacromolecules* **2013,** 14, 2622-2628.

(3) Ahola, S.; Salmi, J.; Johansson, L. S.; Laine, J.; Österberg, M. *Biomacromolecules* **2008,** 9, 1273-1282.

(4) Edgar, C.; Gray, D. *Cellulose* **2003,** 10, 299-306.

(5) Eriksson, J.; Malmsten, M.; Tiberg, F.; Callisen, T. H.; Damhus, T.; Johansen, K. S. *J. Colloid Interface Sci.* **2005,** 284, 99-106.

(6) Fält, S.; Wågberg, L.; Vesterlind, E. L.; Larsson, P. T. *Cellulose* **2004,** 11, 151-162.

(7) Gunnars, S.; Wågberg, L.; Cohen Stuart, M. A. *Cellulose* **2003,** 10, 185-185.

(8) Habibi, Y.; Foulon, L.; Aguié-Béghin, V.; Molinari, M.; Douillard, R. *J. Colloid Interface Sci.* **2007,** 316, 388-397.

(9) Kontturi, E.; Tammelin, T.; Osterberg, M. *Chem. Soc. Rev.* **2006,** 35, 1287-1304.

(10) Kontturi, E.; Thüne, P. C.; Niemantsverdriet, J. W. *Langmuir* **2003,** 19, 5735-5741.

(11) Roman, M. Model Cellulosic Surfaces: History and Recent Advances. In *Model Cellulosic Surfaces*, American Chemical Society: 2009; Vol. 1019, pp 3-53.

(12) Schaub, M.; Wenz, G.; Wegner, G.; Stein, A.; Klemm, D. *Adv. Mater.* **1993,** 5, 919-922.

(13) Yokota, S.; Kitaoka, T.; Sugiyama, J.; Wariishi, H. *Adv. Mater.* **2007,** 19, 3368-3370.

(14) Habibi, Y.; Lucia, L. A.; Rojas, O. J. *Chem. Rev.* **2010,** 110, 3479-3500.

(15) Zeng, J.-B.; He, Y.-S.; Li, S.-L.; Wang, Y.-Z. *Biomacromolecules* **2012,** 13, 1-11.

(16) Goodrich, J. D.; Winter, W. T. *Biomacromolecules* **2007,** 8, 252-257.

(17) Tzoumaki, M. V.; Moschakis, T.; Biliaderis, C. G. *Biomacromolecules* **2010,** 11, 175-181.

(18) Fan, Y.; Saito, T.; Isogai, A. *Biomacromolecules* **2008,** 9, 192-198.

(19) Berger, L. R.; Reynold, D. M. *Biochim. Biophys. Acta* **1958,** 29, 522-534.

(20) Kittle, J. D.; Du, X.; Jiang, F.; Qian, C.; Heinze, T.; Roman, M.; Esker, A. R. *Biomacromolecules* **2011,** 12, 2881-2887.

(21) Minke, R.; Blackwell, J. *J. Mol. Biol.* **1978,** 120, 167-181.

(22) Schiffman, J. D.; Stulga, L. A.; Schauer, C. L. *Polym. Eng. Sci.* **2009,** 49, 1918-1928.

(23) Zhang, Y.; Xue, C.; Li, Z.; Zhang, Y.; Fu, X. *Carbohydr. Polym.* **2006,** 65, 229-234.

(24) Lefebvre, J.; Gray, D. *Cellulose* **2005,** 12, 127-134.

(25) Jiang, F.; Esker, A. R.; Roman, M. *Langmuir* **2010,** 26, 17919-17925.

(26) Kawaguchi, T.; Nakahara, H.; Fukuda, K. *Thin Solid Films* **1985,** 133, 29-38.

(27) Ahola, S.; Turon, X.; Österberg, M.; Laine, J.; Rojas, O. J. *Langmuir* **2008,** 24, 11592-11599.

(28) Fan, L. T.; Lee, Y.-H.; Beardmore, D. H. *Biotechnol. Bioeng.* **1980,** 22, 177-199.

(29) Hall, M.; Bansal, P.; Lee, J. H.; Realff, M. J.; Bommarius, A. S. *FEBS J.* **2010,** 277, 1571-1582.

(30) Kikkawa, Y.; Abe, H.; Iwata, T.; Inoue, Y.; Doi, Y. *Biomacromolecules* **2002,** 3, 350-356.

(31) Kumagai, Y.; Kanesawa, Y.; Doi, Y. *Makromol. Chem.* **1992,** 193, 53-57.

(32) Lee, S. B.; Kim, I. H.; Ryu, D. D. Y.; Taguchi, H. *Biotechnol. Bioeng.* **1983,** 25, 33-51.

(33) Jollès, P.; Muzzarelli, R. A. A., *Chitin and Chitinases*. Birkhäuser Basel: 1999.

(34) Josefsson, P.; Henriksson, G.; Wågberg, L. *Biomacromolecules* **2008,** 9, 249-254.

(35) Cheng, G.; Liu, Z.; Murton, J. K.; Jablin, M.; Dubey, M.; Majewski, J.; Halbert, C.; Browning, J.; Ankner, J.; Akgun, B.; Wang, C.; Esker, A. R.; Sale, K. L.; Simmons, B. A.; Kent, M. S. *Biomacromolecules* **2011,** 12, 2216-2224.

(36) Cheng, G.; Datta, S.; Liu, Z.; Wang, C.; Murton, J. K.; Brown, P. A.; Jablin, M. S.; Dubey, M.; Majewski, J.; Halbert, C. E.; Browning, J. F.; Esker, A. R.; Watson, B. J.; Zhang, H.; Hutcheson, S. W.; Huber, D. L.; Sale, K. L.; Simmons, B. A.; Kent, M. S. *Langmuir* **2012,** 28, 8348-8358.

(37) Cai, H.; Dave, V.; Gross, R. A.; McCarthy, S. P. *J. Polym. Sci., Part B: Polym. Phys.* **1996,** 34, 2701-2708.

(38) Krajewska, B. *Enzyme Microb. Technol.* **2004,** 35, 126-139.

(39) Muzzarelli, R. A. A. *Enzyme Microb. Technol.* **1980,** 2, 177-184.

(40) Ohashi, E.; Karube, I. *J. Biotechnol.* **1995,** 40, 13-19.

(41) Ohashi, E.; Koriyama, T. *Anal. Chim. Acta* **1992,** 262, 19-25.

# Chapter 6: Amorphous Cellulose and Chitin Thin Films and Their Interactions with Human Plasma Proteins

## 6.1 Abstract

Cellulose and chitin are among the most abundant and commonly used natural biomaterials. In this work, the interactions of cellulose and chitin with two human plasma proteins, serum albumin (HSA) and fibrinogen (HFN), were studied by surface plasmon resonance (SPR) and a quartz crystal microbalance with dissipation monitoring (QCM-D). Regenerated cellulose (RC) and chitin (RChitin) thin films were used as model surfaces for cellulose and chitin based biomaterials. Studies by SPR indicated that the adsorption of HSA and HFN formed close-packed monolayers on bare gold surfaces and sub-monolayers on RC and RChitin surfaces, and the adsorption affinity for HSA adsorption onto polysaccharide surfaces was greater than that of HFN. Results from QCM-D and SPR showed that the proteins adsorbed onto polysaccharide surfaces had more associated water than proteins adsorbed onto bare gold surfaces.

## 6.2 Introduction

As the two most abundant natural polymers on earth, cellulose and chitin have attracted increasing attention as a source of functional biomaterials because of their biodegradability and biocompatibility. In the past two decades, a variety of drug carriers,[1-4] gene vectors,[5-7] tissue engineering scaffolds,[8-11] wound healing dressings[12-14] and molecular imaging agents[3, 15, 16] have been fabricated based upon cellulose, chitin and their derivatives.

When biomaterials are implanted into the human body, the soluble proteins in physiological fluids (e.g., plasma and interstitial fluid) usually adsorb onto the biomaterial surfaces rapidly.

Living cells then interact with the adsorbed protein layers instead of the biomaterial surfaces themselves since they move much more slowly than proteins.[17] The interactions between biomaterial surfaces and proteins play essential roles in regulating cell adhesion and triggering inflammatory responses (e.g., thrombosis coagulation and leukocyte activation).[17-19] Therefore, protein-surface interactions are fundamentally important for the design and development of biomaterials and biomedical devices. In the past several decades, many efforts have been made to reduce non-specific protein adsorption via the surface modification of biomaterials with hydrophilic (e.g., polyethylene oxide (PEO)) or zwitterionic (e.g., phosphorylcholine-containing polymers) materials and to promote specific protein adsorption via surface modification with bioactive molecules.[19, 20]

Serum albumin and fibrinogen are among the major proteins in human blood plasma. Human serum albumin (HSA) is most abundant in human blood plasma and is also found in other body fluids. Synthesized in the liver, HSA is a single-chain protein with a molar mass ~ 67 kDa and isoelectric point (pI) of ~ 4.7.[21] In plasma, HSA has a high concentration (typically 35 to 50 $g \cdot L^{-1}$) and plays crucial roles in maintaining the oncotic pressure in blood and transporting hormones, fatty acids, nitric oxide, drugs and many other molecules with low water solubility.[21] Another important role is the ability to inhibit the adhesion of platelets in blood.[22] Human fibrinogen (HFN) is also produced in the liver, and is a glycoprotein with a molar mass ~ 340 kDa and pI ~ 5.5.[21] During blood coagulation, fibrinogen is converted to fibrin by a serine protease, thrombin. Fibrin is then cross-linked by fibrin stabilizing factor (factor XIII) and combined with platelets to form an insoluble blood clot. The normal concentration of fibrinogen in human plasma is 1.5 to 4.0 $g \cdot L^{-1}$.[21]

The adsorption of plasma proteins, especially HSA and HFN, has been studied extensively for their roles in blood coagulation and thrombosis. A large number of techniques, including surface plasmon resonance (SPR),[23-25] ellipsometry,[26-28] quartz crystal microbalance with dissipation monitoring (QCM-D),[29-31] atomic force microscopy (AFM),[32, 33] total internal-reflection fluorescence (TIRF)[34, 35] and optical waveguide lightmode spectroscopy (OWLS)[36, 37] have been applied to investigate protein adsorption onto both natural and synthetic materials. Among those techniques, SPR and QCM-D are among the most sensitive and widely used tools to monitor the adsorption process onto planar surfaces in a real-time and label-free manner.[38] Smooth cellulose thin films have been prepared by spincoating cellulose from dimethylacetamide (DMAc)/LiCl[39, 40] and *N*-methylmorpholine-*N*-oxide (NMMO)/dimethyl sulfoxide (DMSO) solutions,[41, 42] or by regeneration from trimethylsilyl cellulose (TMSC) thin films.[43, 44] Recently, our group reported a simple method to prepare smooth and homogeneous chitin thin films via regeneration from trimethylsilyl chitin (TMSChitin) thin films in the presence of hydrochloric acid vapor.[45] The successful preparation of smooth cellulose and chitin thin films provides good model substrates for SPR and QCM-D to study the adsorption of plasma proteins onto the two most abundant and commonly used natural biomaterials.

In this work, the adsorption of HSA and HFN onto gold and amorphous cellulose and chitin surfaces from phosphate buffer was probed via SPR and QCM-D. Adsorption isotherms for HSA and HFN adsorption onto amorphous cellulose and chitin surfaces under biomimetic conditions of 37°C and pH = 7.4 were obtained from SPR measurements. Water contents of the adsorbed proteins on bare gold, cellulose and chitin surfaces were determined by SPR and QCM-D. This information is expected to provide fundamental insight into the interactions between human plasma proteins and biomaterials based upon cellulose, chitin and their derivatives.

## 6.3 Experimental

Microcrystalline cellulose (Avicel, PH-101, Fluka) was purchased from Sigma-Aldrich, and was converted to TMSC (degree of substitution (DS) = 2.9) as outlined in Chapter 3.1.2. $\alpha$-Chitin from shrimp shells (> 95% acetylated) was purchased from Sigma-Aldrich, and was converted to TMSChitin (DS = 2.0) as outlined in Chapter 3.1.3. Human serum albumin (lyophilized powder, fatty acid and globulin free) and human fibrinogen (≥ 80% of protein is clottable) were purchased from Sigma-Aldrich and used as received. Sodium phosphate monobasic monohydrate and sodium phosphate dibasic heptahydrate were purchased from Sigma-Aldrich and used as received to prepare 50 mM, pH = 7.4 buffer. All other chemicals and solvents were obtained from Fisher Scientific and used as received. Ultrapure water with a resistivity of 18 MΩ·cm and < 5 ppb inorganic impurities was used in all experiments (Milli-QGradient A-10, Millipore).

The AFM and ellipsometry measurements were performed as outlined in Chapter 3.5. All SPR measurements were conducted as outlined in Chapter 3.5.5, with the following details specific to this work. After the SPR sensor slide was placed in the SPR flow cell, buffer (incubated in a water bath at 37 °C) was introduced into the flow cell at a flow rate of 0.200 $mL \cdot min^{-1}$ for 1 to 2 h at 37 °C until a stable baseline was obtained. Degassed protein solutions (incubated in a water bath at 37 °C) with different concentrations were then pumped into the flow cell at the same flow rate and temperature. Protein solution flowed over the sensor for ~ 80 min until equilibrium adsorption was obtained. At the end of the measurement, buffer was typically flowed through the system for the removal of the reversibly adsorbed proteins.

All QCM-D measurements were conducted as outlined in Chapter 3.5.4, with the following details specific to this work. The QCM-D sensor was placed in a flow cell and allowed to

equilibrate for 1 to 2 h in pH = 7.4 buffer to obtain a stable baseline at 37 °C. Protein solutions (100 $mg \cdot L^{-1}$) solutions were then introduced at a rate of 0.200 $mL \cdot min^{-1}$ until equilibrium adsorption was obtained. At the end of the measurement, buffer was flowed through the system for the removal of reversibly adsorbed proteins.

## 6.4 Results and Discussion

### 6.4.1 Amorphous Cellulose and Chitin Thin Films

Morphologies of the RC and RChitin thin films were investigated by AFM, and representative AFM height images are shown in **Figure 6.1**. As seen in **Figure 6.1**, both RC and RChitin films were smooth and uniform, with RMS roughnesses of ~ 1.6 nm and ~ 1.3 nm, respectively. Both RC and RChitin films were determined to be amorphous,[45, 46] although natural cellulose and chitin are highly crystalline. The use of amorphous cellulose and chitin films is motivated by the facts that the dissolution or chemical modification of cellulose and chitin during the preparation of biomaterials usually leads to an increase of the amorphous content.

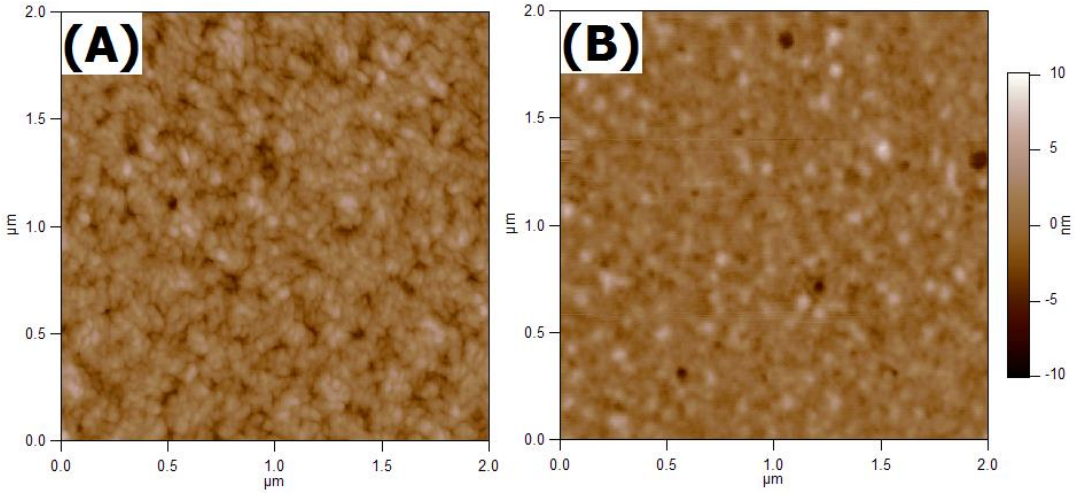


**Figure 6.1.** Representative 2 µm × 2 µm AFM height images of (A) RC and (B) RChitin films on SPR sensors. RMS roughnesses for the images are: (A) ~ 1.6 nm and (B) ~ 1.3 nm.

### 6.4.2 Adsorption of HSA and HFN onto RC and RChitin Surfaces

The structure of HSA is asymmetric and heart-shaped with six helical subdomains.[21, 47] The known size (the size of the smallest box that could contain the protein) of a HSA molecule is about 8 × 8.7 × 6 $nm^3$.[36] Therefore the approximate surface contact areas are ~ 70 $nm^2$ for a side-on orientation, and ~ 48 $nm^2$ for an end-on orientation. These values correspond to theoretical close-packed surface coverages of ~ 1.6 $mg \cdot m^{-2}$ and ~ 2.3 $mg \cdot m^{-2}$, respectively, in the absence of conformational rearrangement.[36] The structure of HFN is elongated and contains two sets of three non-identical polypeptide chains ($\alpha$, $\beta$ and $\gamma$) connected by disulfide bridges.[21, 32] The known size of HFN is about 45 × 9 × 6 $nm^3$.[36] Thus, the approximate surface contact areas are ~405 $nm^2$ for a side-on orientation, and ~ 54 $nm^2$ for an end-on orientation, which correspond to theoretical close-packed surface coverages of ~ 1.4 $mg \cdot m^{-2}$ and ~ 10.5 $mg \cdot m^{-2}$, respectively, in the absence of conformational rearrangement.[36]

Representative SPR data for HSA and HFN adsorption from 100 $mg \cdot L^{-1}$ solutions onto bare gold, RC and RChitin surfaces are shown in **Figure 6.2**. As seen in **Figure 6.2**, most of the adsorption was irreversible as rinsing with fresh buffer hardly altered the surface concentration derived from SPR experiments ($\Gamma_{SPR}$). The adsorption of HSA and HFN onto gold surfaces yielded irreversible $\Gamma_{SPR}$ of 1.5 ± 0.2 $mg \cdot m^{-2}$ and 1.9 ± 0.1 $mg \cdot m^{-2}$, respectively. Values of $\Gamma_{SPR}$ for HSA adsorption onto gold surfaces agreed with the theoretical surface coverage value for a close-packed HSA monolayer with a side-on orientation, and the $\Gamma_{SPR}$ for HFN adsorption is slightly larger than the surface coverage value for a close-packed HFN monolayer with a side-on orientation. The $\Gamma_{SPR}$ for HFN adsorption may indicate that HFN adsorbs onto gold as a mixture of side-on and end-on orientations, with a dominant side-on orientation.

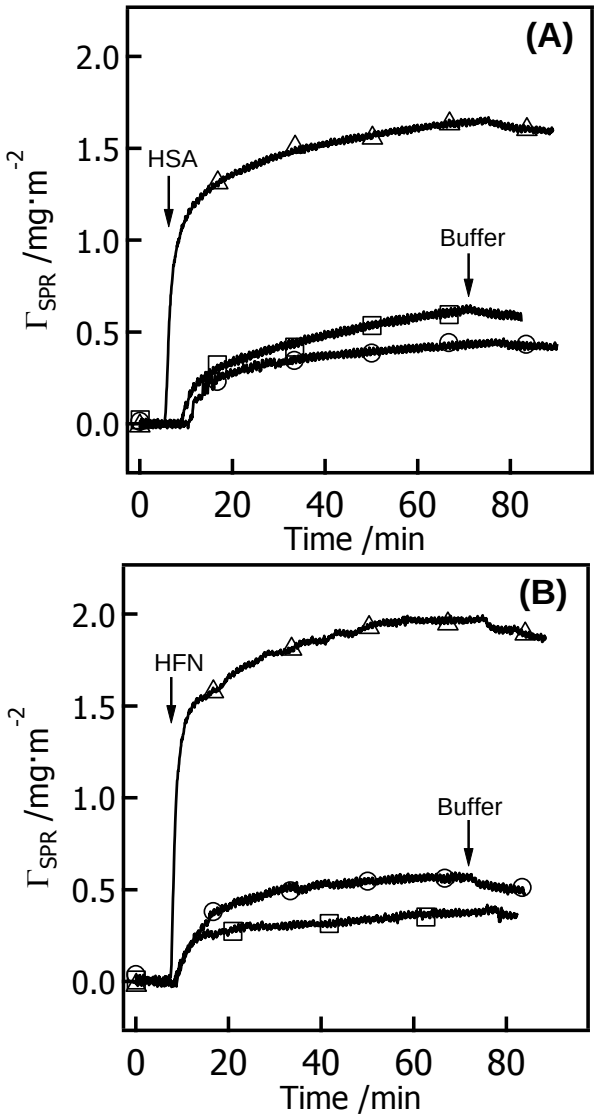


**Figure 6.2.** Representative $\Gamma_{SPR}$ versus time for the adsorption of (A) HSA and (B) HFN onto (Δ) gold, (○) RC and (□) RChitin surfaces from 100 mg·L$^{-1}$ solutions in buffer (pH = 7.4) at 37 °C.

As seen in **Figure 6.2A**, the adsorption of HSA onto RC and RChitin surfaces yielded irreversible $\Gamma_{SPR}$ of 0.44 ± 0.02 mg·m$^{-2}$ and 0.58 ± 0.02 mg·m$^{-2}$, respectively. As seen in **Figure 6.2B**, the adsorption of HFN onto RC and RChitin surfaces yielded irreversible $\Gamma_{SPR}$ of 0.50 ± 0.02 mg·m$^{-2}$ and 0.36 ± 0.01 mg·m$^{-2}$, respectively. The $\Gamma_{SPR}$ values for HSA and HFN adsorption onto both RC and RChitin surfaces are lower than their corresponding $\Gamma_{SPR}$ values for gold

surfaces or the corresponding theoretical values for close-packed protein monolayers. Orelma et al.[48] studied the adsorption of bovine serum albumin (BSA, ~ 66 kDa, structurally and dimensionally similar to HSA) onto Langmuir-Schaeffer deposited RC surfaces via SPR and found that the adsorption of BSA from 100 $mg \cdot L^{-1}$ phosphate buffer (pH = 7.4) solution onto the RC surfaces yielded $\Gamma_{SPR}$ of ~ 0.30 $mg \cdot m^{-2}$ at 25 °C. Kittle et al.[45] studied the adsorption of BSA onto RChitin surfaces via SPR and the results showed that the BSA adsorption from 100 $mg \cdot L^{-1}$ aqueous solution onto RChitin surface yielded $\Gamma_{SPR}$ of ~ 0.78 $mg \cdot m^{-2}$ at 25 °C. Those values are comparable to the $\Gamma_{SPR}$ values obtained in this study for HSA adsorption onto RC and RChitin surfaces, although the temperatures and solvents are not identical. Very few studies about the adsorption of fibrinogen onto cellulose or chitin surfaces have been reported. In 1993, Brash et al.[49] studied the adsorption of $^{125}$I-labelled HFN onto cellulose films (laboratory dialysis tubing with a thickness of ~ 0.05 mm) from pH = 7.4 tris(hydroxymethyl)aminomethane buffer at room temperature. The surface concentration of the adsorbed fibrinogen from 100 $mg \cdot L^{-1}$ buffer was determined to be ~ 0.8 $mg \cdot m^{-2}$ (0.08 $\mu g \cdot cm^{-2}$). Rodrigues et al.[50] also used $^{125}$I-labelled HFN to investigate the adsorption of HFN onto hydroxyl terminated self-assembled monolayers (SAMs) and the results showed that HFN adsorption from 100 $mg \cdot L^{-1}$ phosphate buffer onto hydroxyl terminated SAM surfaces yielded a surface concentration of ~ 1.5 $mg \cdot m^{-2}$. Those values are also of the same magnitude as the $\Gamma_{SPR}$ value for HFN adsorption onto RC surfaces found in this study.

The SPR results in **Figure 6.2** indicated that it was possible to reduce the non-specific protein adsorption seen for gold surfaces via polysaccharide modification or coatings. Previous protein adsorption studies concluded that more water was bound to the more hydrophilic polymer (e.g., polysaccharides) surfaces, and the hydration layer provided an energetic barrier for the

prevention of protein adsorption.[19] Although many hydrophilic polymers can reduce non-specific protein adsorption to some extent, hydrophilic polymers with flexible chain structures, such as PEO and zwitterionic polymers, are usually better candidates as protein resistant surfaces.[20] For instance, Liu et al.[51] modified commercially available cellulose membranes (CM) with zwitterionic brushes by grafting poly [*N*,*N*-dimethyl-*N*-(*p*-vinylbenzyl)-*N*-(3-sulfopropyl) ammonium] onto CM via surface-initiated atomic transfer radical polymerization and studied protein adsorption from platelet-poor plasma onto both bare CM and the modified CMs at 37 °C. The results showed that the surface concentration for protein adsorption decreased from ~ 20 $mg \cdot m^{-2}$ for bare CM to less than 10 $mg \cdot m^{-2}$ for the modified CMs. The protein resistant behavior of PEO and zwitterionic polymers is attributed to both the steric repulsion caused by the flexible chains and the formation of a surface hydration layer.[19, 20] Ostuni et al.[24, 25] investigated protein adsorption onto different SAMs via SPR, and summarized the attributes of groups with the most resistance as hydrophilic, hydrogen-bond acceptors but not hydrogen-bond donors and overall charge neutral.

### 6.4.3 Adsorption Isotherms for HSA and HFN Adsorption onto RC and RChitin Surfaces

Adsorption isotherms from SPR for HSA adsorption onto RC and RChitin surfaces are shown in **Figure 6.3**, and adsorption isotherms for HFN adsorption onto RC and RChitin surfaces are shown in **Figure 6.4**. Representative data for each isotherm data point are provided in **Figure 6.5**. Both RC and RChitin surfaces are neutral, and both HSA and HFN have a net negative charge at pH = 7.4.

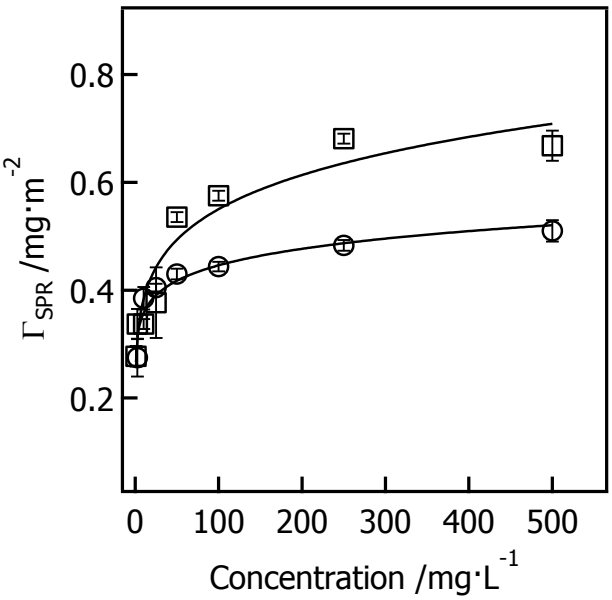


**Figure 6.3.** Adsorption isotherms from SPR for HSA adsorption onto (○) RC and (□) RChitin surfaces from buffer (pH = 7.4) at 37 °C. Solid lines represent fits with Freundlich isotherms.

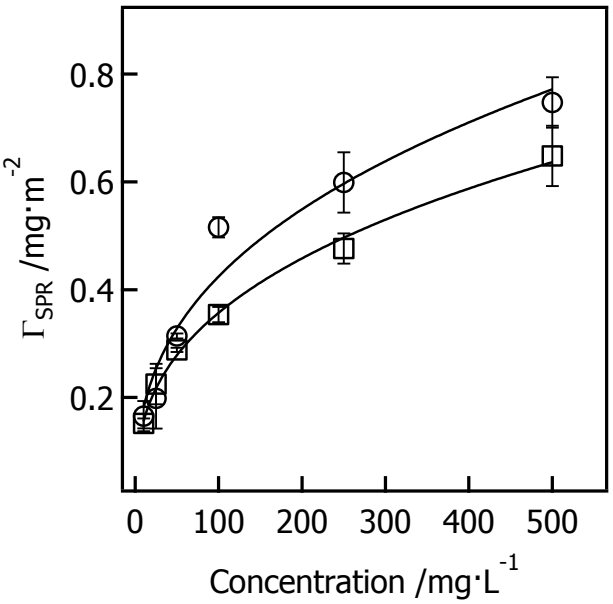


**Figure 6.4.** Adsorption isotherms from SPR for HFN adsorption onto (○) RC and (□) RChitin surfaces from buffer (pH = 7.4) at 37 °C. Solid lines represent fits with Freundlich isotherms.

Langmuir and Freundlich isotherm models have been widely used to fit protein adsorption data even though the assumptions of these models may not strictly apply. The Langmuir isotherm was introduced by Langmuir to describe the adsorption of gas molecules onto homogeneous solid surfaces.[52] The Langmuir isotherm assumes that gas molecules adsorb onto a perfectly flat surface with equivalent and independent binding sites, and with a maximum surface coverage of a monolayer. The Langmuir isotherm is given as:

$$\Gamma = \frac{\Gamma_m K_L c}{1 + K_L c} \; or \; \frac{1}{\Gamma} = \frac{1}{\Gamma_m} + \left(\frac{1}{\Gamma_m K_L}\right)\frac{1}{c} \tag{6.1}$$

where, $K_L$ is the Langmuir constant, the ratio of the adsorption rate constant ($k_{ads}$) to the desorption rate constant ($k_{des}$), $\Gamma_m$ is the maximum surface concentration and $c$ is the bulk concentration of the adsorbate. Compared to gas adsorption onto solid substrates, the adsorption of proteins or polymers onto solid surfaces is usually irreversible and exceeds monolayer coverage. Nonetheless, the high affinity isotherms of proteins and polymers sometimes are reasonably fit by the Langmuir model. On the other hand, a semi-empirical Freundlich isotherm is often used to describe heterogeneous adsorption. The Freundlich isotherm is given as:[53]

$$\Gamma = K_F c^{1/n_f} \; or \; ln\,\Gamma = lnK_F + (1/n_f)lnc \tag{6.2}$$

where, $K_F$ is the adsorbent capacity, $1/n_f$ is the adsorption affinity constant, the adsorption affinity is greater for smaller values of $1/n_f$,, and $c$ is the bulk concentration of the adsorbate.

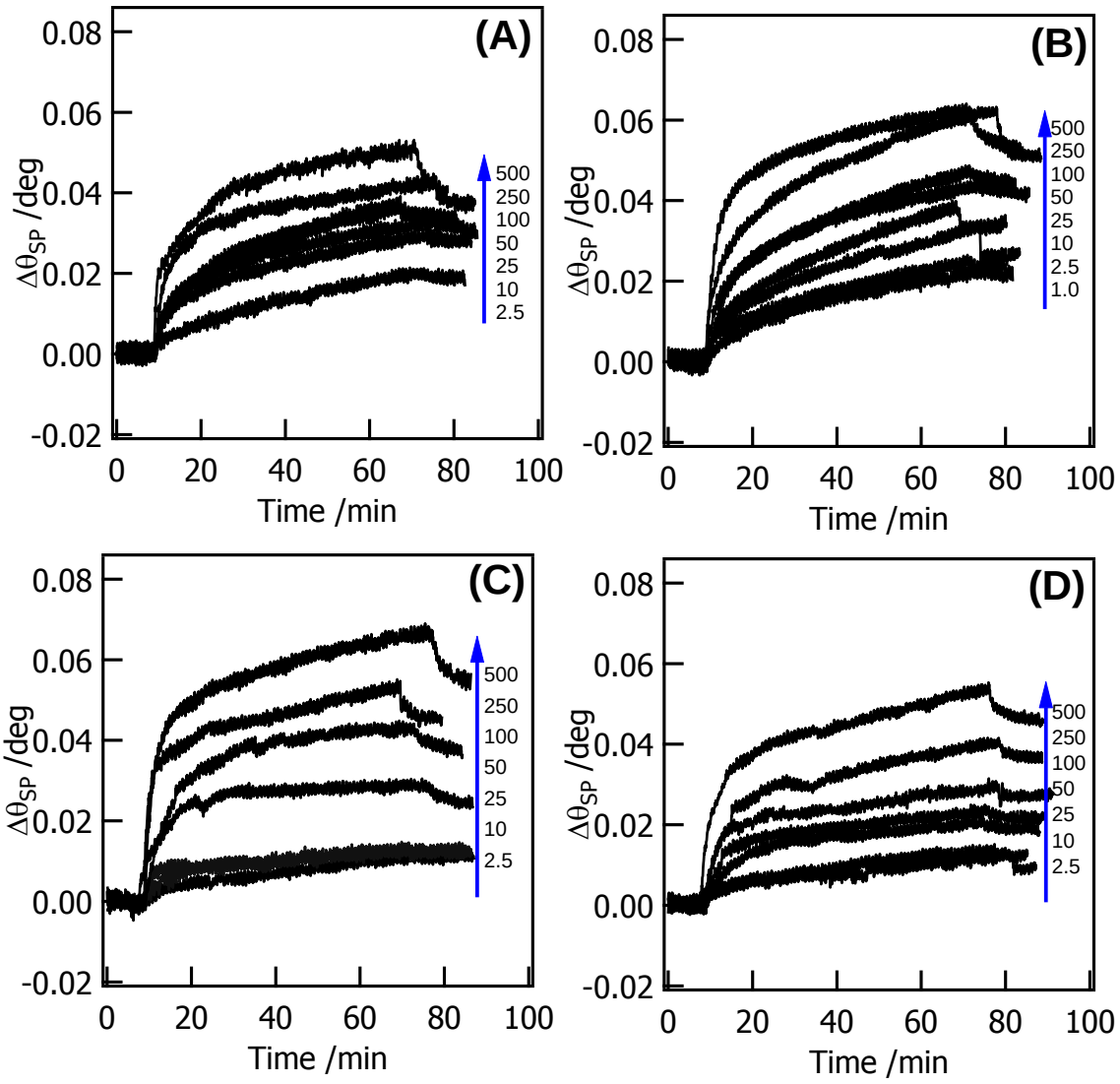


**Figure 6.5.** Representative SPR data for the adsorption of (A) HSA onto RC surfaces, (B) HSA onto RChitin surfaces, (C) HFN onto RC surfaces and (D) HFN onto RChitin surfaces from solutions of different concentration at 37 °C, pH = 7.4. The numbers in the figures indicate the concentrations of each measurement in units of $mg \cdot L^{-1}$.

As HFN adsorption onto RC and RChitin surfaces did not plateau, i.e., reach a maximum adsorption ($\Gamma_m$) for the concentrations probed, Freundlich isotherms were used to fit $\Gamma_{SPR}$ data for HSA and HFN adsorption onto RC and RChitin surfaces. Fitting parameters from the Freundlich isotherms are summarized in **Table 6.1**. As seen from **Table 6.1**, the adsorbent capacity ($K_F$) of

RChitin was slightly greater than that of RC for HSA adsorption, whereas $K_F$ of RC is slightly greater than that of RChitin for HFN adsorption. Values of $K_F$ also indicated that both RC and RChitin had greater adsorbent capacity for HSA than HFN. Values of $1/n_f$ showed that HSA had a slightly stronger preference for RChitin surfaces than RC surfaces, whereas HFN had an equivalent preference for RC or RChitin surfaces. Values of $1/n_f$ also revealed that the adsorption affinity of HSA for RC or RChitin surfaces was greater than that of HFN.

**Table 6.1.** Freundlich isotherm fitting parameters for HSA and HFN adsorption onto RC and RChitin surfaces as determined from SPR data.[a]

| | **HSA** | | **HFN** | |
|---|---|---|---|---|
| | $K_F$ **/L·mg$^{-1}$** | $1/n_f$ | $K_F$ **/L·mg$^{-1}$** | $1/n_f$ |
| **RC** | 0.27 ± 0.03 | 0.16 ± 0.02 | 0.077 ± 0.020 | 0.37 ± 0.05 |
| **RChitin** | 0.29 ± 0.02 | 0.10 ± 0.01 | 0.068 ± 0.005 | 0.36 ± 0.02 |

[a]Error bars represent ± one standard deviation

### 6.4.4 Water Contents of Adsorbed HSA and HFN Layers on RC and RChitin Surfaces

Adsorption experiments for HSA and HFN adsorption onto RC and RChitin surfaces were also performed by QCM-D. Representative QCM-D frequency data is provided in **Figure 6.6**. As seen from **Figure 6.6A**, the adsorption of HSA onto bare gold, RC and RChitin surfaces yielded irreversible $\Delta f/n \approx$ -34 ± 2, -25 ± 3 and -19 ± 1 Hz, or $\Gamma_{QCM}$ = 6.0 ± 0.3, 4.4 ± 0.6 and 3.3 ± 0.2 mg·m$^{-2}$, assuming the Sauerbrey equation (Equation 3.1) is valid. As seen from **Figure 6.6B**, the adsorption of HFN onto bare gold, RC and RChitin surfaces yielded irreversible $\Delta f/n \approx$ -66 ± 2, -48 ± 2 and -40 ± 4 Hz, or $\Gamma_{QCM}$ = 12 ± 1, 8.5 ± 0.2 and 7.2 ± 0.6 mg·m$^{-2}$, assuming the Sauerbrey equation (Equation 3.1) is valid. Differences in the viscoelastic properties of the

resulting protein layers are consistent with the Δ*D* profile (**Figure 6.7**). As seen from **Figure 6.7**, the Δ*D* values for protein adsorption onto bare gold, RC and RChitin surfaces were relatively small (~ $1 \times 10^{-6}$ for HSA adsorption and ~ $3 \times 10^{-6}$ for HFN adsorption), hence the Sauerbrey equation (Equation 3.1) is probably valid for the calculation of $\Gamma_{QCM}$.

**Table 6.2.** Water contents of HSA and HFN layers adsorbed onto gold, RC and RChitin surfaces from 100 mg·L$^{-1}$ solutions in buffer (pH = 7.4) at 37 °C.[a]

| Water Content /% | Gold | RC | RChitin |
|---|---|---|---|
| **HSA** | 78 ± 3 | 90 ± 2 | 84 ± 2 |
| **HFN** | 83 ± 1 | 95 ± 2 | 95 ± 1 |

[a]Error bars represent ± one standard deviation

As an acoustic technique, QCM-D measures both the adsorbed proteins and the water associated with the adsorbed layers. On the other hand, SPR is an optical technique and it is only sensitive to the mass of proteins. The greater $\Gamma_{QCM}$ values relative to $\Gamma_{SPR}$ was attributed to the water associated within the adsorbed proteins on solid surfaces. The water contents of the proteins adsorbed on different solid surfaces could be calculated from $\Gamma_{SPR}$ and $\Gamma_{QCM}$ assuming ideal solution behavior:[65]

$$\%\, Water = \left(1 - \frac{\Gamma_{SPR}}{\Gamma_{QCM}}\right) \times 100\% \qquad (6.3)$$

The water contents of the adsorbed HSA and HFN on bare gold, RC and RChitin surfaces from 100 mg·L$^{-1}$ solutions are shown in **Table 6.2**. As seen in **Table 6.2**, both HSA and HFN formed highly hydrated layers on bare gold, RC and RChitin surfaces. However, the water contents of adsorbed proteins on polysaccharide surfaces were greater than on bare gold surfaces. As

discussed previously, both HSA and HFN formed close-packed monolayers on gold surfaces and sub-monolayers on polysaccharide surfaces. The relatively greater water contents on polysaccharide surfaces are most likely caused by water trapped in the spaces between protein molecules in the sub-monolayer coverage films.

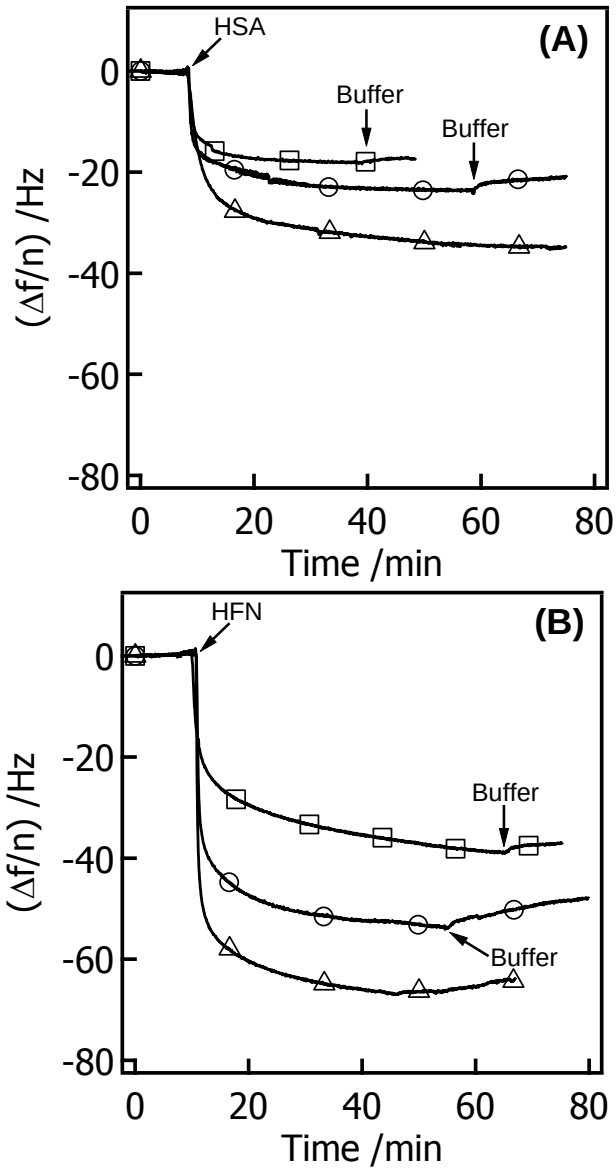


**Figure 6.6.** Representative Δ*f*/*n* versus time for (A) HSA and (B) HFN adsorption onto (Δ) gold, (○) RC and (□) RChitin surfaces from 100 mg·L$^{-1}$ solutions in buffer (pH = 7.4) at 37 °C.

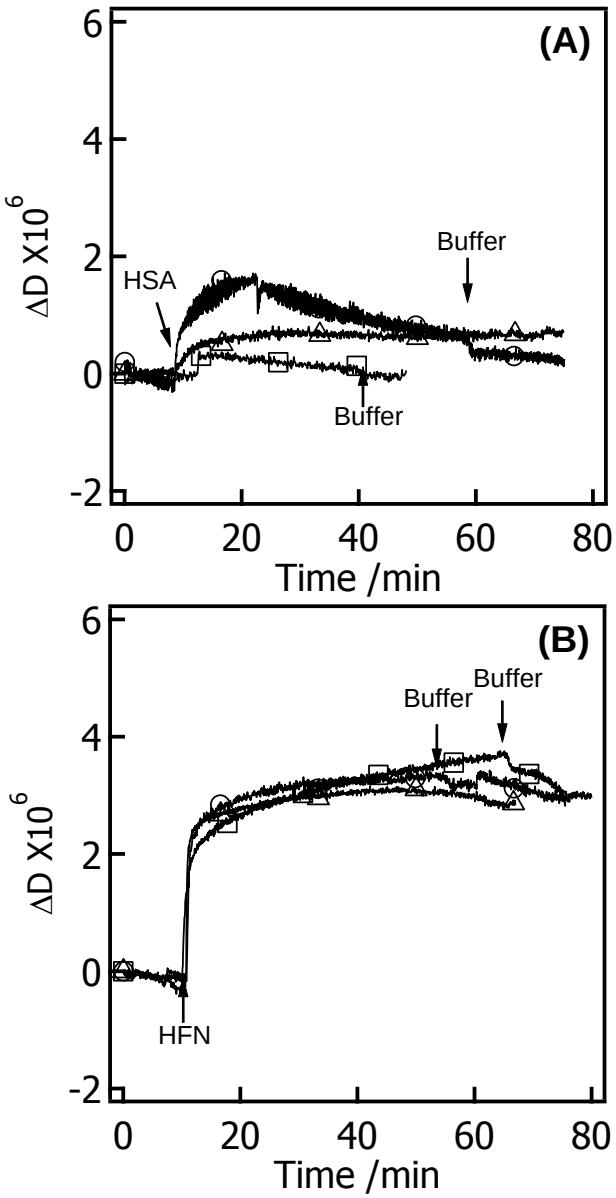


**Figure 6.7.** Representative Δ*D* versus time for (A) HSA and (B) HFN adsorption onto (Δ) gold, (○) RC and (□) RChitin surfaces from 100 mg·L$^{-1}$ solutions in buffer (pH = 7.4) at 37 °C.

## 6.5 Conclusions

The adsorption of two human plasma proteins, HSA and HFN, onto regenerated cellulose and chitin surfaces was investigated by SPR and QCM-D. Data from SPR showed that the adsorption of HSA and HFN formed close-packed monolayers on bare gold surfaces and the protein

adsorption was greatly reduced when gold surfaces were coated with cellulose or chitin. Adsorption isotherms for HSA and HFN adsorption onto RC and RChitin surfaces were determined by SPR and fitted with Freundlich adsorption isotherms. The data indicated that the two proteins did not show strong preferences for RC or RChitin surfaces; however, the adsorption affinity for HSA onto polysaccharide surfaces was greater than that of HFN. A combination of QCM-D and SPR data also showed that proteins adsorbed onto polysaccharide surfaces had more associated water than proteins adsorbed onto gold surfaces, which might be attributed to the water entrapped in the spaces between protein molecules in the sub-monolayer coverage films on polysaccharide surfaces. This information is expected to provide fundamental insight into the interactions of human plasma proteins with biomaterials based upon cellulose, chitin and their derivatives.

### 6.6 References


(1) Müller, A.; Ni, Z.; Hessler, N.; Wesarg, F.; Müller, F. A.; Kralisch, D.; Fischer, D. *J. Pharm. Sci.* **2013,** 102, 579-592.

(2) Edgar, K. J. *Cellulose* **2007,** 14, 49-64.

(3) Rejinold N, S.; Chennazhi, K. P.; Tamura, H.; Nair, S. V.; Rangasamy, J. *ACS Appl. Mater. Interfaces* **2011,** 3, 3654-3665.

(4) Agnihotri, S. A.; Mallikarjuna, N. N.; Aminabhavi, T. M. *J. Controlled Release* **2004,** 100, 5-28.

(5) Roy, K.; Mao, H.-Q.; Huang, S. K.; Leong, K. W. *Nat. Med.* **1999,** 5, 387-391.

(6) Sato, T.; Ishii, T.; Okahata, Y. *Biomaterials* **2001,** 22, 2075-2080.

(7) Borchard, G. *Adv. Drug Del. Rev.* **2001,** 52, 145-150.

(8) Svensson, A.; Nicklasson, E.; Harrah, T.; Panilaitis, B.; Kaplan, D. L.; Brittberg, M.; Gatenholm, P. *Biomaterials* **2005,** 26, 419-431.

(9) Müller, F. A.; Müller, L.; Hofmann, I.; Greil, P.; Wenzel, M. M.; Staudenmaier, R. *Biomaterials* **2006,** 27, 3955-3963.

(10) Freier, T.; Montenegro, R.; Shan Koh, H.; Shoichet, M. S. *Biomaterials* **2005,** 26, 4624-4632.

(11) Madihally, S. V.; Matthew, H. W. T. *Biomaterials* **1999,** 20, 1133-1142.

(12) Czaja, W.; Krystynowicz, A.; Bielecki, S.; Brown Jr, R. M. *Biomaterials* **2006,** 27, 145-151.

(13) Jayakumar, R.; Prabaharan, M.; Sudheesh Kumar, P. T.; Nair, S. V.; Tamura, H. *Biotechnol. Adv.* **2011,** 29, 322-337.

(14) Khor, E.; Lim, L. Y. *Biomaterials* **2003,** 24, 2339-2349.

(15) Agrawal, P.; Strijkers, G. J.; Nicolay, K. *Adv. Drug Del. Rev.* **2010,** 62, 42-58.

(16) Potara, M.; Boca, S.; Licarete, E.; Damert, A.; Alupei, M.-C.; Chiriac, M. T.; Popescu, O.; Schmidt, U.; Astilean, S. *Nanoscale* **2013,** 5, 6013-6022.

(17) Latour, R. A. Biomaterials: Protein-Surface Interactions. In *Encyclopedia of Biomaterials and Biomedical Engineering*, 2nd ed.; Wnek, G. E.; Bowlin, G. L., Eds.; Informa Healthcare: London, 2008; pp 270-284.

(18) Gray, J. J. *Curr. Opin. Struct. Biol.* **2004,** 14, 110-115.

(19) Chen, S.; Li, L.; Zhao, C.; Zheng, J. *Polymer* **2010,** 51, 5283-5293.

(20) Chen, H.; Yuan, L.; Song, W.; Wu, Z.; Li, D. *Prog. Polym. Sci.* **2008,** 33, 1059-1087.

(21) Schaller, J.; Gerber, S.; Kämpfer, U.; Lejon, S.; Trachsel, C. *Human Blood Plasma Proteins: Structure and Function*; John Wiley & Sons, Ltd: England, 2008.

(22) Sharma, N. C.; Mohammad, S. F.; Chuang, H. Y.; Mason, R. G. *Proc. Natl. Acad. Sci. U.S.A.* **1981,** 78, 7750-7753.

(23) Mrksich, M.; Sigal, G. B.; Whitesides, G. M. *Langmuir* **1995,** 11, 4383-4385.

(24) Chapman, R. G.; Ostuni, E.; Takayama, S.; Holmlin, R. E.; Yan, L.; Whitesides, G. M. *J. Am. Chem. Soc.* **2000,** 122, 8303-8304.

(25) Ostuni, E.; Chapman, R. G.; Holmlin, R. E.; Takayama, S.; Whitesides, G. M. *Langmuir* **2001,** 17, 5605-5620.

(26) Malmsten, M.; Muller, D.; Lassen, B. *J. Colloid Interface Sci.* **1997,** 193, 88-95.

(27) Malmsten, M. *J. Colloid Interface Sci.* **1994,** 166, 333-342.

(28) Warkentin, P.; Wälivaara, B.; Lundström, I.; Tengvall, P. *Biomaterials* **1994,** 15, 786-795.

(29) Roach, P.; Farrar, D.; Perry, C. C. *J. Am. Chem. Soc.* **2005,** 127, 8168-8173.

(30) Glasmästar, K.; Larsson, C.; Höök, F.; Kasemo, B. *J. Colloid Interface Sci.* **2002,** 246, 40-47.

(31) Rechendorff, K.; Hovgaard, M. B.; Foss, M.; Zhdanov, V. P.; Besenbacher, F. *Langmuir* **2006,** 22, 10885-10888.

(32) Cacciafesta, P.; Humphris, A. D. L.; Jandt, K. D.; Miles, M. J. *Langmuir* **2000,** 16, 8167-8175.

(33) Sheller, N. B.; Petrash, S.; Foster, M. D.; Tsukruk, V. V. *Langmuir* **1998,** 14, 4535-4544.

(34) Hlady, V.; Reinecke, D. R.; Andrade, J. D. *J. Colloid Interface Sci.* **1986,** 111, 555-569.

(35) Wertz, C. F.; Santore, M. M. *Langmuir* **1999,** 15, 8884-8894.

(36) Höök, F.; Vörös, J.; Rodahl, M.; Kurrat, R.; Böni, P.; Ramsden, J. J.; Textor, M.; Spencer, N. D.; Tengvall, P.; Gold, J.; Kasemo, B. *Colloids Surf., B: Biointerfaces* **2002,** 24, 155-170.

(37) Kurrat, R.; Wälivaara, B.; Marti, A.; Textor, M.; Tengvall, P.; Ramsden, J. J.; Spencer, N. D. *Colloids Surf., B: Biointerfaces* **1998,** 11, 187-201.

(38) Green, R. J.; Frazier, R. A.; Shakesheff, K. M.; Davies, M. C.; Roberts, C. J.; Tendler, S. J. B. *Biomaterials* **2000,** 21, 1823-1835.

(39) Aulin, C.; Ahola, S.; Josefsson, P.; Nishino, T.; Hirose, Y.; Österberg, M.; Wågberg, L. *Langmuir* **2009,** 25, 7675-7685.

(40) Eriksson, J.; Malmsten, M.; Tiberg, F.; Callisen, T. H.; Damhus, T.; Johansen, K. S. *J. Colloid Interface Sci.* **2005,** 284, 99-106.

(41) Hu, G.; Heitmann, J. A.; Rojas, O. J. *J. Phys. Chem. B* **2009,** 113, 14761-14768.

(42) Turon, X.; Rojas, O. J.; Deinhammer, R. S. *Langmuir* **2008,** 24, 3880-3887.

(43) Schaub, M.; Wenz, G.; Wegner, G.; Stein, A.; Klemm, D. *Adv. Mater.* **1993,** 5, 919-922.

(44) Kontturi, E.; Thüne, P. C.; Niemantsverdriet, J. W. *Langmuir* **2003,** 19, 5735-5741.

(45) Kittle, J. D.; Wang, C.; Qian, C.; Zhang, Y.; Zhang, M.; Roman, M.; Morris, J. R.; Moore, R. B.; Esker, A. R. *Biomacromolecules* **2012,** 13, 714-718.

(46) Kontturi, E.; Suchy, M.; Penttilä, P.; Jean, B.; Pirkkalainen, K.; Torkkeli, M.; Serimaa, R. *Biomacromolecules* **2011,** 12, 770-777.

(47) He, X. M.; Carter, D. C. *Nature* **1992,** 358, 209-215.

(48) Orelma, H.; Filpponen, I.; Johansson, L.-S.; Laine, J.; Rojas, O. J. *Biomacromolecules* **2011,** 12, 4311-4318.

(49) Brash, J. L.; Ten Hove, P. *J. Biomater. Sci. Polym. Ed.* **1993,** 4, 591-599.

(50) Rodrigues, S. N.; Gonçalves, I. C.; Martins, M. C. L.; Barbosa, M. A.; Ratner, B. D. *Biomaterials* **2006,** 27, 5357-5367.

(51) Liu, P.-S.; Chen, Q.; Liu, X.; Yuan, B.; Wu, S.-S.; Shen, J.; Lin, S.-C. *Biomacromolecules* **2009,** 10, 2809-2816.

(52) Langmuir, I. *J. Am. Chem. Soc.* **1918,** 40, 1361-1403.

(53) Kaggwa, G. B.; Froebe, S.; Huynh, L.; Ralston, J.; Bremmell, K. *Langmuir* **2005,** 21, 4695-4704.

# Chapter 7: Lignin Thin Films from Surface-initiated Dehydrogenative Polymerization of Monolignols

Published Chapter: Wang, C.; Qian, C.; Roman, M.; Glasser, W. G.; Esker, A. R. *Biomacromolecules* **2013**, 14 (11), 3964-3972.

## 7.1 Abstract

This work highlights a real-time and label-free method to monitor the dehydrogenative polymerization of monolignols initiated by horseradish peroxidase (HRP) physically immobilized on various surfaces using a quartz crystal microbalance with dissipation monitoring (QCM-D). The resulting dehydrogenative polymer (DHP) films provide good model substrates for ligninolytic enzymes (Chapter 8) and thus enable the application of surface science techniques to lignin biodegradation. The HRP was adsorbed onto gold or silica surfaces or onto and within porous desulfated nanocrystalline cellulose films from an aqueous solution. Surface-immobilized HRP retained its activity and selectivity for monolignols as coniferyl and *p*-coumaryl alcohol underwent dehydrogenative polymerization in the presence of hydrogen peroxide, whereas sinapyl alcohol also required the addition of a nucleophile for polymerization. The morphologies of the DHP layers formed on the surfaces were investigated via atomic force microscopy (AFM). Data from both QCM-D and AFM showed that the surface-immobilized HRP-initiated dehydrogenative polymerization of monolignols was greatly affected by the support surface, monolignol concentration, hydrogen peroxide concentration and temperature.

## 7.2 Introduction

Much of the current understanding about the polymerization mechanisms and bonding patterns of native lignin come from the study of dehydrogenative polymer (DHP), a model compound for native lignin. Normally, DHP is prepared by the *in vitro* polymerization of monolignols in the presence of horseradish peroxidase (HRP) and $H_2O_2$. Two synthetic procedures were reported by Freudenberg to prepare DHP, namely the Zutropfverfahren (ZT) and Zulaufverfahren (ZL) methods.[1] In the ZT method, separate solutions of monolignol and $H_2O_2$ are added slowly and continuously into a HRP solution, whereas the monolignol, HRP and $H_2O_2$ solutions are mixed simultaneously in the ZL method.[2] The "end-wise" DHP from the ZT procedure has a larger molar mass and a structure more similar to isolated wood lignin than the "bulk" DHP obtained from the ZL procedure. The DHP systems mimic the biosynthesis of native lignin in a simplified way by controlling the structure and the composition of the precursors,[3-6] polymerization conditions (*e.g.* pH,[7-9] solvent[10-12] and enzyme/monolignol ratio),[13] enzyme type,[14-17] the presence of cell wall components and soluble carbohydrates,[18-22] isotopic labeling[2, 23] and the presence of mediators.[24-26] The resulting DHPs also provide good substrates to study the biodegradation of lignin in the presence of various ligninolytic enzymes, enzymes which oxidatively produce reactive species capable of attacking chemical bonds in lignin.[27-29] On the other hand, DHP cannot fully mimic the structure of native lignin. Synthesized DHP has lower molar mass and a higher proportion of ether linkages (e.g. $\beta$-O-4) and end groups (15 ~ 40 %) than native lignin,[13, 30] although contradictory studies exist.[31, 32]

Most studies of the dehydrogenative polymerization of monolignols focus upon the molecular structure of the DHP obtained under different conditions, whereas reaction kinetics are rarely reported. One important reason for this bias is that the generation and coupling of the radicals are

usually fast, which makes it difficult to monitor the polymerization process. The quartz crystal microbalance with dissipation monitoring (QCM-D) is a highly sensitive technique that provides real-time and label-free monitoring of molecular adsorption on surfaces, enzymatic degradation of thin films and surface-initiated polymerizations. The QCM-D technique has been successfully used to study the polymerization kinetics of both natural and synthetic monomers, including the enzymatic polymerization of oligonucleotides[33] and a phenolic polymer extracted from a marine alga,[34] the interfacial fibrin polymerization of bovine insulin,[35] fibrinogen[36] and glucagon,[37] surface-initiated atom transfer radical polymerization of oligoethylene glycol methylmethacrylate,[38-40] methyl methacrylate,[40, 41] ethyl methacrylate,[40] [2-(methacryloyloxy) ethyl] trimethylammonium chloride[42] and a methacrylated benzo-15-crown-5 derivative,[43] and the photopolymerization of methacrylic acid.[44, 45]

In this work, the kinetics of dehydrogenative polymerization of monolignols initiated by HRP immobilized on various surfaces was monitored by QCM-D, while the morphologies of the resulting DHP thin films were investigated by atomic force microscopy (AFM). This information is expected to provide a convenient and sensitive method for the determination of the precursor preference and optimal conditions for peroxidases and other enzymes involved in lignification. The resulting DHP thin films are expected to provide good model substrates for various ligninolytic enzymes and thus open the door for the application of surface characterization techniques to lignin biodegradation.

### 7.3 Experimental

Monolignols were synthesized through a two-step reaction from their corresponding hydroxycinnamic acids as outlined in Chapter 3.3. Horseradish peroxidase (type I, lyophilized

powder, 50 ~ 150 units/mg solid) with a molar mass of ~ 44 kDa was purchased from Sigma-Aldrich. Hydrogen peroxide (30 wt %) for polymerization was purchased from Sigma-Aldrich. All other chemicals and solvents were obtained from Fisher Scientific. Ultrapure water with a resistivity of 18 MΩ·cm and < 5 ppb inorganic impurities was used in all experiments (Milli-Q Gradient A-10, Millipore).

AFM and ellipsometry measurements were performed as outlined in Chapter 3.5, respectively. All QCM-D measurements were conducted as outlined in Chapter 3.5.4, with the following details specific to this work. The QCM-D sensor was placed in a flow cell and allowed to equilibrate for 1 to 1.5 h in water until a flat baseline was obtained. 1.0 mL of HRP solution (1.0 $mg \cdot mL^{-1}$) was introduced into the flow cell at a rate of 0.100 $mL \cdot min^{-1}$ at the indicated temperature. After rinsing with water for ~ 20 min, 5 mL of monolignol aqueous solution with a controlled concentration of $H_2O_2$ was subsequently introduced into the flow cell at the same rate. At the end of the measurement, water was flowed through the system for the removal of reversibly adsorbed monolignols and soluble DHP.

## 7.4 Results and Discussion

In this work, DHP on surfaces was prepared through a modified ZT method. The HRP was adsorbed onto silica, gold or DNC surfaces followed by a water rinse for the removal of reversibly adsorbed enzyme. Aqueous monolignol solutions with controlled concentrations of $H_2O_2$ were then flowed over the surfaces. Both HRP adsorption and polymerization of monolignols were monitored by QCM-D.

### 7.4.1 Effects of Solid Supports on the Dehydrogenative Polymerization of Monolignols

Representative QCM-D data for HRP adsorption onto silica, gold and DNC surfaces are shown in **Figure 7.1**. The adsorption of HRP onto both silica and gold occurred quickly with equilibrium adsorption obtained in less than 10 min. The adsorption of HRP onto both silica and gold yielded a scaled frequency change of $\Delta f/n \approx -21 \pm 2$ Hz, or a surface concentration from QCM-D of $\Gamma_{QCM} = 3.7 \pm 0.4$ mg·m$^{-2}$ according to the Sauerbrey equation (Equation 3.1). The $\Gamma_{QCM}$ value included both the adsorbed enzyme layer plus any water coupled to that layer. Previous studies of HRP adsorption onto silica via *in situ* ellipsometry and fluorescence measurements suggest a monolayer of HRP is formed on silica surfaces.[46, 47] Hence, HRP adsorption onto gold surfaces is also consistent with a monolayer. The adsorption of HRP onto DNC films was slow and yielded an irreversible $\Delta f/n \approx -44 \pm 2$ Hz, or $\Gamma_{QCM} = 7.8 \pm 0.4$ mg·m$^{-2}$ in ~ 60 min according to the Sauerbrey equation (Equation 3.1). As reported previously, the interiors of DNC films are known to be accessible to biomacromolecules due to a porous structure caused by voids between cellulose nanocrystals in the film.[48, 49] Thus, HRP not only adsorbed onto the surfaces of DNC films (~ 16 nm thick), but also penetrated into the films. In order to keep the amount of HRP irreversibly adsorbed onto different surfaces consistent, the adsorption of HRP onto DNC films was stopped after ~ 10 min, well before equilibrium adsorption occurred.

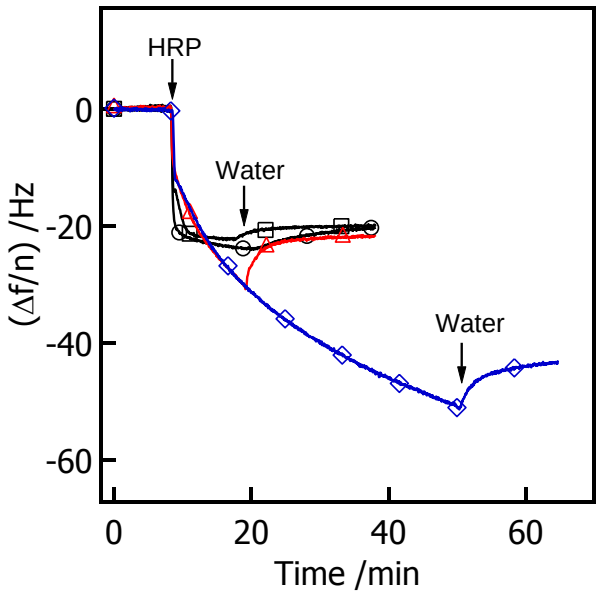


**Figure 7.1.** Representative Δ*f*/*n* versus time at 20 °C for HRP adsorption onto (□) a silica-coated QCM-D sensor, (○) a gold-coated QCM-D sensor, (Δ) a DNC film with a relatively short adsorption time and (◊) a DNC film with a relatively long adsorption time. Arrows and labels indicate where different solutions were introduced into the flow cell after the initial baselines were set in water. HRP was adsorbed onto the surfaces from a 1.0 mg·mL$^{-1}$ aqueous solution.

It is well known that the immobilization of enzymes can lead to a reduction in catalytic activity due to conformational changes during physisorption and chemisorption. Naves et al.[46] immobilized HRP on silicon wafers (with surface $SiO_2$ layers) via adsorption and determined the catalytic activity for free HRP and immobilized HRP from the oxidation of 2,2'-azino-bis-(3-ethylbenzothiazoline-6-sulfonic acid) and the emulsion polymerization of ethylene glycol dimethacrylate. Their results showed that immobilized HRP had a small reduction in catalytic activity relative to free HRP. The decreased activity was attributed to a conformational change upon adsorption. Takahashi et al.[50] studied the catalytic activity of HRP immobilized in mesoporous silica with different pore sizes through the oxidation of 1,2-diaminobenzene. Their

results showed that HRP immobilized in mesoporous silica with a pore diameter of 5.0 nm showed the highest activity because the pore size matched the molecular dimensions of HRP and thus prevented HRP denaturation.

**Figure 7.2** shows typical QCM-D data for the adsorption of HRP onto gold surfaces and the subsequent polymerization of three monolignols. The nearly instantaneous $\Delta f/n$ decrease for both coniferyl alcohol and *p*-coumaryl alcohol after the injection of aqueous monolignol solution with 20 mM $H_2O_2$[51] was attributed to the formation of DHP on the surface via HRP-initiated dehydrogenative polymerization of monolignols. The polymerization was fast and $\Delta f/n$ achieved a plateau in ~ 3 min. The polymerization of coniferyl alcohol and *p*-coumaryl alcohol yielded changes in $\Delta f/n \approx -310 \pm 15$ and $-150 \pm 10$ Hz from the enzyme coated surfaces, or $\Gamma_{QCM} = 55 \pm 3$ and $26 \pm 2$ mg·m$^{-2}$, respectively, from the Sauerbrey equation (Equation 3.1). The $\Gamma_{QCM}$ values assumed the mass was evenly distributed. In contrast, no appreciable $\Delta f/n$ change was monitored for sinapyl alcohol, which suggested that the reactivity of sinapyl alcohol is low in the presence of HRP/$H_2O_2$. It should be noted that the Sauerbrey equation (Equation 3.1) is probably not valid for the heterogeneous DHP films formed in this study. Thus, the provided conversions of the raw data via the Sauerbrey equation (Equation 3.1) should only be regarded as rough estimates of $\Gamma_{QCM}$. After polymerization, the DHP layers were rinsed with water for another ~ 40 min for the removal of soluble DHP or reversibly adsorbed monolignols. As seen in **Figure 7.2**, the DHP layers on gold were stable. Differences in the viscoelastic properties of the resulting DHP layers are consistent with the energy dissipation profile. The greater $\Delta D$ for G-DHP relative to H-DHP may be indicative of a smoother H-DHP layer with less coupled water on the gold surfaces.

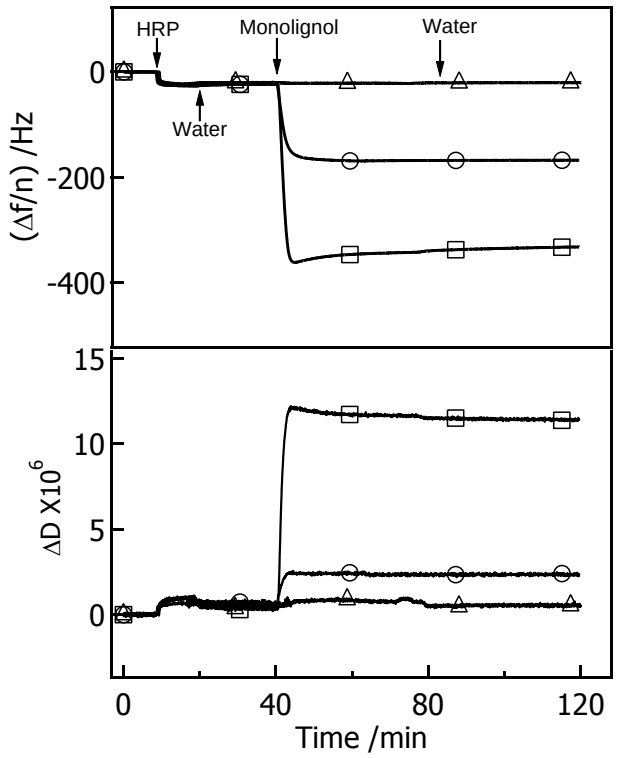


**Figure 7.2.** Representative $\Delta f/n$ and $\Delta D$ versus time at 20 °C for dehydrogenative polymerization of 0.5 mg·mL$^{-1}$ (□) coniferyl alcohol, (○) *p*-coumaryl alcohol and (Δ) sinapyl alcohol initiated by HRP immobilized on gold. Arrows and labels indicate where different solutions were introduced into the flow cell after the initial baselines were set in water. The HRP was adsorbed onto the surfaces from a 1.0 mg·mL$^{-1}$ aqueous solution and the aqueous monolignol solutions contained 20 mM $H_2O_2$.

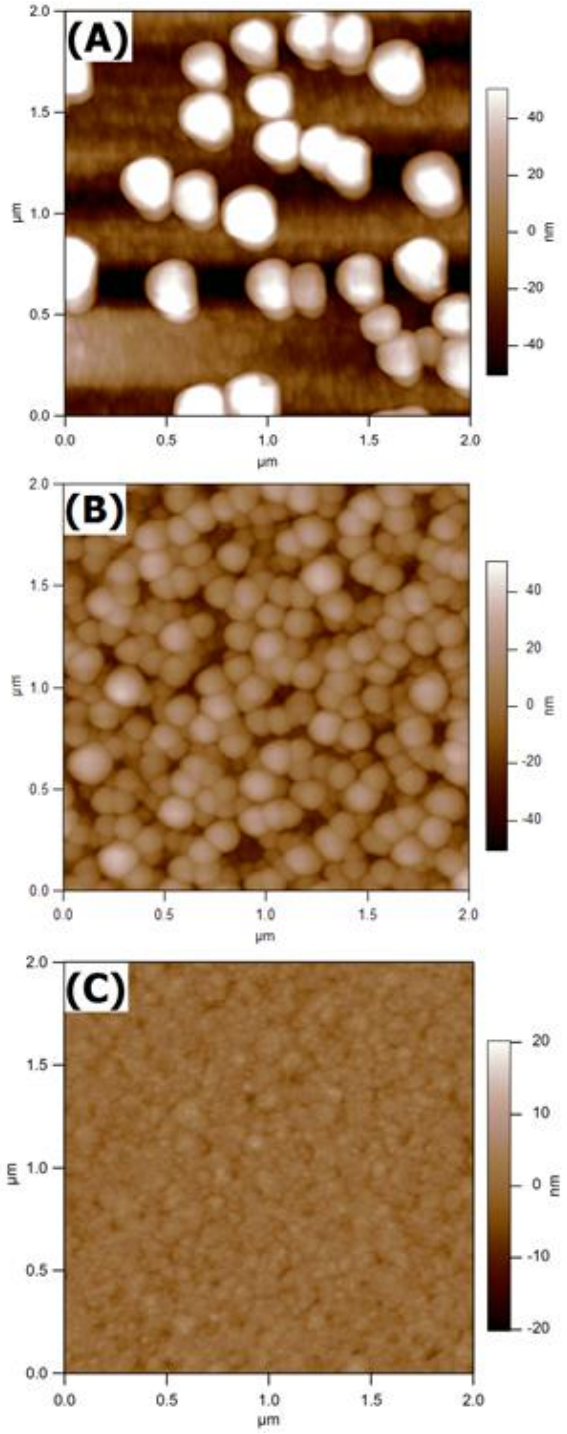


**Figure 7.3.** Representative 2 µm × 2 µm AFM height images of (A) G-DHP, (B) H-DHP and (C) S-DHP layers formed on gold coated QCM-D sensors. RMS roughnesses for each AFM image are: (A) ~ 33, (B) ~ 12 and (C) ~ 1.7 nm. An AFM image for a bare gold coated QCM-D sensor can be found in **Figure 7.10**.

The morphologies of the DHP layers after polymerization were investigated by AFM. Height images from AFM for G-DHP, H-DHP and S-DHP on gold surfaces are shown in **Figure 7.3**. As seen in **Figure 7.3**, both G-DHP and H-DHP formed irregular globular aggregates on gold surfaces. The G-DHP existed as large aggregates with observed diameters ranging from 200 to 350 nm, while H-GDP formed smaller and more uniform aggregates with diameters ranging from 150 to 200 nm. No appreciable S-DHP aggregates were observed on the gold surfaces from AFM images, in agreement with the QCM-D data that showed no reactivity for sinapyl alcohol in the presence of HRP/$H_2O_2$. The size of the DHP aggregates formed on the surfaces is smaller than the size of G-DHP polymerized in bulk solutions. Radotic et al. synthesized G-DHP in phosphate buffer and prepared the DHP samples for imaging by depositing DHP suspensions onto various surfaces, such as gold,[52] mica,[53] highly oriented pyrolytic graphite[53] and cellulose esters.[54] The morphology of the DHP supramolecular structures was observed via environmental scanning electron microscopy and AFM, and the results showed that the DHP globules had an average diameter of ~ 400 nm and the DHP morphology was affected by the nature of the matrix. They also proposed a mechanism for the self-assembly of DHP in aqueous solution, in which the self-assembly was divided into four structural levels of ordering: modules composed of ~ 20 monomers formed first, these modules polymerized into "super modules" containing ~ 500 monomers, "super modules" aggregated into globules, and finally globules clustered into larger colloidal crystalline aggregates.[52-55] It is noteworthy that the particle density estimated from AFM images from at least 5 films was much larger for H-DHP (71 ± 6 $\mu m^{-2}$) than G-DHP (7 ± 1 $\mu m^{-2}$) although the H-DHP aggregates were smaller than the G-DHP aggregates. In order for a DHP aggregate to form, two things had to happen: initiation of a radical had to occur and the propagation of that radical to form insoluble polymer had to occur before the radical could

diffuse away from the surface. The differences in DHP particle density and size suggested that *p*-coumaryl alcohol might be a better substrate for HRP for radical initiation, while coniferyl alcohol-based radicals underwent faster propagation to form larger insoluble DHP aggregates.

The low reactivity of sinapyl alcohol in the presence of HRP/$H_2O_2$ was also observed in bulk systems[24, 25] and the reasons were attributed to: (1) sinaplyl alcohol being a poor substrate for HRP and (2) the low reactivity of syringyl quinone methide intermediates (S-QM). Henriksen et al.[56-58] studied the crystal structures of HRP and an anionic *Arabidopsis thaliana* peroxidase (ATP) and observed that sinapyl alcohol could not fit into the substrate binding site of HRP or ATP due to steric hindrance caused by the two methoxyl groups. However, Sasaki et al.[16, 17] reported a cationic cell wall peroxidase (CWPO-C) isoenzyme from poplar (*Populus alba* L.) callus that showed a strong substrate preference for sinapyl alcohol, the sinapyl alcohol dimer and even high-molar-mass sinapyl alcohol polymers. Thus, CWPO-C was identified as an important enzyme for the deposition of syringyl-rich lignin in the plant cell wall of angiosperms. The low reactivity of S-QMs was attributed to a decrease of positive charge density at the α-positions of S-QM, which is caused by the presence of the two electron-donating methoxyl groups. Tobimatsu et al.[24, 25] studied HRP-catalyzed dehydrogenative polymerization of sinapyl alcohol in the presence of nucleophiles (e.g. azide ions) as S-QM scavengers and found that the nucleophiles promoted the production of S-DHP oligomers. The explanation for this behavior is that nucleophiles promote rearomatization of S-QM via nucleophilic additions to the α-carbon to regenerate phenolic hydroxyl groups. In order to further understand the lack of S-DHP formation, the dehydrogenative polymerization of sinapyl alcohol in the presence of sodium azide ($NaN_3$) initiated by HRP immobilized on gold was also investigated by QCM-D and AFM. Representative QCM-D data and AFM height images are shown in **Figure 7.4**. A molar ratio of

1:1 between sinapyl alcohol and $NaN_3$ was chosen because Tobimatsu et al.[24] found this ratio gave the highest yield of S-DHP (54.2 %) in bulk systems. As seen in **Figure 7.4A**, the polymerization of sinapyl alcohol in the presence of $NaN_3$ on gold yielded $\Delta f/n \approx -31 \pm 11$ Hz for the enzyme coated surface, or $\Gamma_{QCM} = 5.5 \pm 1.9$ mg·m$^{-2}$ assuming the Sauerbrey equation (Equation 3.1) is valid. The magnitude of this $\Delta f/n$ change is much smaller than the surface-initiated polymerization of coniferyl alcohol and *p*-coumaryl alcohol seen in **Figure 7.2**. The polymerization was also slower than the polymerization of coniferyl alcohol and *p*-coumaryl alcohol and $\Delta f/n$ achieved a plateau in ~ 10 min for sinapyl alcohol versus ~ 3 min for the other two monolignols. As seen in **Figure 7.4B**, S-DHP formed a few mostly spherical aggregates on the gold surface with observed diameters ranging from ~ 250 to 400 nm. In this respect, the aggregates in **Figure 7.4B** are most similar to the G-DHP in **Figure 7.3A**; however, the particle density (< 1 μm$^{-2}$) is much lower. Therefore, the low reactivity of sinapyl alcohol in the presence of HRP/$H_2O_2$ presumably arises from both slow radical initiation and propagation in the absence of nucleophiles.

In general, different solid supports have different effects upon the catalytic activity of immobilized enzymes because of different degrees of conformational change that occur when enzymes adsorb onto solids. Norin et al.[59] studied the catalysis of alcohol esterification by lipase adsorbed onto both hydrophilic and hydrophobic surfaces and Quiquampoix et al.[60] studied the catalysis of 4-nitrophenyl-3-D-glucopyranose hydrolysis by sweet almond *β*-D-glucosidase adsorbed onto various mineral surfaces. Both studies showed that the immobilized enzyme activity was greatly affected by the nature of the interactions between the enzymes and the support materials.

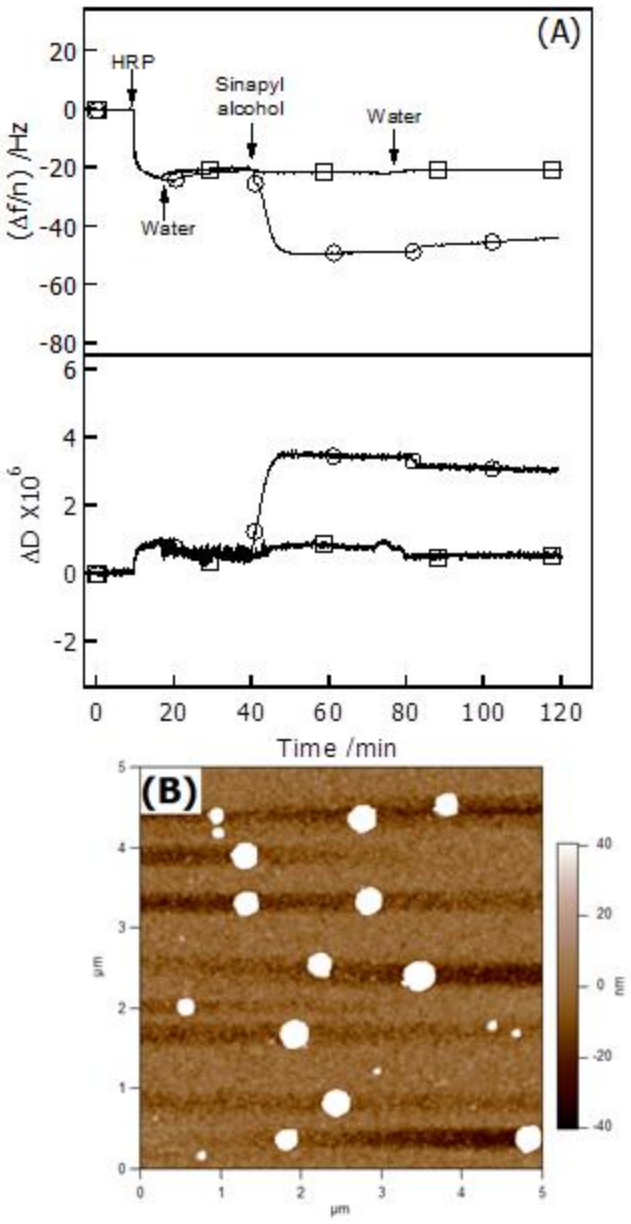


**Figure 7.4.** (A) Representative Δ*f*/*n* and *ΔD* versus time for dehydrogenative polymerization of 0.5 mg·mL$^{-1}$ sinapyl alcohol initiated by HRP immobilized on gold at 20 °C (○) with $NaN_3$ (1:1 molar ratio for sinapyl alcohol:$NaN_3$) and (□) without $NaN_3$. Arrows and labels indicate where different solutions were introduced into the flow cell after the initial baselines were set in water. HRP was adsorbed from a 1.0 mg·mL$^{-1}$ aqueous solution. Aqueous sinapyl alcohol solutions contained 20 mM $H_2O_2$. (B) A 5 μm × 5 μm AFM height image of a S-DHP "layer" on gold. The RMS roughness is ~ 20 nm.

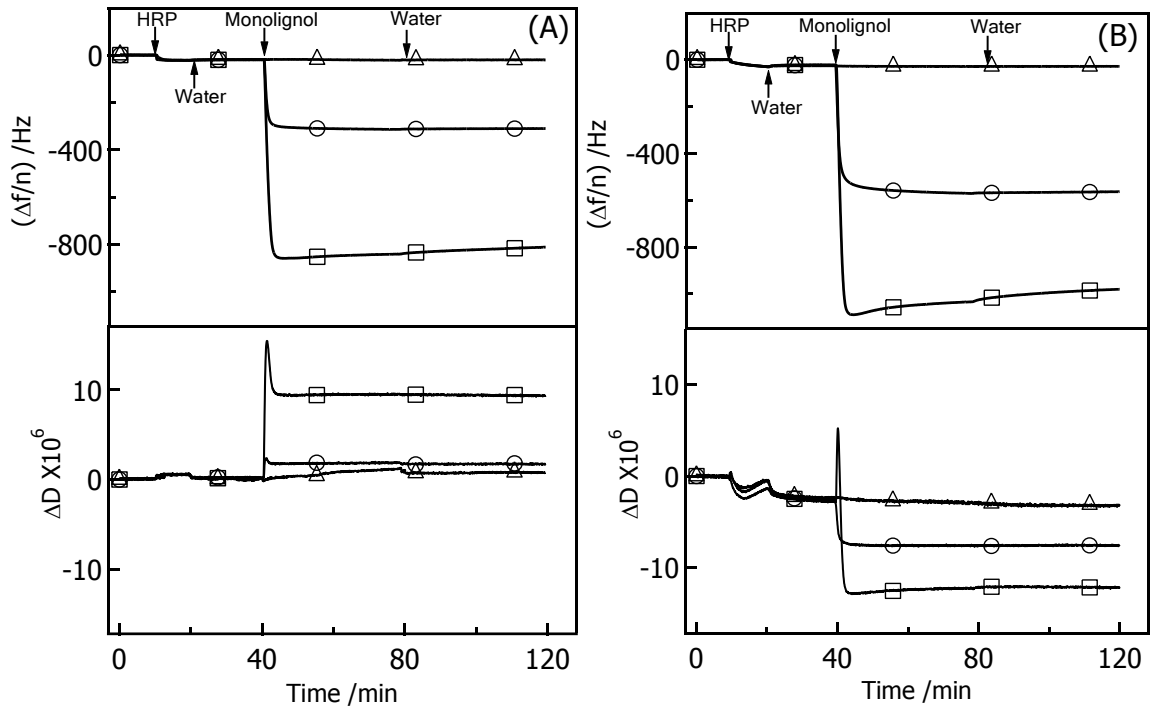


**Figure 7.5.** Representative Δ*f*/*n* and Δ*D* versus time for dehydrogenative polymerization of 0.5 mg·mL$^{-1}$ (□) coniferyl alcohol, (○) *p*-coumaryl alcohol and (Δ) sinapyl alcohol initiated by HRP immobilized on (A) silica and (B) DNC surfaces at 20 °C. Arrows and labels indicate where different solutions were introduced into the flow cell after the initial baselines were set in water. The HRP was adsorbed onto the surfaces from a 1.0 mg·mL$^{-1}$ aqueous solution and the aqueous monolignol solutions contained 20 mM $H_2O_2$.

The dehydrogenative polymerization of monolignols initiated by HRP immobilized on silica and DNC films was monitored by QCM-D and AFM. Representative QCM-D data for different surfaces is shown in **Figure 7.5** and representative AFM height images for G-DHP, H-DHP and S-DHP on silica and DNC surfaces are provided in **Figure 7.6**. As seen in **Figure 7.5A**, the dehydrogenative polymerization of monolignols on silica surfaces was fast and the polymerization of coniferyl alcohol and *p*-coumaryl alcohol on silica yielded changes in $\Delta f/n \approx$ -790 ± 20 and -290 ± 20 Hz relative to the enzyme coated surfaces, or $\Gamma_{QCM}$ = 140 ± 4 and 51 ± 4 mg·m$^{-2}$, respectively, assuming the Sauerbrey equation (Equation 3.1) is valid. From the AFM images in **Figure 7.6**, G-DHP formed larger aggregates on silica surfaces than on gold surfaces and the size of the aggregates ranged from 350 to 500 nm, although the RMS roughnesses of the "films" were similar. The diameters of H-DHP aggregates on silica surfaces were similar to those on gold and ranged from 100 to 200 nm. For the case of coniferyl alcohol and *p*-coumaryl alcohol polymerization on DNC films (**Figure 7.5B**), changes in $\Delta f/n \approx$ -960 ± 25 and -545 ± 25 Hz, relative to the enzyme coated surfaces, or $\Gamma_{QCM}$ = 170 ± 5 and 96 ± 5 mg·m$^{-2}$, respectively, assuming the Sauerbrey equation (Equation 3.1) is valid. As discussed above, DNC films are porous and biomacromolecules can penetrate into the films. As small molecules, monolignols and $H_2O_2$ were able to penetrate into the DNC films which enabled dehydrogenative polymerization within the interior of the DNC films. The $\Delta D$ decreases for the polymerization of coniferyl alcohol and *p*-coumaryl alcohol on DNC films suggested that the formation of DHP within the DNC films led to a decrease in the viscous damping of the system. However, it is not clear whether this decrease is due to displacement of water from the porous DNC film as DHP forms, effective crosslinking of various nanocrystals via the formation of DHP around them, or even the formation of covalent crosslinks between DHP and cellulose. In the natural cell wall

environment there is no conclusive evidence for covalent linkages between lignin and cellulose. However, there is growing evidence for lignin linkages with other polysaccharides as LCCs,[22, 61-65] and evidence for enhanced interactions between lignin and cellulose during some pulping processes that may or may not be covalent.[66] In the absence of definitive proof of covalent interactions between cellulose and lignin, it is more likely that the DHP primarily acts as a filler rather than a crosslinker between the nanocrystals. Thus, a cellulose/DHP composite film is actually obtained from this work, and such a composite film might be useful as a substrate to study the effect of lignin on the enzymatic degradation of crystalline cellulose. As seen in **Figure 7.6**, both G-DHP and H-DHP formed larger aggregates on DNC films than on gold or silica surfaces. The diameters of G-DHP ranged from 450 to 600 nm, and the diameters of H-DHP ranged from 150 to 300 nm. Similar to polymerization on gold surfaces, sinapyl alcohol did not undergo appreciable DHP formation on silica or DNC surfaces because of its low reactivity in the presence of HRP/$H_2O_2$ and the absence of strong enough nucleophiles.

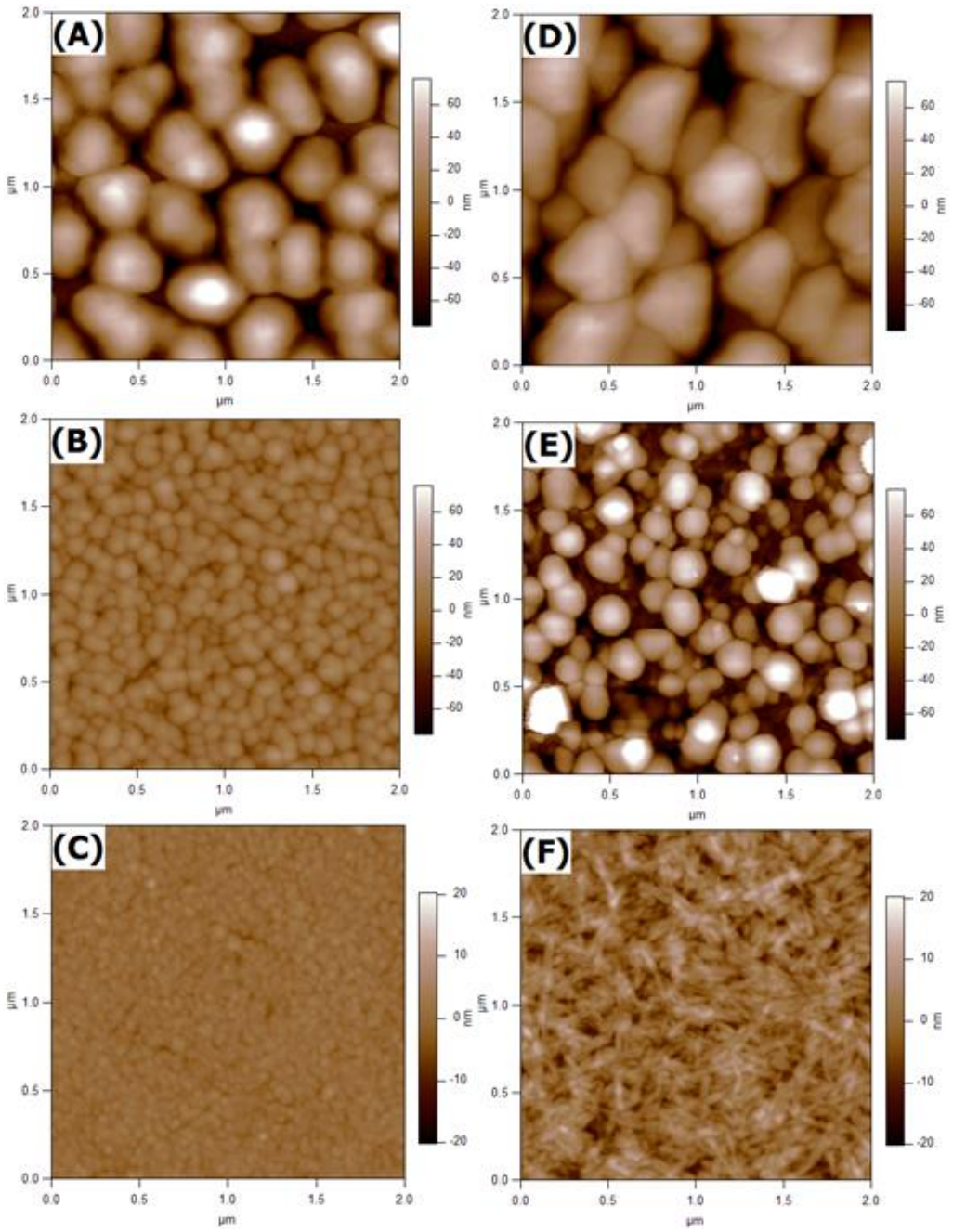


**Figure 7.6.** Representative 2 µm × 2 µm AFM height images of (A) G-DHP, (B) H-DHP and (C) S-DHP on silica, and (D) G-DHP, (E) H-DHP and (F) S-DHP on DNC films. RMS roughnesses for the AFM images are: (A) ~ 33 nm, (B) ~ 9.3 nm, (C) ~ 1.2 nm, (D) ~ 31 nm, (E) ~ 41 nm and (F) ~ 4.2 nm. Equivalent images for an unaltered silica coated QCM-D sensor and a DNC surface are provided in **Figure 7.10** for comparison.

### 7.4.2 Effects of Monolignol Concentration on the Dehydrogenative Polymerization of Coniferyl Alcohol

The effects of monolignol concentration, $H_2O_2$ concentration and temperature on the surface-initiated dehydrogenative polymerization of coniferyl alcohol were also investigated via QCM-D. Representative QCM-D data for the dehydrogenative polymerization of different concentrations of coniferyl alcohol on gold surfaces are shown in **Figure 7.7A** and $\Gamma_{QCM}$ from the Sauerbrey equation (Equation 3.1) as a function of coniferyl alcohol concentration ($C_{ca}$) are plotted in **Figure 7.7B**. As seen in **Figure 7.7A**, the polymerization was fast over a $C_{ca}$ range of 0.05 to 0.1 mg·mL$^{-1}$. However, no detectible $\Delta f/n$ were observed for very dilute aqueous coniferyl alcohol solutions (e.g. 0.01 mg·mL$^{-1}$). This observation may mean that substrate concentrations are too low to drive binding to the enzyme or that radicals initiated at the surface diffuse away from the surface faster than insoluble DHP can form during the subsequent propagation step. On the other hand, the portion of DHP that was soluble or unattached to the surfaces increased at higher concentrations (e.g. 1.0 mg·mL$^{-1}$) where $\Delta f/n$ increased by ~ 90 Hz above the minimum value during rinsing. As seen in **Figure 7.7B**, $\Gamma_{QCM}$ was proportional to the concentration of coniferyl alcohol within experimental error over the range of concentrations ($C_{ca}$ < 0.5 mg·mL$^{-1}$) where no significant desorption of DHP was seen in **Figure 7.7A**.

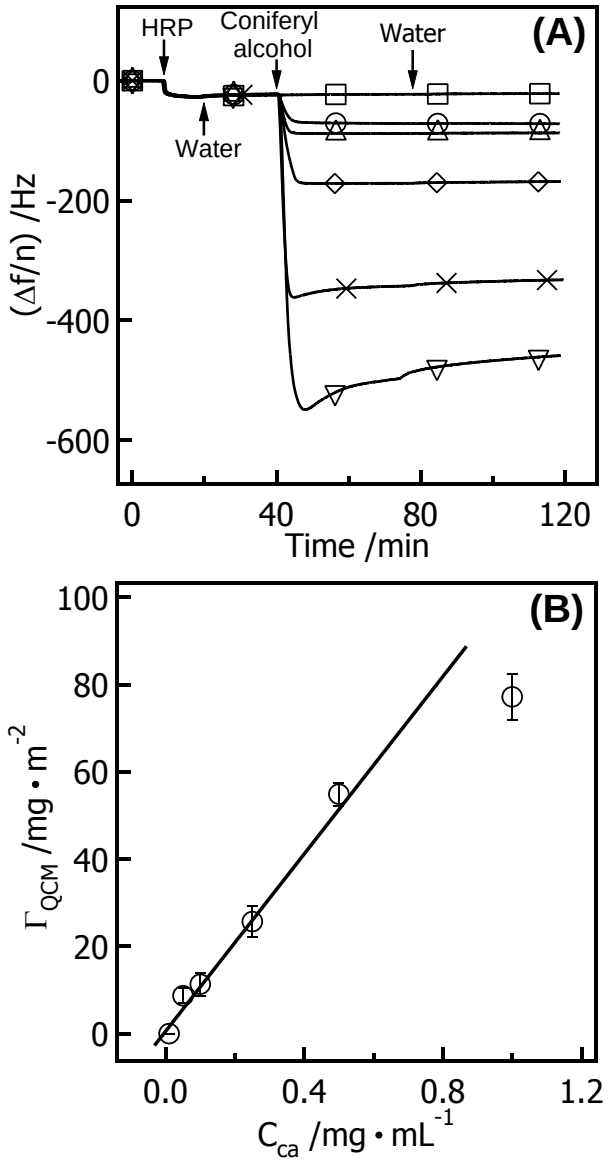


**Figure 7.7.** (A) Representative Δ*f*/*n* versus time for dehydrogenative polymerization of coniferyl alcohol by HRP immobilized on gold at 20 °C for aqueous solutions with $C_{ca}$ of (□) 0.01, (○) 0.05, (Δ) 0.1, (◊) 0.25, (×) 0.5 and (▽) 1.0 mg·mL$^{-1}$. Arrows and labels indicate where different solutions were introduced into the flow cell after the initial baselines were set in water. The HRP was adsorbed onto the surfaces from a 1.0 mg·mL$^{-1}$ aqueous solution and the aqueous coniferyl alcohol solution contained 20 mM $H_2O_2$. (B) $\Gamma_{QCM}$ versus $C_{ca}$, where the straight line represents a linear least-squares fit excluding the point at $C_{ca}$ = 1.0 mg·mL$^{-1}$.

### 7.4.3 Effects of Hydrogen Peroxide Concentration on the Dehydrogenative Polymerization of Coniferyl Alcohol

Hydrogen peroxide plays a crucial role in peroxidase-catalyzed reactions. However, peroxidases are readily inactivated by $H_2O_2$, especially in the presence of excess $H_2O_2$ or in the absence of reducing substrates. The effect of $H_2O_2$ concentration on surface-immobilized HRP activity was studied by QCM-D. Representative QCM-D data for the dehydrogenative polymerization of coniferyl alcohol by HRP immobilized on gold for different $H_2O_2$ concentrations are shown in **Figure 7.8A** and $\Gamma_{QCM}$ as a function of $H_2O_2$ concentration ($C_{H2O2}$) is plotted in **Figure 7.8B**. As seen in **Figure 7.8A** and **7.8B**, the activity of surface-immobilized HRP was strongly affected by $H_2O_2$ concentration. Surface-immobilized HRP showed the greatest activity at a $H_2O_2$ concentration of 4.0 mM where $\Gamma_{QCM}$ showed a maximum. The activity of the surface-immobilized HRP, taken as $\Gamma_{QCM}$, decreased exponentially as $H_2O_2$ concentration increased from 4.0 to 200 mM. The mechanism for the $H_2O_2$-mediated inactivation (suicide inactivation) of peroxidases was reviewed by Valderrama et al.[67] In a general catalytic cycle of peroxidase, the Fe (III) ground state of the peroxidase donates two electrons to $H_2O_2$ to form an intermediate termed compound I and water. Compound I consists of an oxo-Fe (IV) center and a porphyrin-based cation radical. The cation radical in compound I is reduced by electron-donating substrates, such as the monolignols in this work, to generate an oxo-Fe (IV) porphyrin intermediate compound II. Compound II is further reduced through a one-electron reduction step to regenerate the Fe (III) ground state.[67, 68] However, in the presence of high $H_2O_2$ concentration or in the absence of reducing substrates, compound II is converted by $H_2O_2$ (as a suicide substrate) to a peroxy-Fe (III) porphyrin free-radical intermediate compound III. Compound III then decomposes into a variety of species via different pathways.[67]

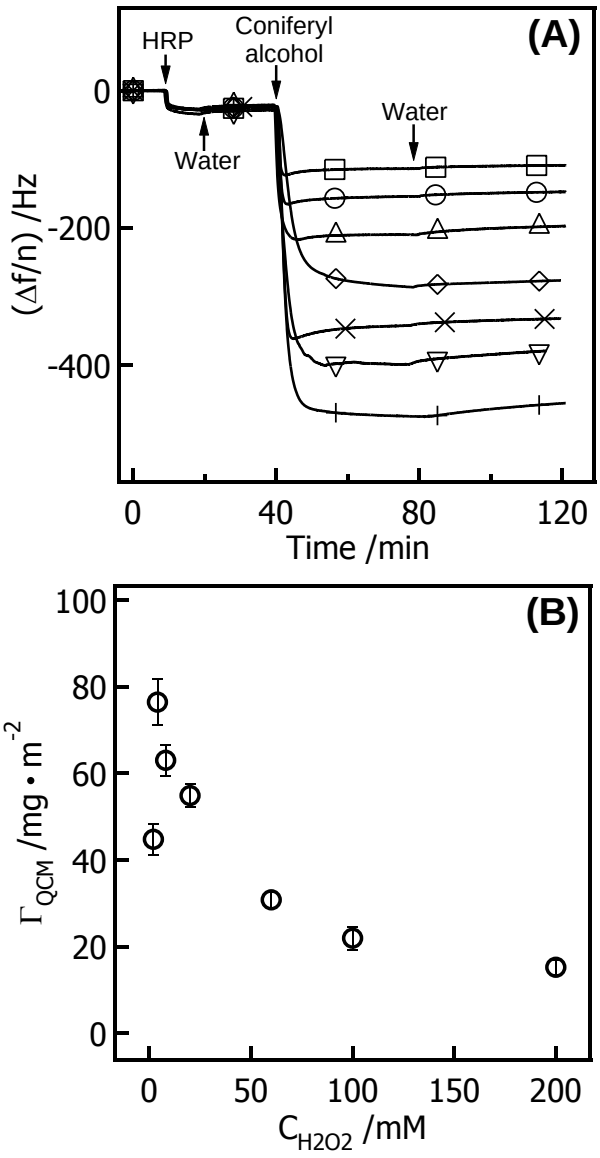


**Figure 7.8.** (A) Representative $\Delta f/n$ versus time for dehydrogenative polymerization of 0.5 mg·mL$^{-1}$ coniferyl alcohol by HRP immobilized on gold at 20 °C for different $C_{H2O2}$: (◊) 2.0, (+) 4.0, (▽) 8.0, (×) 20, (Δ) 60, (○) 100 and (□) 200 mM. Arrows and labels indicate where different solutions were introduced into the flow cell after the initial baselines were set in water. HRP was adsorbed onto the surfaces from a 1.0 mg·mL$^{-1}$ aqueous solution. (B) $\Gamma_{QCM}$ versus $C_{H2O2}$.

### 7.4.4 Effects of Temperature on the Dehydrogenative Polymerization of Coniferyl Alcohol

**Figure 7.9** contains representative QCM-D data for the dehydrogenative polymerization of coniferyl alcohol initiated by HRP immobilized on gold at different temperatures. **Figure 7.9A** shows raw QCM-D data whereas **Figure 7.9B** has $\Gamma_{QCM}$ calculated (Equation 3.1) from the plateau value after polymerization and rinsing with water as a function of temperature. As seen in **Figure 7.9B**, the greatest amount of DHP formed through the dehydrogenative polymerization at 20 °C for the temperatures probed. Values of $\Gamma_{QCM}$ decreased more or less linearly within experimental error with increasing temperature over the range of 20 to 50 °C. This behavior is slightly different from the bulk activity of HRP which has a reported optimal temperature of ~ 45 °C in solution.[69, 70] In order to observe DHP at the surface, the DHP must achieve an insoluble molar mass before radical species diffuse away from the interface. Here, the lower optimal temperature may reflect diffusion of the radical species away from the interface with increasing temperature that limit the growth of DHP rather than a decrease in inherent enzyme activity.

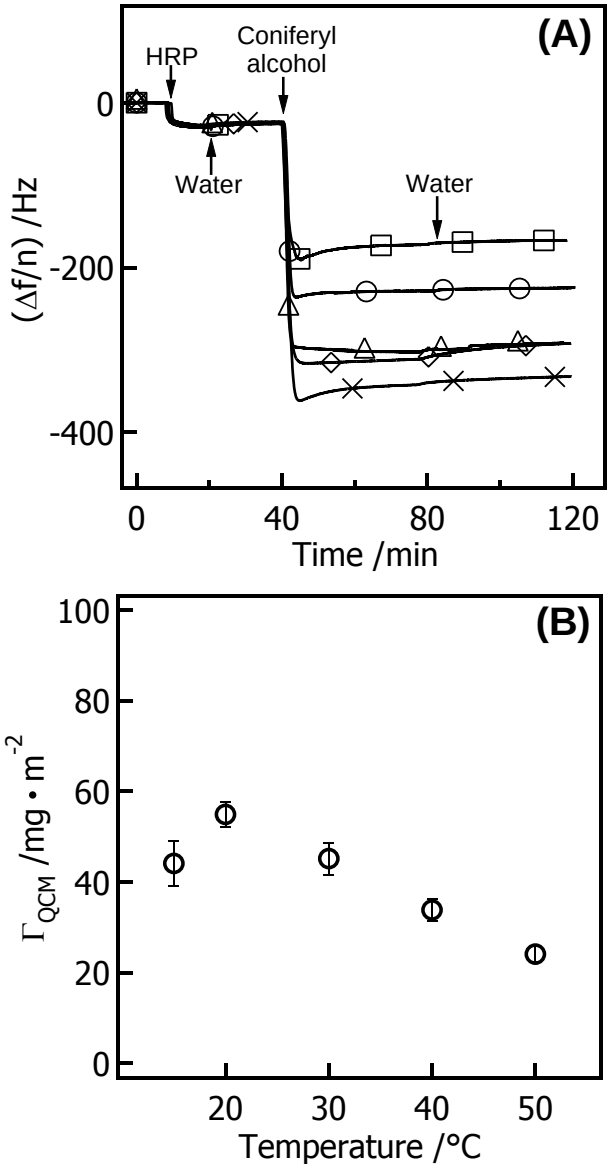


**Figure 7.9.** (A) Representative $\Delta f/n$ versus time for dehydrogenative polymerization of 0.5 mg·mL$^{-1}$ coniferyl alcohol by HRP immobilized on gold at (◊) 15, (×) 20, (Δ) 30, (○) 40 and (□) 50 °C. Arrows and labels indicate where different solutions were introduced into the flow cell after the initial baselines were set in water. The HRP was adsorbed from a 1.0 mg·mL$^{-1}$ aqueous solution and the aqueous coniferyl alcohol solution contained 20 mM $H_2O_2$. (B) $\Gamma_{QCM}$ versus temperature.

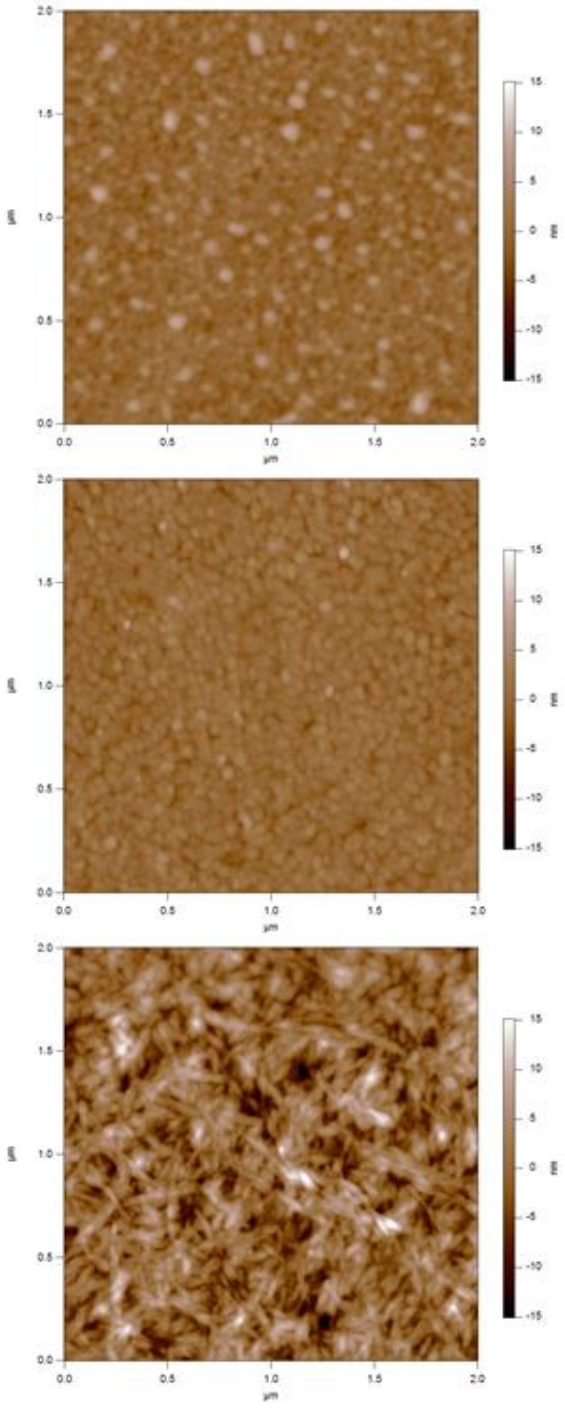

**Figure 7.10.** Representative 2 μm × 2 μm AFM height images of (A) a gold coated QCM-D sensor, (B) a silica coated QCM-D sensor and (C) a DNC film. RMS roughnesses for the AFM images are: (A) ~ 1.3 nm, (B) ~ 2.6 nm and (C) ~ 3.8 nm.

## 7.5 Conclusions

Similar amounts of HRP were physically immobilized on gold and silica surfaces, and on and within porous DNC films via adsorption from aqueous solution. The surface-immobilized HRP directly polymerized coniferyl alcohol and *p*-coumaryl alcohol in the presence of hydrogen peroxide, but not sinapyl alcohol. Limited polymerization of sinapyl alcohol was observed when azide ion was added as a nucleophile. Stable G-DHP and H-DHP layers were formed on gold and silica surfaces after polymerization while cellulose/DHP composite films were obtained through the dehydrogenative polymerization of monolignols within and on the surfaces of porous DNC films. Surface densities of DHP aggregates that formed seem to reflect HRP substrate preferences for initiation of *p*-coumaryl > coniferyl > sinapyl alcohol. However, larger DHP aggregates formed for coniferyl alcohol are consistent with faster propagation. Both QCM-D and AFM data showed that the surface-initiated dehydrogenative polymerization of monolignols was greatly affected by the support surfaces, monolignol concentration, hydrogen peroxide concentration and temperature. Optimal conditions for G-DHP formation occurred at 20 °C with 4.0 mM $H_2O_2$. These films are expected to provide a sensitive and label-free method to determine the precursor preference, monolignols as well as other aromatic species that can be incorporated into lignin,[4, 5, 32, 71, 72] and optimal conditions for peroxidases and other enzymes involved in lignification. Furthermore, the resulting DHP films can serve as sensors for ligninolytic enzyme activity (Chapter 8), thereby opening the characterization of lignin biodegradation to previously unused surface science techniques.

## 7.6 References


(1) Freudenberg, K. *Angew. Chem.* **1956,** 68, 508-512.

(2) Lewis, N. G.; Newman, J.; Just, G.; Ripmeister, J. *Macromolecules* **1987,** 20, 1752-1756.

(3) Tobimatsu, Y.; Takano, T.; Kamitakahara, H.; Nakatsubo, F. *Holzforschung* **2008,** 62, 495-500.

(4) Ralph, J.; Helm, R. F.; Quideau, S.; Hatfield, R. D. *J. Chem. Soc., Perkin Trans. 1* **1992**, 2961-2969.

(5) Ralph, J.; Helm, R. F.; Quideau, S. *J. Chem. Soc., Perkin Trans. 1* **1992**, 2971-2980.

(6) Ito, T.; Hayase, R.; Kawai, S.; Ohashi, H.; Higuchi, T. *J. Wood Sci.* **2002,** 48, 216-221.

(7) Grabber, J. H.; Hatfield, R. D.; Ralph, J. *J. Agric. Food Chem.* **2003,** 51, 4984-4989.

(8) Terashima, N.; Atalla, R. H.; Ralph, S. A.; Landucci, L. L.; Lapierre, C.; Monties, B. *Holzforschung* **1996,** 50, 9-14.

(9) Fournand, D.; Cathala, B.; Lapierre, C. *Phytochemistry* **2003,** 62, 139-146.

(10) Houtman Carl, J. *Holzforschung* **1999,** 53, 585-589.

(11) Micic, M.; Orbulescu, J.; Radotic, K.; Jeremic, M.; Sui, G.; Zheng, Y.; Leblanc, R. M. *Biophys. Chem.* **2002,** 99, 55-62.

(12) Cathala, B.; Aguié-Béghin, V.; Douillard, R. *C. R. Biol.* **2004,** 327, 777-784.

(13) Méchin, V.; Baumberger, S.; Pollet, B.; Lapierre, C. *Phytochemistry* **2007,** 68, 571-579.

(14) Sterjiades, R.; Dean, J. F. D.; Eriksson, K.-E. L. *Plant Physiol.* **1992,** 99, 1162-1168.

(15) Yoshida, S.; Chatani, A.; Tanahashi, M.; Honda, Y.; Watanabe, T.; Kuwahara, M. *Holzforschung* **1998,** 52, 282-286.

(16) Aoyama, W.; Sasaki, S.; Matsumura, S.; Mitsunaga, T.; Hirai, H.; Tsutsumi, Y.; Nishida, T. *J. Wood Sci.* **2002,** 48, 497-504.

(17) Sasaki, S.; Nishida, T.; Tsutsumi, Y.; Kondo, R. *FEBS Lett.* **2004,** 562, 197-201.

(18) Barakat, A.; Putaux, J.-L.; Saulnier, L.; Chabbert, B.; Cathala, B. *Biomacromolecules* **2007,** 8, 1236-1245.

(19) Nakamura, R.; Matsushita, Y.; Umemoto, K.; Usuki, A.; Fukushima, K. *Biomacromolecules* **2006,** 7, 1929-1934.

(20) Lairez, D.; Cathala, B.; Monties, B.; Bedos-Belval, F.; Duran, H.; Gorrichon, L. *Biomacromolecules* **2005,** 6, 763-774.

(21) Boukari, I.; Putaux, J.-L.; Cathala, B.; Barakat, A.; Saake, B.; Rémond, C.; O'Donohue, M.; Chabbert, B. *Biomacromolecules* **2009,** 10, 2489-2498.

(22) Barakat, A.; Winter, H.; Rondeau-Mouro, C.; Saake, B.; Chabbert, B.; Cathala, B. *Planta* **2007,** 226, 267-281.

(23) Ralph, J.; Zhang, Y.; M. Ede, R. *J. Chem. Soc., Perkin Trans. 1* **1998**, 2609-2614.

(24) Tobimatsu, Y.; Takano, T.; Kamitakahara, H.; Nakatsubo, F. *J. Wood Sci.* **2008,** 54, 87-89.

(25) Tobimatsu, Y.; Takano, T.; Kamitakahara, H.; Nakatsubo, F. *J. Wood Sci.* **2010,** 56, 233-241.

(26) Guan, S.-Y.; Mlynár, J.; Sarkanen, S. *Phytochemistry* **1997,** 45, 911-918.

(27) Tien, M.; Kirk, T. K. *Science* **1983,** 221, 661-663.

(28) Hammel, K. E.; Jensen, K. A.; Mozuch, M. D.; Landucci, L. L.; Tien, M.; Pease, E. A. *J. Biol. Chem.* **1993,** 268, 12274-81.

(29) Wariishi, H.; Valli, K.; Gold, M. H. *Biochem. Biophys. Res. Commun.* **1991,** 176, 269-275.

(30) Grabber, J. H. *Crop Sci.* **2005,** 45, 820-831.

(31) Balakshin, M.; Capanema, E.; Gracz, H.; Chang, H.-m.; Jameel, H. *Planta* **2011,** 233, 1097-1110.

(32) Tobimatsu, Y.; Elumalai, S.; Grabber, J. H.; Davidson, C. L.; Pan, X.; Ralph, J. *ChemSusChem* **2012,** 5, 676-686.

(33) Stengel, G.; Höök, F.; Knoll, W. *Anal. Chem.* **2005,** 77, 3709-3714.

(34) Berglin, M.; Delage, L.; Potin, P.; Vilter, H.; Elwing, H. *Biomacromolecules* **2004,** 5, 2376-2383.

(35) Knowles, T. P. J.; Shu, W.; Devlin, G. L.; Meehan, S.; Auer, S.; Dobson, C. M.; Welland, M. E. *Proc. Natl. Acad. Sci. U.S.A.* **2007,** 104, 10016-10021.

(36) Dolatshahi-Pirouz, A.; Foss, M.; Besenbacher, F. *J. Phys. Chem. C* **2011,** 115, 13617-13623.

(37) Hovgaard, M. B.; Dong, M.; Otzen, D. E.; Besenbacher, F. *Biophys. J.* **2007,** 93, 2162-2169.

(38) Ma, H.; Textor, M.; Clark, R.; Chilkoti, A. *Biointerphases* **2006,** 1, 35-39.

(39) Fu, L.; Chen, X.; He, J.; Xiong, C.; Ma, H. *Langmuir* **2008,** 24, 6100-6106.

(40) He, J.; Wu, Y.; Wu, J.; Mao, X.; Fu, L.; Qian, T.; Fang, J.; Xiong, C.; Xie, J.; Ma, H. *Macromolecules* **2007,** 40, 3090-3096.

(41) Chernyy, S.; Iruthayaraj, J.; Ceccato, M.; Hinge, M.; Pedersen, S. U.; Daasbjerg, K. *J. Polym. Sci., Part A: Polym. Chem.* **2012,** 50, 4465-4475.

(42) Moya, S. E.; Brown, A. A.; Azzaroni, O.; Huck, W. T. S. *Macromol. Rapid Commun.* **2005,** 26, 1117-1121.

(43) Schüwer, N.; Klok, H.-A. *Adv. Mater.* **2010,** 22, 3251-3255.

(44) Heeb, R.; Bielecki, R. M.; Lee, S.; Spencer, N. D. *Macromolecules* **2009,** 42, 9124-9132.

(45) Benetti, E. M.; Reimhult, E.; de Bruin, J.; Zapotoczny, S.; Textor, M.; Vancso, G. J. *Macromolecules* **2009,** 42, 1640-1647.

(46) Naves, A. F.; Carmona-Ribeiro, A. M.; Petri, D. F. S. *Langmuir* **2006,** 23, 1981-1987.

(47) Vianello, F.; Zennaro, L.; Di Paolo, M. L.; Rigo, A.; Malacarne, C.; Scarpa, M. *Biotechnol. Bioeng.* **2000,** 68, 488-495.

(48) Kittle, J. D.; Du, X.; Jiang, F.; Qian, C.; Heinze, T.; Roman, M.; Esker, A. R. *Biomacromolecules* **2011,** 12, 2881-2887.

(49) Kittle, J. D.; Wondraczek, H.; Wang, C.; Jiang, F.; Roman, M.; Heinze, T.; Esker, A. R. *Langmuir* **2012,** 28, 11086-11094.

(50) Takahashi, H.; Li, B.; Sasaki, T.; Miyazaki, C.; Kajino, T.; Inagaki, S. *Chem. Mater.* **2000,** 12, 3301-3305.

(51) Kirk, T. K.; Brunow, G. Synthetic 14C-labeled lignins. In *Methods Enzymol.*, Willis A. Wood, S. T. K., Ed. Academic Press: 1988; Vol. Volume 161, pp 65-73.

(52) Radotic, K.; Simic-Krstic, J.; Jeremic, M.; Trifunovic, M. *Biophys. J.* **1994,** 66, 1763-1767.

(53) Micic, M.; Jeremic, M.; Radotic, K.; Mavers, M.; Leblanc, R. M. *Scanning* **2000,** 22, 288-294.

(54) Micic, M.; Radotic, K.; Jeremic, M.; Leblanc, R. M. *Macromol. Biosci.* **2003,** 3, 100-106.

(55) Micic, M.; Radotic, K.; Jeremic, M.; Djikanovic, D.; Kämmer, S. B. *Colloids Surf., B: Biointerfaces* **2004,** 34, 33-40.

(56) Østergaard, L.; Teilum, K.; Mirza, O.; Mattsson, O.; Petersen, M.; Welinder, K.; Mundy, J.; Gajhede, M.; Henriksen, A. *Plant Mol. Biol.* **2000,** 44, 231-243.

(57) Nielsen, K. L.; Indiani, C.; Henriksen, A.; Feis, A.; Becucci, M.; Gajhede, M.; Smulevich, G.; Welinder, K. G. *Biochemistry* **2001,** 40, 11013-11021.

(58) Henriksen, A.; Smith, A. T.; Gajhede, M. *J. Biol. Chem.* **1999,** 274, 35005-35011.

(59) Norin, M.; Boutelje, J.; Holmberg, E.; Hult, K. *Appl. Microbiol. Biotechnol.* **1988,** 28, 527-530.

(60) Quiquampoix, H. *Biochimie* **1987,** 69, 753-763.

(61) Takahashi, N.; Koshijima, T. *Wood Sci. Technol.* **1988,** 22, 231-241.

(62) Iversen, T.; Wännström, S. *Holzforschung* **1986,** 40, 19-22.

(63) Karlsson O.; Pettersson B.; Westermark U. *J. Pulp Pap. Sci.* **2001,** 27, 310-316.

(64) Choi, J.; Choi, D.-H.; Faix, O. *J. Wood Sci.* **2007,** 53, 309-313.

(65) Li, K.; Helm, R. F. *J. Agric. Food. Chem.* **1995,** 43, 2098-2103.

(66) Mogharab L.; Glasser W. G. *Tappi J.* **1976,** 59, 110-113.

(67) Valderrama, B.; Ayala, M.; Vazquez-Duhalt, R. *Chem. Biol.* **2002,** 9, 555-565.

(68) Veitch, N. C. *Phytochemistry* **2004,** 65, 249-259.

(69) Monier, M.; Ayad, D. M.; Wei, Y.; Sarhan, A. A. *Int. J. Biol. Macromol.* **2010,** 46, 324-330.

(70) Temoçin, Z.; Yiğitoğlu, M. *Bioprocess Biosystems Eng.* **2009,** 32, 467-474.

(71) Chen, F.; Tobimatsu, Y.; Havkin-Frenkel, D.; Dixon, R. A.; Ralph, J. *Proc. Natl. Acad. Sci. U.S.A.* **2012,** 109, 1772-1777.

(72) Grabber, J.; Schatz, P.; Kim, H.; Lu, F.; Ralph, J. *BMC Plant Biol.* **2010,** 10, 114.

# Chapter 8: Enzymatic Degradation of Lignin Thin Films

## 8.1 Abstract

Lignin degradation is crucial for maintaining the carbon cycle in the biosphere, and is an important feature of biofuel production, biopulping and biobleaching. This work highlights a real-time and label-free method to investigate the enzymatic degradation of lignin with controlled monolignol composition via a quartz crystal microbalance with dissipation monitoring (QCM-D) and atomic force microscopy (AFM). Different dehydrogenative polymer (DHP) and chemically isolated lignin thin films were prepared as model lignin substrates. Initial rates for degradation mediated by lignin peroxidase increased in the order: kraft lignin < organosolv lignin < milled wood lignin < guaiacyl DHP (G-DHP) < *p*-hydroxyphenyl DHP (H-DHP). In contrast, manganese peroxidase only degraded DHP films with a faster initial degradation rate for G-DHP than H-DHP. Morphological changes were clearly observed in AFM images for DHP films after enzymatic degradation.

## 8.2 Introduction

Lignin is a complex phenylpropanoid heteropolymer derived mainly from three hydroxycinnamyl alcohol monomers (monolignols), namely 4-hydroxycinnamyl (*p*-coumaryl), 4-hydroxy-3-methoxycinnamyl (coniferyl) and 4-hydroxy-3,5-dimethoxycinnamyl (sinapyl) alcohol. These monolignols are incorporated into lignin as *p*-hydroxyphenyl (H), guaiacyl (G), and syringyl (S) phenylpropanoids, respectively. Lignin is one of the most abundant biopolymers, and accounts for about 30% of the organic carbon on earth.[1] As one of the most hydrophobic components in plant cell walls, lignin plays important roles in strengthening and waterproofing the vascular tissues, thereby enabling the transport of water and nutrients, and protecting plants

against pathogens.[1-3] However, lignin also inhibits access to cellulose and hemicelluloses for fermentable sugar production, and increases the cost of cellulose fiber production during pulp and paper processing.[3, 4] Therefore, the degradation of lignin is not only essential for maintaining the carbon cycle in biosphere, but also crucial for many industrial applications, such as biofuel production, biopulping, biobleaching and wastewater treatment.[5-7]

Many lignin model compounds have been used to study the enzymatic degradation of lignin. Among these model compounds, dehydrogenative polymer (DHP) prepared via the *in vitro* polymerization of monolignols in the presence of HRP and $H_2O_2$,[8] is widely used. Recently, our group reported a method to prepare DHP thin films via surface-initiated dehydrogenative polymerization of monolignols.[9] The combination of these DHP thin films and various surface characterization techniques (e.g., a quartz crystal microbalance with dissipation monitoring (QCM-D)) is expected to provide a convenient and sensitive approach to study the enzymatic degradation of lignin. A QCM-D is an instrument based upon the piezoelectric properties of a quartz crystal that provides real-time and label-free monitoring of molecular adsorption on surfaces, enzymatic degradation of thin films and surface-initiated polymerizations. The QCM-D technique has been successfully used to study the enzymatic degradation of a variety of natural and synthetic polymers, including cellulose,[10-17] chitin,[18, 19] xyloglucan,[20] amylopectin,[21] pullulan,[21] dextran,[22] lipids,[23] poly-L-lysine-polygalacturonic acid multilayers,[24] and poly(ε-caprolactone).[25]

In this work, lignin thin films based upon DHP and chemically isolated lignins (including a kraft lignin (KL), an organosolv lignin (OL) and a milled wood lignin (MWL)) were prepared via surface-initiated dehydrogenative polymerization of monolignols and spincoating, respectively. The lignin peroxidase (LiP) and manganese peroxidase (MnP) catalyzed enzymatic

degradation of these lignin thin films was investigated by QCM-D and atomic force microscopy (AFM).

### 8.3 Experimental

All starting materials were used as received without further purification. Horseradish peroxidase (type I, lyophilized powder, 50 to 150 units·mg$^{-1}$ solid) with a molar mass of ~ 44 kDa was purchased from Sigma-Aldrich. Lignin peroxidase (0.17 units·mg$^{-1}$ determined via the oxidation of 3,4-dimethoxybenzyl alcohol at pH 3.0 and 30 °C) and manganese peroxidase (from *Phanerochaete chrysosporium*, a mixture of isozymes with a range of molar masses from 40 to 65 kDa, 21.3 units/g determined via the oxidation of $Mn^{2+}$ to $Mn^{3+}$ at pH 4.5 and 25 °C) were purchased from Sigma-Aldrich. Monolignols were synthesized through a two-step reaction from their corresponding hydroxycinnamic acids as reported previously.[9] Kraft lignin with a number-average molar mass ($M_n$) of ~ 5 kDa and a weight-average molar mass ($M_w$) of ~ 28 kDa was purchased from Sigma-Aldrich. Milled wood lignin (extracted from hemlock (*Tsuga sp*.) with aqueous dioxane, $M_n$ ~ 2.6 kDa and $M_w$ ~ 15.2 kDa)[26] and organosolv lignin (extracted from *Populus trichocharpa* with aqueous ethanol, $M_n$ ~ 1 kDa and $M_w$ ~ 3 kDa)[26] were kindly provided by Prof. Wolfgang G. Glasser, Virginia Tech. Hydrogen peroxide (30 wt %) for the polymerization of monolignols was purchased from Sigma-Aldrich. L-(+)-Tartaric acid and sodium hydroxide were purchased from Sigma-Aldrich and used for the preparation of buffer solutions (pH = 3.0 and 4.5). Manganese (II) sulfate monohydrate ($MnSO_4 \cdot H_2O$) was purchased from Sigma-Aldrich. Hydrogen peroxide (30 wt %), $H_2SO_4$ (conc), and ammonium hydroxide (28 % w/w) were used for QCM-D sensor cleaning and were purchased from EM Science, VWR International, and Fisher Scientific, respectively. All other chemicals and solvents were obtained

from Fisher Scientific. Ultrapure water with a resistivity of 18 MΩ·cm and < 5 ppb inorganic impurities was used in all experiments (Milli-Q Gradient A-10, Millipore).

Ellipsometry and AFM measurements were performed as outlined in Chapter 3.5. All QCM-D measurements were conducted as outlined in Chapter 3.5.4, with the following details specific to this work. The QCM-D sensor was placed in a flow cell and allowed to equilibrate for 1.5 to 2 h in buffer until a flat baseline was obtained. 1.0 mL of 0.3 mg·mL$^{-1}$ LiP or MnP (with 0.5 mM $MnSO_4$) solutions containing the indicated amount of $H_2O_2$ was introduced into the flow cell at a rate of 0.100 mL·min$^{-1}$ at 37 °C. The flow was stopped and the measurements were made in the absence of flow. Frequency ($\Delta f$) and dissipation ($\Delta D$) changes for the fundamental frequency (4.95 MHz for both silica coated quartz crystals) and six odd overtones ($n$ = 3 ~ 13) were monitored simultaneously. At the end of the measurement, buffer was flowed through the system for the removal of residual and reversibly adsorbed enzyme and products.

## 8.4 Results and Discussion

### 8.4.1 Lignin Thin Films

The contents of hydroxyl (-OH) and carboxyl (-COOH) groups of the chemically isolated lignin samples used in this work were determined by Jiang et al. via quantitative $^{31}$P NMR,[27] and the results are summarized in **Table 8.1**. The chemically isolated lignin thin films were prepared by spincoating KL, OL and MWL from their aqueous ammonia solutions onto gold surfaces following the procedure reported by Norgren et al.[28-30] As seen from the AFM height images provided in **Figure 8.1**, the spincoated KL, OL and MWL were smooth and uniform with RMS roughnesses around 2 nm.

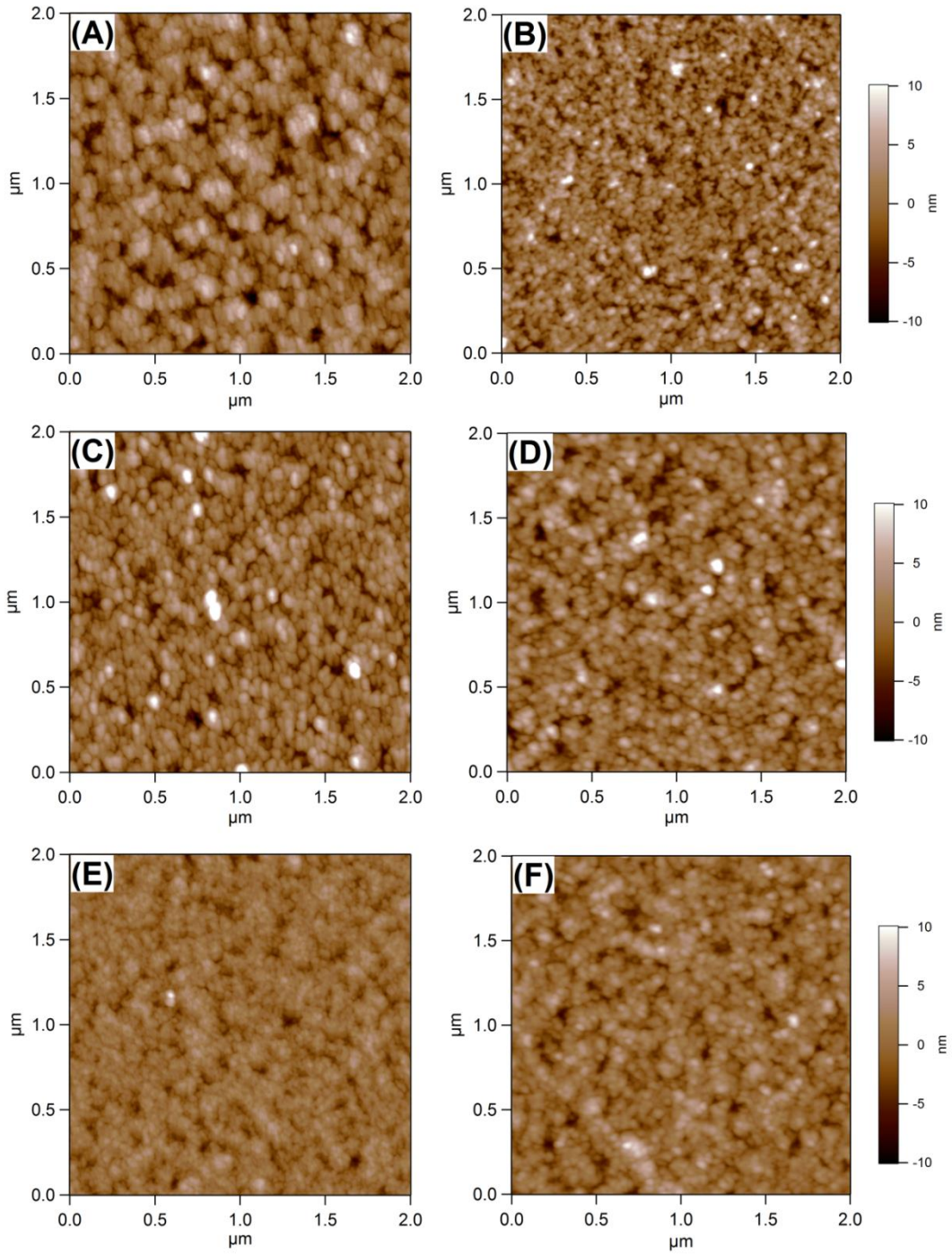


**Figure 8.1.** Representative 2 µm × 2 µm AFM height images of (A) MWL, (B) MWL incubated with LiP, (C) OL, (D) OL incubated with LiP, (E) KL and (F) KL incubated with LiP. RMS roughnesses for the AFM images are: (A) ~ 2.8 nm, (B) ~ 2.7 nm, (C) ~ 2.6 nm, (D) ~ 2.5 nm, (E) ~ 1.6 nm and (F) ~ 2.0 nm.

**Table 8.1.** Hydroxyl and carboxyl group contents of KL, OL and MWL determined by $^{31}$P NMR spectroscopy. Adapted from Jiang et al.[27]

| Functional group | KL | | OL | | MWL | |
|---|---|---|---|---|---|---|
| | mmol·g$^{-1}$ | % | mmol·g$^{-1}$ | % | mmol·g$^{-1}$ | % |
| Aliphatic -OH | 2.3 | 46 | 0.9 | 28 | 4.2 | 87 |
| Phenolic -OH | 2.5 | 49 | 2.2 | 66 | 0.5 | 10 |
| -COOH | 0.3 | 5 | 0.2 | 7 | 0.1 | 3 |
| Total | 5.1 | 100 | 3.3 | 100 | 4.8 | 100 |

The DHP thin films were prepared via surface-immobilized HRP-initiated dehydrogenative polymerization of monolignols (Chapter 7).[9] Representative QCM-D data are shown in **Figure 8.2**. As seen in **Figure 8.2**, the surface-immobilized HRP directly polymerized coniferyl alcohol and *p*-coumaryl alcohol in the presence of hydrogen peroxide to form DHP layers on gold surfaces. Both LiP and MnP were also physically immobilized on gold surfaces via adsorption from aqueous solutions, and the surface-immobilized LiP and MnP-catalyzed polymerization of monolignols was investigated using QCM-D. As indicated by the QCM-D data in **Figure 8.3**, no appreciable polymerization of coniferyl alcohol or *p*-coumaryl alcohol was observed on surfaces. In aqueous buffers, LiP has been reported to catalyze the coupling of ferulic acid to form dehydro-dimers and trimers,[31] while MnP has been reported to polymerize monolignols[32] and other phenolic compounds (e.g., guaiacol)[33] in aqueous organic solvents when Mn (II) and chelators were present. Therefore, the absence of monolignol polymerization in the presence of LiP and MnP might be attributed to the absence of redox-mediators and proper solvents, or the diffusion of radical species away from the interface before an insoluble molar mass was achieved.

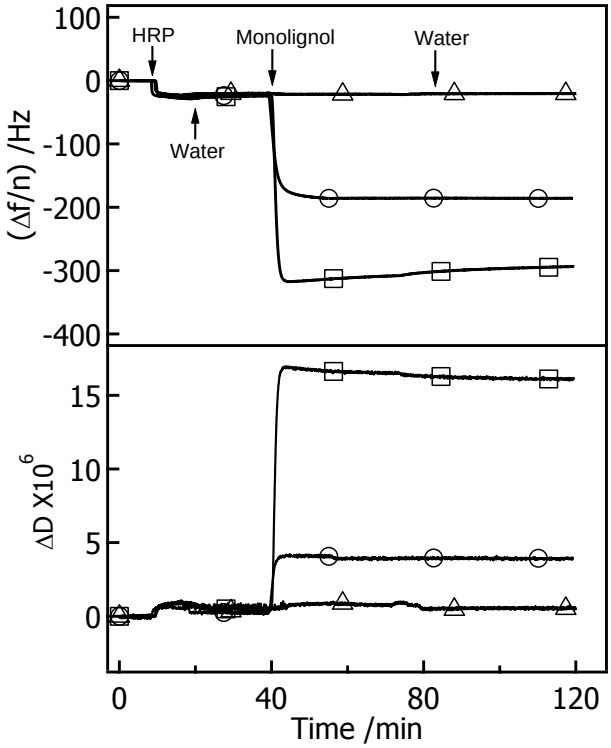


**Figure 8.2.** Representative Δ*f*/*n* and Δ*D* versus time at 20 °C for dehydrogenative polymerization of 0.5 mg·mL$^{-1}$ (□) coniferyl alcohol, (○) *p*-coumaryl alcohol and (Δ) sinapyl alcohol initiated by HRP immobilized on gold. Arrows and labels indicate where different solutions were introduced into the flow cell after the initial baselines were set in water. The HRP was adsorbed onto the surfaces from a 1.0 mg·mL$^{-1}$ aqueous solution and the aqueous monolignol solutions contained 20 mM $H_2O_2$.

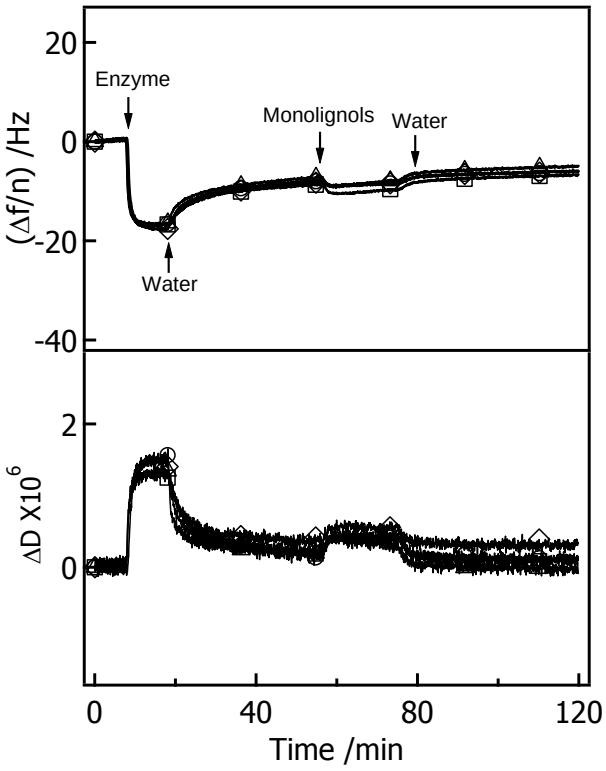


**Figure 8.3.** Representative Δ*f*/*n* and Δ*D* versus time at 20 °C for incubation of 0.5 mg·mL$^{-1}$ (○) coniferyl alcohol and (□) *p*-coumaryl alcohol initiated by LiP immobilized on gold, and (◊) coniferyl alcohol and (Δ) *p*-coumaryl alcohol initiated by MnP immobilized on gold. Arrows and labels indicate where different solutions were introduced into the flow cell after the initial baselines were set in water. The LiP and MnP were adsorbed onto the surfaces from a 0.3 mg·mL$^{-1}$ aqueous solution and the aqueous monolignol solutions contained 4 mM $H_2O_2$.

### 8.4.2 Enzymatic Degradation of Lignin Thin Films in the Presence of Lignin Peroxidase

The enzymatic degradation kinetics of these lignin thin films in the presence of LiP/$H_2O_2$ was monitored via QCM-D. **Figure 8.4** shows representative QCM-D data for the LiP-catalyzed degradation of DHP and spincoated films of isolated lignins in pH = 3.0 sodium tartrate buffer at 37 °C. The instantaneous frequency decrease, corresponding to Δ*f*/*n* ~ -40 Hz for all these lignin

films after the injection of LiP/$H_2O_2$ solutions (**Figure 8.4A**) was attributed to the adsorption of LiP onto the lignin films. The initial degradation rate could be obtained from the initial slopes of $\Delta f/n$ versus time after the minimum in $\Delta f/n$. The calculated initial degradation rates for H-DHP, G-DHP, MWL, OL and KL were 0.76 ± 0.08, 0.42 ± 0.02, 0.24 ± 0.03, 0.11 ± 0.02 and 0.05 ± 0.01 $Hz \cdot min^{-1}$, respectively, or 0.13 ± 0.02, 0.074 ± 0.003, 0.042 ± 0.005, 0.019 ± 0.004 and 0.009 ± 0.002 $mg \cdot m^{-2} \cdot min^{-1}$, respectively, assuming the Sauerbrey equation (Equation 3.1) is valid. The degradation rate decreased gradually possibly due to the exhaustion of $H_2O_2$ and the inactivation of LiP by $H_2O_2$ caused by the accumulation of a peroxy-Fe (III) porphyrin free-radical intermediate (compound III).[34, 35] Overall, $\Delta f/n$ (relative to the minima obtained upon enzyme adsorption) of 67, 50, 15, 7 and 5 Hz were observed for H-DHP, G-DHP, MWL, OL and KL films, respectively, after incubation with LiP for ~ 19 h. Fresh buffer was then introduced into the flow cell for the removal of the reversibly adsorbed LiP and degradation products, causing an additional $\Delta f/n$ increase. Changes in the viscoelastic properties of the lignin films were indicated by the energy dissipation profile (**Figure 8.4B**). The $\Delta D$ increase after the injection of enzyme solution was attributed to the adsorption of LiP and its coupled water. Maximums in $\Delta D$ ranged from ~ $2\times10^{-6}$ to ~ $3.5\times10^{-6}$ and were obtained almost instantaneously. For the enzymatic hydrolysis of cellulose thin films monitored by QCM-D, [11, 12] this point corresponded to the maximum accessibility of the films to enzymatic attack, and was considered to coincide with the maximum hydrolysis rate.

In nature, the composition of lignin varies among tissues and species. Softwood (gymnosperm) lignin contains mostly G with some H, and hardwood (dicotyledonous angiosperm) lignin is composed of G and S, with traces of H, whereas lignin from grasses is usually a mixture of H, G and S.[1, 3, 36] The microbial degradation of lignin with different

monolignol compositions by white-rot and brown-rot fungi has been reported,[37-39] however, the results are inconsistent because of the variation in lignin substrates and fungi. Faix et al.[37] demonstrated that G/S-DHP was degraded more readily than G-DHP by the white-rot fungus *P. chrysosporium*. However, Skyba et al.[38] studied the degradation of transgenic poplar with different S/G ratios by various white-rot and brown-rot fungi, and found that S-rich lignin was more resistant to microbial degradation. On the other hand, the effects of monolignol type and composition on the enzymatic degradation of lignin by isolated enzymes are rarely reported. As indicated by the QCM-D data in this work, the LiP-catalyzed degradation of H-DHP is a little faster than G-DHP, but the effect of a relatively larger surface area for the H-DHP aggregates cannot be ruled out. The lower degradability of the chemically isolated lignin films compared to the DHP films might be attributed to several factors: 1) lower enzyme accessibility caused by a relatively smaller surface area of the smooth chemically isolated lignin films compared to the DHP nano-aggregates; 2) structural changes of the chemically isolated lignin derived from fragmentation (mainly $\alpha$-aryl ether and $\beta$-aryl ether cleavage) and subsequent condensation during harsh chemical isolation conditions,[36, 40, 41] and the introduction of different chemical functional groups on lignin by the external nucleophiles (e.g., $OH^-$ and $HS^-$) in the cooking liquors; and 3) possible structural changes (e.g., formation of imine and salt with carbonyl and carboxylic acid groups) during the dissolution of lignin in aqueous ammonia,[42] followed by incomplete protonation of the lignin in the films prior to the enzyme studies.

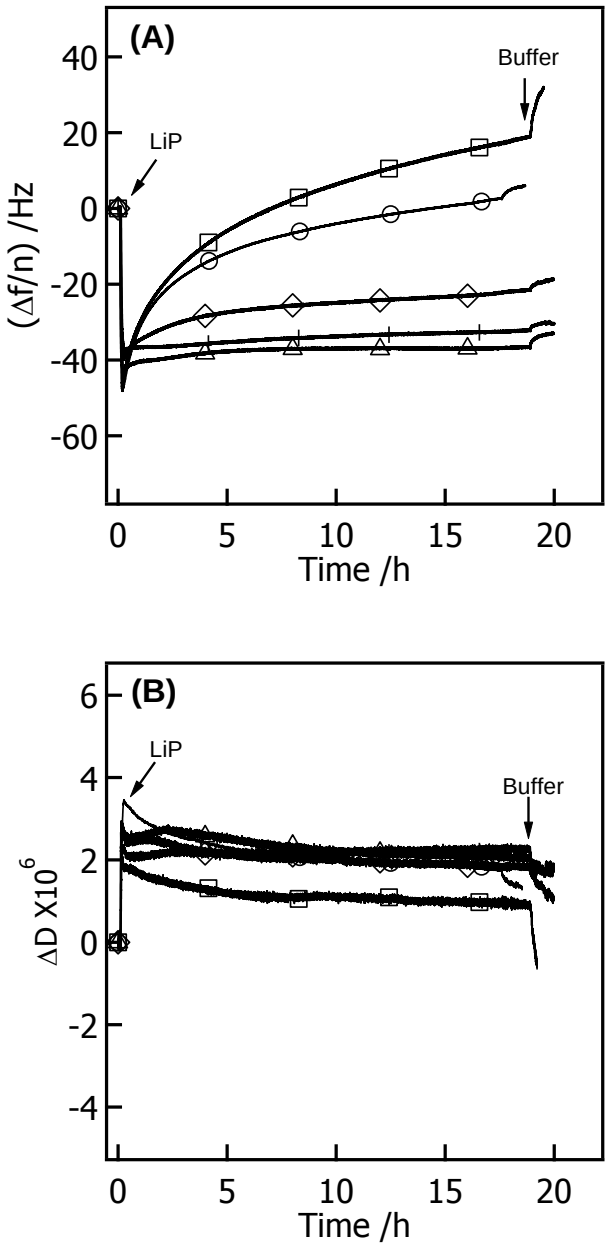


**Figure 8.4.** Representative (A) Δ*f*/*n* and (B) Δ*D* versus time at 37 °C for the enzymatic degradation of (○) G-DHP, (□) H-DHP, (◊) MWL, (Δ) OL and (|) KL films in the presence of 0.3 mg·mL$^{-1}$ LiP solution in a 10 mM sodium tartrate buffer (pH = 3.0) containing 2 mM $H_2O_2$. Arrows and labels indicate where different solutions were introduced into the flow cell after the initial baselines were set in buffer.

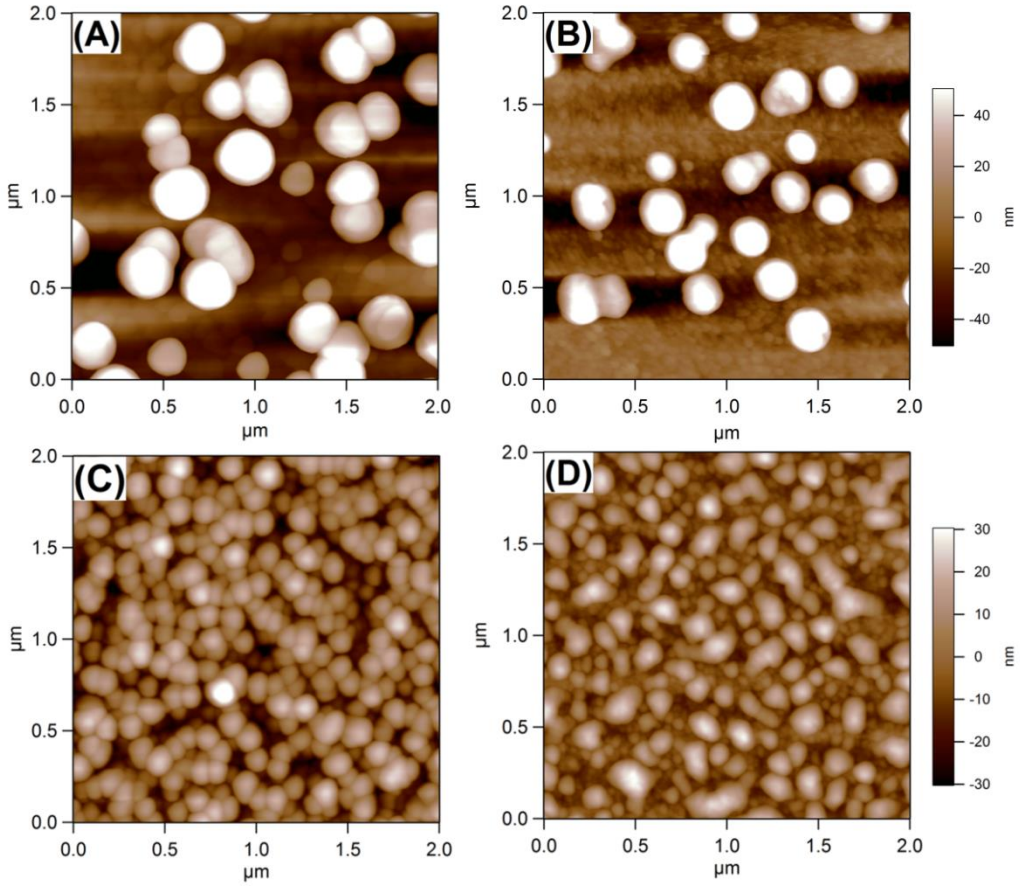


**Figure 8.5.** Representative 2 µm × 2 µm AFM height images of (A) G-DHP, (B) G-DHP incubated with LiP, (C) H-DHP and (D) H-DHP incubated with LiP. RMS roughnesses for each AFM image are: (A) ~ 33, (B) ~ 28, (C) ~ 12 and (D) ~ 10 nm.

Morphological changes of the lignin films associated with degradation were investigated by AFM. Height images from AFM for G-DHP and H-DHP before and after incubation with LiP/$H_2O_2$ are shown in **Figure 8.5**. As seen in **Figure 8.5A** and **B**, the average diameters of the irregular globular G-DHP aggregates on gold surfaces decreased from 275 ± 35 to 235 ± 20 nm after incubation with LiP/$H_2O_2$ for ~ 19 h, and the RMS roughness of the film also decreased from ~ 33 to ~ 28 nm. For H-DHP, where the initial state had a higher density of smaller but more uniform aggregates on gold surfaces, the density of the H-DHP aggregates decreased and

the sizes of the aggregates became less uniform after treatment with LiP/$H_2O_2$ as seen in **Figure 8.5D**. The RMS roughness of the H-DHP film in **Figure 8.5** also decreased from ~ 12 nm to ~ 10 nm. Height images from AFM for KL, OL and MWL before and after incubation with LiP/$H_2O_2$ are provided in **Figure 8.1**. As seen from **Figure 8.1**, the chemically isolated lignin films were still fairly smooth and uniform with similar RMS roughnesses before and after incubation with LiP/$H_2O_2$. This observation was also in agreement with the QCM-D data where only a small portion of these films were degraded by LiP.

### 8.4.3 Enzymatic Degradation of Lignin Thin Films in the Presence of Manganese Peroxidase

Manganese peroxidase has a strong preference for Mn (II) as a substrate and oxidation/reduction of Mn (II)/Mn (III) plays a crucial role in the MnP-catalyzed degradation of lignin. Therefore, 0.5 mM $MnSO_4$ was added to MnP solutions. Representative QCM-D data for the enzymatic degradation of DHP and chemically isolated lignin thin films in the presence of MnP/$H_2O_2$/Mn (II) in a sodium tartrate buffer (pH = 4.5) at 37 °C are provided in **Figure 8.6**. In contrast to LiP, MnP did not degrade chemically isolated lignin films, even though the DHP films still underwent degradation. As indicated by the QCM-D data, the degradation of G-DHP was much faster than H-DHP especially at the early stage of the enzymatic degradation with the calculated initial degradation rates of 2.35 ± 0.28 and 0.09 ± 0.02 Hz·min$^{-1}$, or 0.42 ± 0.05 and 0.016 ± 0.004 mg·m$^{-2}$·min$^{-1}$ (assuming the Sauerbrey Equation is valid) for G-DHP and H-DHP, respectively. Overall, $\Delta f/n$ (relative to the minima obtained upon enzyme adsorption) of 48 and 39 Hz were obtained for G-DHP and H-DHP films after incubation with MnP for ~ 19 h and rising with fresh buffer. On the other hand, MnP irreversibly adsorbed onto KL, OL and MWL films without yielding any significant degradation after incubation with MnP at 37 °C for times

as long as ~ 19 h. As seen from **Figure 8.6B**, the dissipation decreased slowly in the DHP films after the initial increase. The ΔD trends for DHP films incubated with MnP were similar to the DHP films incubated with LiP. On the other hand, the dissipation remained constant for KL, OL and MWL films, in agreement with the frequency data and the interpretation that the chemically isolated lignin films were not degraded by MnP.

Differences in MnP and LiP reactivity are partially explained by their redox potentials. For the case of LiP, it has a higher redox potential (1.2 ~ 1.4 V) than classical peroxidases[43, 44] and the Mn (III)-oxalate complex (~ 0.8 V).[45] Thus, LiP could oxidize both phenolic and non-phenolic lignin, but MnP was believed to only oxidize phenolic lignin.[46] The applications of LiP and MnP in biopulping and biobleaching of lignin-rich waste have attracted increasing interest over the last two decades. Lignin peroxidase was reported to be a more effective lignin degrader than MnP in the treatment of softwood kraft pulp[47] and olive mill wastewaters,[48] however, controversies exist.[49] In the biobleaching of kraft pulp, MnP did not degrade lignin to soluble fragments without the assistance of other enzymes but led to a rapid demethoxylation of the lignin.[47, 50] In this work, the degradation rate for G-DHP in the first ~ 1 h after the injection of the MnP solution was much faster than H-DHP even though H-DHP films had relatively greater surface area than G-DHP films. This observation may arise from the mass loss caused by the demethoxylation of the G-DHP. The lack of degradation for the KL, OL and MWL films was most likely caused by: 1) the relatively smaller redox potential of the catalytic species in the MnP system compared to LiP system; 2) the lower enzyme accessibility of the smooth chemically isolated lignin films compared to the DHP nano-aggregates; and 3) possible structural changes during chemical isolation and dissolution as discussed in Chpater 8.4.2.

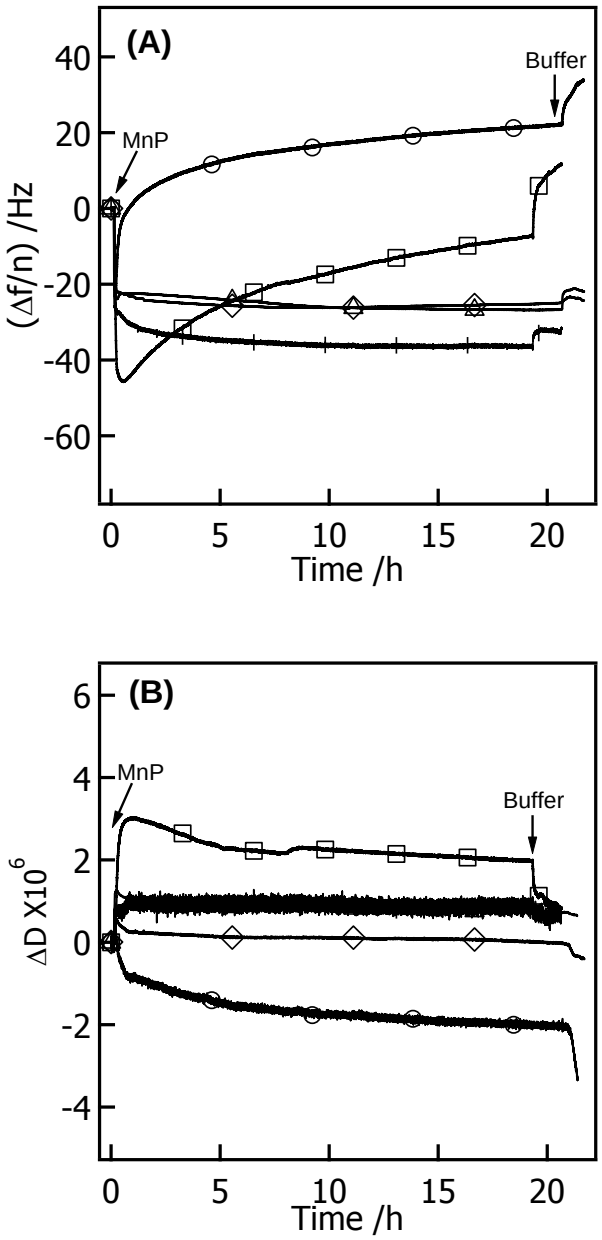


**Figure 8.6.** Representative (A) Δ*f*/*n* and (B) Δ*D* versus time at 37 °C for the enzymatic degradation of (○) G-DHP, (□) H-DHP, (◊) MWL, (Δ) OL and (|) KL films in the presence of 0.3 mg·mL$^{-1}$ MnP solution in a 10 mM sodium tartrate buffer (pH = 4.5) containing 2 mM $H_2O_2$ and 0.5 mM $MnSO_4$. Arrows and labels indicate where different solutions were introduced into the flow cell after the initial baselines were set in buffer.

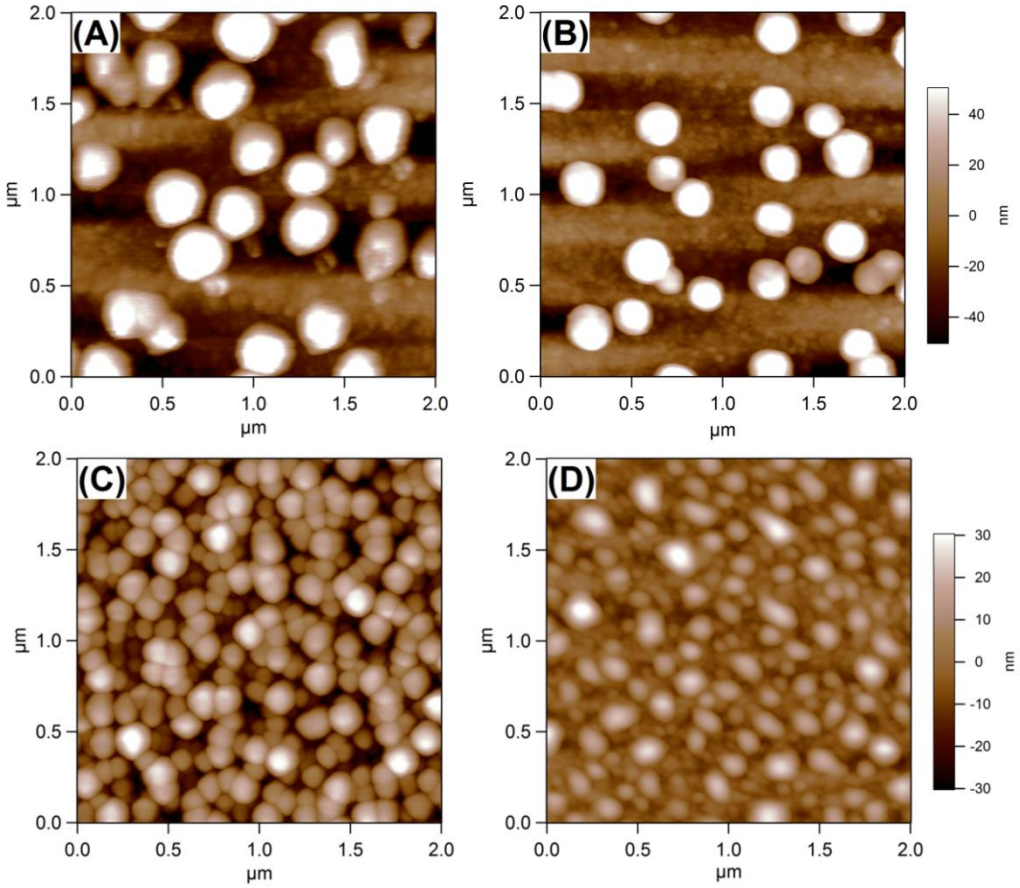


**Figure 8.7.** Representative 2 µm × 2 µm AFM height images of (A) G-DHP, (B) G-DHP incubated with MnP, (C) H-DHP and (D) H-DHP incubated with MnP. RMS roughnesses for each AFM image are: (A) ~ 34, (B) ~ 29, (C) ~ 13 and (D) ~ 9 nm.

The AFM height images for G-DHP and H-DHP before and after incubation with MnP in the presence of $H_2O_2$ and Mn (II) are shown in **Figure 8.7**. Observed morphological changes were comparable to those observed for LiP-catalyzed degradation of DHP films. As seen in **Figure 8.7**, the average diameters of the irregular globular G-DHP aggregates decreased from 290 ± 30 to 250 ± 25 nm after incubation with MnP for ~ 19 h, and the RMS roughness of the film also decreased from ~ 34 to ~ 29 nm. For the H-DHP films in **Figure 8.7**, the aggregate density and

size of the aggregates decreased with time for the MnP treatment, and the RMS roughness of the film decreased from ~ 13 nm to ~ 9 nm.

As controls, the DHP films were incubated with sodium tartrate buffer and buffer containing 2 mM $H_2O_2$ at 37 °C, and the representative QCM-D data is provided in **Figure 8.8** and **Figure 8.9**. As seen in **Figure 8.8**, the DHP films were relatively stable when incubated with pH = 3.0 and pH = 4.5 sodium tartrate buffers. However, the DHP films were slightly degraded when incubated with buffer containing 2 mM $H_2O_2$ as indicated by the small $\Delta f/n$ increase in **Figure 8.9**. This slight degradation of the DHP films might be caused by free radicals generated during the decomposition of $H_2O_2$. The DHP films were also incubated with HRP/$H_2O_2$, and representative QCM-D data are shown in **Figure 8.10**. As seen in **Figure 8.10**, HRP adsorbed onto the DHP films and yielded $\Delta f/n$ decreases of ~ -40 and -45 Hz for G-DHP and H-DHP films, respectively. However, no appreciable degradation of the G-DHP or H-DHP film was observed. Hartenstein et al.[51] investigated the action of HRP on chemically isolated hardwood lignins and lignin model compounds (e.g., $\alpha$-methyl guaiacyl alcohol and $\alpha$-methyl syringyl alcohol) in the presence of $H_2O_2$ in aqueous buffers, and the results showed that HRP/$H_2O_2$ induced the rearrangement of lignin model compounds (e.g., oxidation of guaiacyl alcohol to vanillone) but not the degradation or depolymerization of the lignin substrates. On the other hand, HRP/$H_2O_2$ was reported to degrade DHP, MWL and KL extensively in aqueous organic media (e.g., dioxane, dimethylformamide or methyl formate containing a 5% aqueous buffer).[52, 53]

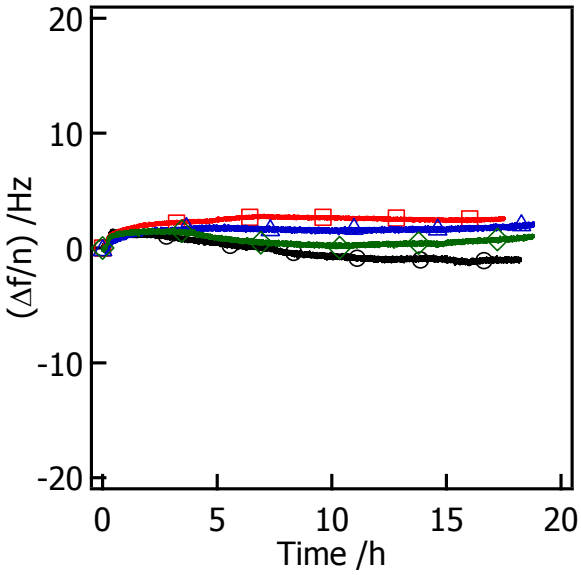


**Figure 8.8.** Representative Δ*f*/*n* versus time for a (○) G-DHP film incubated at pH = 3.0 buffer, (□) G-DHP film incubated at pH = 4.5 buffer, (Δ) H-DHP film incubated at pH = 3.0 buffer and (◊) H-DHP film incubated at pH = 4.5 buffer at 37 °C.

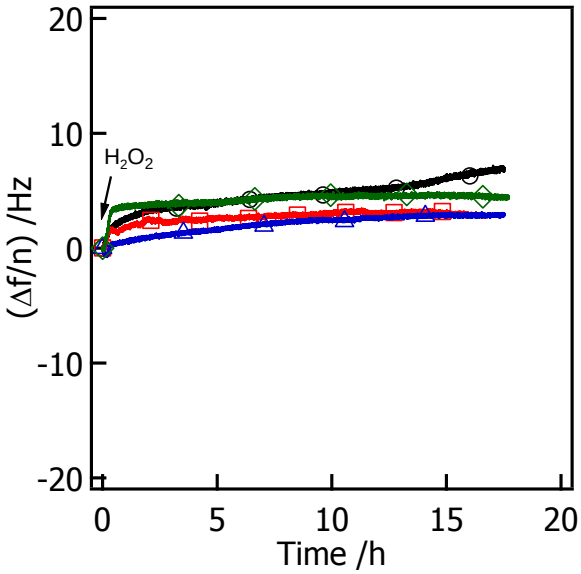


**Figure 8.9.** Representative Δ*f*/*n* versus time at 37 °C for the degradation of a (○) G-DHP in pH = 3.0 buffer, (□) G-DHP in pH = 4.5 buffer, (Δ) H-DHP in pH = 3.0 buffer and (◊) H-DHP in pH = 4.5 buffer containing 2 mM $H_2O_2$. Arrows and labels indicate where different solutions were introduced into the flow cell after the initial baselines were set in buffer.

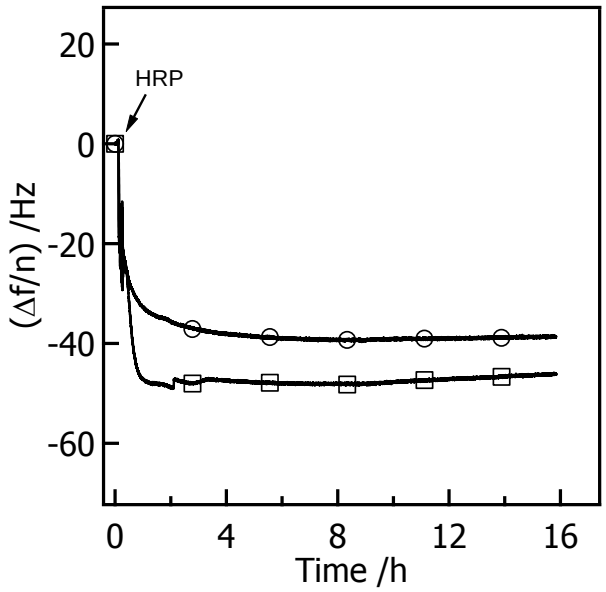


**Figure 8.10.** Representative Δ*f*/*n* versus time at 37 °C for the incubation of (○) G-DHP and (□) H-DHP in the presence of 0.3 mg·mL$^{-1}$ HRP aqueous solution containing 2 mM $H_2O_2$. Arrows and labels indicate where different solutions were introduced into the flow cell after the initial baselines were set in water.

### 8.5 Conclusions

In summary, this work highlights a real-time and label-free method to study the enzymatic degradation of lignin via QCM-D and AFM. Thin films of DHP were prepared by surface-immobilized HRP-initiated dehydrogenative polymerization of monolignols, and chemically isolated lignin films were prepared via spincoating KL, OL and MWL from their aqueous ammonia solutions onto gold surfaces. Data from QCM-D indicated that LiP degraded both DHP and chemically isolated lignin films where the initial degradation rate increased in the order: KL < OL < MWL < G-DHP < H-DHP. However, MnP only degraded DHP films and not the chemically isolated lignin films. The initial degradation rate for G-DHP was faster than H-DHP. Images from AFM were consistent with degradation rather than lignin desorption where G-DHP

aggregates had smaller average diameters and H-DHP aggregates had lower DHP particle densities and smaller sizes after incubation with LiP/$H_2O_2$ or MnP/$H_2O_2$/Mn (II). The lignin thin films and the combination of various surface characterization techniques are expected to provide a convenient and promising way to investigate mechanistic aspects of enzymatic degradation of DHP lignin with controlled monolignol type and composition, and for isolated lignins obtained under different processing conditions.

### 8.6 References


(1) Boerjan, W.; Ralph, J.; Baucher, M. *Annu. Rev. Plant Biol.* **2003,** 54, 519-546.

(2) Whetten, R.; Sederoff, R. *Plant Cell* **1995,** 7, 1001-1013.

(3) Bonawitz, N. D.; Chapple, C. *Annu. Rev. Genet.* **2010,** 44, 337-363.

(4) Vanholme, R.; Cesarino, I.; Rataj, K.; Xiao, Y.; Sundin, L.; Goeminne, G.; Kim, H.; Cross, J.; Morreel, K.; Araujo, P.; Welsh, L.; Haustraete, J.; McClellan, C.; Vanholme, B.; Ralph, J.; Simpson, G. G.; Halpin, C.; Boerjan, W. *Science* **2013,** 341, 1103-1106.

(5) Abdel-Hamid, A. M.; Solbiati, J. O.; Cann, I. K. *Adv. Appl. Microbiol.* **2013,** 82, 1-28.

(6) Hatakka, A. Biodegradation of Lignin. In *Biopolymers Online*, Wiley-VCH Verlag GmbH & Co. KGaA: 2005.

(7) Scott, G. M.; Akhtar, M. Biotechnological Applications of Lignin-Degrading Fungi (White-Rot Fungi). In *Biopolymers Online*, Wiley-VCH Verlag GmbH & Co. KGaA: 2005.

(8) Freudenberg, K. *Angew. Chem.* **1956,** 68, 508-512.

(9) Wang, C.; Qian, C.; Roman, M.; Glasser, W. G.; Esker, A. R. *Biomacromolecules* **2013,** 14, 3964-3972.

(10) Rojas, O. J.; Jeong, C.; Turon, X.; Argyropoulos, D. S. Measurement of Cellulase Activity with Piezoelectric Resonators. In *Materials, Chemicals, and Energy from Forest Biomass*, American Chemical Society: 2007; Vol. 954, pp 478-494.

(11) Turon, X.; Rojas, O. J.; Deinhammer, R. S. *Langmuir* **2008,** 24, 3880-3887.

(12) Hu, G.; Heitmann, J. A.; Rojas, O. J. *J. Phys. Chem. B* **2009,** 113, 14761-14768.

(13) Cheng, G.; Liu, Z.; Murton, J. K.; Jablin, M.; Dubey, M.; Majewski, J.; Halbert, C.; Browning, J.; Ankner, J.; Akgun, B.; Wang, C.; Esker, A. R.; Sale, K. L.; Simmons, B. A.; Kent, M. S. *Biomacromolecules* **2011,** 12, 2216-2224.

(14) Cheng, G.; Datta, S.; Liu, Z.; Wang, C.; Murton, J. K.; Brown, P. A.; Jablin, M. S.; Dubey, M.; Majewski, J.; Halbert, C. E.; Browning, J. F.; Esker, A. R.; Watson, B. J.; Zhang, H.; Hutcheson, S. W.; Huber, D. L.; Sale, K. L.; Simmons, B. A.; Kent, M. S. *Langmuir* **2012,** 28, 8348-8358.

(15) Ahola, S.; Turon, X.; Österberg, M.; Laine, J.; Rojas, O. J. *Langmuir* **2008,** 24, 11592-11599.

(16) Aulin, C.; Ahola, S.; Josefsson, P.; Nishino, T.; Hirose, Y.; Österberg, M.; Wågberg, L. *Langmuir* **2009,** 25, 7675-7685.

(17) Kittle, J. D.; Du, X.; Jiang, F.; Qian, C.; Heinze, T.; Roman, M.; Esker, A. R. *Biomacromolecules* **2011,** 12, 2881-2887.

(18) Wang, C.; Kittle, J. D.; Qian, C.; Roman, M.; Esker, A. R. *Biomacromolecules* **2013,** 14, 2622-2628.

(19) Wang, C.; Esker, A. R. *Carbohydr. Polym.* **2014,** 102, 151-158.

(20) Nordgren, N.; Eklöf, J.; Zhou, Q.; Brumer, H.; Rutland, M. W. *Biomacromolecules* **2008,** 9, 942-948.

(21) Nishino, H.; Nihira, T.; Mori, T.; Okahata, Y. *J. Am. Chem. Soc.* **2004,** 126, 2264-2265.

(22) Nihira, T.; Mizuno, M.; Tonozuka, T.; Sakano, Y.; Mori, T.; Okahata, Y. *Biochemistry* **2005,** 44, 9456-9461.

(23) Snabe, T.; Petersen, S. B. *Chem. Phys. Lipids* **2003,** 125, 69-82.

(24) Westwood, M.; Roberts, D.; Parker, R. *Carbohydr. Polym.* **2011,** 84, 960-969.

(25) Hou, Y.; Chen, J.; Sun, P.; Gan, Z.; Zhang, G. *Polymer* **2007,** 48, 6348-6353.

(26) Glasser, W. G.; Barnett, C. A.; Sano, Y. *J. Appl. Polym. Sci.: Appl. Polym. Symp.* **1983,** 37, 441-460.

(27) Jiang, F. PhD Thesis, Virginia Tech, Blacksburg, VA, 2011.

(28) Norgren, M.; Notley, S. M.; Majtnerova, A.; Gellerstedt, G. *Langmuir* **2006,** 22, 1209-1214.

(29) Norgren, M.; Gärdlund, L.; Notley, S. M.; Htun, M.; Wågberg, L. *Langmuir* **2007,** 23, 3737-3743.

(30) Notley, S. M.; Norgren, M. *Langmuir* **2010,** 26, 5484-5490.

(31) Ward, G.; Hadar, Y.; Bilkis, I.; Konstantinovsky, L.; Dosoretz, C. G. *J. Biol. Chem.* **2001,** 276, 18734-18741.

(32) Yoshida, S.; Chatani, A.; Tanahashi, M.; Honda, Y.; Watanabe, T.; Kuwahara, M. *Holzforschung* **1998,** 52, 282-286.

(33) Iwahara, K.; Honda, Y.; Watanabe, T.; Kuwahara, M. *Appl. Microbiol. Biotechnol.* **2000,** 54, 104-111.

(34) Veitch, N. C. *Phytochemistry* **2004,** 65, 249-259.

(35) Chung, N.; Aust, S. D. *Arch. Biochem. Biophys.* **1995,** 316, 851-855.

(36) Zakzeski, J.; Bruijnincx, P. C. A.; Jongerius, A. L.; Weckhuysen, B. M. *Chem. Rev.* **2010,** 110, 3552-3599.

(37) Faix, O.; Mozuch, M. D.; Kirk, T. K. *Holzforschung* **1985,** 39, 203-208.

(38) Skyba, O.; Douglas, C. J.; Mansfield, S. D. *Appl. Environ. Microbiol.* **2013,** 79, 2560-2571.

(39) Obst, J.; Highley, T.; Miller, R. Influence of Lignin Type on the Decay of Woody Angiosperms by Trametes Versicolor. In *Mycotoxins, Wood Decay, Plant Stress, Biocorrosion, and General Biodeterioration*, Llewellyn, G.; Dashek, W.; O'Rear, C., Eds.; Springer US: 1994; Vol. 4, pp 357-374.

(40) Chakar, F. S.; Ragauskas, A. J. *Ind. Crop. Prod.* **2004,** 20, 131-141.

(41) McDonough, T. J. *Tappi J.* **1993,** 76, 186-193.

(42) Rahikainen, J. L.; Martin-Sampedro, R.; Heikkinen, H.; Rovio, S.; Marjamaa, K.; Tamminen, T.; Rojas, O. J.; Kruus, K. *Bioresour. Technol.* **2013,** 133, 270-278.

(43) Kersten, P. J.; Kalyanaraman, B.; Hammel, K. E.; Reinhammar, B.; Kirk, T. K. *Biochem. J* **1990,** 268, 475-480.

(44) Smith, A. T.; Doyle, W. A.; Dorlet, P.; Ivancich, A. *Proc. Natl. Acad. Sci. U.S.A.* **2009**.

(45) Cui, F.; Dolphin, D. *Holzforschung* **1990,** 44, 279-283.

(46) Hammel, K. E.; Jensen, K. A.; Mozuch, M. D.; Landucci, L. L.; Tien, M.; Pease, E. A. *J. Biol. Chem.* **1993,** 268, 12274-12281.

(47) Reid, I. D.; Paice, M. G. *Appl. Environ. Microbiol.* **1998,** 64, 2273-2274.

(48) Sayadi, S.; Ellouz, R. *Appl. Environ. Microbiol.* **1995,** 61, 1098-103.

(49) Michel, F. C.; Dass, S. B.; Grulke, E. A.; Reddy, C. A. *Appl. Environ. Microbiol.* **1991,** 57, 2368-2375.

(50) Paice, M. G.; Reid, I. D.; Bourbonnais, R.; Archibald, F. S.; Jurasek, L. *Appl. Environ. Microbiol.* **1993,** 59, 260-265.

(51) Hartenstein, R.; Neuhauser, E. F.; Mulligan, R. M. *Phytochemistry* **1977,** 16, 1855-1857.

(52) Dordick, J. S.; Marletta, M. A.; Klibanov, A. M. *Proc. Natl. Acad. Sci. U.S.A.* **1986,** 83, 6255-6257.

(53) Lewis, N. G.; Razal, R. A.; Yamamoto, E. *Proc. Natl. Acad. Sci. U.S.A.* **1987,** 84, 7925-7927.

# Chapter 9: Lignin Thin Films and Their Interactions with Hemicelluloses

## 9.1 Abstract

Interactions between hemicelluloses and lignin are of fundamental importance for understanding the structure and formation of secondary plant cell walls. In this work, smooth and uniform lignin thin films were prepared by spincoating a kraft lignin (KL), organosolv lignin (OL) and milled wood lignin (MWL) from aqueous ammonia solutions onto gold substrates, and the physical interactions between various hemicelluloses and these lignin thin films were investigated with a quartz crystal microbalance with dissipation monitoring (QCM-D) and surface plasmon resonance (SPR). The QCM-D data showed that xyloglucan (from tamarind seeds) and glucomannan (from konjac) irreversibly adsorbed onto the lignin surfaces, galactomannan (from carob) reversibly adsorbed onto the lignin surfaces, and glucuronoarabinoxylan (from spruce) and arabinoxylan (from wheat) showed weak interactions with the lignin surfaces. Adsorption isotherms from QCM-D and SPR for xyloglucan adsorption onto the lignin thin films indicated that xyloglucan showed stronger affinity for KL and OL surfaces than MWL surfaces. Through the combination of QCM-D and SPR, it was found that xyloglucan formed less hydrated layers on lignin surfaces compared to regenerated cellulose surfaces, and the adsorbed xyloglucan layers on different lignin surfaces had similar percentages of coupled water within experimental error.

## 9.2 Introduction

Lignin and hemicelluloses bind to each other through both covalent and physical interactions in plant cell walls. Many efforts have been made to study covalent interactions between lignin and hemicelluloses in lignin-carbohydrate complexes (LCCs) from native wood,[1-3] chemical

pulps (e.g., kraft pulp)[1, 4] and model systems (e.g., dehydrogenative polymers formed in the presence of hemicelluloses).[5-7] Several types of covalent bonds in LCCs have been reported, including benzyl ethers, benzyl esters, phenyl glycosidic and carbon-carbon bonds, which are either formed in native wood or during pulping.[4, 8, 9] However, physical interactions between lignin and hemicelluloses are rarely reported.[10, 11]

Smooth and uniform lignin thin films provide good model surfaces for investigating physical interactions between lignin and hemicelluloses. Lignin or lignin model compounds from different resources, including kraft lignin (KL) from softwood,[12-15] milled wood lignin (MWL) from softwood[10, 11, 15, 16] and hardwood,[15] organosolv lignin (OL) from softwood[17] and sugar cane bagasse,[17-20] and dehydrogenative polymer[21-23] have been used to prepare lignin thin films on various substrates via spincoating,[12-15, 22] Langmuir-Blodgett deposition[17-20] and solvent casting.[21] Lignin thin films along with quartz crystal microbalance with dissipation monitoring (QCM-D) and surface plasmon resonance (SPR) studies afford an opportunity for real-time and label-free monitoring of molecular interactions (e.g., adsorption and desorption) between lignin and other compounds. Both QCM-D and SPR have been used to investigate cellulose-hemicellulose interactions,[24-26] and QCM-D has also been used to characterize the adsorption of polyelectrolytes,[13, 14] laccases[16] and hemicelluloses[10, 11] onto lignin surfaces. By combining these two techniques, both the adsorbed mass and the viscoelastic properties of the adsorbed layers could be determined.[27-30]

In this work, lignin thin films were prepared by spincoating KL, OL and MWL aqueous ammonia solutions onto gold substrates, and these thin films were determined to be smooth and uniform via atomic force microscopy (AFM). Adsorption of xyloglucan (from tamarind seeds), glucuronoarabinoxylan (from spruce), arabinoxylan (from wheat), glucomannan (from konjac)

and galactomannan (from carob) onto these lignin thin films was investigated using QCM-D. Complete adsorption isotherms for xyloglucan adsorption onto the lignin films were obtained using QCM-D and SPR. The combination of the two techniques allowed estimation of water contents for the adsorbed xyloglucan layers. This information is expected to enhance fundamental understanding of the physical interactions between hemicelluloses and lignin in plant cell walls.

## 9.3 Experimental

**Materials.** Kraft lignin with a number-average molar mass ($M_n$) of ~ 5 kDa and a weight-average molar mass ($M_w$) of ~ 28 kDa was purchased from Sigma-Aldrich. Milled wood lignin (extracted from hemlock (T*suga sp*.) with aqueous dioxane, $M_n$ ~ 2.6 kDa and $M_w$ ~ 15.2 kDa)[31] and organosolv lignin (extracted from P*opulus trichocharpa* with aqueous ethanol, $M_n$ ~ 1 kDa and $M_w$ ~ 3 kDa)[31] were kindly provided by Prof. Wolfgang G. Glasser, Virginia Tech. Xyloglucan (from tamarind seeds, $M_n$ ~ 202 kDa, contains ~ 45 % glucose, ~ 34 % xylose, ~ 18 % galactose and ~ 3 % arabinose), glucomannan (from konjac, $M_n$ ~ 120 kDa, contains ~ 60 % mannose and ~ 40 % glucose), galactomannan (from carob, $M_n$ ~ 200 kDa, contains ~ 78 % mannose and ~ 22 % galactose) and arabinoxylan (from wheat, $M_n$ ~ 150 kDa, contains ~ 37 % arabinose, ~ 61 % xylose) were purchased from Megazyme, Inc. and used as received. The isolation and characterization of glucuronoarabinoxylan (from spruce, $M_w$ ~ 13 kDa, contains ~ 81 % xylose, ~ 10 % 4-O-methyl-glucuronic acid, ~ 7 % arabinose and ~ 2 % other sugars (mannose, glucose and galactose)) was reported elsewhere.[32] Hydrogen peroxide (30 wt %), $H_2SO_4$ (conc), and ammonium hydroxide (28 % w/w) were used to clean the QCM-D and SPR sensors and were purchased from EM Science, VWR International, and Fisher Scientific, respectively. All other chemicals and solvents were obtained from Fisher Scientific. Ultrapure

water with a resistivity of 18 MΩ·cm and < 5 ppb inorganic impurities was used in all experiments (Milli-Q Gradient A-10, Millipore).

AFM and ellipsometry measurements were performed as outlined in Chapter 3.5. All QCM-D measurements were conducted as outlined in Chapter 3.5.4, with the following details specific to this work. The QCM-D sensor was placed in a flow cell and allowed to equilibrate for 1 to 2 h in water to obtain a stable baseline at 20 °C. Hemicellulose solutions (100 $mg \cdot L^{-1}$) or xyloglucan solutions with different concentrations in ultrapure water were then introduced at the rate of 0.200 $mL \cdot min^{-1}$ until equilibrium adsorption was obtained. At the end of the measurement, water was flowed through the system for the removal of reversibly adsorbed hemicelluloses.

All SPR measurements were conducted as outlined in Chapter 3.5.5, with the following details specific to this work. After the SPR sensor slide was placed in the SPR flow cell, water was introduced into the flow cell at a flow rate of 0.200 $mL \cdot min^{-1}$ for 1 to 2 h at 20 °C until a stable baseline was obtained. Degassed xyloglucan solutions with different concentrations were then pumped into the flow cell at the same flow rate and temperature. Xyloglucan solution flowed over the sensor until equilibrium adsorption was obtained. At the end of the measurement, water was flowed through the system for the removal of reversibly adsorbed xyloglucan. Changes in resonant angle were converted to surface concentration ($\Gamma_{SPR}$) using the equation of de Feijter et al. (Equation 3.4) with the parameters listed in Chapter 3.5.5.

## 9.4 Results and Discussion

### 9.4.1 Lignin Thin Films

Lignin films were spincoated from aqueous ammonia solutions with subsequent washing of the films to ensure re-protonation of the films. Norgren et al. previously showed that this process

leads to almost fully protonated lignin.[12] Properties of lignins are intimately tied to the isolation process. In a kraft process, lignin is fragmented by the hydroxide and hydrosulfide anions in the cooking liquor (solution of sodium hydroxide and sodium sulfide) at ~ 170 °C. Cleavage of the $\alpha$-aryl ether and $\beta$-aryl ether bonds is primarily responsible for the fragmentation.[33] For an organosolv process, lignin is extracted from wood chips with organic solvents (e.g., alcohols, ketones and glycols) with a little water, acid or base as a catalyst under relatively mild conditions.[34, 35] The prevalent reaction is also the cleavage of the ether bonds under both acidic and alkaline conditions.[35] In general, MWL is isolated via neutral solvent (e.g., aqueous dioxane or acetone) extraction of finely milled wood meal at room temperature. As such, MWL is considered to a structure that is more representative of native lignin (especially lignin in secondary cell walls).[15, 36] Jiang et al. previously used $^{31}$P NMR (with 2-chloro-4,4,5,5-tetramethyl-1,3,2-dioxaphospholane as a phosphitylation reagent) to determine the hydroxyl (-OH) and carboxyl (-COOH) group contents in KL, OL and MWL samples used in this study.[37] Results from his work are summarized in **Table 9.1**.

**Table 9.1.** Hydroxyl and carboxyl group contents of KL, OL and MWL determined by $^{31}$P NMR spectroscopy. Adapted from Jiang et al.[37]

| Functional group | KL | | OL | | MWL | |
|---|---|---|---|---|---|---|
| | mmol·g$^{-1}$ | % | mmol·g$^{-1}$ | % | mmol·g$^{-1}$ | % |
| Aliphatic -OH | 2.3 | 46 | 0.9 | 28 | 4.2 | 87 |
| Phenolic -OH | 2.5 | 49 | 2.2 | 66 | 0.5 | 10 |
| -COOH | 0.3 | 5 | 0.2 | 7 | 0.1 | 3 |
| Total | 5.1 | 100 | 3.3 | 100 | 4.8 | 100 |

Morphologies of the spincoated KL, OL and MWL films were investigated by AFM, and the AFM height images are shown in **Figure 9.1**. As seen in **Figure 9.1**, all lignin films were smooth and homogeneous, although individual, small and uniform lignin particles were observed on all lignin surfaces. The RMS roughnesses of the images in **Figure 9.1** are ~ 2.0, 2.3 and 2.6 nm for KL, OL and MWL films on gold substrates, respectively. On the basis of contact angle data of water, diiodomethane and formamide, Jiang et al. also calculated the surface energies as well as the polar and dispersive contributions to the surface energies for the lignin films using the Owens–Wendt–Rabel–Kaelble method.[37] Surface energy results are summarized in **Table 9.2**. The water contact angles for KL, OL and MWL films were ~ 62 , 65 and 54°.[37] For comparison purposes with other literature, the water contact angles for MWL films are similar to the value reported by Norgren et al. for spincoated MWL films (~ 52 ° for softwood MWL and ~ 56 ° for hardwood MWL),[15] while the water contact angles for KL films were higher than those previously reported for spincoated KL films (~ 46°),[12, 15] which might be attributed to differences in the lignin source and isolation procedures.

**Table 9.2.** Surface energies and their polar and dispersive components calculated from Owens–Wendt–Rabel–Kaelble method.[a] Adapted from Jiang et al.[37]

| Functional group | KL /mN·m$^{-1}$ | OL /mN·m$^{-1}$ | MWL /mN·m$^{-1}$ |
|---|---|---|---|
| Surface energy | 55.5 ± 0.5 | 54.2 ± 1.7 | 58.1 ± 2.9 |
| Polar component | 9.3 ± 0.2 | 8.1 ± 0.7 | 13.4 ± 1.4 |
| Dispersive component | 46.2 ± 0.5 | 46.1 ± 1.6 | 44.7 ± 2.5 |

[a]Error bars represent ± one standard deviation

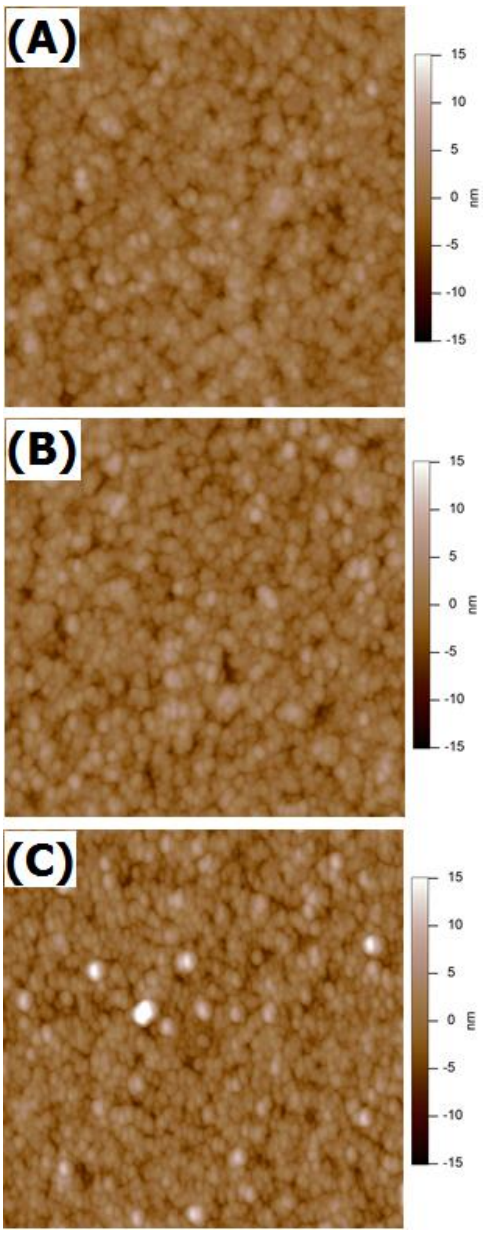


**Figure 9.1.** Representative 2 μm × 2 μm AFM height images of (A) KL, (B) OL and (C) MWL films on SPR sensors. RMS roughnesses for the images are: (A) ~ 2.0 nm, (B) ~ 2.3 nm and (C) ~ 2.6 nm.

### 9.4.2 Adsorption of Hemicelluloses onto Lignin Thin Films

Adsorption of different hemicelluloses onto KL, OL and MWL surfaces was probed by QCM-D. Representative frequency data are shown in **Figure 9.2**, and the representative dissipation data is provided as **Figure 9.3**. As seen in **Figure 9.2**, xyloglucan showed irreversible adsorption onto all the three lignin surfaces and yielded $\Delta f/n \approx$ -10.8 ± 1.3, -11.9 ± 1.0 and -3.5 ± 0.6 Hz for KL, OL and MWL surfaces, respectively. As seen in **Figure 9.3**, the $\Delta D$ values for xyloglucan adsorption onto these lignin surfaces were small (~ $2 \times 10^{-6}$ for KL and OL surfaces and ~ $1 \times 10^{-6}$ for MWL surfaces), hence the Sauerbrey equation (Equation 3.1) is valid for the calculation of $\Gamma_{QCM}$. Adsorption of xyloglucan onto KL, OL and MWL surfaces yielded $\Gamma_{QCM}$ = 1.9 ± 0.3, 2.1 ± 0.2 and 0.6 ± 0.1 mg·m$^{-2}$, respectively. Glucomannan also showed irreversible adsorption onto the lignin surfaces. Adsorption of glucomannan onto KL, OL and MWL surfaces yielded smaller $\Delta f/n \approx$ -5.0 ± 0.6, -4.8 ± 0.7 and -1.8 ± 0.4 Hz, respectively, or $\Gamma_{QCM}$ = 0.9 ± 0.1, 0.8 ± 0.1 and 0.3 ± 0.1 mg·m$^{-2}$, respectively. Galactomannan showed reversible adsorption onto all three lignin surfaces. Both glucuronoarabinoxylan and arabinoxylan showed extremely weak to no interactions with the lignin surfaces.

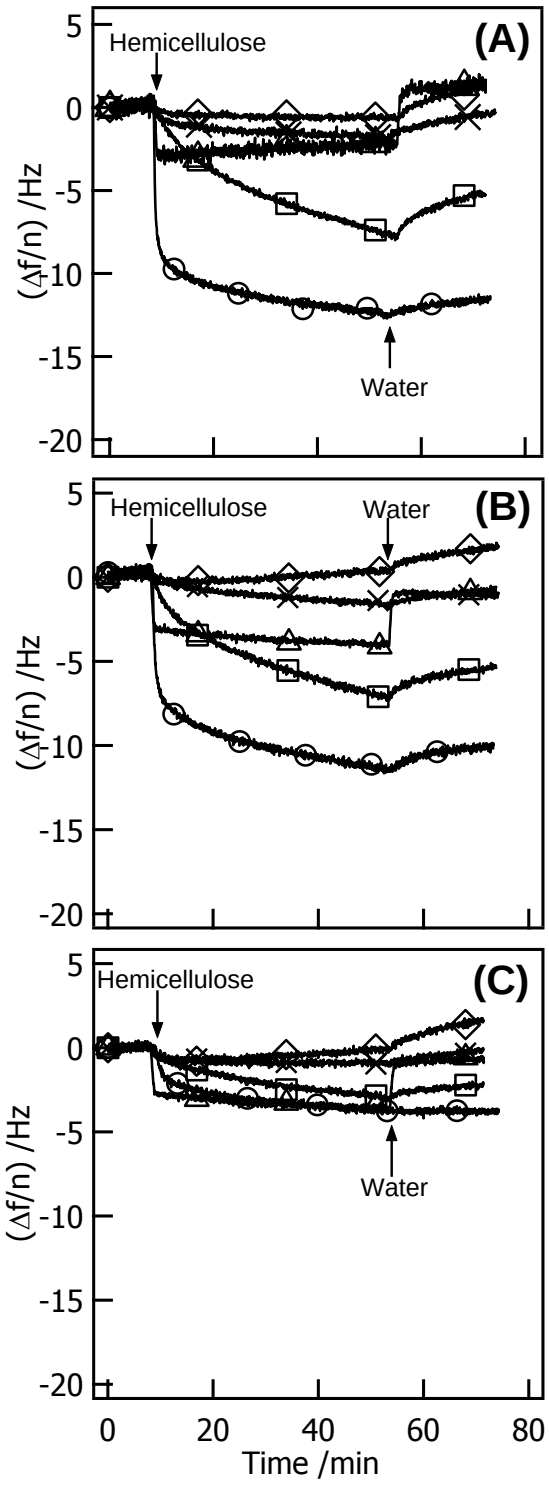


**Figure 9.2.** Representative Δ*f*/*n* versus time for (○) xyloglucan, (□) glucomannan, (Δ) galactomannan, (◊) glucuronoarabinoxylan and (×) arabinoxylan adsorption onto (A) KL, (B) OL and (C) MWL films from 100 mg·L$^{-1}$ aqueous solutions.

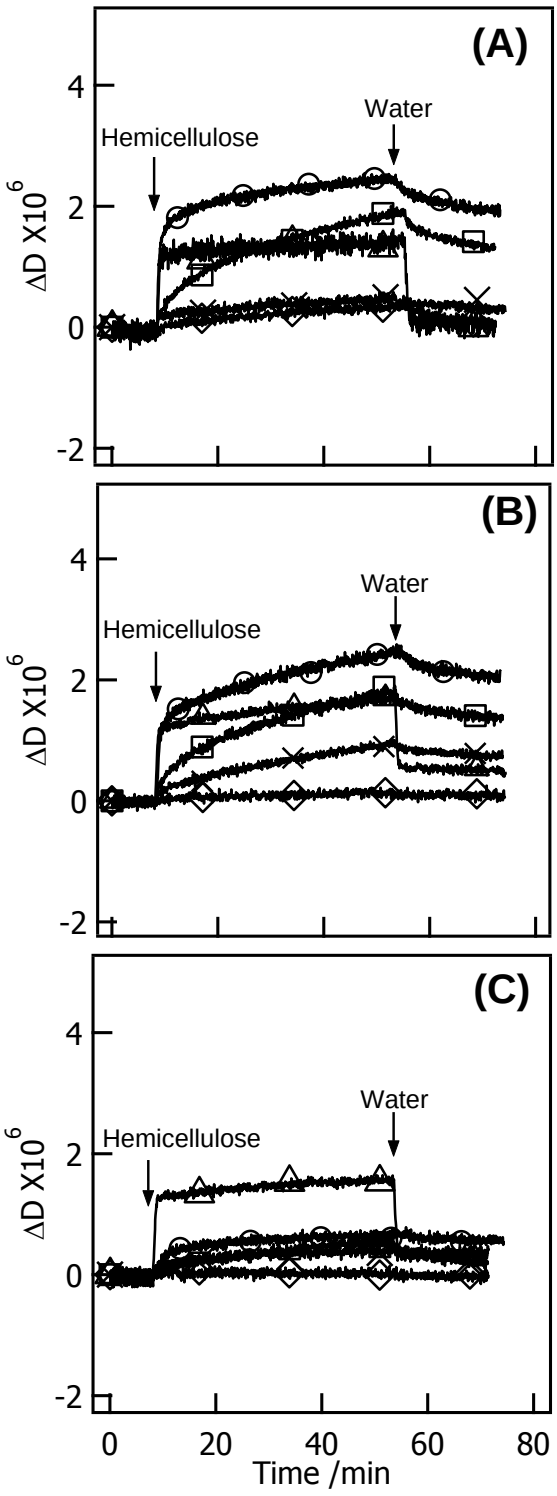


**Figure 9.3.** Representative Δ*D* versus time for (○) xyloglucan, (□) glucomannan, (Δ) galactomannan, (◊) glucuronoarabinoxylan and (×) arabinoxylan adsorption onto (A) KL, (B) OL and (C) MWL films from 100 mg·L$^{-1}$ aqueous solutions.

### 9.4.3 Adsorption Isotherms for Xyloglucan Adsorption onto Lignin Thin Films

Adsorption isotherms for xyloglucan adsorption onto KL, OL, and MWL surfaces shown in **Figures 9.4** and **9.5** were measured using SPR and QCM-D. Representative data for each isotherm data point are provided as **Figures 9.6** and **9.7**. As seen in **Figures 9.4** and **9.5**, $\Gamma_{SPR}$ and $\Gamma_{QCM}$ for xyloglucan adsorption onto KL and OL surfaces are in quantitative agreement with each other. The maximum surface coverages from SPR and QCM-D measurements are 1.3 ± 0.1 and 3.5 ± 0.6 mg·m$^{-2}$ for xyloglucan adsorption onto KL surfaces, and 1.2 ± 0.1 and 3.6 ± 0.7 mg·m$^{-2}$ for xyloglucan adsorption onto OL surfaces. However, $\Gamma_{SPR}$ and $\Gamma_{QCM}$ for xyloglucan adsorption onto MWL surfaces are smaller compared to those on KL and OL surfaces with the maximum surface coverage of 0.5 ± 0.1 and 2.0 ± 0.5 mg·m$^{-2}$ from SPR and QCM-D data. As seen from **Table 9.2**, KL and OL surfaces had larger dispersive surface energy components and smaller polar surface energy components than MWL surfaces. The water contact angle also indicated that KL and OL surfaces were more hydrophobic than MWL surfaces. The greater adsorption for hemicelluloses onto KL and OL surfaces compared to MWL surfaces might be attributed to the greater hydrophobic interactions, such as van der Waals interactions between the anhydroglucose units (AGU) in hemicelluloses and lignin. Kaya et al.[25] studied the adsorption of a water-soluble polysaccharide, pullulan, onto different alkanethiol self-assembled monolayers (SAM) and found that pullulan showed much stronger adsorption onto methyl-terminated self-assembled monolayer (SAM-$CH_3$) than hydroxyl-terminated self-assembled monolayer (SAM-OH) due to the stronger interactions with a hydrophobic surface.

As an acoustic technique, QCM-D measures the adsorbed polymer and any associated water in the adsorbed layers. On the other hand, SPR is an optical technique and it is only sensitive to the mass of polymers. The relatively greater surface coverage values determined by QCM-D

compared to SPR could be attributed to the water entrapped within the xyloglucan layers on lignin surfaces.

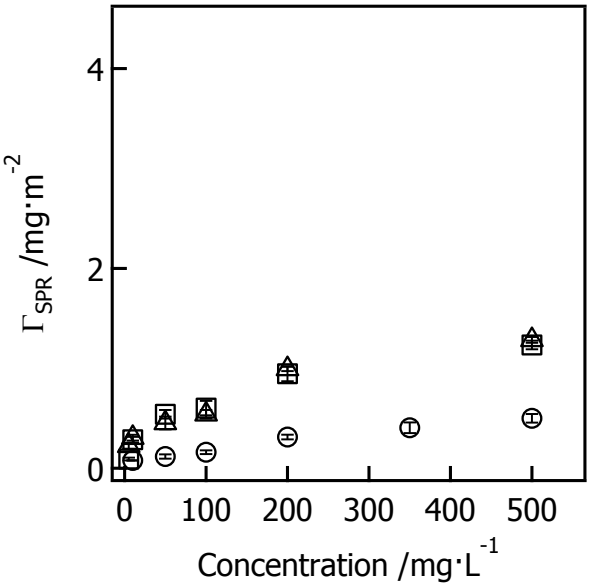


**Figure 9.4.** Adsorption isotherms from SPR for xyloglucan adsorption onto (Δ) KL, (□) OL and (○) MWL surfaces.

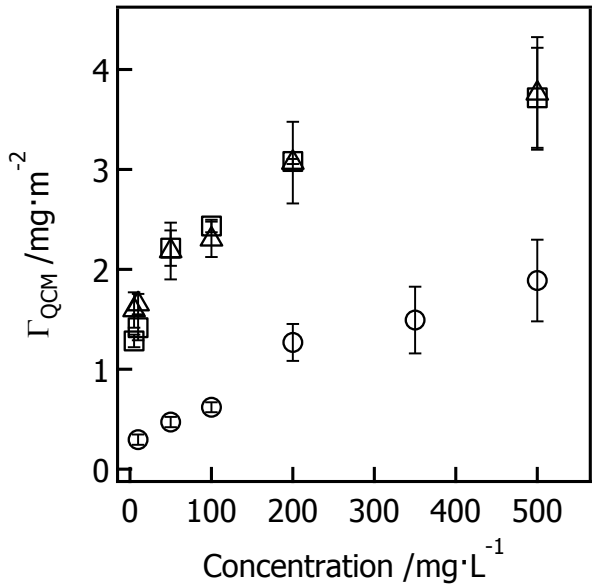


**Figure 9.5.** Adsorption isotherms from QCM-D for xyloglucan adsorption onto (Δ) KL, (□) OL and (○) MWL surfaces.

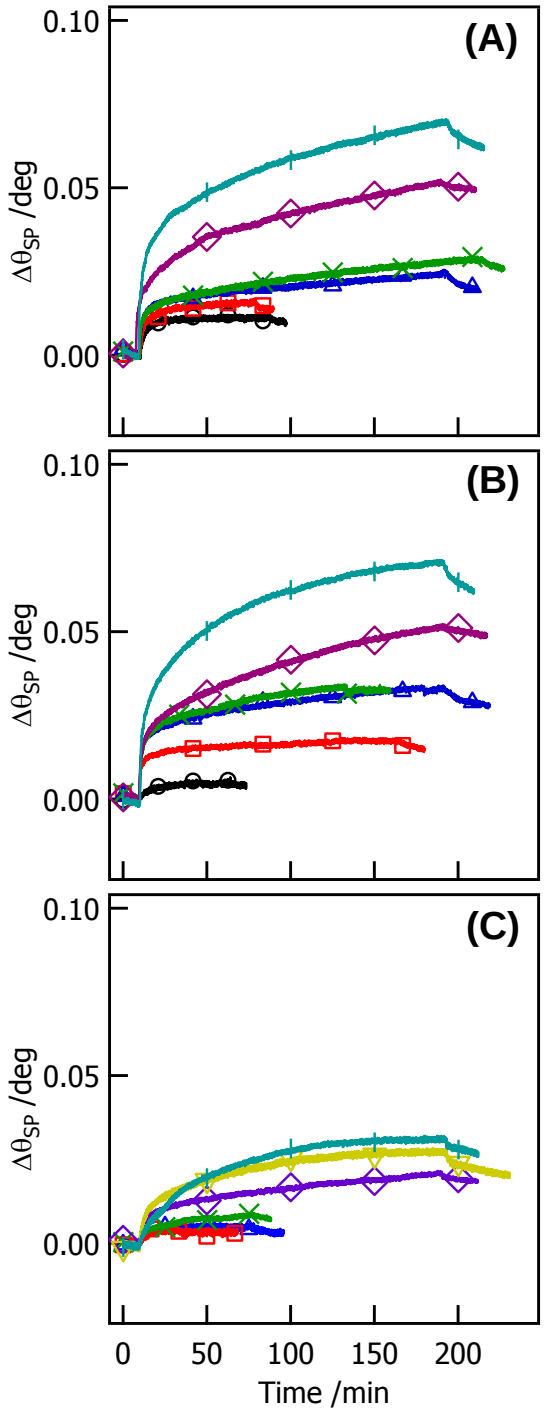


**Figure 9.6.** Representative $\Delta\theta_{SP}$ versus time from SPR for the adsorption of xyloglucan onto (A) KL, (B) OL and (C) MWL films from solutions of different concentration. Symbols correspond to xyloglucan concentrations of (○) 5 mg·L$^{-1}$, (□) 10 mg·L$^{-1}$, (Δ) 50 mg·L$^{-1}$, (×) 100 mg·L$^{-1}$, (◊) 200 mg·L$^{-1}$, (▽) 350 mg·L$^{-1}$ and (|) 500 mg·L$^{-1}$.

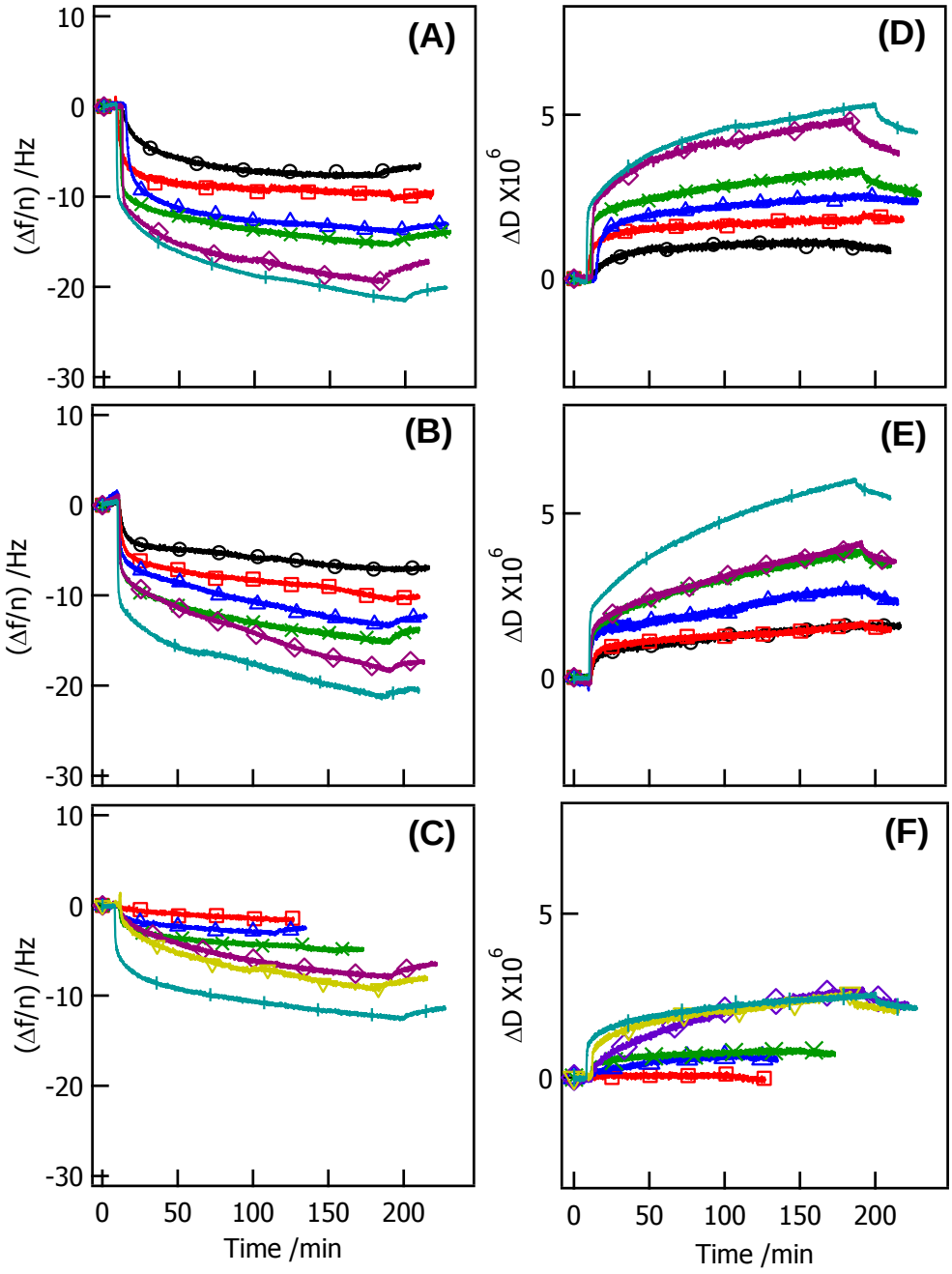


**Figure 9.7.** Representative Δ*f*/*n* versus time for the adsorption of xyloglucan onto (A) KL, (B) OL and (C) MWL films from solutions of different concentration, and representative Δ*D* versus time for the adsorption of xyloglucan onto (D) KL, (E) OL and (F) MWL films from solutions of different concentration. Symbols correspond to xyloglucan concentrations of (○) 5 mg·L$^{-1}$, (□) 10 mg·L$^{-1}$, (Δ) 50 mg·L$^{-1}$, (×) 100 mg·L$^{-1}$, (◊) 200 mg·L$^{-1}$, (▽) 350 mg·L$^{-1}$ and (|) 500 mg·L$^{-1}$.

To the best of our knowledge, no reports are available describing the adsorption of xyloglucan onto lignin substrates. However, Tammelin et al.[10, 11] studied the adsorption of dissolved hemicelluloses (a low molecular weight hemicellulose mixture extracted from spruce thermomechanical pulp with hexane) and acetylated galactoglucomannan (separated from the dissolved hemicelluloses, $M_w$ ~ 50 kDa) onto MWL (from spruce) films (spincoated from 1,4-dioxane onto polystyrene coated QCM-D sensors) using QCM-D. The results showed that adsorption of dissolved hemicelluloses and acetylated galactoglucomannan from 100 $mg \cdot L^{-1}$ solutions yielded $\Gamma_{QCM}$ of ~ 2.5 and ~ 4.0 $mg \cdot m^{-2}$, respectively.[10, 11] Zhou et al.[38] studied the adsorption of xyloglucan (from tamarind seed, $M_w$ ~ 450 kDa) onto bleached chemical and mechanical wood pulps with different percentage of surface coverage of lignin and found that more xyloglucan adsorbed onto pulp fibres with greater surface coverage of lignin. On the other hand, xyloglucan adsorption onto various cellulose substrates has been investigated by several groups, and the reported surface concentration ranged from 0.4 to 27 $mg \cdot m^{-2}$ due to the differences in the cellulose substrates and characterization techniques. Ahola et al.[26] studied the adsorption of xyloglucan (from tamarind) onto sulfated cellulose nanofibrillar films via SPR and QCM-D and found that xyloglucan adsorption from 100 $mg \cdot L^{-1}$ solutions yielded $\Gamma_{SPR}$ and $\Gamma_{QCM}$ of 0.4 and 2.5 $mg \cdot m^{-2}$ in 30 min. Cerclier et al.[24] investigated the adsorption of xyloglucan (from T*amarindus indica*, $M_w$ ~ 670 kDa and $M_n$ ~ 394 kDa) onto sulfated nanocrystalline cellulose films via QCM-D and found that xyloglucan adsorption from 500 $mg \cdot L^{-1}$ solutions yielded $\Gamma_{QCM}$ of ~ 5.0 $mg \cdot m^{-2}$, although the porosity of the cellulose substrate and the water entrapped in the adsorbed xyloglucan layers would also contribute in this value. Kittle et al.[39] measured adsorption isotherms for xyloglucan (from tamarind, $M_w$ ~ 200 kDa) from aqueous solutions onto nonporous amorphous cellulose films (regenerated from trimethylsilyl cellulose films) using

SPR and QCM-D and the results showed that the maximum $\Gamma_{SPR}$ and $\Gamma_{QCM}$ were 0.9 and 3.8 mg·m$^{-2}$, respectively, thereby showing xyloglucan formed highly hydrated layers on cellulose surfaces.

The blob model and scaling theory have been successfully used to predict the static and dynamic properties of the semi-dilute polymer solutions.[40-42] In the blob model, a polymer chain is divided into a sequence of blobs of identical size. Inside the blobs, the conformation of the polymer chain is essentially unperturbed. At larger length scales, polymer chain behavior is represented by the spatial arrangement of blobs.[43] The size of the blobs ($\xi$) is given by:[44]

$$\xi \sim b g^{\nu} \tag{9.1}$$

where, $b$ is the size of the monomer, $g$ is the number of monomers in a blob and $\nu$ is the scaling exponent which is dependent upon the solvent quality, e.g., $\nu$ = 3/5 for polymer chains in good solvents and $\nu$ = 1/2 for $\theta$ solvents for mean field theories.

When polymer chains adsorb onto a solid surface, two distinct adsorbed layers form: the proximal layer includes the segments in direct contact with the surface (trains), and the second layer contains loops and tails extending into solutions. The adsorbed amount ($\Gamma$) is controlled by the first layer. The correlation thickness of the proximal layer is defined by the size of the adsorption blobs ($\xi_{ads}$), and the size of the adsorption blobs can be calculated from:[45]

$$\xi_{ads} \sim \frac{b}{\delta^{\nu/(1-\nu)}} \tag{9.2}$$

where, $\delta$ is the adsorption strength factor. For this model, $\Gamma$ is proportional to:[45]

$$\Gamma \sim \frac{\delta^{(2\nu-1)/(1-\nu)}}{b^2} \tag{9.3}$$

In good solvents, Equation 9.3 becomes:

$$\Gamma \sim \frac{\delta^{0.5}}{b^2} \tag{9.4}$$

By combing Equation 9.2 and 9.3, $\Gamma$ can be related to $\xi_{ads}$:

$$\Gamma \sim \frac{\left(\frac{b}{\xi_{ads}}\right)^{(2\nu-1)/(1-\nu)}}{b^2} \tag{9.5}$$

In good solvent, Equation 9.5 becomes:

$$\xi_{ads} \sim \frac{1}{\Gamma^3 b^5} \tag{9.6}$$

As seen from **Figure 9.4**, the equlibrium $\Gamma_{SPR}$ for xyloglucan adsorption onto KL, OL and MWL surfaces were 1.3, 1.2 and 0.5 mg·m$^{-2}$, respectively. The adsorption strength ratio calculated from Equation 9.4 for xyloglucan adsorption onto KL and OL surfaces was 7: 6: 1, which indicated that xyloglucan showed stronger adsorption affinity onto KL and OL surfaces than MWL surfaces. Additionally, the $\xi_{ads}$ ratio calculated from Equation 9.6 for xyloglucan layers on KL, OL and MWL surfaces was 1: 1.3: 18, which showed that xyloglucan formed denser proximal layers on KL and OL surfaces than MWL surfaces.

### 9.4.4 Water Contents of Adsorbed Xyloglucan Layers on Lignin Thin Films

The mass determined via QCM-D, the so-called "wet mass", and the mass obtained from SPR, the so-called "dry mass", can yield the overall water content of the film if one assumes ideal solution behavior. The overall water contents of the xyloglucan layers adsorbed onto different lignin surfaces were calculated from $\Gamma_{SPR}$ and $\Gamma_{QCM}$ using:[28]

$$\% \, Water = \left(1 - \frac{\Gamma_{SPR}}{\Gamma_{QCM}}\right) \times 100\% \tag{9.7}$$

The overall water content as a function of the concentration for xyloglucan is shown in **Figure 9.8**. Generally, the overall water content decreased as the bulk concentration of xyloglucan solutions increased. $\Gamma_{QCM}$ and $\Gamma_{SPR}$ for the xyloglucan layers adsorbed from bulk concentration greater than 10 mg·L$^{-1}$ were used to calculate an average water content. The average overall water contents were 74 ± 9, 73 ± 5 and 72 ± 3 % for xyloglucan layers adsorbed onto KL, OL and MWL surfaces, respectively, which indicated that the adsorbed xyloglucan layers had similar amounts of associated water on different lignin surfaces within experimental error. Additionally, the xyloglucan layers adsorbed onto lignin surfaces contained less water compared to the xyloglucan layers adsorbed onto regenerated cellulose surfaces determined by Kittle et al. (~ 81 %).[39] This observation indicated that xyloglucan formed denser layers on lignin surfaces than cellulose surfaces.

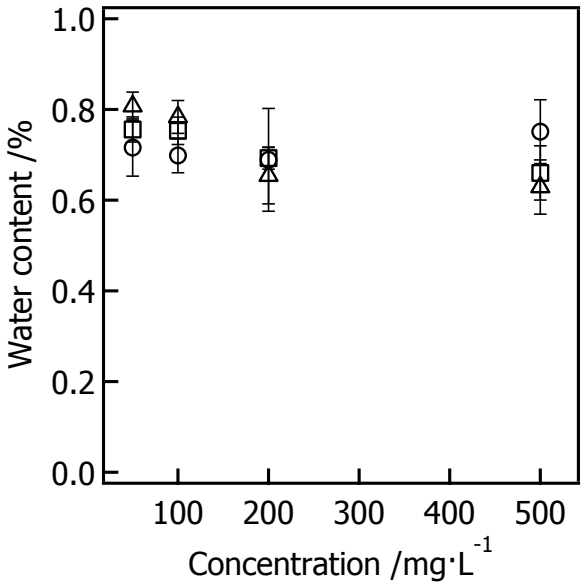


**Figure 9.8.** Overall water contents of the adsorbed xyloglucan layers on (Δ) KL, (□) OL and (○) MWL surfaces as a function of the bulk concentration of the xyloglucan solution.

## 9.5 Conclusions

Smooth and uniform lignin thin films were prepared by spincoating KL, OL and MWL from aqueous ammonia solutions onto gold substrates. Since MWL is considered to have a structure closer to native lignin than KL or OL, MWL thin films might be a better model surface. Adsorption of hemicelluloses onto these lignin films was investigated via QCM-D. The data showed that xyloglucan (from tamarind seeds) and glucomannan (from konjac) irreversibly adsorbed onto the lignin surfaces, galactomannan (from carob) reversibly adsorbed onto the lignin surfaces, and glucuronoarabinoxylan (from spruce) and arabinoxylan (from wheat) showed weak interactions with the lignin surfaces. For each of the hemicelluloses, stronger adsorption onto KL and OL surfaces than onto MWL surfaces was detected. Adsorption isotherms for xyloglucan onto the lignin surfaces were determined via QCM-D and SPR and the data indicated that xyloglucan showed stronger adsorption affinity onto KL and OL surfaces than MWL surfaces, however, the adsorbed xyloglucan layers on different lignin surfaces had similar overall water contents within experimental error. The information obtained from this work is expected to improve the fundamental understanding of physical interactions between hemicelluloses and lignin in plant cell walls.

## 9.6 References

(1) Lawoko, M.; Henriksson, G.; Gellerstedt, G. *Biomacromolecules* **2005,** 6, 3467-3473.

(2) Imamura, T.; Watanabe, T.; Kuwahara, M.; Koshijima, T. *Phytochemistry* **1994,** 37, 1165-1173.

(3) Balakshin, M.; Capanema, E.; Gracz, H.; Chang, H.-m.; Jameel, H. *Planta* **2011,** 233, 1097-1110.

(4) Lawoko, M.; Henriksson, G.; Gellerstedt, G. *Holzforschung* **2006,** 60, 162-165.

(5) Boukari, I.; Putaux, J.-L.; Cathala, B.; Barakat, A.; Saake, B.; Rémond, C.; O'Donohue, M.; Chabbert, B. *Biomacromolecules* **2009,** 10, 2489-2498.

(6) Barakat, A.; Putaux, J.-L.; Saulnier, L.; Chabbert, B.; Cathala, B. *Biomacromolecules* **2007,** 8, 1236-1245.

(7) Barakat, A.; Winter, H.; Rondeau-Mouro, C.; Saake, B.; Chabbert, B.; Cathala, B. *Planta* **2007,** 226, 267-281.

(8) Gierer, J.; Wännström, S. *Holzforschung* **1984,** 38, 181-184.

(9) Helm, R. F. Lignin-Polysaccharide Interactions in Woody Plants. In *Lignin: Historical, Biological, and Materials Perspectives,* American Chemical Society: 1999; Vol. 742, pp 161-171.

(10) Tammelin, T.; Österberg, M.; Johansson, L.-S.; Laine, J. *Nord. Pulp Paper Res. J.* **2006,** 21, 444-450.

(11) Tammelin, T.; Johnsen, I. A.; Österberg, M.; Stenius, P.; Laine, J. *Nord. Pulp Paper Res. J.* **2007,** 22, 93-101.

(12) Norgren, M.; Notley, S. M.; Majtnerova, A.; Gellerstedt, G. *Langmuir* **2006,** 22, 1209-1214.

(13) Norgren, M.; Gärdlund, L.; Notley, S. M.; Htun, M.; Wågberg, L. *Langmuir* **2007,** 23, 3737-3743.

(14) Notley, S. M.; Norgren, M. *Biomacromolecules* **2008,** 9, 2081-2086.

(15) Notley, S. M.; Norgren, M. *Langmuir* **2010,** 26, 5484-5490.

(16) Saarinen, T.; Orelma, H.; Grönqvist, S.; Andberg, M.; Holappa, S.; Laine, J. *BioResources* **2009,** 4, 94-110.

(17) Constantino, C. J. L.; Juliani, L. P.; Botaro, V. R.; Balogh, D. T.; Pereira, M. R.; Ticianelli, E. A.; Curvelo, A. A. S.; Oliveira Jr, O. N. *Thin Solid Films* **1996,** 284–285, 191-194.

(18) Constantino, C. J. L.; Dhanabalan, A.; Curvelo, A. A. S.; Oliveira Jr, O. N. *Thin Solid Films* **1998,** 327–329, 47-51.

(19) Pasquini, D.; Balogh, D. T.; Antunes, P. A.; Constantino, C. J. L.; Curvelo, A. A. S.; Aroca, R. F.; Oliveira, O. N. *Langmuir* **2002,** 18, 6593-6596.

(20) Pasquini, D.; Balogh, D. T.; Oliveira Jr, O. N.; Curvelo, A. A. S. *Colloids Surf. Physicochem. Eng. Aspects* **2005,** 252, 193-200.

(21) Micic, M.; Radotic, K.; Jeremic, M.; Leblanc, R. M. *Macromol. Biosci.* **2003,** 3, 100-106.

(22) Micic, M.; Radotic, K.; Jeremic, M.; Djikanovic, D.; Kämmer, S. B. *Colloids Surf., B: Biointerfaces* **2004,** 34, 33-40.

(23) Wang, C.; Qian, C.; Roman, M.; Glasser, W. G.; Esker, A. R. *Biomacromolecules* **2013**.

(24) Cerclier, C.; Cousin, F.; Bizot, H.; Moreau, C. l.; Cathala, B. *Langmuir* **2010,** 26, 17248-17255.

(25) Kaya, A.; Du, X.; Liu, Z.; Lu, J. W.; Morris, J. R.; Glasser, W. G.; Heinze, T.; Esker, A. R. *Biomacromolecules* **2009,** 10, 2451-2459.

(26) Ahola, S.; Myllytie, P.; Österberg, M.; Teerinen, T.; Laine, J. *Bioresources* **2008,** 3, 1315-1328.

(27) Höök, F.; Kasemo, B.; Nylander, T.; Fant, C.; Sott, K.; Elwing, H. *Anal. Chem.* **2001,** 73, 5796-5804.

(28) Hedin, J.; Löfroth, J.-E.; Nydén, M. *Langmuir* **2007,** 23, 6148-6155.

(29) Liu, Z.; Choi, H.; Gatenholm, P.; Esker, A. R. *Langmuir* **2011,** 27, 8718-8728.

(30) Wang, C.; Esker, A. R. *Carbohydr. Polym.* **2014,** 102, 151-158.

(31) Glasser, W. G.; Barnett, C. A.; Sano, Y. *J. Appl. Polym. Sci.: Appl. Polym. Symp.* **1983,** 37, 441-460.

(32) Escalante, A.; Gonçalves, A.; Bodin, A.; Stepan, A.; Sandström, C.; Toriz, G.; Gatenholm, P. *Carbohydr. Polym.* **2012,** 87, 2381-2387.

(33) Chakar, F. S.; Ragauskas, A. J. *Ind. Crop. Prod.* **2004,** 20, 131-141.

(34) Zakzeski, J.; Bruijnincx, P. C. A.; Jongerius, A. L.; Weckhuysen, B. M. *Chem. Rev.* **2010,** 110, 3552-3599.

(35) McDonough, T. J. *Tappi J.* **1993,** 76, 186-193.

(36) Ikeda, T.; Holtman, K.; Kadla, J. F.; Chang, H.-m.; Jameel, H. *J. Agric. Food Chem.* **2001,** 50, 129-135.

(37) Jiang, F. PhD Thesis, Virginia Tech, Blacksburg, VA, 2011.

(38) Zhou, Q.; Baumann, M. J.; Brumer, H.; Teeri, T. T. *Carbohydr. Polym.* **2006,** 63, 449-458.

(39) Kittle, J. D. PhD Thesis, Virginia Tech, Blacksburg, VA, 2012.

(40) De Gennes, P. G. *Macromolecules* **1981,** 14, 1637-1644.

(41) Kawaguchi, M.; Takahashi, A. *Adv. Colloid Interface Sci.* **1992,** 37, 219-317.

(42) Duhamel, J.; Yekta, A.; Winnik, M. A.; Jao, T. C.; Mishra, M. K.; Rubin, I. D. *J. Phys. Chem.* **1993,** 97, 13708-13712.

(43) de Gennes, P.-G. *Scaling Concepts in Polymer Physics*; Cornell University Press: Ithaca, NY, and London, 1979.

(44) Teraoka, I. *Polymer Solutions: An Introduction to Physical Properties*; John Wiley & Sons, Inc.: New York, 2002.

(45) Rubinstein, M.; Colby, R. H. *Polymer Physics*; Oxford University Press Inc.: New York, 2003.

# Chapter 10: Conclusions and Suggested Future Work

## 10.1 Overall Conclusions

The studies in this thesis focused on natural polymer (i.e., cellulose, chitin and lignin) thin films and their interactions with enzymes, proteins and polysaccharides. A variety of surface characterization techniques, including quartz crystal microbalance with dissipation monitoring (QCM-D), surface plasmon resonance (SPR), atomic force microscopy (AFM), ellipsometry and X-ray photoelectron spectroscopy (XPS), were employed to investigate the enzymatic degradation of chitin and lignin thin films, the adsorption of proteins and polysaccharides onto these natural polymer thin films, and the surface-initiated polymerization of lignin precursors.

Smooth and uniform amorphous chitin (RChitin) thin films were prepared by spincoating trimethylsilyl chitin (TMSChitin) solutions onto silica or gold surfaces, followed by regeneration to amorphous chitin. Nanocrystalline chitin (Chitin NC) thin films were prepared by spincoating nanocrystalline chitin colloidal suspensions onto gold surfaces modified by amine-terminated self-assembled monolayers. Solvent exchange experiments with $H_2O/D_2O$ revealed that Chitin NC films held twice as much water as RChitin films of similar thickness. Bovine serum albumin (BSA) adsorption studies demonstrated that Chitin NC films showed higher protein loading capacity than RChitin films due to their relatively larger accessible surface areas.

Chitinase (from *Streptomyces griseus*) was used as a model enzyme complex to study the enzymatic degradation of chitin thin films. Both QCM-D and AFM studies showed that the enzymatic degradation of chitin films was strongly affected by temperature, pH, enzyme concentration, degree of acetylation and crystallinity of the chitin substrates. The optimal temperature and pH for chitinase activity on RChitin films were ~ 37 °C and 6 to 8, respectively,

which were consistent with colloidal studies in the literature. Chitinase showed greater activity on fully acetylated chitin than highly deacetylated chitosan. Results from QCM-D also showed that chitinase-catalyzed hydrolysis of Chitin NC films was much slower than that of RChitin films. Chitinase not only degraded, but also caused swelling of the chitin nanocrystals.

The adsorption of human serum albumin (HSA) and human fibrinogen (HFN) onto amorphous cellulose (RC) and chitin surfaces at physiological temperature (37 °C) and pH (7.4) was studied via SPR and QCM-D. Studies by SPR indicated that protein adsorption onto RC and RChitin surfaces was greatly reduced compared to gold surfaces, and the adsorption affinity for HSA onto polysaccharide surfaces was greater than that of HFN. A combination of QCM-D and SPR results showed that the proteins adsorbed onto polysaccharide surfaces had more associated water than proteins adsorbed onto gold surfaces.

The dehydrogenative polymerization of three major lignin precursors (monolignols), namely coniferyl alcohol, *p*-coumaryl alcohol and sinapyl alcohol, was initiated by physically immobilized HRP on different solid surfaces. The polymerization kinetics were monitored by QCM-D and the morphologies of the resulting dehydrogenative polymer (DHP) lignin films were studied by AFM. Results from QCM-D and AFM showed that surface-immobilized HRP retained its activity and selectivity for monolignols as coniferyl and *p*-coumaryl alcohol underwent dehydrogenative polymerization in the presence of hydrogen peroxide, whereas sinapyl alcohol required an additional nucleophile for polymerization. Surface densities of DHP aggregates that formed seem to reflect HRP substrate preferences for initiation of *p*-coumaryl > coniferyl > sinapyl alcohol. However, larger DHP aggregates formed for coniferyl alcohol would be consistent with faster propagation. Both QCM-D and AFM data showed that the surface-initiated dehydrogenative polymerization of monolignols was greatly affected by the support

surfaces, monolignol concentration, hydrogen peroxide concentration and temperature. The resulting DHP films served as sensors for ligninolytic enzyme activity, thereby opening the characterization of lignin biodegradation to previously unutilized surface science techniques.

Thin films of DHP, kraft (KL), organosolv (OL) and milled wood (MWL) lignins were used as model lignin substrates to investigate lignin peroxidase (LiP) and manganese peroxidase (MnP)-catalyzed degradation of native lignin via QCM-D and AFM. Results from QCM-D indicated that LiP degraded both DHP and isolated lignin films with an initial degradation rate that increased in the order: KL < OL < MWL < guaiacyl DHP (G-DHP) < *p*-hydroxyphenyl DHP (H-DHP). However, MnP only degraded DHP films. The initial degradation rate for G-DHP was faster than H-DHP in the presence of MnP. Images from AFM showed G-DHP aggregates had smaller average diameters and H-DHP aggregates had lower particle densities after incubation with the enzymatic LiP/$H_2O_2$ and MnP/$H_2O_2$/Mn (II) systems.

Smooth and uniform KL, OL and MWL thin films were used to study physical interactions between hemicelluloses and lignin using QCM-D and SPR. QCM-D studies showed that xyloglucan (from tamarind seeds) and glucomannan (from konjac) irreversibly adsorbed onto these lignin surfaces, galactomannan (from carob) reversibly adsorbed onto these lignin surfaces, and glucuronoarabinoxylan (from spruce) and arabinoxylan (from wheat) showed weak interactions with these lignin surfaces. For each of the hemicelluloses, stronger adsorption onto KL and OL surfaces than onto MWL surfaces was detected. Adsorption isotherms from QCM-D and SPR for xyloglucan adsorption onto the lignin surfaces indicated that xyloglucan showed stronger adsorption onto KL and OL surfaces than MWL surfaces. Data from QCM-D and SPR also revealed that xyloglucan formed less hydrated layers on model lignin surfaces compared to

regenerated cellulose surfaces, although the adsorbed xyloglucan layers had similar percentages of coupled water on different lignin surfaces within experimental error.

The results obtained from the studies in this thesis are expected to provide convenient and promising assays and methodologies for studying various natural polymer degrading enzymes, assisting the design of biocompatible and biodegradable natural polymer-based biomaterials, determining the precursor preference and optimal conditions for peroxidases involved in lignification, and offering useful information to enhance the fundamental understanding of plant cell wall architecture.

## 10.2 Suggested Future Work

### 10.2.1 Surface-initiated Polymerization of Monolignols in the Presence of Hemicelluloses and Pectin

In Chapter 7, QCM-D and AFM studies showed that the surface-immobilized HRP-initiated dehydrogenative polymerization of monolignols was greatly affected by the support surface, monolignol concentration, hydrogen peroxide concentration and temperature. As evident from Chapter 8, the resulting DHP films provided good model substrates for ligninolytic enzymes and thus enabled the application of surface science techniques to lignin biodegradation. In Chapter 9, the adsorption of different hemicelluloses onto three chemically isolated lignin surfaces was also studied using QCM-D and SPR.

In plant cell walls, lignin and hemicelluloses bind to each other through covalent interactions to form lignin-carbohydrate complexes (LCCs).[1-3] Therefore, it would be interesting to study the dehydrogenative polymerization of monolignols in the presence of hemicelluloses and pectin. The polymerization kinetics, the morphologies and the structures of the resulting

DHP/carbohydrate polymer composite films could be investigated by QCM-D, AFM and reflection absorption infrared spectroscopy (RAIRS), respectively. The resulting DHP/carbohydrate polymer composite films are expected to provide model LCC substrates for ligninolytic and carbohydrate polymer-degrading enzymes.

Preliminary QCM-D and AFM data for the dehydrogenative polymerization of monolignols in the presence of hemicelluloses are shown in **Figure 10.1** and **Figure 10.2**, respectively. As implied by the frequency profiles in **Figure 10.1**, less coniferyl alcohol was polymerized on gold surfaces when hemicelluloses were present. This observation might be attributed to possible coupling between propagating DHP and hemicelluloses. As seen in **Figure 10.2**, smaller and more uniform G-DHP aggregates were obtained when hemicelluloses were present.

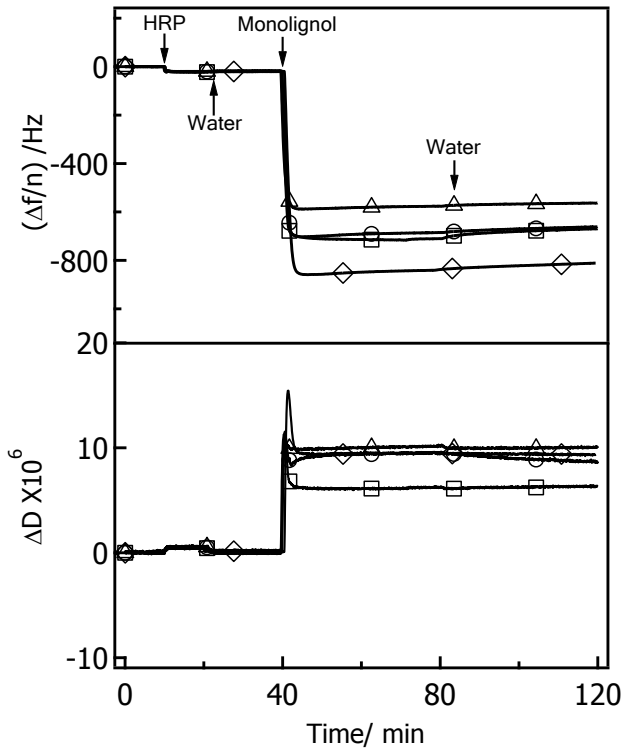


**Figure 10.1.** Representative Δ*f*/*n* and Δ*D* versus time for dehydrogenative polymerization of (◊) 0.5 mg·mL$^{-1}$ coniferyl alcohol, (Δ) 0.5 mg·mL$^{-1}$ coniferyl alcohol with 0.1 mg·mL$^{-1}$ galactoglucomannan (from spruce), (○) 0.5 mg·mL$^{-1}$ coniferyl alcohol with 0.1 mg·mL$^{-1}$ xyloglucan (from tamarind seed) and (□) 0.5 mg·mL$^{-1}$ coniferyl alcohol with 0.1 mg·mL$^{-1}$ glucuronoarabinoxylan (from spruce) initiated by HRP immobilized on silica at 20 °C. Arrows and labels indicate where different solutions were introduced into the flow cell after the initial baselines were set in water. The HRP was adsorbed onto the surfaces from a 1.0 mg·mL$^{-1}$ aqueous solution and the aqueous monolignol solutions contained 20 mM $H_2O_2$.

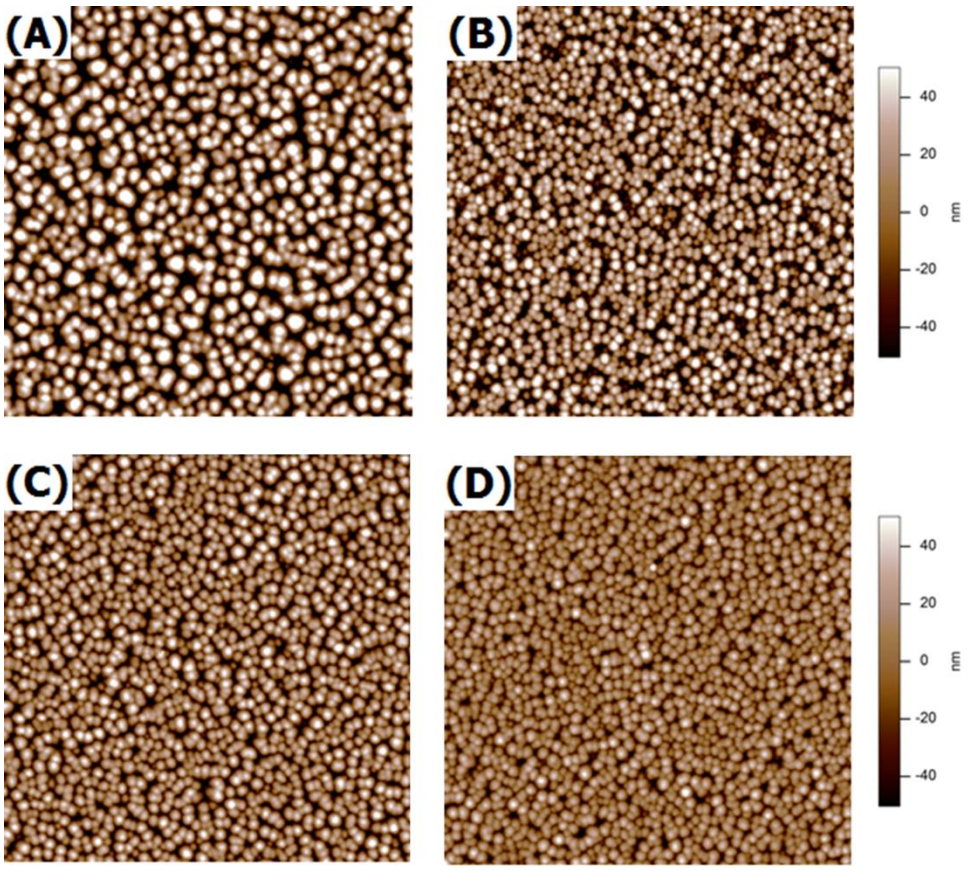


**Figure 10.2.** Representative 10 μm × 10 μm AFM height images of (A) G-DHP, (B) G-DHP formed in the presence of galactoglucomannan, (C) G-DHP formed in the presence of glucuronoarabinoxylan, and (D) G-DHP formed in the presence of xyloglucan. Root-mean square (RMS) roughnesses for the AFM images are: (A) ~ 38 nm, (B) ~ 30 nm, (C) ~ 25 nm and (D) ~ 19 nm.

### 10.2.2 Preparation of New DHP Films via the Incorporation of Possible Lignin Precursors

Native lignin primarily arises from the dehydrogenative polymerization of three monolignols, namely *p*-coumaryl alcohol, coniferyl alcohol and sinapyl alcohol. However, several other monomers have also been reported as precursors for native lignin, such as acylated monolignols and hydroxycinnamyl aldehydes.[4-6] Recently, new precursors (e.g., monolignol ferulate

conjugates) were introduced into bioengineered lignin that yielded lignin that could undergo depolymerization with lower energy and chemical inputs.[7, 8]

Similar to the work presented in Chapter 7 for the preparation of DHP thin films via the surface-initiated dehydrogenative polymerization of monolignols, DHP films with new monomers or controlled chemical linkages could be prepared. Studies by QCM-D, AFM and RAIRS could be used to monitor the polymerization kinetics, the morphologies and the structures of the resulting DHP films, respectively. The resulting DHP films with controlled precursor composition or chemical linkages could be employed as model lignin substrates for ligninolytic enzymes to study the enzymatic degradation of native or bioengineered lignin, which is also similar to the work presented in Chapter 8.

In a preliminary study, the surface-initiated dehydrogenative polymerizations of three possible lignin monomers, including ferulic acid, *p*-coumaric acid ethyl ester and guaiacylglycerol-*β*-guaiacyl ether (**Figure 10.3**) were monitored by QCM-D. Preliminary QCM-D data for the dehydrogenative polymerization of three monomers is shown in **Figure 10.4**. As indicated by **Figure 10.4**, DHP films could be prepared from all three monomers. The polymerization of ferulic acid, *p*-coumaric acid ethyl ester and guaiacylglycerol-*β*-guaiacyl ether yielded irreversible changes in $\Delta f/n \approx$ -30, -490 and -540 Hz from the enzyme coated surfaces, or $\Gamma_{QCM}$ = 5.3, 87 and 96 mg·m$^{-2}$, respectively, assuming the Sauerbrey Equation (Equation 3.1) is valid.

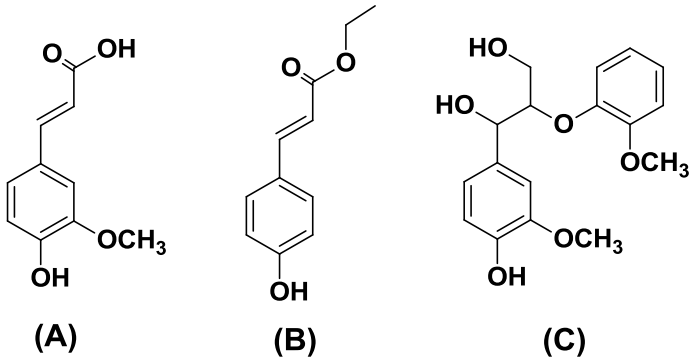


**Figure 10.3.** Chemical structures of (A) ferulic acid, (B) *p*-coumaric acid ethyl ester and (C) guaiacylglycerol-*β*-guaiacyl ether.

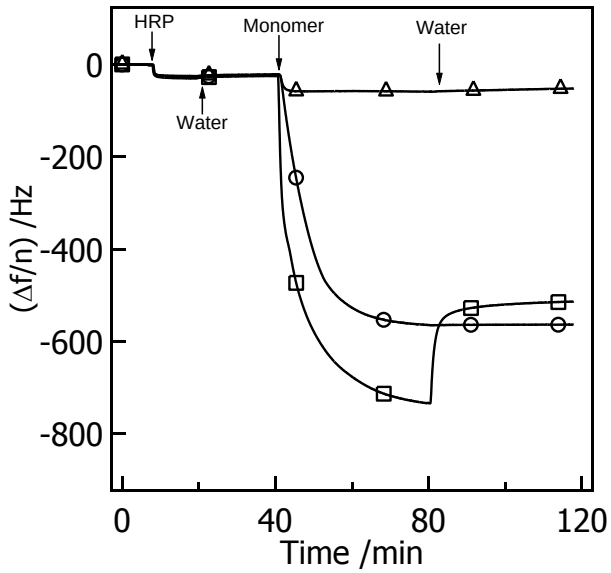


**Figure 10.4.** Representative Δ*f*/*n* and Δ*D* versus time at 20 °C for dehydrogenative polymerization of 0.5 mg·mL$^{-1}$ (□) *p*-coumaric acid ethyl ester, (○) guaiacylglycerol-β-guaiacyl ether and (Δ) ferulic acid initiated by HRP immobilized on gold. Arrows and labels indicate where different solutions were introduced into the flow cell after the initial baselines were set in water. The HRP was adsorbed onto the surfaces from a 1.0 mg·mL$^{-1}$ aqueous solution and the aqueous monomer solutions contained 20 mM $H_2O_2$.

### 10.2.3 Adsorption of Monolignols and Lignin Oligomers onto Cellulose Surfaces

In plant cells, monolignols are biosynthesized from phenylalanine through a multistep process under strict regulation,[4, 9] and are transported across the cell membrane to the cell wall by Golgi-derived vesicles or ATP-binding cassette-like transporters.[10-12] In the cell wall, monolignols are dehydrogenated to phenolic radicals by cell wall-bound enzymes and these radicals couple to form polymeric species.

Elucidating the interactions between lignin monomers/oligomers and cellulose is important for understanding the molecular architecture of plant cell walls. As a surface sensitive technique, SPR provides a highly sensitive method for the study of the surface interactions between small molecules (e.g., surfactants) and solid surfaces.[13, 14]

In a preliminary study, the adsorption of three monolignols and a lignin dimer model compound (guaiacylglycerol-$\beta$-guaiacyl ether) onto regenerated cellulose (RC) surfaces was investigated using SPR. Preliminary SPR data for coniferyl alcohol adsorption onto RC surfaces was shown in **Figure 10.5**. As SPR measures the refractive index change near the solid/liquid interface, SPR is sensitive to both the adsorbed analyte at the interface and analyte in the bulk solutions near the interface. The bulk solution near the interface generates a change in angle ($\Delta\theta$) which is proportional to the analyte concentration in the bulk solution, and this effect is called the "bulk" effect. Final values of $\Delta\theta$ from the adsorbed analyte are obtained after the "bulk" effect is subtracted. **Figure 10.5B** shows raw $\Delta\theta$ values as well as $\Delta\theta$ values obtained after the background correction for coniferyl alcohol adsorption onto RC surfaces. Adsorption isotherms (obtained after subtraction of the "bulk" contribution) for the adsorption of three monolignols and a lignin dimer model compound (**Figure 10.3C**) onto RC surfaces are shown **Figure 10.6**.

As seen in **Figure 10.6**, the surface interaction between lignin monomers/oligomers and cellulose decreased in the order: sinapyl alcohol > *p*-coumaryl alcohol > guaiacylglycerol-*β*-guaiacyl ether ≈ coniferyl alcohol.

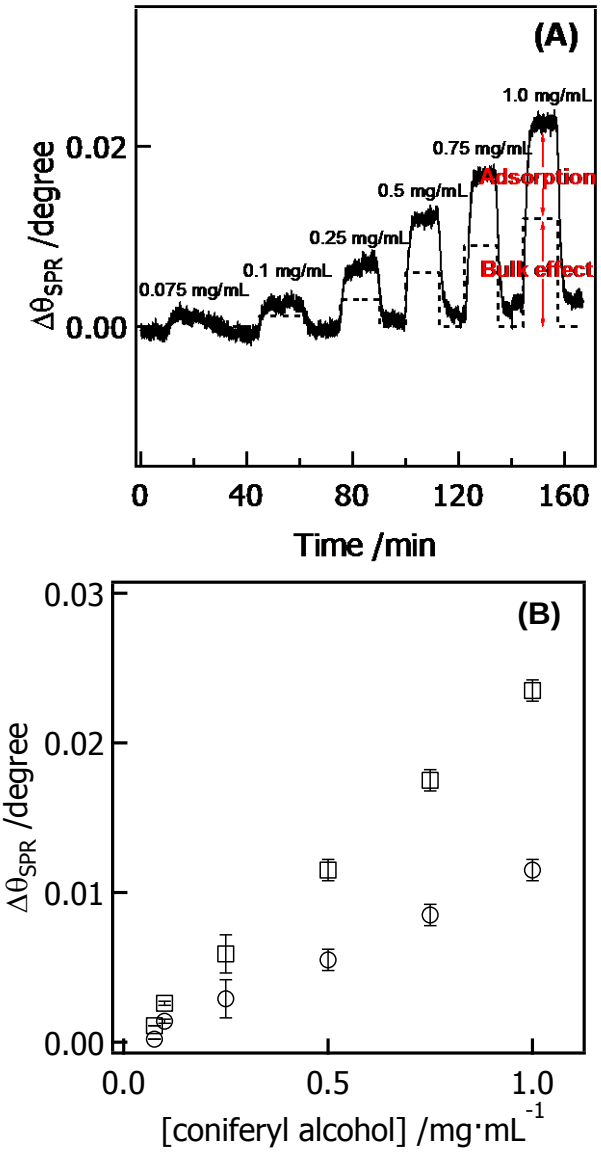


**Figure 10.5.** (A) Representative SPR data for the adsorption of coniferyl alcohol from aqueous solutions onto RC surfaces at 20 °C. (B) Changes in angle (□) before and (○) after subtracting the "bulk" contribution for the adsorption of coniferyl alcohol onto RC surfaces from aqueous solutions at 20 °C.

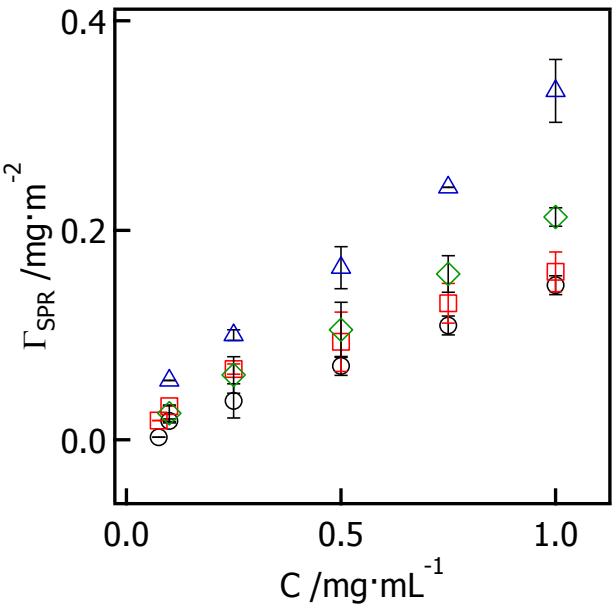


**Figure 10.6.** Adsorption isotherms from SPR for the adsorption of (○) coniferyl alcohol, (◊) *p*-coumaryl alcohol, (Δ) sinapyl alcohol and (□) guaiacylglycerol-*β*-guaiacyl ether onto RC surfaces from aqueous solutions at 20 °C.

### 10.2.4 Chitinase Activity on Amorphous Chitin Thin Films

Chitinases can be classified into two major families, namely family 18 and 19, on the basis of the similarity of their gene sequences, structures and catalytic mechanisms.[15-17] Family 18 chitinases contain the chitinases from microorganisms (e.g., bacteria and fungi) and animals, while family 19 chitinases are found almost exclusively in plants. There are a few exceptions, such as the chitinases from *Streptomyces griseus* which are classified in family 19.[17]

In Chapter 4, family 19 chitinase (from *Streptomyces griseus*) activity on amorphous regenerated chitin (RChitin) thin films at different conditions such as enzyme concentration, temperature, pH and degree of acetylation was studied via QCM-D and AFM. The smooth and homogeneous chitin thin films and the combination of QCM-D and AFM provided a convenient

and promising method to assay the activity of chitinases and other chitinolytic enzymes. Similar to the work presented in Chapter 4, the activity of commercially available family 18 chitinase (e.g., chitinases from *Trichoderma viride* and *Clostridium thermocellum*) on RChitin thin films could also be investigated using QCM-D and AFM.

Neutron reflectometry and QCM-D have been used to study the activity of different cellulases on RC thin films.[18, 19] By combining neutron reflectometry and QCM-D, an in-depth understanding about the interactions between different chitinases and RChitin films could be obtained.

### 10.2.5 Inhibitor Effects on Chitinase Activity

Chitin is one of the major structural components in arthropod exoskeletons and fungal cell walls, and the regulation of chitin metabolism is important for the growth of insects and fungi. Chitinases play essential roles in regulating chitin metabolism, and the inhibitors for specific chitinases are expected to provide safe and effective insecticides or fungicides.[20] Many chitinase inhibitors have been reported in the past two decades. Generally, the chitinase inhibitors are classified into three categories, including oligo- or polysaccharides (e.g., chitosan and allosamidin), peptides (e.g., cyclic dipeptides and cyclopentapeptides) and divalent cations (e.g., $Hg^{2+}$ and $Mn^{2+}$).[21-23]

Similar to the work presented in Chapter 4, the combination of smooth RChitin thin films and a variety of surface characterization techniques is expected to provide a convenient and promising way to investigate the inhibitory effects of different chitinase inhibitors on chitinase activity.

## 10.3 References


(1) Lawoko, M.; Henriksson, G.; Gellerstedt, G. *Biomacromolecules* **2005,** 6, 3467-3473.

(2) Imamura, T.; Watanabe, T.; Kuwahara, M.; Koshijima, T. *Phytochemistry* **1994,** 37, 1165-1173.

(3) Balakshin, M.; Capanema, E.; Gracz, H.; Chang, H.-m.; Jameel, H. *Planta* **2011,** 233, 1097-1110.

(4) Boerjan, W.; Ralph, J.; Baucher, M. *Annu. Rev. Plant Biol.* **2003,** 54, 519-546.

(5) Ralph, J.; Helm, R. F.; Quideau, S.; Hatfield, R. D. *J. Chem. Soc., Perkin Trans. 1* **1992**, 2961-2969.

(6) Ralph, J.; Helm, R. F.; Quideau, S. *J. Chem. Soc., Perkin Trans. 1* **1992**, 2971-2980.

(7) Wilkerson, C. G.; Mansfield, S. D.; Lu, F.; Withers, S.; Park, J.-Y.; Karlen, S. D.; Gonzales-Vigil, E.; Padmakshan, D.; Unda, F.; Rencoret, J.; Ralph, J. *Science* **2014,** 344, 90-93.

(8) Grabber, J.; Schatz, P.; Kim, H.; Lu, F.; Ralph, J. *BMC Plant Biol.* **2010,** 10, 114.

(9) Whetten, R.; Sederoff, R. *Plant Cell* **1995,** 7, 1001-1013.

(10) Miao, Y.-C.; Liu, C.-J. *Proc. Natl. Acad. Sci. U.S.A.* **2010**.

(11) Sibout, R.; Höfte, H. *Curr. Biol.* **2012,** 22, 533-535.

(12) Li, X.; Chapple, C. *Plant Physiol.* **2010,** 154, 449-452.

(13) Tulpar, A.; Ducker, W. A. *J. Phys. Chem. B* **2004,** 108, 1667-1676.

(14) Sigal, G. B.; Mrksich, M.; Whitesides, G. M. *Langmuir* **1997,** 13, 2749-2755.

(15) Patil, R. S.; Ghormade, V.; Deshpande, M. V. *Enzyme Microb. Technol.* **2000,** 26, 473-483.

(16) Dahiya, N.; Tewari, R.; Hoondal, G. *Appl. Microbiol. Biotechnol.* **2006,** 71, 773-782.

(17) Watanabe, T.; Kanai, R.; Kawase, T.; Tanabe, T.; Mitsutomi, M.; Sakuda, S.; Miyashita, K. *Microbiology* **1999,** 145, 3353-3363.

(18) Cheng, G.; Liu, Z.; Murton, J. K.; Jablin, M.; Dubey, M.; Majewski, J.; Halbert, C.; Browning, J.; Ankner, J.; Akgun, B.; Wang, C.; Esker, A. R.; Sale, K. L.; Simmons, B. A.; Kent, M. S. *Biomacromolecules* **2011,** 12, 2216-2224.

(19) Cheng, G.; Datta, S.; Liu, Z.; Wang, C.; Murton, J. K.; Brown, P. A.; Jablin, M. S.; Dubey, M.; Majewski, J.; Halbert, C. E.; Browning, J. F.; Esker, A. R.; Watson, B. J.; Zhang, H.; Hutcheson, S. W.; Huber, D. L.; Sale, K. L.; Simmons, B. A.; Kent, M. S. *Langmuir* **2012,** 28, 8348-8358.

(20) Sakuda, S.; Inoue, H.; Nagasawa, H. *Molecules* **2013,** 18, 6952-6968.

(21) Saguez, J.; Vincent, C.; Giordanengo, P. *Pest Technol.* **2008,** 2, 81-86.

(22) Gupta, R.; Saxena, R. K.; Chaturvedi, P.; Virdi, J. S. *J. Appl. Bacteriol.* **1995,** 78, 378-383.

(23) Spindler, K. D.; Spindler-Barth, M. *EXS* **1999,** 87.